Imaging Mass Spectrometry and Microbial Pathogenesis: The Effect of Calprotectin on Pathogen-Host Interactions

By

Jessica Lindsey Moore

Dissertation
Submitted to the Faculty of the
Graduate School of Vanderbilt University
in partial fulfillment of the requirements
for the degree of

DOCTOR OF PHILOSOPHY
in

Chemistry
May, 2017
Nashville, Tennessee

Approved:

Richard Caprioli, Ph.D.

Eric Skaar, Ph.D., M.P.H.

David Cliffel, PS.D.

Walter Chazin, Ph.D.

John McLean, Ph.D.

ACKNOWLEDGEMENTS

Many people have helped me along this journey, and many thanks are required. First and foremost, my advisors, Dr. Richard Caprioli and Dr. Eric Skaar, who have served as compassionate advocates and mentors as I made my journey into scholarhood. You have encouraged me to think broader, take risks, and never give up. And for this, I am incredibly grateful. I am also grateful for the opportunity to study in both of your laboratories; my access to cutting edge technology and biology has enabled me to understand incredible biology in advanced ways. To my committee, David Cliffel, Walter Chazin, and John McLean, I am also thankful. Thank you for taking the time to guide me and for always pushing me to excellence during my time at Vanderbilt.

Special thanks to our funding sources at the National Institutes of Health through whose confidence and support I was able to pursue truly interesting biological problems with mass spectrometry (NIH/NIGMS grants 8P41 GM103391 and S10 RR026742). Thank you to the Burroughs Wellcome Fund in Microbial Pathogenesis for enabling these studies. I thank the Vanderbilt Chemical Biology Interface Training Program not only for their funding but also for extensive career development to help me along my way (T32 GM065086). Thank you to the Vanderbilt Institute for Chemical Biology and the Vanderbilt Warren Fellowship for funding me as a scholar, and to the Vanderbilt Prize Scholar program for their recognition of my work.

My laboratory mates have been my foundation and my constant cheerleaders. Thank you for your wonderful support of my ideas and willingness to help me. Thank you for listening to endless chatter about neutrophils and calprotectin. Thank you for taking me to Sitar when I got bad reviews and when I got good ones. Thanks to David Rizzo and Chad Chumbley, my fellow

graduate students who trail-blazed a year before me. Thank you to Boone Prentice, my source of ion chemistry, Kristie Rose for top-down sequencing, and Jeff Spraggins, the guru of FTICR. Special thanks to Jamie Allen, a true friend and the most thoughtful person to walk this Earth. And finally to the magnificent Maureen Casey, who is truly the foundation of the MSRC. We don't know what we would do without you.

Special thanks to my microbiologists, who helped me understand the vast world of tiny bugs. To Thomas Kehl-fie, who was my first "staph scientist" and had incredible patience when I was brand new. To Neal Hammer, who never hesitated to help me chase crazy hypotheses and helped me with countless infections. And of course to Catherine Wakeman, the queen of the biofilm, who was never afraid to become the creator of some truly disgusting and foul-smelling endeavors.

Thank you to my family who supported me along the way. To my loving husband Eli who was a rock of my sanity the entire way. Thank you for always making me coffee. To our lovely puppies, China and Donnie, whose cuddles make even the darkest day brighter. To our daughter Hazel, who continues to amaze me every day and caused me to write a lot of this dissertation one-handed. And to my wonderful parents, Leonard and Kim, and my brother Hal, who have supported me every step of my 10+ year college career.

TABLE OF CONTENTS

LIST OF TABLES

LIST OF FIGURES

LIST OF ABBREVIATIONS

2D: Two Dimensional

3D: Three Dimensional

AGC: Automatic Gain Control

AQ: Alkyl-Hydroxyquinolones

BLI: Bioluminescence Imaging

B-PER: Bacterial Protein Extraction Reagent

Ca: Calcium

CAD: Collision Activated Dissociation

CF: Cystic Fibrosis

CFU: Colony Forming Units

CHCA: α-Cyano 4-Hydroxycinnamic Acid

CID: Collision Induced Dissociation

CP: Calprotectin

CPKO: Calprotectin Knock-out

d: Distance

Da: Dalton

DAMP: Damage-Associated Molecular Pattern Marker

DFR: Drip-flow Reactor

DHA: 2,5-Dihydroxyacetophenone

DHB: 2,5-Dihydroxybenzoic Acid

DNA: Deoxyribonucleic Acid

DPI: Days Post Infection

ESI: Electrospray Ionization

ETD: Electron Transfer Dissociation

FDR: False Discovery Rate

Fe: Iron

FFPE: Formalin-fixed Paraffin Embedded

FOV: Field of View

FTICR: Fourier-Transform Ion Cyclotron Resonance

GLNB: Glucose Supplemented Low Nutrients Broth

H&E: Hematoxylin and Eosin

HPI: Hours Post Infection

HPLC: High Performance Liquid Chromatography

HQNO: 4-hydroxy-2-heptylquiniline-N-oxide

Hz: Hertz

ICP: Inductively Coupled Plasma

ICU: Intensive Care Unit

IMS: Imaging Mass Spectrometry

ITO: Indium-Tin Oxide

kDa: Kilodalton

KE: Kinetic Energy

LA-ICP-MS: Laser-Ablation Inductively Coupled Plasma Mass Spectrometry

LB: Luria-Bertani Medium

LOD: Limit of Detection

m: mass

MALDI: Matrix-Assisted Laser Desorption/Ionization

min: minutes

Mn: Manganese

MRI: Magnetic Resonance Imaging

MS: Mass Spectrometry

MS/MS: Tandem Mass Spectrometry

m/z: Mass-to-Charge Ratio

ND:YAG: Neodymium-doped Yttrium Aluminum Garnet

ND:YLF: Neodymium-doped Yttrium Lithium Fluoride

NETs: Neutrophil Extracellular Traps

OCT: Optimal Cutting Temperature Polymer

PAMP: Pathogen-associated Molecular Pattern Marker

PBS: Phosphate Buffered Saline

ppb: Parts Per Billion

ppm: Parts Per Million

PQS: 2-heptyl-3-hydroxy-4-quinolone

PTM: Post-Translational Modification

qRT-PCR: Quantitative Real Time Polymerase Chain Reaction

QS: Quorum Sensing

RF: Radiofrequency

RNA-Seq: Ribonucleic Acid (RNA) Sequencing

ROS: Reactive Oxygen Species

SA: Sinapinic Acid

SEM: Scanning Electron Microscope

t: Time

TE: Echo Time

TFA: Trifluoroacetic Acid

TFE: Trifluoroethanol

TOF: Time-of-Flight

T-PER: Tissue Protein Extraction Reagent

TR: Repetition Time

TSB: Tryptic Soy Broth

UV: Ultraviolet

V: Voltage

v: Velocity

YESCA: Yeast Extract with Casamino Acid

z: charge

Zn: Zinc

CHAPTER I

MASS SPECTROMETRY AND PATHOGENESIS

A version of the following chapter was previously published and has been adapted from Moore et al., *Current Opinion in Microbiology,* Copyright 2014 by Elsevier[1], Spraggins, Rizzo, Moore et al., Proteomics, Copyright 2016 by Wiley and Sons[2], and from Moore et al., *Proceedings of the NATO Advanced Study Institute in Rapid Threat Detection*, Copyright 2017 by Springer.[3]

Overview

Human disease is characterized by signature changes at a molecular level that present in affected tissues and organs. Diseases cause disruption and dysregulation of a number of biological molecules, including proteins, lipids, metal, and small molecules. Often, disruption can involve rearrangement of biomolecules in a way that is regiospecific. Understanding the spatial distribution of biomolecules as it relates to human disease is incredibly important; it represents a way to study disease-associated changes in tissues. Certain technologies have been leveraged for such studies, including immunohistochemistry, fluorescent *in situ* hybridization, and other molecular tagging approaches. These analytical approaches are limited as they require prior knowledge of the analytical target and optimized reagents to perform such analyses. This work utilizes Imaging Mass Spectrometry (IMS), a discovery-based analytical approach that enables the detection of biological molecules spatially within diseased tissues. For diseases that are hallmarked by small regional areas of inflammatory response, such as bacterial infections, IMS proves to be a powerful

analytical technology to discover novel molecular changes specific to areas in the tissue where pathogens interact with their vertebrate hosts. This region, deemed the pathogen-host interface, presents a wealth of information about how vertebrate hosts defend themselves from invading pathogens. Further study of these interactions in the field of infectious diseases is paramount to understand microbial pathogenesis and to continue to find therapeutic strategies to treat infections.

Matrix-Assisted Laser Desorption/Ionization Imaging Mass Spectrometry

Matrix-assisted laser desorption/ionization mass spectrometry (MALDI MS) is an analytical technology that enables direct analysis of biomolecules. MALDI utilizes a matrix, typically a small organic acid with strong ultraviolet (UV) absorbance, which is uniformly mixed with analytes to aid desorption and ionization.[4] MALDI employs the use of a laser that generates light in the UV range to provide the energy for desorption and ionization. Historically, nitrogen lasers (337 nm) were used extensively in MALDI instruments, but have seen a decline due to their low repetition rates, short lifespans, and the increase of more efficient laser technology. Solid-state lasers such as the frequency-tripled neodymium-doped yttrium aluminum garnet (ND:YAG, 335 nm) and neodymium-doped yttrium lithium fluoride (ND:YLF, 349 nm) have become the standard for the majority of MALDI experiments. Gas phase ions are generated post laser pulse and are mass analyzed in the mass spectrometer. Ions are detected and displayed in a spectrum according to their mass-to-charge ratios (*m/z*), which yield specific molecular signatures within complex samples. Figure 1.1 represents a cartoon schematic of this process. This label-free technology can be used without prior knowledge of sample composition, allowing for the detection of a variety of analytes, from small molecules to large proteins.[5] Combined with efficient analyte identification strategies and the emergence of online searchable databases [6, 7], MALDI MS has been successfully

applied to a variety of biological samples, including tissue sections [8], plants [9], insects [10], whole animals [11], and microbial colonies.[12] The ability to analyze such a wide range of systems has led to the use of MALDI MS as a clinical tool, particularly in diagnostic microbiology. Additionally, it can be used in a histology-directed manner, where regions of interest are annotated and then interrogated using MALDI MS.[13] This approach allows researchers to interrogate only certain regions of biological interest to save resources, or to use the technology as a diagnostic tool for molecular pathology.[14-16]

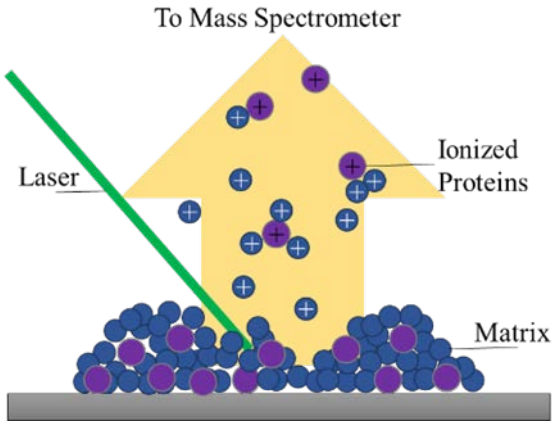

Figure 1.1: Schematic of MALDI

Cartoon schematic of matrix assisted laser desorption/ionization. Here a matrix, pictorially depicted as blue circles, is mixed with analytes, depicted as purple circles. The mixture is provided energy using a laser pulse, which in turn causes the analytes to ionize and desorb into the gas phase, where ions can be separated and measured. Reprinted from *Proceedings of the NATO Advanced Study Institute in Rapid Threat Detection*, 2017, *Imaging Infection*, with permission from Springer Publishing Company[3].

Mass spectrometry can be used as an imaging modality by systematically interrogating samples at defined *x/y* coordinates, shown in Figure 1.2. Samples are thinly sectioned and mounted onto surfaces, typically gold sample plates, stainless steel targets, or glass slides. Next, a matrix is applied homogeneously across the sample. The laser is used to interrogate the sample at defined *x/y* coordinates across the sample in entirety. At each *x/y* coordinate, ions are generated and a mass spectrum is recorded. The spectral data can be correlated back to the *x/y* position to generate heat maps for each ion of interest. Heat maps can be generated based on the maximum spectral intensity or on the total integrated value of each defined *m/*z window or bin. Image spatial resolution is the term used to define the spacing between pixels, though a number of factors affect spatial resolution. Spatial resolution is affected both by the size of the laser spot on the target used to interrogate the section as well as the step size between the points in the array. IMS reveals not only the specific *m/z* of the analyte but also the spatial origin of that analyte. Using this modality, molecular species of interest can be tracked regiospecifically to biological foci to help draw conclusions.

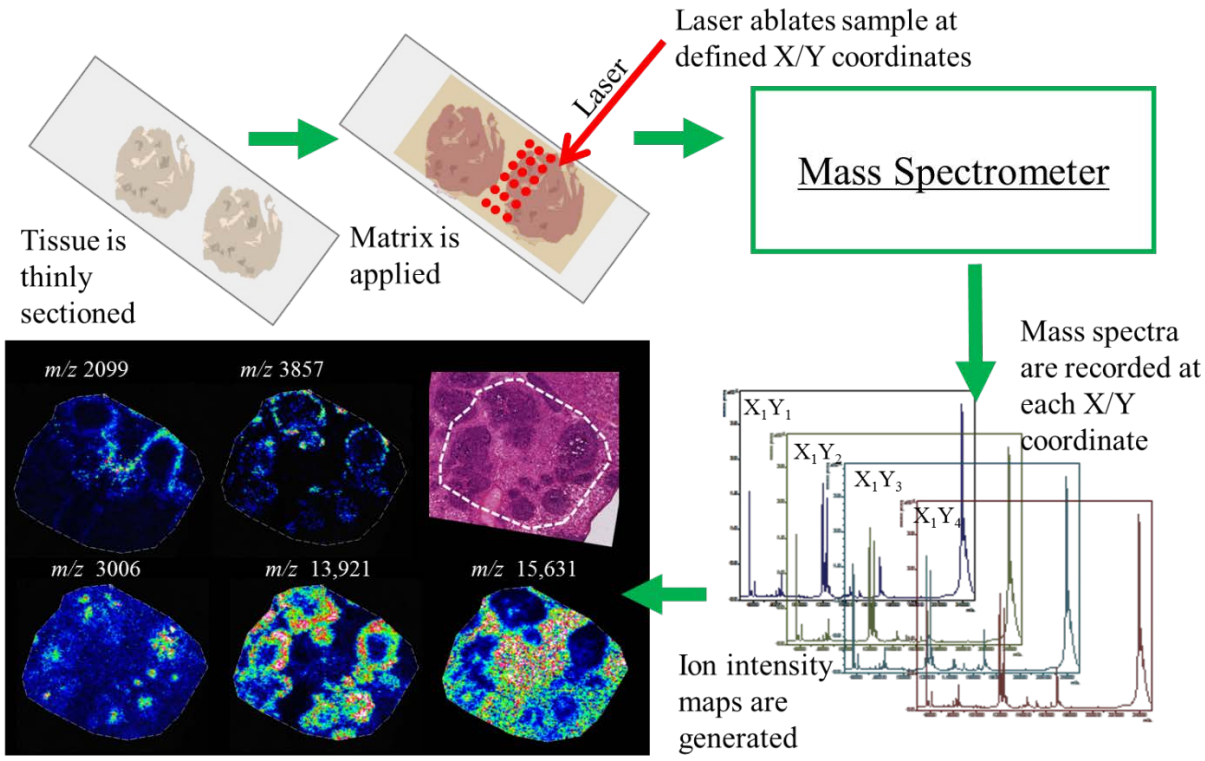

Figure 1.2: Schematic of MALDI Imaging Mass Spectrometry

The MALDI Imaging Mass Spectrometry workflow begins with tissues sectioned very thinly and mounted to a slide. Tissues can be washed to remove interfering lipids and salts or not treated at all. MALDI matrix, typically small organic acids, are then applied to the surface in a homogeneous way. A laser is used to interrogate the sample at defined *x/y* coordinates and a mass spectrum is collected at each location. Heat maps can be generated by setting mass windows and integrating the area under the peak in the selected windows. These heat maps reveal the spatial distribution of analytes within thin sections. Reprinted from *Proceedings of the NATO Advanced Study Institute in Rapid Threat Detection*, 2017, *Imaging Infection*, with permission from Springer Publishing Company.[3]

Time-of-Flight Mass Spectrometry

The most commonly employed MALDI mass spectrometers is the time-of-flight mass spectrometer (MALDI TOF MS.) TOF mass analyzers are used to determine the *m/z* of ions based on the time it takes them to transverse a field-free region. Figure 1.3A represents a schematic of a TOF mass analyzer. The components are relatively simple: there is an accelerating electrode which serves to start all ions at the same time, a field-free drift region to allow them to separate, and a detector to monitor when the ions transverse the drift region. Ions are given the same initial kinetic energy from the electrode, but ions will have different velocities based on their masses, thus separating them in time. The initial kinetic energy (KE) is defined as the charge of ion (z) times the accelerating voltage (V.)

$$\mathrm{KE} = \mathrm{zV}$$

This is set equal to the traditional equations for kinetic energy, where the mass of the ion (m) is multiplied by the velocity (v.)

$$\mathrm{KE} = z\mathrm{V} = \frac{\mathrm{m}v^2}{2}$$

The velocity of the ions can be represented as distance (d) over time (t.) Substituting those parameters, the equation can be rearranged to use the time-of-flight to discern the mass to charge ratios, since the distance traveled and accelerating voltage are constant.

$$\mathrm{t} = \mathrm{d}\sqrt{\frac{m}{2z\mathrm{V}}}$$

MALDI-TOF mass spectrometers are the primary instrument for molecular imaging experiments. They are highly sensitive and have a large practical mass range, allowing them to analyze a plethora of biomolecules. They also have high duty cycles, a factor important for imaging

experiments when many mass spectra must be collected in a reasonable amount of time. New MALDI-TOF systems are equipped with ultrafast lasers, allowing rapid data generation.[17]

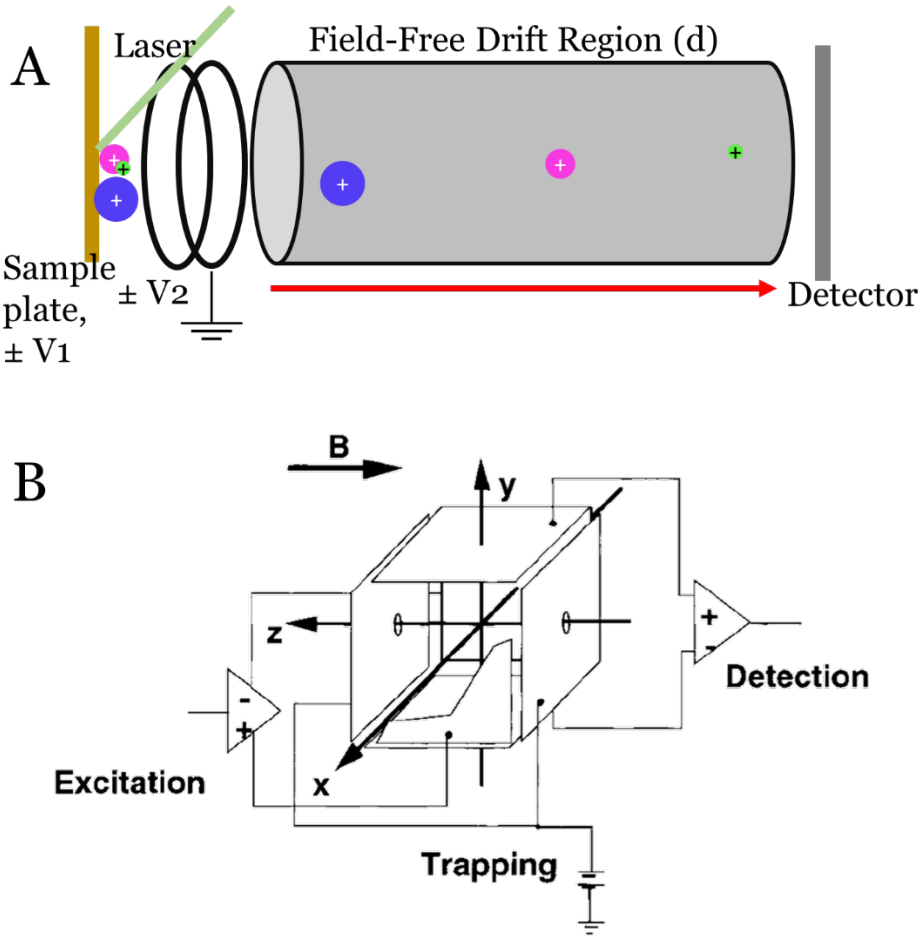

Figure 1.3: Time-of-Flight and Fourier Transform Ion Cyclotron Resonance Mass Analyzers

This schematic shows two common types of mass analyzers. A time-of-flight mass analyzer is shown in A. Ions are accelerated through an electric field, giving the ions the same kinetic energy. The velocity of the ions through the field-free drift region is dictated by their *m/z* ratio. B. shows the electronic circuitry and set-up of a Fourier transform ion cyclotron resonance mass analyzer. Ions undergo cyclotron motion within the magnetic field, where they are excited and detected using perpendicular electronic plates. B was reprinted from "Fourier Transform Ion Cyclotron Resonance Mass Spectrometry: A Primer" page 1-35, 1998, with permission from John Wiley and Sons.[18]

Fourier Transform Ion Cyclotron Resonance Mass Spectrometry

MALDI sources can also be coupled to other mass analyzers, including Fourier transform mass spectrometers. One such examples is the Fourier Transform Ion Cyclotron Resonance (FTICR) mass spectrometer, which is explained in great detail by Marshall et al..[18] These mass analyzers provide the highest mass resolution and accuracy. The mass spectrometer consists of a super conducting magnet, which provides a uniform magnetic field, and an ICR cell located in the center of the magnet. Ions are introduced to the ICR cell where they are subjected to a Lorentz force, causing the ions to move in a direction perpendicular to the magnetic field. The ion motion will bend into a circular path, orbiting the cell, with a frequency that is directly proportional to the *m/z* ratios. The motion of the ions is related to their mass, which dictates the frequency with which they orbit within the cell. A simple schematic of this is shown in Figure 1.3B. The ICR cell contains two trapping plates, two excitation plates, and two detection plates. The trapping plates are placed at the end of the ICR cell to confine the ions in the x-plane as shown in Figure 1.3. Upon injection into the ICR cell, ion motion is incoherent and not yet useful to determine the mass. To generate a detectable signal, a radio frequency is applied between the two excitation plates at a frequency that matches the cyclotron frequency of the ion. Upon resonant excitation, ions are accelerated to a larger, detectable radius. As a packet of ion moves closer to the detection plate, an image current is induced allowing for the ions to be measured.

These instruments have the unique ability to provide multiple detection events for a single laser shot, and even have the ability to accumulate ion populations from multiple laser shots prior to detection[19]. This is unlike MALDI-TOF mass spectrometers, where a single laser shot generates a single detection event, and helps contribute to the high mass resolving power of these instruments. These mass spectrometers have achieved high resolution in MALDI IMS

experiments, with reported mass resolving powers of greater than 50,000 ($m/\Delta m_{50\%}$) and mass accuracy of sub 5 ppm.[20, 21] Such performance is quite important for IMS experiments, where on-tissue analysis demands the ability to distinguish both overlapping isotopic distributions as well as nominal isobars. This improvement in resolving power is counterbalanced by time needed for analysis; detection events are much longer than those in MALDI-TOF systems, sometimes lasting seconds per pixel. This is particularly important for MALDI IMS experiments, which each pixel in the image represents a mass spectrum and long detection times can greatly contribute to analysis times that are not amicable to clinical workflows.

Laser Ablation Inductively Coupled Plasma Mass Spectrometry

LA-ICP IMS is a technology enabling *in situ* analysis of elemental distribution within a two dimensional sample.[22] Similar to the MALDI IMS workflow, samples are thinly sectioned and mounted onto slides for analysis. A UV laser is used to systematically ablate material into a sheath gas, which carries the material to the ICP torch for ionization.[23] This can be used to visualize the spatial distributions of elements within samples, including tissue sections. Heterogeneities of metal availability during disease can be determined using this method. The nutrient metal localization can then be compared to the protein patterns assessed by MALDI IMS to identify subpopulations of analytes that correlate with differential nutrient availability.

Analyte Identification Strategies

MALDI IMS experiments uncover a number of spatially resolved species, revealing novel molecular information from a variety of systems. However, in order to drive biological conclusions, identification of these analytes is necessary. The sheer volume of targets from the

robust data can be overwhelming; however, many recent advancements in the field have aided analyte identification. Though others have focused on identification of endogenous metabolites, small molecules, and lipids; this work will focus on protein and peptide identification strategies. An overview of these strategies is depicted in Figure 1.4.

Protein identification strategies can be classified in three general categories: bottom-up, top-down, and indirect. Bottom-up experiments involve a solution-phase enzymatic digestion of protein targets prior to analysis.[24] This can be performed *in situ*, allowing histology-directed or imaging MS experiments to be performed on a peptide level, or on purified protein targets. Special consideration must be made during *in situ* digestion to not cause peptide delocalization during enzymatic digestions. Matrix is applied and MS and tandem MS (MS/MS) analyses can be performed directly from tissue sections.[25] MALDI generated ions tend to be singly charged and commonly employed MS/MS techniques such as collision-induced dissociation (CID) yield insufficient fragmentation data. Additionally, it can be difficult to fragment peptides directly from tissue sections both because it is difficult to effectively isolate parent ions from the complex background and because the fragmentation efficiency from singly charged parent ions are low. Enzymatic digestion of proteins is favorable because it extends the mass range of observable proteins by allowing peptides of very large proteins to be analyzed.

Top-down proteomics approaches provide another approach for protein identification from MALDI IMS experiments. Here a high mass resolution measurement is taken from an intact molecular weight species, such as a protein, which is then followed by gas phase fragmentation.[26] Top-down fragmentation from MALDI MS typically utilizes post-source decay and therefore relies on analytes that are both abundant and pure, making *in situ* MS/MS measurements challenging. More efficient fragmentation techniques, such as electron transfer dissociation (ETD,)

provide an alternative approach to gather useful fragmentation data from an intact protein. Although efficient, this technique relies on analytes being in higher charge states and tends to be ineffective for MALDI ions. Top-down approaches such as ETD are ideal for studying intact proteins as they can characterize different proteoforms of a protein and have been shown to keep the labile post-translational modifications (PTMs) intact.

Indirect identification strategies rely on secondary information generated from additional experiments completed in tandem with the imaging experiment. Typical workflows utilize electrospray ionization (ESI) to generate peptides and protein in higher charge states, making them more amenable for common MS/MS techniques. These indirect methods first involve the collection of a MALDI image from a tissue section of interest. In indirect methods, a MALDI image is typically collected on a tissue section while proteins are extracted from either serial sections or bulk homogenate for either top-down or bottom-up LC-MS/MS based strategies. Indirect identification strategies are advantageous because they allow both the imaging and proteomics experiments to be operated under optimal conditions to maximize the sensitivity for both analytical approaches.

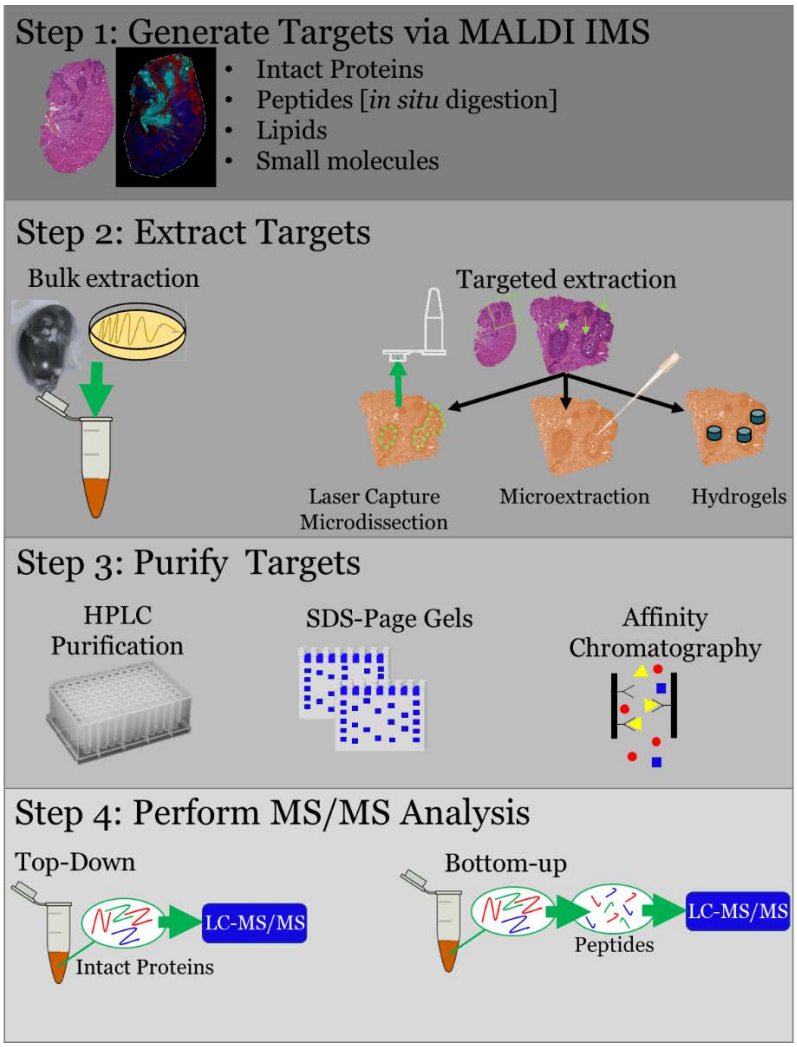

Figure 1.4: General Protein Identification Workflow

Step 1 includes generating targets from MALDI IMS experiments. These can be a range of analytes from proteins to lipids and small molecules. An ideal analyte is robust, appearing in technical replicates of the same tissue sections and reproducible, appearing in biological replicates of the same biological model. Step 2 involves physically extracting the targets from the tissue. This can be done from bulk homogenates or spatially from a tissue section. Care should be taken to match the sample preparation used in IMS experiments when using the tissue section methods. This includes washing strategies to remove interfering analytes. Step 3 is to further purify samples if needed. A broad range of strategies can be used, including offline HPLC fractionation, SDS-PAGE gels, or affinity chromatography. Step 4 is used to actually fragment the analyte of interest. Two main proteomics approaches are used: top-down sequencing which fragments intact proteins and bottom-up, which utilized an enzymatic digestion to create peptides which are fragmented. Reprinted from *Proceedings of the NATO Advanced Study Institute in Rapid Threat Detection*, 2017, *Imaging Infection*, with permission from Springer Publishing Company.[3]

Protein Identification Strategies

A majority of intact MALDI IMS and histology-directed experiments focus on small proteins, typically under 30 kDas. Protein identification strategies typically begin with analyte extraction (Figure 1.4, Step 2). This can be performed in bulk, by homogenization of the sample, or in more spatially directed approaches, including laser capture microdissection or punch biopsies. Another recent method, called microextraction, allows researchers to extract directly from tissue sections in a spatially refined manner.[27] When trying to identify species from IMS experiments, enriching the sample for the species of interest by spatially directed extraction can greatly enhance the chance at analyte identification.

Bottom-up proteomics approaches have been used with success for protein identification. In these experiments, an enzyme, typically trypsin or LysC, is used to cleave the protein of interest to peptides for traditional LC-MS/MS analyses. Since the MS/MS analysis is performed at the peptide level, it is sometimes difficult to isolate which intact protein mass corresponds to the MALDI MS target. In solution digestions of bulk extracts are very rich and will yield a large number of protein identifications. While this presents a wealth of knowledge related to the biology of the sample, it is not the best approach for matching protein identities to MALDI MS experiments.

A large majority of identification of small proteins from MALDI MS experiments have utilized in-gel digestions for identification. In this strategy, the protein of interest is loaded into a high percentage SDS-PAGE gel. The gel band or region of interest is excised and subjected to in-gel tryptic digestion and analyzed by LC-MS/MS analysis. This method is relatively straightforward and has been used with success.[28, 29] However, a plethora of proteins are successfully identified from a single gel band or a region of a gel. This requires the researcher to

make an educated association for identification. Identifications should be made with consideration of peptide counts for each identified species as well as the theoretical mass of the protein. The analyte of interest could be a small fragment of a much larger protein, introducing uncertainty in the identification. Additionally, this method has difficulties in assessing post-translational modifications or truncations that cause deviation from the anticipated intact mass. Additional certainty can be gained by adding a separation before the gel step (Figure 1.4, Step 3). Here, a protein extract is fractionated by another analytical technique, traditionally HPLC or affinity chromatography, with fractions collected and stored. When MALDI MS is used to interrogate the fractions, the analyte of interest can be isolated to a more purified fraction. Using this approach will decrease the amount of protein identified from the gel band and can therefore give the researcher more confidence in the identification.[29]

Top-down sequencing presents an ideal method for protein identification. In this workflow, the intact protein is fragmented using ETD. In this approach, the intact mass of the protein is recorded prior to fragmentation. This removes any ambiguity about which parent ion the fragments derived from. When trying to assign identities to MALDI MS experiments, this approach is superior because the mass of the parent can be matched back to MALDI data.[30]

Peptide Identification Strategies

MALDI MS profiling and imaging experiments are not limited to intact proteins. Performing a digestion step either in solution or *in situ* prior to MALDI analyses has great benefit. It allows for the analysis of proteins that are very large or for the analysis of biopsies that have been fixed. Traditional enzymatic digestion protocols require an incubation step to allow the enzyme to act upon the proteins in the sample. *In situ* enzymatic digestion has been performed on

both fresh-frozen and formalin-fixed, paraffin embedded (FFPE) tissue for peptide profiling and classification.[31, 32] Though these methods have not yet been applied to infectious diseases, it is an attractive solution for handling clinical biopsies of unknown origin or those of significant biosafety risk. Additionally, since the analytes measured in this approach are peptides, it is much easier to match the analyte mass to the species sequenced in a parallel LC-MS/MS analysis using indirect identification strategies, circumventing the problems discussed above.

Another emerging technology that can be used for peptide identification is the hydrogel. Here a small punch of acrylamide is loaded with enzyme and placed on the tissue for digestion.[33] Spatially defined proteomics can be performed on the surface of tissue samples using such an approach. Hydrogel technologies have been used to successfully interrogate both fresh-frozen and formalin-fixed biopsies.[14] Additionally, hydrogel technologies have been coupled to microwave-assisted enzymatic digestion to decrease the time needed to perform a digest.[34] Rapid tryptic digestion allows the analysis of peptides to be within the time range needed for practical implementation into clinical workflows.

Infectious Diseases

According to the Centers for Disease Control, an estimated 2 million people each year become infected with antibiotic-resistant bacteria. Of these 2 million, there are a reported 23,000 deaths directly attributed to the microbes.[35] Compounding this threat is the tremendous rate at which pathogens are gaining resistance to antimicrobial strategies. This is partially because antibiotics are overly prescribed, with suboptimal prescriptions occurring in as often as 50% of all cases. Between 1935 and 2003, there were fourteen emerging classes of antibiotics.[36] The decrease in emerging therapeutics is convoluted; novel antibiotic development is an expensive endeavor

that is not often profitable for pharmaceutical companies.[36] In addition, the time from antibiotic deployment to emergence of clinically relevant resistance has dramatically decreased when new antimicrobials do become available.[37] This led the Infectious Disease Society of America to release a 2009 call to action to study microbial resistance and to target seven bacteria of particular concern.[38] These pathogens were deemed the "ESKAPE" pathogens and include *Enterococcus faecium, Staphylococcus aureus, Klebsiella pneumonia, Acinetobacter baumannii, Pseudomonas aeruginosa*, and *Enterobacter* species. In order to continue treating infections caused by these bacteria, it is important to study their pathogenesis using novel and emerging analytical technologies. The application of such technologies might isolate novel targets for antimicrobial intervention, and further aid the treatment of antimicrobial resistance at the cusp of the post-antibiotic era.

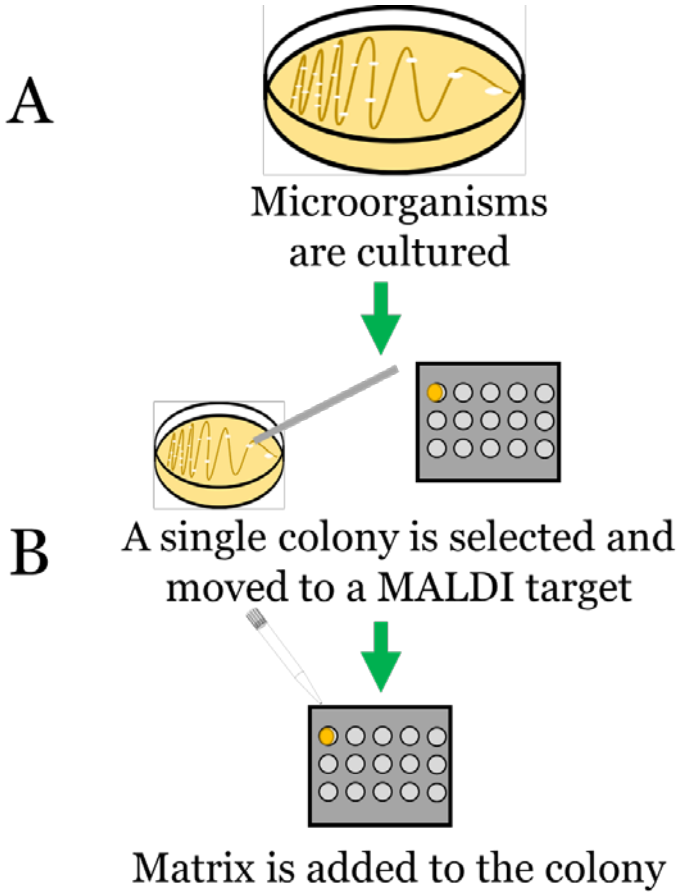

Figure 1.5: Traditional Workflow for MALDI MS Identification of Microorganisms
A typical workflow for MALDI MS-based spectral matching for microbial identification. A) The unknown pathogen is cultured using standard techniques on agar plates. A single colony is selected and moved onto a MALDI target using a sterile device. Care is taken to not move agar with the colony, as it introduces interferences into the sample. Finally, cells are lysed on target when they are mixed with a MALDI matrix in an organic solvent, typically α-cyanocinnamic acid in 50% acetonitrile. B) Once the cells are lysed, the proteins extracted into the organic solvent will co-crystalize with the MALDI matrix. Upon interrogation in the mass spectrometer, a laser passes energy to the matrix, ionizing the small proteins. The ionized proteins are measured using a mass spectrometer and result in a characteristic mass spectrum that can be used to classify bacteria. Reprinted from *Proceedings of the NATO Advanced Study Institute in Rapid Threat Detection*, 2017, *Imaging Infection*, with permission from Springer Publishing Company.[3]

MALDI Mass Spectrometry and Infectious Diseases

MALDI MS can distinguish molecular fingerprints associated with specific microorganisms, allowing for the rapid identification of infectious agents. MALDI MS presents a means to interrogate intact cells from agar plates or liquid media, leading to robust *m/z* signatures independent of culture conditions.[39] Microbial colonies from culture are moved onto MALDI targets, mixed with matrix, and analyzed using a mass spectrometer (Figure 1.5). This has been expanded to include identification of fungi and bacteria that are difficult to culture, such as anaerobic or highly infectious bacteria.[40-43] Advances in sample preparation have improved the reproducibility of MALDI MS measurements from intact cells, making it a promising tool for diagnostic microbiology.[12, 44, 45]

Microbial fingerprinting using MALDI MS can provide accurate determination of spectral peaks specific to both species and genus.[46, 47] Initial studies have been compiled into a collection of databases that can be used to classify clinical isolates quickly and accurately. [12] Instrumental set-ups, automated analyses, and database searching platforms tailored to these applications are available from commercial instrument manufacturers, including FDA-approved systems like the MALDI BioTyper system (Bruker Daltonics) and the Vitek microbial identification system (Biomérieux).[48] Databases are perpetually evolving to meet biological needs and to include emerging strains, bacterial subtypes, and to differentiate pathogenic and non-pathogenic strains.[46, 47 49 50] Furthermore, comparative analyses of spectral information can be used to determine microbial lineage, which provides a rapid and sensitive tool to diagnose and control outbreaks of pathogenic microbes.[51] Clinical analyses have also included profiles from complex mixtures, including blood cultures and complex polymicrobial infections.[52] For example, direct MALDI MS analysis of centrifuged blood culture broths from patients with bacteremia in intensive care units

has been utilized to accurately identify microbes from complex, polymicrobial samples. The approach also requires substantially less time than previous diagnostic methods.[52] These continued advancements decrease the time needed to identify a pathogen, shortening the amount of time until antibiotic intervention and therefore decreasing the cost of care.[53] This has revolutionized clinical care of bacterial infections, in particular in cases of sepsis.[54] Successful implementation of this workflow has been extended from clinical diagnostic laboratories to botany labs for the study of plant pathogens and to the food service industry to study food-spoiling pathogens.[55, 56]

Such advancements greatly decrease both time and cost associated with microbial identification, leading to more efficient antimicrobial intervention. Integration of MALDI MS technologies into clinical laboratories therefore has the potential to dramatically affect infectious disease medicine and have a positive impact on human health.[53]

MALDI Profiling of Infected Human Tissues

The analytical power to rapidly identify microorganisms from culture has been a major advancement. However, a culture step is still required, removing the microorganism from the complex environment of the host organism, and severely delaying the time required to positively identify the causative agent of infection. This approach makes the study of microbial pathogenesis and virulence difficult because microorganisms in culture are not experiencing the same conditions as microorganisms growing within the host. However, there are significant analytical challenges associated with the study of bacteria actively causing diseases within the host. Bacteria and their products are generally of limited abundance when compared to host markers and require high sensitivity in analytical technology. However, MALDI MS is emerging to fill this gap and to perform analyses from complex mixtures.

MALDI MS profiling experiments collect a number of discrete spectra from various cell types within samples for comparison. This approach was used in a recent study that searched for serum host-response biomarkers for sepsis in neonates in intensive care units. Sepsis-associated *m/z* values, including *m/z* 11,528, identified as a variant of the host inflammatory protein serum amyloid A, provided diagnostic markers which could be detected from serum at birth. Scoring of these biomarkers will allow clinicians to determine which patients should be placed on antimicrobial therapies and has prompted the design of a triage strategy for suspected cases of neonatal sepsis.[57]

Another study utilized MALDI MS profiling to study the host response to *Staphylococcus aureus* infected skin wounds over time. Skin lesions infected with *S. aureus* were swabbed into sterile water at various time points post-infection. Both swab samples and wound exudate were analyzed by MALDI MS. Comparison of collected spectra from wound beds and cultured *S. aureus* revealed several matching *m/z* values. Additional signals were detected from the wound bed thought to belong to mouse defensins and blood, highlighting the ability of MALDI profiling to monitor bacterial signals, host response to infection, and wound healing over time.[58] Such analyses could lead to direct microbial analysis from soft tissue infections and aid in diagnosis of chronic wound infections.

In addition to analyzing spotted tissue homogenates or serum, MALDI MS provides the distinct advantage of *in situ* tissue profiling. This method allows molecular signals to be obtained directly from tissue sections in a spatially-targeted approach, allowing pathologists to focus analyses on histological regions of disease.[59] Approaching large sample sets in a histologically-directed way presents a reasonable method to differentiate signals associated with disease in a high-throughput manner. This approach also presents an alternative way to characterize bacterial

signatures *in vivo* at a point when these organisms are actively causing disease within host tissues. The histology-directed approach has been applied to the study of bacterial sarcoidosis in snap-frozen human tissue. Targeting only the granulomas, *m/*z values were observed to correlate with either bacterial infectious foci or control tissue.[60]

Staphylococcus aureus

One noted ESKAPE pathogen that has been extensively studied by IMS is *Staphylococcus aureus. S. aureus* colonizes the anterior nares of approximately 30% of the population, with approximately 2% of those strains being antibiotic resistant.[61] It is a cause of significant morbidity, accounting for half of all reported deaths from antibiotic resistant bacteria reported in the CDC's 2013 report.[35] *S. aureus* can colonize virtually all sites in the human body to cause diseases, including skin and soft tissue infections, osteomyelitis, endocarditis, sepsis, and pneumonia.

S. aureus infection causes the formation of purulent inflammatory foci, called abscesses, which are characterized by the recruitment of host immune cells, in particular neutrophils (Figure 1.6.)[62] Abscesses consist of a bacterial microcolony in the center surrounded by a sphere of necrotic and viable neutrophils. This is further encapsulated in a fibrin sheath.[63] Because these lesions are inherently heterogeneous and bacterial pathogens occupy only a small fraction of the abscess, it has been difficult to determine the presence and spatial distribution of bacterial and host proteins that are localized to the host-pathogen interface. Additionally, the mechanisms by which bacterial pathogens obtain essential nutrients during abscess growth, as well as the nutrient-withholding defense strategies employed by infected hosts, are not completely understood. For these reasons, this system is an ideal model for MALDI IMS characterization.

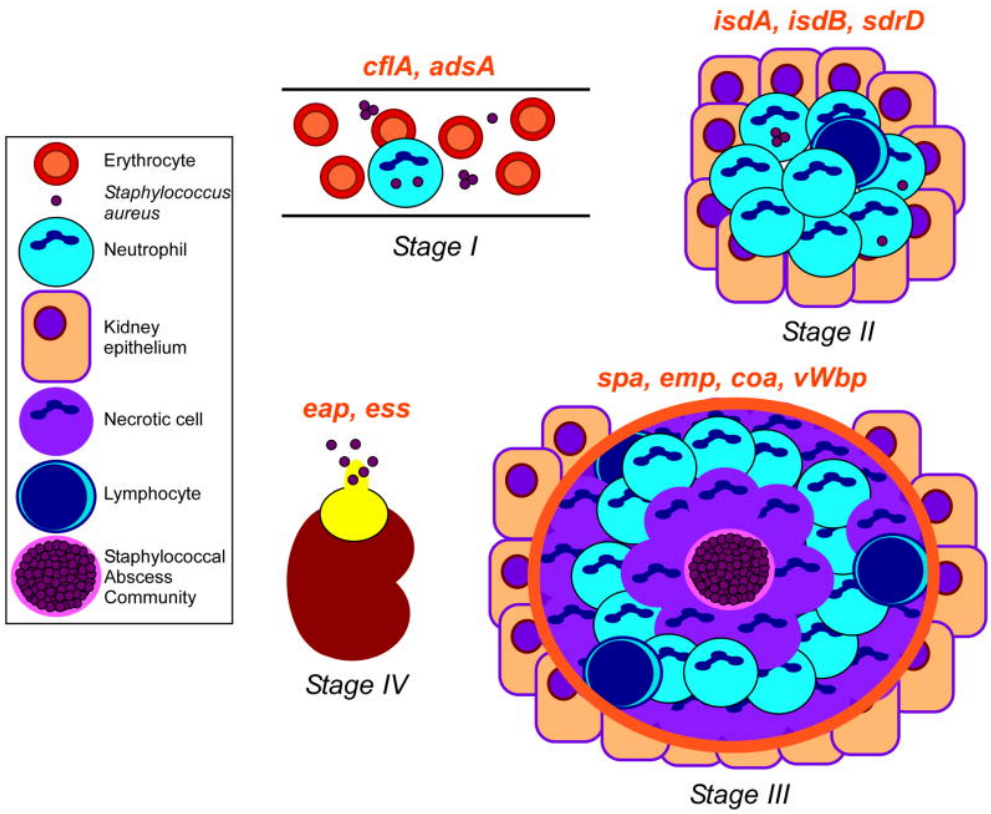

Figure 1.6: Working Model of Abscess Formation

"Working model for staphylococcal abscess formation and persistence in host tissues. Stage I: following intravenous inoculation, *S. aureus* survives in the bloodstream and disseminates via the vasculature to peripheral organ tissues. Stage II: staphylococci in renal tissue attract a massive infiltrate of polymorphonuclear leukocytes and other immune cells. Stage III: abscesses mature showing a central accumulation of the pathogen (SAC) surrounded by a pseudocapsule of fibrin deposits (pink rim), and zones of necrotic and healthy polymorphonuclear neutrophils (PMNs; purple and light blue cells, respectively), and finally a rim of eosinophilic material (orange rim). Stage IV: abscesses mature and rupture on the organ surface to initiate new rounds of infections. Genes required for specific stages of staphylococcal abscess development are in red above the corresponding stage of infection. Figure adapted with the authors' permission from an article published by Cheng and colleagues[14]." Reprinted from Trends in Microbiology, 19(5), "A play in four acts: *Staphylococcus aureus* abscess formation" 2011 with Permission from Elsevier.[64]

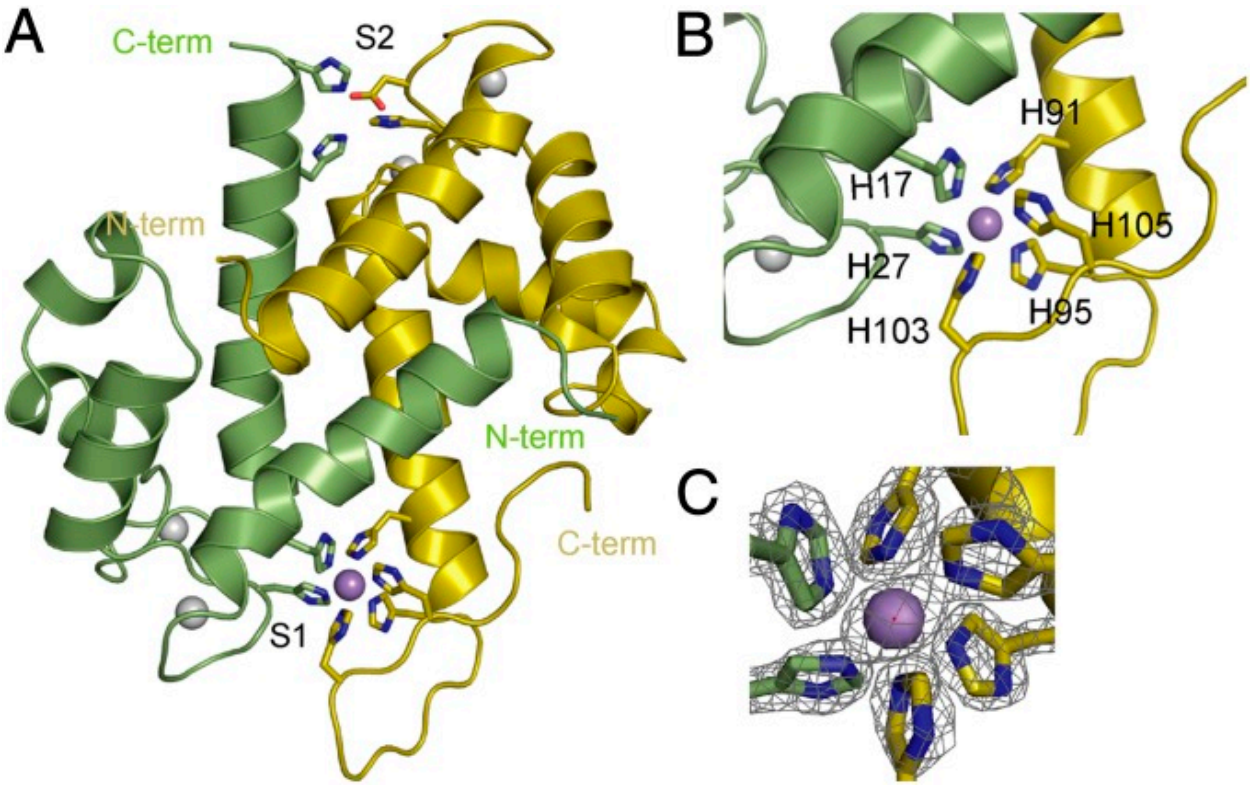

Figure 1.7: Metal Binding Sites of Calprotectin

"X-ray crystal structure of Mn-bound CP. (*A*) Ribbon diagram of Mn-bound S100A8 (green) and S100A9 (yellow) heterodimer refined to 1.6-Å resolution. The Zn-specific (S2) and Mn/Zn (S1) binding sites are labeled. Ca ions are shown as gray spheres, and the Mn ion is shown in purple. (*B*) Close-up view of the Mn/Zn site (S1) with the six histidine residues that chelate the Mn ion labeled. (*C*) Electron density ($2F_O$-$F_C$map contoured at 2σ) for the Mn ion and histidine side chains showing the nearly perfect octahedral geometry." Figure and caption reprinted from Proceedings of the National Academy of Science, 110, 10, "Molecular basis for manganese sequestration by calprptectin and roles in the innate immune response to invading bacterial pathogens."[65]

Nutritional Immunity

Metals are an essential part of biological function for all cells. It is estimated that 30-45% of all enzymes utilize a transition metal cofactor to enhance catalysis and reactivity.[66, 67] Conversely, too much metal can have toxic effects, so their bioavailability must be tightly regulated. For pathogens invading a vertebrate host, they must acquire these nutrient

metals from the host in order to thrive and cause disease. Vertebrate hosts have evolved strategies to attempt to sequester such metals from invading pathogens, a process called nutritional immunity. A considerable amount of research has focused on the mechanisms by which microbes obtain and hosts withhold essential metals.[68] Nutritional immunity of iron is well-studied, most likely because it is the most abundant transition metal in the human body. It is the metal center of the protoporphyrin heme, which is essential for cytochromes and hemoglobin. To access this pool of iron, invading pathogens must lyse red blood cells to obtain the iron from the center of heme.[69, 70] However, there is also a role for manganese and zinc in these processes.[71]

An important class of proteins involved in nutritional immunity are the S100 proteins. This class of proteins is an EF-handed calcium-binding family. Typically forming dimers, this family exists as both homo and heterodimers.[72] An example of an S100 protein capable of binding both manganese and zinc is the protein calprotectin (CP). This protein has been reported to make up to 40-50% of the cytosolic protein content of a neutrophil.[69, 73] Calprotectin is a metal-chelating heterodimer consisting of the protein subunits S100A8 and S100A9.[74] This protein was found in mouse abscess fluid supernatants and displayed antimicrobial activity that was decreased with the addition of exogenous zinc.[75] Such studies highlight the importance of metal sequestration for the control of bacterial infections. Calprotectin is unique in that it is a heterodimer, and that the junction of the two subunits form two distinct transition metal-binding sites, shown in Figure 1.7.[76-79]

The first binding site is formed by six histidines, while the second binding site contains three histidines and one aspartic acid.[77] Both sites are able to bind zinc with high affinity, but only the hexa-histidine site is capable of binding manganese. The individual contributions of zinc and manganese sequestration to nutritional immunity are therefore hard to differentiate, since this

single protein is capable of chelating both. Calprotectin also contains four calcium-binding domains, annotated in Figure 1.7. Calprotectin is known to accumulate at infectious foci and has been shown to be antimicrobial against a broad range of pathogens, including *Staphylococcus aureus*[28, 80], *Acinetobacter baumannii*[81], *Borrelia burgdorferi*[82], *Candida albicans*[83], *Helicobacter pylori*[84], and *Clostridium difficile.*[85] Nutrient metal chelation of zinc and manganese contributes to the antimicrobial and antifungal properties of the protein by disrupting microbial processes and inhibiting superoxide defense, leading to enhanced neutrophil killing.[80, 86, 87] Interestingly, calprotectin-mediated antimicrobial activity can be overcome by the addition of exogenous manganese and zinc.

There are other S100 proteins known to play a role in nutritional immunity. S100A7, for example, is a homodimer that binds two zinc molecules. S100A12 is reported to bind both zinc and copper.

Innate Immune Response and Oxidative Damage

The innate immune system represents the universal form of host defense. Innate immune response relies on the host recognition of a number of conserved pathogen-associated molecular patterns, or PAMPs.[88] Once triggered, the host will recruit a number of cells to sites of infections, including macrophages, neutrophils, and mast cells. Neutrophils are the most abundant vertebrate immune cell, equipped with a range of antimicrobial agents.[89] Some of these molecular markers allow the immune system to signal that an invading pathogen is present. These markers, called damage-associated molecular pattern markers, or DAMPs, are important for sustained immune response to bacterial infections. One such DAMP is calprotectin, which was discussed above.

Neutrophil response is the hallmarked by the generation of reactive oxygen species (ROS), which can damage both pathogen and host cells.[89] Aggregated neutrophils at sites of infection can cause excessive tissue damage and require clearance by monocytes and macrophages to resolve inflammation. This can only be accomplished once the original inflammatory signal (the pathogen) has been eliminated.[90, 91] Excessive tissue damage can expand from infected cells to neighboring uninfected areas, a process called bystander damage. The repair of protein modifications generated under oxidative stress has been studied, and some radical modifications are difficult for the host to repair or are considered irreparable.[92-95]

Another major component of the neutrophils' antimicrobial repertoire is the ability to form neutrophil extracellular traps (NETs) via a unique form of cell death that requires ROS.[96] Neutrophils create an extracellular fibrous network composed of DNA and histones. These fibers are decorated with antimicrobial peptides and proteins, including calprotectin.[83] NETs trap microbes and hold them in close proximity to high local concentrations of antimicrobial molecules, aiding pathogen-killing.[96] This is further supported because disassembly of NETs via DNase effectively removes antimicrobial activity.[97] Additionally, these adherent neutrophils are capable of trapping bacteria in high shear flow environments, like blood during sepsis, but often at the expense of damaging surrounding tissue.[98]

Sepsis

Sepsis is described as a systemic host response to infection. Left untreated, the uncontrolled inflammatory response can lead to severe sepsis, which is hallmarked by organ dysfunction, or to septic shock, hallmarked by a decrease in blood pressure.[99] When untreated, bacterial infections often persist to cause sepsis, which is a life-threatening condition. Septic shock kills one in four

patients, and the incidence of septic shock is increasing as bacteria are becoming more resistant to therapeutic strategies. The speed at which appropriate medical intervention, such as the correct antibiotic, can be administered has a large impact on patient outcome.[99] It is recommended that antimicrobial therapy be administered within the first hour that septic shock is recognized and that a combinatorial empirical approach be used. Here, a wide range of antimicrobials is administered and patients are monitored for antimicrobial resistance. Clinicians often drain excessive pus and wound fluid from infectious foci in attempts to control the inflammatory response.[99] Sepsis remains a large problem affecting human health. Sepsis is difficult to treat because a majority of the damage to otherwise healthy tissue is due to the host's own inflammatory response. Because therapeutic options are limited in autoimmune situations, the study of sepsis and the host response to inflammatory stimuli, such as invading bacteria, remains very necessary and important for human health.

CHAPTER II

CALPROTECTIN AGGREGATES AT INFECTIOUS FOCI DURING ACTIVE INFECTION

A version of the following chapter was previously published and has been adapted from Moore et al., *Proteomics,* Copyright 2013 by Wiley and Sons.[100]

Overview

Calprotectin (CP) is an important antimicrobial protein involved in nutritional immunity. Understanding how calprotectin responds to active infection is important, including how proteins are spatially localized within infected regions. To analyze this, two models are employed: an acute model of bacterial pneumonia, which is eventually cleared by the host, and a systemic sepsis model, which is not cleared. Imaging Mass Spectrometry (IMS) can reveal the spatial distribution of proteins in each of these models and reveals that CP accumulates at infectious foci during active infection.

Introduction

Proteins are dynamic molecules. Though the genome dictates what proteins an organism has the ability to make, their transcription and translation is a very complex process and a delicate balance within cells. The ability to study proteins as they change over time is very important. Fluorescent approaches have been implemented successfully, yet still have certain caveats.[101] Molecules of interest must be tagged before experimentation with a fluorescent reporter, which

should be specific for the species of interest and must exhibit spectroscopic characteristics that facilitate easy detection. However, altering the protein with a tag can impair or impede its normal function within the system.[101] Additionally, it is difficult to multiplex fluorescence-based approaches.[102] Protein microarrays and immunoblots have successfully studied differential expression, but they require homogenized samples and therefore sacrifice any information about spatial distribution of analytes within a sample.[103-106] Immunohistochemistry staining can provide spatial information, but requires available antibodies or stains for proteins of interest and cannot easily be multiplexed.[107] Additionally, all of the above methods struggle to accurately discern proteoforms, including proteins with post-translational modifications or mutations. For these reasons, MALDI IMS presents an attractive alternative to monitor relative changes in protein abundance over time.

Previous work in our laboratories has employed MALDI IMS of intact proteins to study the inflammatory response in animal models of bacterial infection. Studies utilized a mouse model of sepsis to visualize infectious foci. In these studies, mice were systemically infected with *Staphylococcus aureus* and it was determined that the host S100 proteins comprising the calprotectin heterodimer localize to abscesses.[28, 107] The same protein has been detected via MALDI IMS in lung tissue of mice infected with *Acinetobacter baumannii* acute pulmonary infections.[81]

Acinetobacter baumannii

A. baumannii is a pathogen of global public health concern. It is pervasive in the environment and capable of surviving for extended periods on hospital surfaces.[108, 109] *A. baumannii* can present clinically as a wide range of diseases, including wound infections,

pneumonia, urinary tract infections, and sepsis.[110] This bacterium has two compounding factors that make it an especially significant threat. First, it often strikes immunocompromised patients and is therefore a major concern in the Intensive Care Unit (ICU). Second, *A. baumannii* is quite adept at acquiring and maintaining resistance to antimicrobial therapies.[111, 112] Imipenem-non-susceptible *A. baumannii* strains have been correlated to longer lengths of treatment in the ICU.[113] In one setting, *A. baumannii* nosocomial pneumonia occurred more often than pneumonias caused by other bacteria, and those patients with *A. baumannii* pneumonia exhibited increased mortality.[114] Even with the increasing clinical importance, relatively little is known concerning the interactions between the host and this pathogen.

Human *A. baumannii* pulmonary infection is often characterized with lobar pneumonia, where one lobe experiences dense infection while the remaining lung is spared.[115, 116] In response to *A. baumannii* pneumonia, neutrophils are quickly recruited to the lungs leading to a subsequent increase in the levels of pro-inflammatory cytokines and a heightened inflammatory response.[117] We have previously shown that calprotectin is recruited to *A. baumannii* infected lungs and enhances the clearance of bacteria from the alveolar spaces. Additionally, calprotectin-deficient (CPKO) mice exhibit increased bacterial burdens in the lung and higher levels of dissemination to the liver.[81] This model presents an acute infection with *A. baumannii*; if left untreated, mice can resolve this inoculum without intervention from researchers.

Results and Discussion

Inflammatory Response Correlates to Bacterial Burden in A. baumannii *infection*

In order to successfully visualize protein accumulation and dissemination, the bacterial burden necessary to establish a detectable inflammatory response in immunocompetent mice was determined. A range of inoculum were tested and lung tissue samples were assessed by a pathologist. Higher doses of *A. baumannii* resulted in increased inflammation, as seen in the histological staining in Figure 2.1A-B. This is consistent with the idea that the magnitude of the immune response is impacted by bacterial burden. IMS analysis of S100A8 and S100A9, Figure 2.1C-D, showed increased intensity correlating with bacterial burden. This highlights the sensitivity of MALDI IMS to detect relative changes in protein abundance. Increasing inoculae [from left to right] lead to an increase in inflammation and more signal from both subunits of calprotectin. Figure 2.1E shows bacterial enumeration from lungs at 36 hours post infection (hpi), further emphasizing a correlation of dose to bacterial burden. There is a trend showing that increased bacterial inoculum yield larger bacterial burdens at 36 hpi. Interestingly, when compared to the initial inoculum, the mice are able to reduce the burden in lungs by almost three orders of magnitude by 36 hpi. This strengthens the model of *A. baumannii* pulmonary infection to be used as an acute model of infection to study protein dynamics. The dotted line in Figure 2.1E represents the limit of detection. This trend was reproduced 3 additional times, represented in Figure 2.2. Though care was taken to orient lungs in the same way and section to the same depth for each analysis, it is clear that there is some biological variability in these infections. This provides a pictorial representation of the bacterial burden data represented in Figure 2.1E, where each dot on

the graph represents a unique mouse. Though provided the same inoculum, there is variation in the infection model that is visually apparent in the histological and MALDI IMS data.

Using these data, it was determined that bacterial burden of approximately 10^8 CFUs, delivered in 30 μL of a 1×10^7 CFU/μL inoculum, is necessary to cause inflammation and robust calprotectin accumulation detectable by MALDI IMS. This inoculum was used in time course studies of infection.

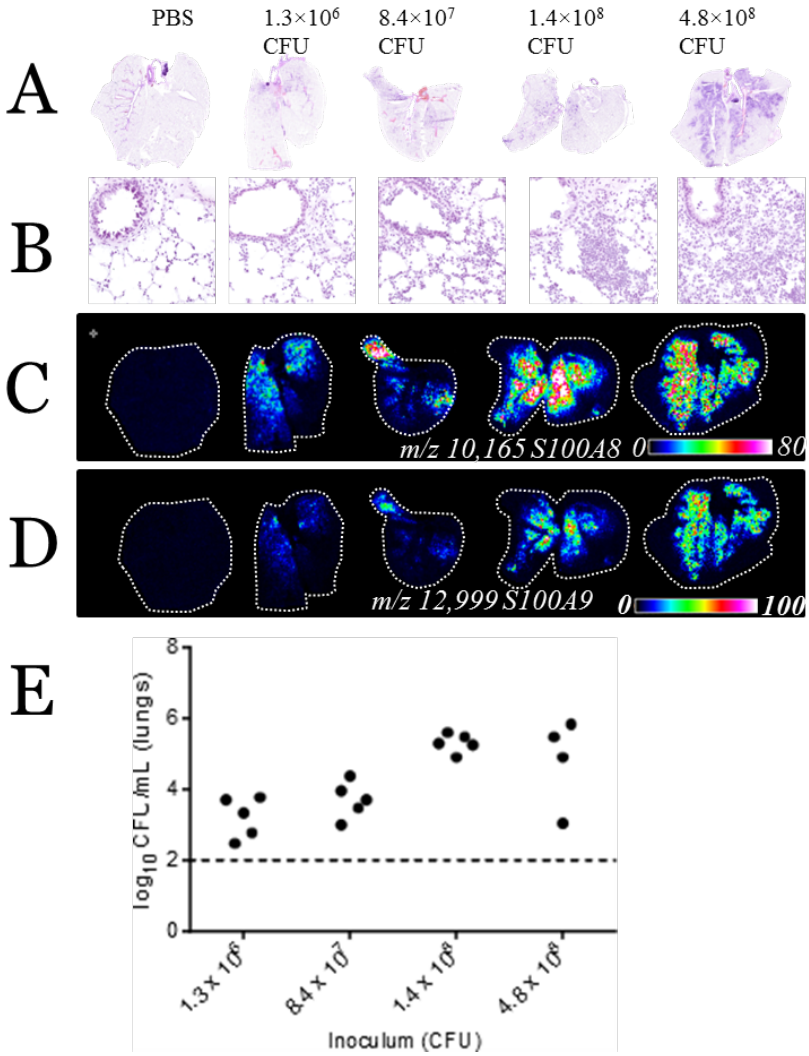

Figure 2.1: Calprotectin Levels Increase with Bacterial Challenge

Levels of calprotectin in the lung increase as the bacterial challenge is increased. Seven-week-old mice were intranasally infected with varying doses of *A. baumannii*. (A) hematoxylin and eosin (H&E) stained serial sections of lung, (B) 40× magnification of areas with inflammation, (C) ion intensity map of *m/z* 10,165, S100A8, collected at 300 μm spatial resolution, (D) ion intensity map of *m/z* 12,999, S100A9, collected at 300 μm spatial resolution, (E) bacterial burden in the lungs of mice at each inoculum. The dashed line represents the detection limit. $*p < 0.05$ by ANOVA. Reprinted from *Proteomics*, 14, 0, "Imaging Mass Spectrometry for assessing temporal proteomics: Analysis of calprotectin in *Acinetobacter baumannii* pulmonary infection." 2014, 820-828 with permission from John Wiley and Sons.[100]

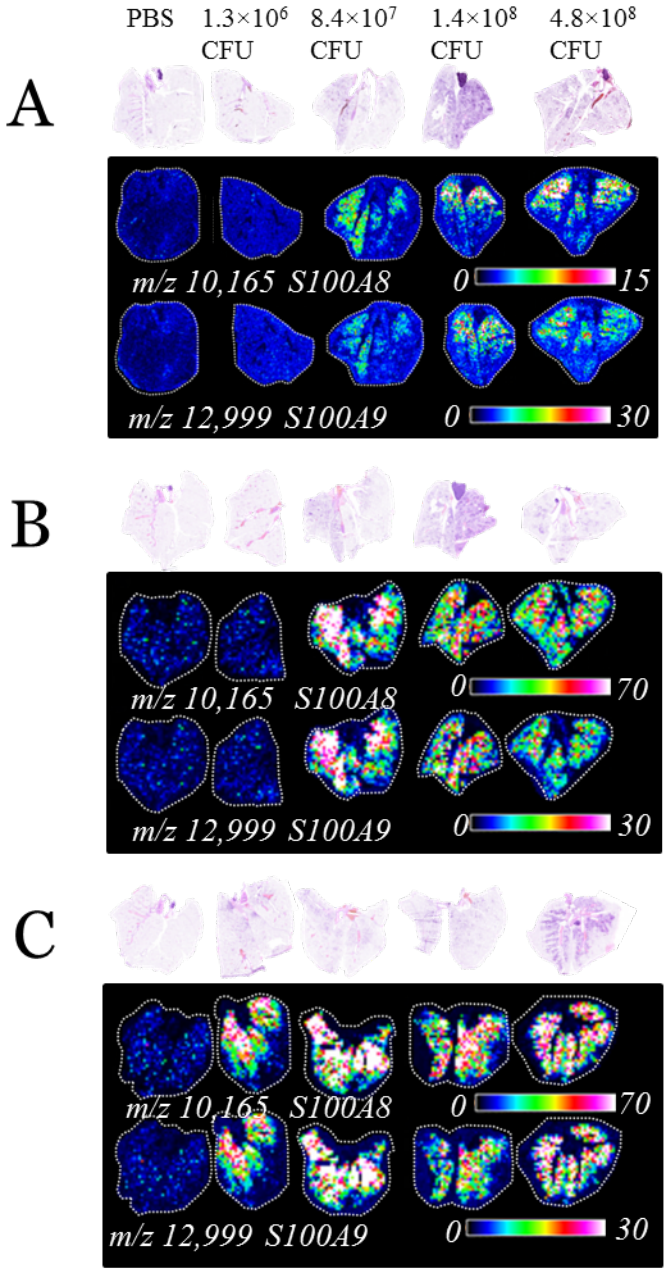

Figure 2.2 Biological and Technical Replicates Show Calprotectin Levels Correlated with Bacterial Burden

Replicates of Figure 2.1, from left: PBS, 1.3×106 CFU, 8.4×107 CFU, 1.4×108 CFU, and 4.8×108 3 CFU. 4 Ion intensity maps of S100A8, S100A9, and Histone H2A.1 are shown for each trial. (A) Shows a 5 biological replicate of increasing bacterial burden, analyzed at 300 μm spatial resolution. (B) and (C) 6 show technical replicates, analyzed at 500 μm spatial resolution. Reprinted from *Proteomics,* 14, 0, "Imaging Mass Spectrometry for assessing temporal proteomics: Analysis of calprotectin in *Acinetobacter baumannii* pulmonary infection." 2014, 820-828 with permission from John Wiley and Sons.[100]

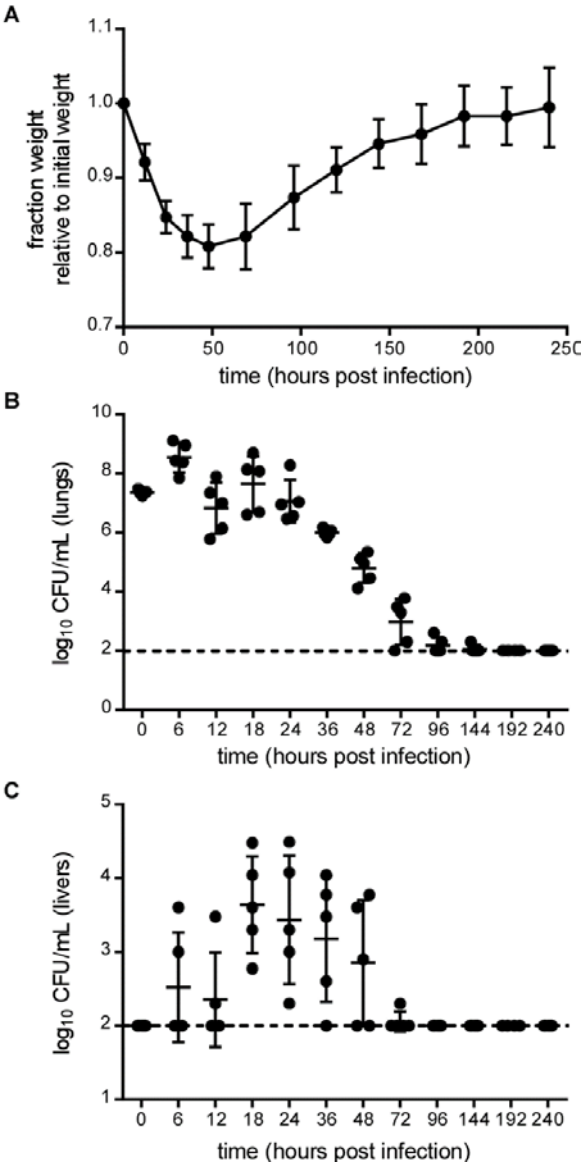

Figure 2.3: *A. baumannii* is Rapidly Cleared from Sites of Infection

A. baumannii is rapidly cleared from sites of infection. Seven-week-old mice were intranasally infected with 10^8 CFUs *A. baumannii* and monitored over time in hours post infection (hpi) for (A) weight change. Values from 6 to 216 hpi were statistically decreased ($p < 0.05$) from uninfected animals by two-way ANOVA. (B) Bacterial burden in the lung, $n = 5$. Values from 0 to 72 hpi were statistically different ($p < 0.05$) from uninfected animals by Student's *t* test. (C) Bacterial dissemination to the liver, $n = 5$. Values from 18 to 36 hpi were statistically different ($p < 0.05$) from uninfected animals by Student's *t* test. Reprinted from *Proteomics*, 14, 0, "Imaging Mass Spectrometry for assessing temporal proteomics: Analysis of calprotectin in *Acinetobacter baumannii* pulmonary infection." 2014, 820-828 with permission from John Wiley and Sons.[100]

Calprotectin is Temporally Expressed in Acute Infection of A. baumannii *Pneumonia*

To define the kinetics of the inflammatory response to *A. baumannii* pulmonary infection, a time course study was employed. Lungs were harvested at twelve time points following infection (0, 6, 12, 18, 24, 36, 48, 72, 96, 144, 192, and 240 hpi.) Animal weight was used to monitor overall health (Figure 2.3A). It can be noted that upon initial inoculation, the mice consistently lost weight, which is indicative of sickness. However, around 50 hpi, the mice begin to regain weight, indicative of improved health. Around 200 hpi, or approximately 8 days, mice have recovered weight to preinfection levels and continue to gain weight. This supports the *A. baumannii* acute pneumonia infections as a model to study proteins that respond to infection and their resolution.

Bacterial burden was also evaluated from the primary site of infection in the lungs (Figure 2.3B) and livers (Figure 2.3C), a site of secondary dissemination. These data indicate that the majority of the bacterial burden is cleared by 96-144 hpi when compared to the limit of detection, which is denoted with a dotted line. Dissemination to the liver also seems to be cleared by 72 hpi. This further supports that mice can resolve acute pulmonary infection by *A. baumannii* within the presented time course of infection.

MALDI IMS was used to study temporal dynamics of the calprotectin subunits at these time points. These experiments revealed a strong correlation between calprotectin expression and bacterial burden during the time course of infection (Figure 2.4). Signal for S100A8 and S100A9, appearing at *m/z* 10,165 and 12,999, respectively, is first detected at 6 hpi, showing a rapid response of the innate immune system to *A. baumannii*. The signals continue to accumulate in a manner that corresponds to the bacterial burdens. A maximal accumulation of the antimicrobial proteins occurs at 36-48 hpi and can be correlated to the decrease in bacterial burden shown in Figure 2.3B.

Signals from S100A8 and S100A9 begin to decrease near 96-144 hpi corresponding to the clearance of *A. baumannii* from lungs (Figure 2.3B). These experiments were performed in both biological and technical replicates (Figures 2.5, 2.6). Additionally, S100A8 or S100A9 were not detected in the PBS control tissue (Figure 2.7). In these experiments, mice were anesthetized and inoculated with PBS alone. There is a slight signal for S100A8 at 6 hours post infection in the PBS mock-infected lung. This is most likely due to the act of mock-infecting the lungs. For all images, an ion map of *m/z* 14,050, an abundant peak in collected spectra belonging to histone H2A.1, was generated to demonstrate that changes in calprotectin abundance were not an effect of ubiquitous changes in protein signal. The histone signal may also be used to monitor variations in tissue density caused by atelectasis of inflamed lungs or perfusion effects. In some instances, tissue did not fully perfuse upon resection. The dark-staining regions of the H&E can be correlated to atelectasis, or regions of lung that have collapsed. This is also apparent in the PBS mock-infected lungs, shown in Figure 2.7. Figure 2.8 shows two tissues from 96 hpi stained for neutrophils using an immunohistochemical stain and correlating with MALDI IMS data. Even in regions of resection-induced atelectasis, such as the PBS mock-infected lung, there is no detectable staining for neutrophils, which is marked by the brown stain. However, in both infected lungs, there is considerable brown staining, marking the presence of neutrophils in these organs. This demonstrates histological differences introduced by pneumonia and confirms the presence of neutrophils in infected lungs.

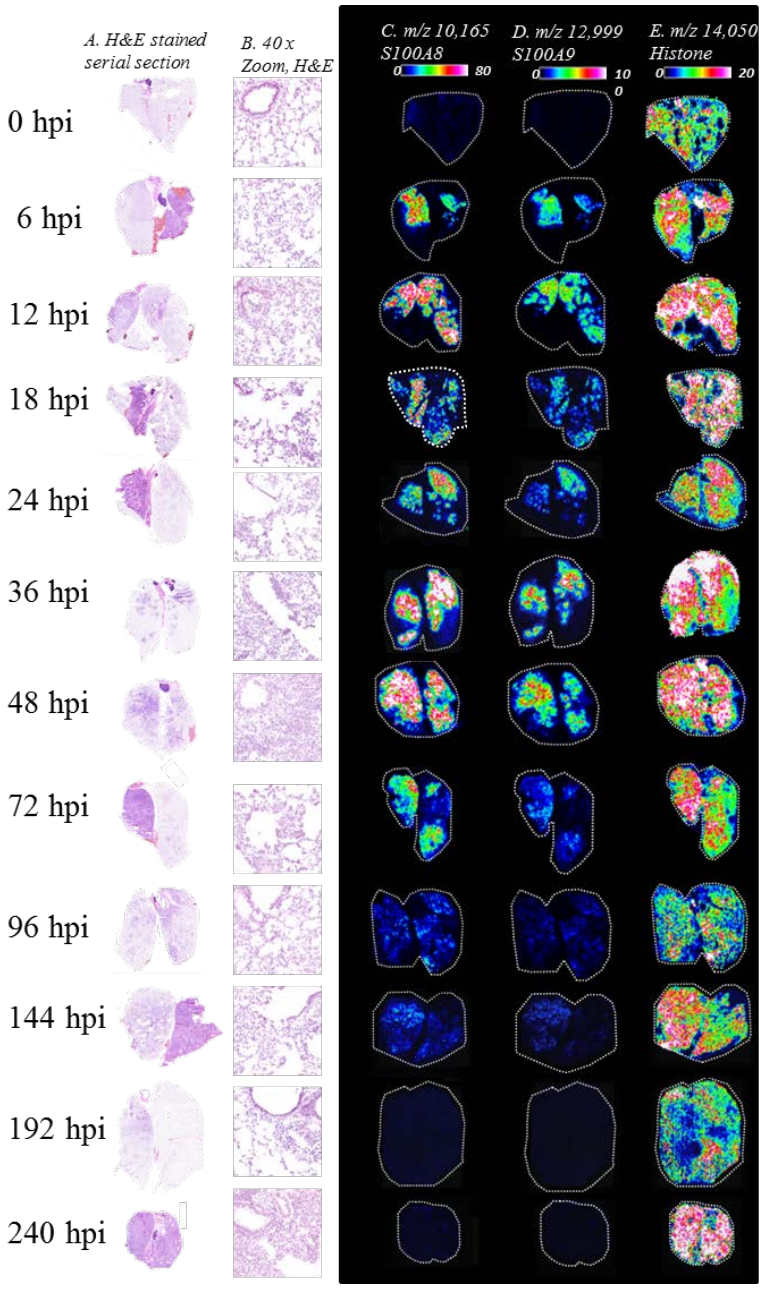

Figure 2.4: Calprotectin is Recruited to Sites of Infection

Calprotectin is recruited to sites of infection and signal decreases following bacterial clearance. Columns, left to right: (A) H&E stained serial sections of lung, (B) 40× magnification of areas with inflammation, (C) ion intensity map of *m/z* 10,165, S100A8 collected at 300 μm spatial resolution, (D) ion intensity map of *m/z* 12,999, S100A9 collected at 300 μm spatial resolution, and (E) ion intensity map of *m/z* 14,050, histone H2A.1 collected at 300 μm spatial resolution. Reprinted from *Proteomics,* 14, 0, "Imaging Mass Spectrometry for assessing temporal proteomics: Analysis of calprotectin in *Acinetobacter baumannii* pulmonary infection." 2014, 820-828 with permission from John Wiley and Sons.[100]

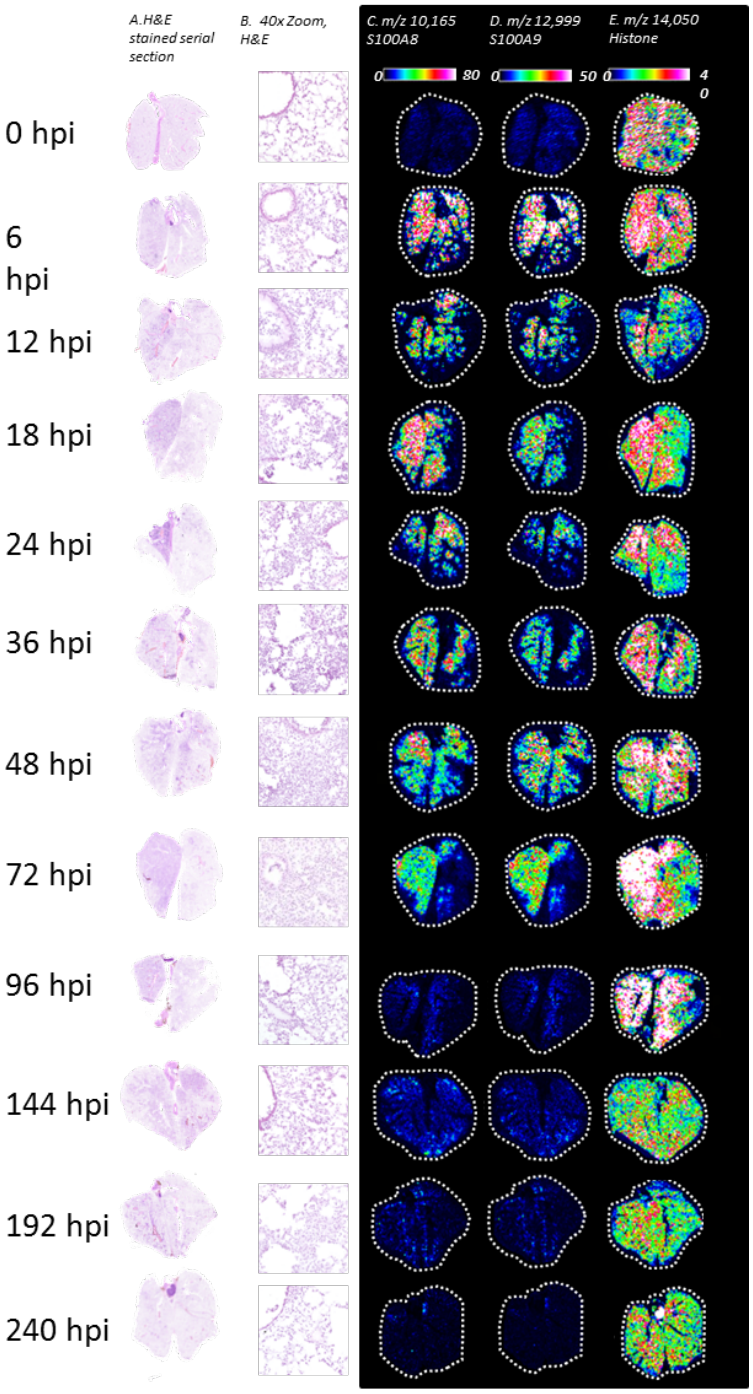

Figure 2.5: Biological Replicates Show Calprotectin is Recruited to Sites of Infection
Biological replicate of Figure 2.4, analyzed at 300 μm spatial resolution. (A) H&E stained serial 9 sections of lung. (B) 40× magnification of areas with inflammation. (C) Ion intensity map of *m/z* 10,165, S100A8. (D) Ion intensity map of *m/z* 12,999, S100A9. (E) Ion intensity map of *m/z* 14,050, Histone H2A.1. Reprinted from *Proteomics,* 14, 0, "Imaging Mass Spectrometry for assessing temporal proteomics: Analysis of calprotectin in *Acinetobacter baumannii* pulmonary infection." 2014, 820-828 with permission from John Wiley and Sons.[100]

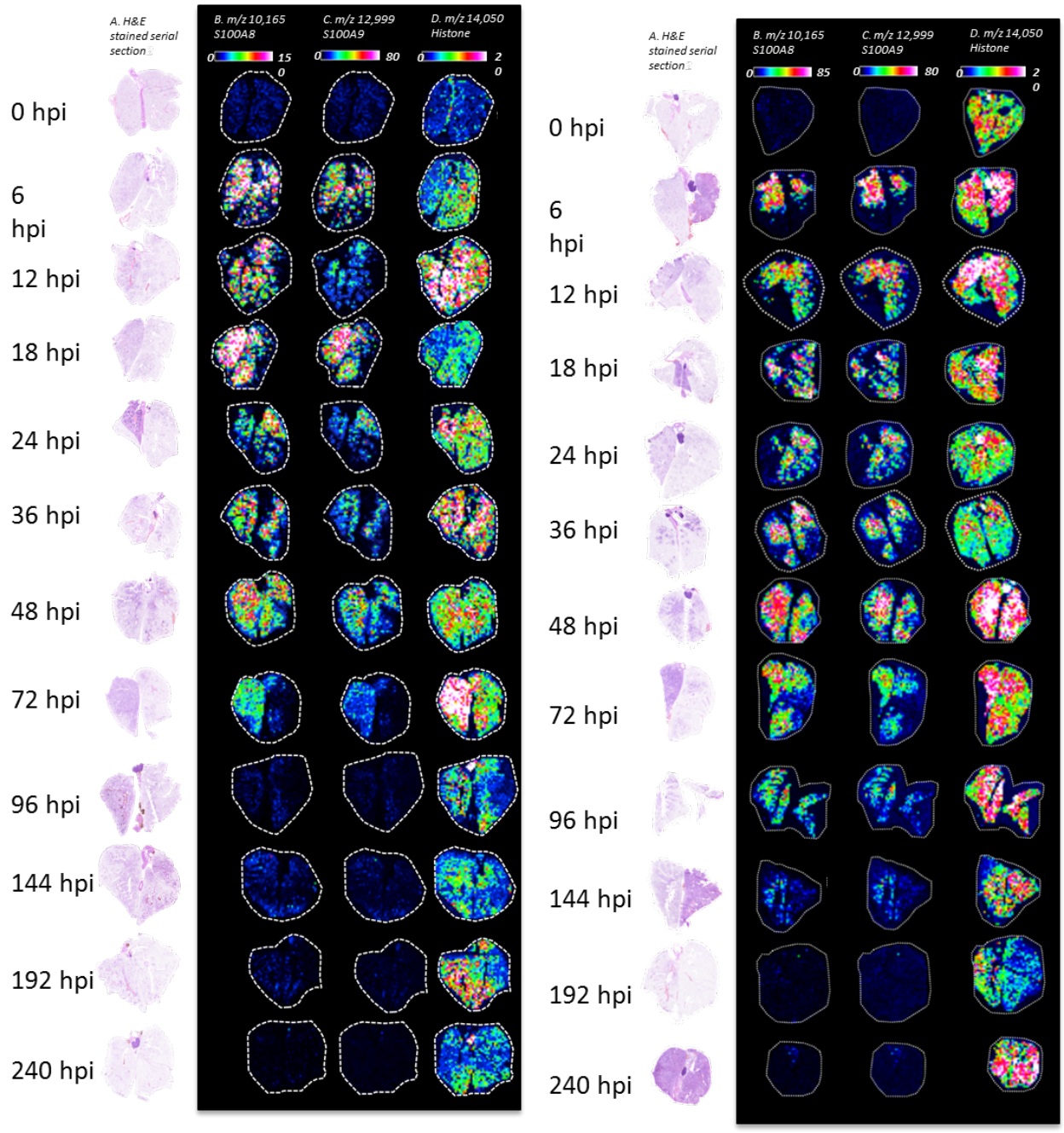

Figure 2.6: Technical Replicates Show Calprotectin is Recruited to Sites of Infection
Technical replicates analyzed at 500 μm spatial resolution. (A) H&E stained serial sections of lung. (B) Ion intensity map of *m/z* 10,165, S100A8. (C) Ion intensity map of *m/z* 12,999, S100A9. (D) Ion intensity map of *m/z* 14,050, Histone H2A.1. Reprinted from *Proteomics*, 14, 0, "Imaging Mass Spectrometry for assessing temporal proteomics: Analysis of calprotectin in *Acinetobacter baumannii* pulmonary infection." 2014, 820-828 with permission from John Wiley and Sons.[100]

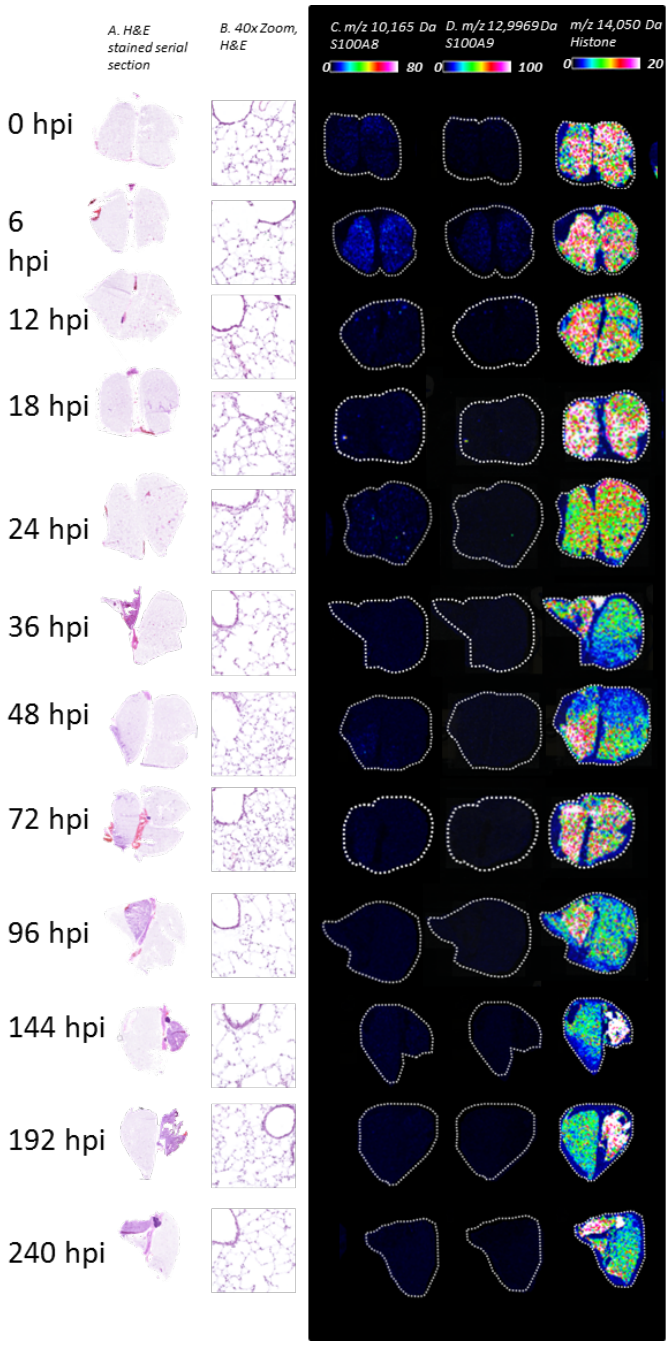

Figure 2.7: PBS control lungs contain no appreciable signal for S100A8 or S100A9
Lungs from mice mock-infected with 30 µl of PBS harvested at each time point, analyzed at 300 µm spatial resolution. (A) H&E stained serial sections of lung. (B) 40 × magnification of tissue. (C) Ion intensity map of *m/z* 10,165, S100A8. (D) Ion intensity map of *m/z* 12,999, S100A9. (E) Ion intensity map of *m/z* 14,050, Histone H2A.1. Reprinted from *Proteomics,* 14, 0, "Imaging Mass Spectrometry for assessing temporal proteomics: Analysis of calprotectin in *Acinetobacter baumannii* pulmonary infection." 2014, 820-828 with permission from John Wiley and Sons.[100]

To further assess signal differences in the time course (Figure 2.4) compared to the uninfected controls (Figure 2.7), average pixel intensity was determined by selecting regions of interest at random using flexImaging. Average pixel intensities for S100A8 and S100A9 were calculated and plotted in Figure 2.9. Though not intended to be quantitative, this provides a descriptive assessment of protein changes with time. Trends in the signal for inflammatory proteins is somewhat Gaussian, peaking around 36 hours post infection following the highest bacterial burdens and then resolving over time.

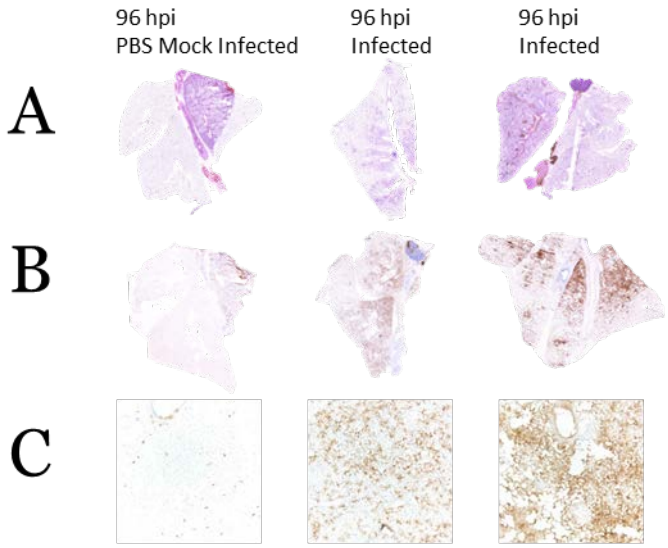

Figure 2.8: Immunohistochemistry Confirms the Presence of Neutrophils
Histological comparison of atelectasis in inflamed lungs versus uninfected at 96 hpi. Lungs from 96 hour time point. From left, PBS mock-infected and *A. baumannii* infected. (A) H&E stained sections of lung. (B) Immunohistochemistry stain for neutrophils. (D) 10× magnification of immunohistochemistry stain for neutrophils. Reprinted from *Proteomics*, 14, 0, "Imaging Mass Spectrometry for assessing temporal proteomics: Analysis of calprotectin in *Acinetobacter baumannii* pulmonary infection." 2014, 820-828 with permission from John Wiley and Sons.[100]

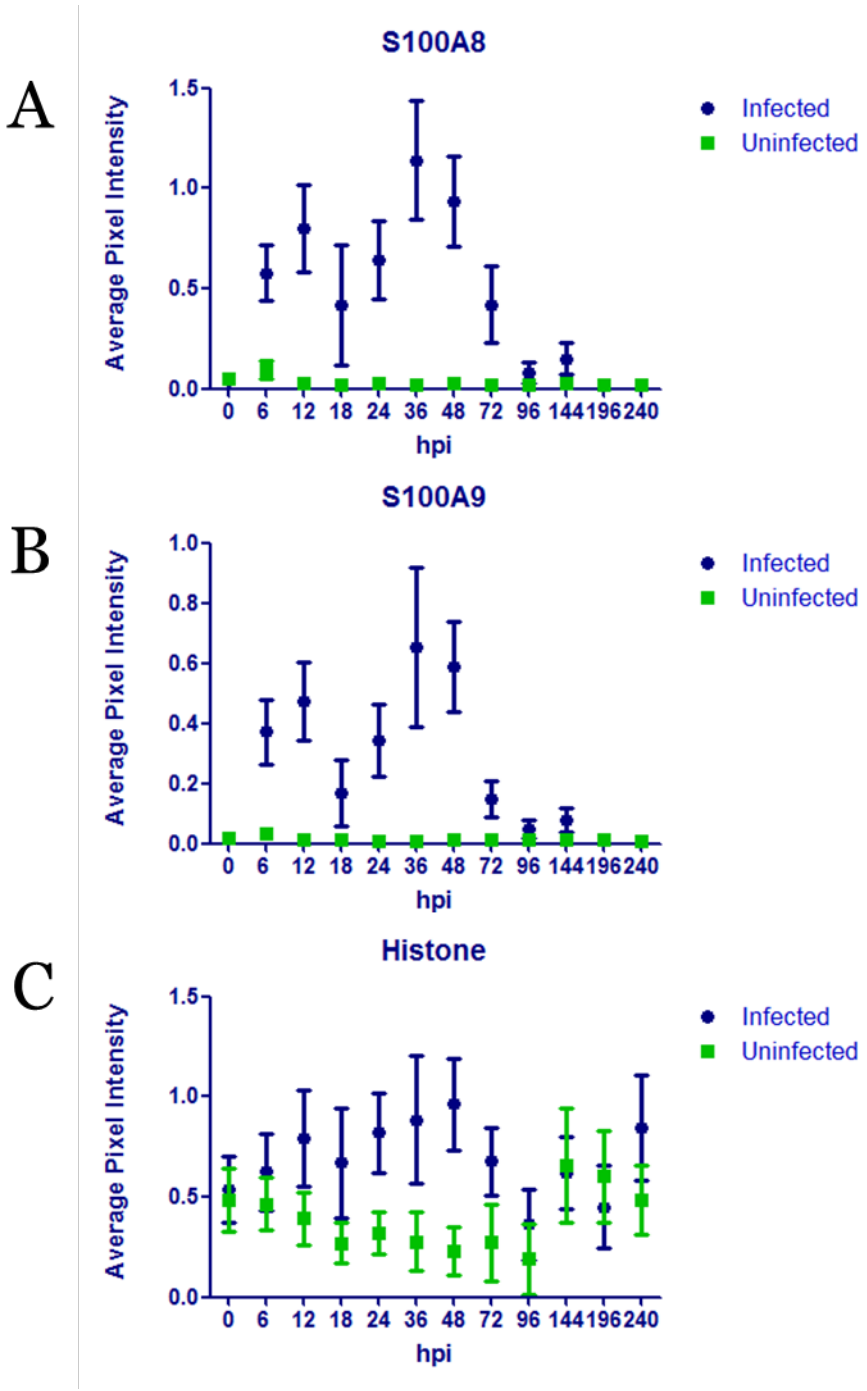

Figure 2.9: Average Pixel Intensity Shows Differences in Protein Abundance with Time
Average Pixel intensity extracted from regions of interest from time course in Figure 2.4 and 2.7 (A) *m/z* 10,165, S100A8. (B) *m/z* 12,999 S100A9. (C) Histone. Reprinted from *Proteomics*, 14, 0, "Imaging Mass Spectrometry for assessing temporal proteomics: Analysis of calprotectin in *Acinetobacter baumannii* pulmonary infection." 2014, 820-828 with permission from John Wiley and Sons.[100]

Calprotectin is Identified from A. baumannii *Infected Lungs*

In order to confirm that the signals used for these analyses were indeed from calprotectin, the protein was sequenced from infected lungs. Lungs at 36 hpi were selected for protein identification because they consistently had a robust inflammatory response. A spectrum taken from the MALDI IMS data is shown in Figure 2.10A. In this spectrum, robust signals were annotated that were thought to belong to S100A8 and S100A9. In order to identify these peaks of interest, a bottom-up protein identification strategy was employed. To have more confidence in the identification, an extract of proteins was fractionated using a C8 column to decrease the complexity of the mixture. 96 fractions were collected over a 75 minute HPLC separation. Each of these fractions were analyzed using MALDI MS to isolate the fractions which contained the *m/z* values of interest. The mass spectra of these two fractions are displayed in Figure 2.10B. Comparing these two spectra with the spectrum in 2.11A, it is apparent that the complexity of the mixture has been reduced while still maintaining robust signal from the two analytes of interest. Both fractions of interest were digested using the endoproteinase trypsin and subjected to an additional LC-MS/MS analysis. Peptides from the proteins were sequenced to confirm the identity.

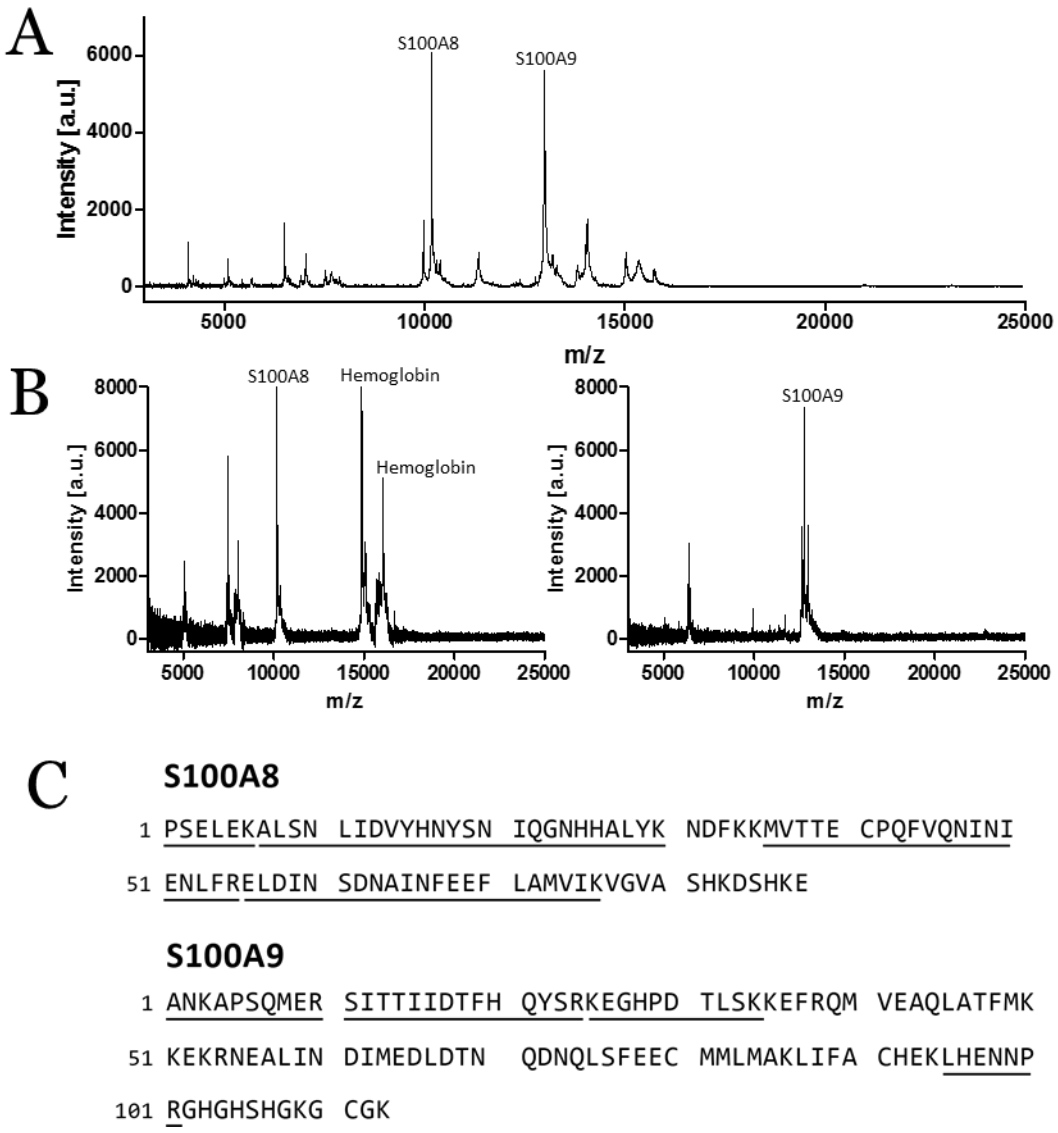

Figure 2.10: Identification of S100A8 and S100A9 from Murine Lung

Identification of S100A8 and S100A9 from murine lung. Identification of S100A8 and S100A9: (A) Spectrum extracted from a single pixel of IMS data from the 48 hpi lung. (B) Spectra taken from selected fractions of HPLC fractionated homogenate, showing S100A8 (left) and S100A9 (right). (C) Sequence coverage for mouse S100A8 and S100A9 are shown. Underlined peptides were detected following recovery of the species of interest by offline HPLC fractionation, tryptic digestion, and subsequent LC-MS/MS analysis. Reprinted from *Proteomics,* 14, 0, "Imaging Mass Spectrometry for assessing temporal proteomics: Analysis of calprotectin in *Acinetobacter baumannii* pulmonary infection." 2014, 820-828 with permission from John Wiley and Sons.[100]

S. aureus *Sepsis is an Ideal Model of Severe Infection*

In order to study calprotectin in a more severe infection, we needed to extend our current animal models to allow sepsis to progress. To monitor the progression of infection, a time course was developed. Female six-week-old mice were retro-orbitally infected with 10^6 CFU of *S. aureus*. Mice were sacrificed at various time points post infection (0, 3, 6, and 9 days post infection [dpi]) and monitored post-mortem for abscess lesions. Throughout the time course, animal weights were monitored as an overall measure of health. Figure 2.11A shows percent weight loss of animals over time. Each dot represents an individual mouse. Both wildtype and mice lacking calprotectin (CPKO) were monitored. Figure 2.11A shows no statistically significant increase in weight loss as the time course of sepsis progresses. Organs were also homogenized at each time point to quantify bacterial burden in major organ systems. Hearts, kidneys, and livers were plated for bacterial burdens in Figure 2.11B. These data showed that over the course of infection the mice are unable to clear their bacterial burden, making this model an ideal system to study severe infection. Additionally, the visual appearance of these organs showed significant pathology over the course of infection. The 3, 6, and 9 dpi organs had visual lesions that were apparent when they were resected, making these foci exemplary for study by IMS (Figure 2.11C). Histological analysis of these organs is shown in Figure 2.12. Figure 2.12A shows the gross anatomy of mouse kidney as sepsis continues through the time course. Early in the progression, at 0 dpi, the mice were infected and immediately sacrificed, giving very little time for bacterial dissemination. No visible lesions are apparent at this time. By 3 dpi, abscesses have begun forming in the kidney. Figure 2.12B shows zooms of these histological regions of interest. Green arrows indicate neutrophil infiltration at sites of colonization. Yellow arrows denote staphylococcal colonies. As disease

progresses to 6 dpi, large areas of necrosis can be visualized, annotated with blue arrows. We would anticipate these regions to be filled with dead cells, including dead neutrophils and NETs.

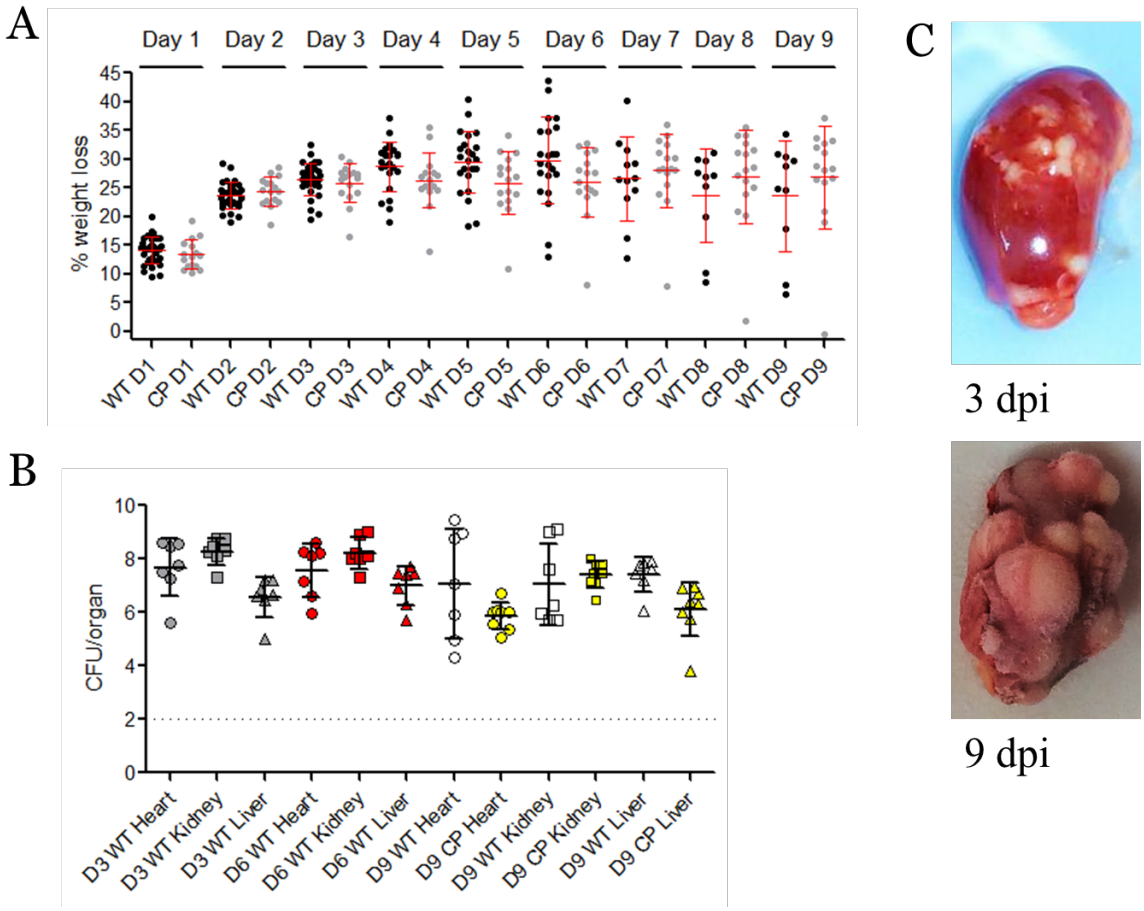

Figure 2.11: *S. aureus* is a model of Severe Infection

A) The overall health of mice systemically infected with *S. aureus* was monitored by weight over the course of infection. Percent weight loss was tracked over the course of the 9 day infection in both wildtype (WT) and calprotectin knockout (CP) mice to monitor disease progression. B) Mice sacrificed at 3, 6, and 9 dpi were analyzed for bacterial burdens in hearts, kidneys, and liver tissues. C) Despite no statistically significant increase in bacterial burdens from 3 to 9 dpi, the visual morphology of organs was dramatically different. Shown are two mouse kidneys taken from 3 and 9 dpi to show the striking difference in lesions, clearly visible to the eye.

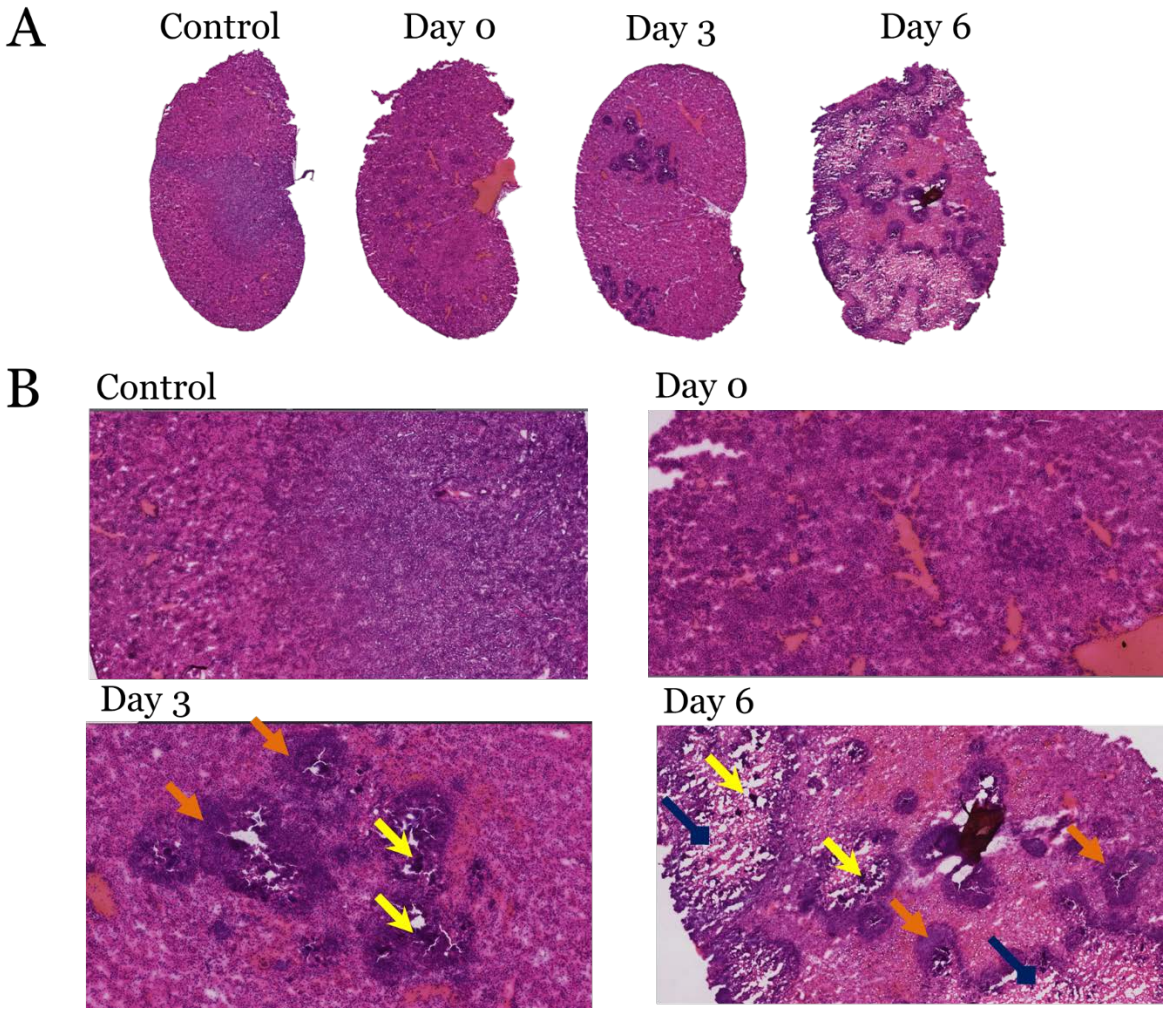

Figure 2.12: Histological Analysis of *S. aureus* Sepsis Progression in Mouse Kidney
Hemotoxylin and Eosin stained sections of mouse kidney taken from various time points in a systemic infection of *S. aureus.* A) shows gross morphology of kidney sections, with visible lesions appearing at day 3. B) shows magnifications of regions of interest. Lesions are present at days 3 and 6. Aggregated neutrophils are annotated with orange arrows while staphylococcal colonies are annotated with yellow arrows. Tissue necrosis is present at 6 dpi and is annotated in dark blue.

Calprotectin Accumulates in Severe Infection

MALDI IMS analysis was performed on this time course model of sepsis using a linear TOF MS. An ion intensity map of S100A8 at *m/z* 10,165 is shown in Figure 2.13. There is very little detectable signal for S100A8 in the control and the 0 dpi kidney, supporting the idea that CP responds to bacterial threats. By 3 dpi, when there are well-formed lesions in the kidney, we see signal for S100A8 robustly co-localized with neutrophils in the lesions. By 6 dpi, when there is considerable necrosis, S100A8 signal is very robust and almost encompasses the entire kidney. This supports the idea that calprotectin will not be cleared in cases of severe infection where the host cannot resolve the threat by killing the pathogen. In these cases, calprotectin continues to accumulate at sites of infection without resolution. This could have serious impact on the host, as calprotectin is a known signaling molecule and is known to sustain inflammatory response. Such sustained inflammatory response is a hallmark of sepsis, making this an important model for continued study. Finally, sustained inflammatory response most likely leads to the accumulation of neutrophils in regions of infection, causing continued damage to host cells and immune cells recruitment.

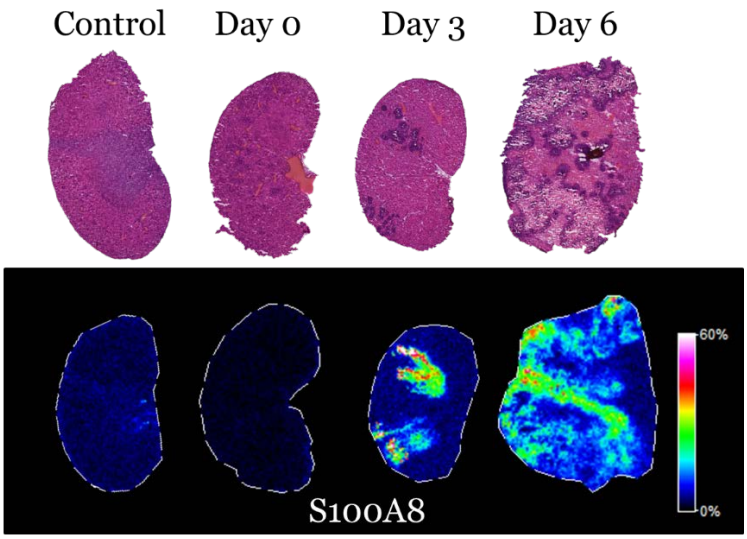

Figure 2.13: Calprotectin Accumulates in Severe Infection
H&E stained sections of mouse kidney and an ion intensity map for S100A8, appearing at *m/z* 10,165. This subunit represents the spatial localization of calprotectin. This shows a dramatic accumulation of signal as disease progresses and necrosis encompasses the organ.

Methods

Bacterial Strains and Infection

A. baumannii strain ATCC 17978 (Ab17978) was obtained from the American Type Culture Collection and was used for all experiments.

All animal experiments were approved by the Vanderbilt Institutional Animal Care and Use Committee. For pulmonary infections, a previously established pneumonia model with minor modifications was used.[81, 118] Briefly, cultures of Ab17978 were grown to logarithmic phase in Luria-Bertani medium (LB), washed, and resuspended in PBS. Seven week old, female Swiss Webster mice (Charles River Laboratories) were anesthetized and intranasally infected with 30 μL bacterial suspension. The weights of the animals were measured daily to serve as an indicator of overall health. Mice were euthanized at the indicated time points post infection and lungs and livers were aseptically removed. Lungs for imaging experiments were perfused with 1 mL 1:1 OCT:water, marked for histological orientation using dye-based drawing ink, snap-frozen in a dry ice/hexane mixture, and stored at -80°C until analysis. Lungs and livers for bacterial enumeration were homogenized in 1 mL PBS, serially diluted, and plated on LB agar.

For experiments to determine optimal dose of Ab17978 needed to cause infection, inoculae ranging from 10^6 to 10^8 colony forming units (CFUs) were used. Mice mock-infected with 30 μL of PBS served as controls. Seven mice were infected for each inoculum, with five mice used for CFU enumeration and two mice used for MALDI IMS. Lungs were harvested at 36 hpi.

For time course studies, 30 μL of Ab17978 at a concentration of 1 x 10^7 CFU/μL were administered and organs were harvested at twelve time points following infection (0, 6, 12, 18, 24, 36, 48, 72, 96, 144, 192, and 240 hpi). For each time point, five mice were used for CFU

enumeration and two mice for MALDI IMS. Twelve mice were mock-infected with PBS to serve as controls, one at each time point.

The *S. aureus* clinical isolate Newman served as the genetic background for all experiments.[119] Bacteria were grown in tryptic soy broth (TSB) at 37°C with 180 revolutions per minute shaking. To prepare inoculae for the disseminated infection model, overnight cultures were back-diluted 1:100 and grown for an additional 3 hours, after which time the bacteria were harvested by centrifugation and washed in PBS. Washed bacteria were resuspended to a final concentration of approximately 5 x 10^8 colony forming units (CFU) per milliliter, and kept on ice until used for retro-orbital injection.

Female 6-8 week old C57bl/6 mice (Jackson Laboratories) were infected using a retro-orbital intravenous injection of *S. aureus.* Mice were anesthetized using Avertin (2-2-tribromoethanol) and injected with 100 µL of inoculum in PBS. Mice were monitored as they recovered from anesthesia and were provided free access to food and water throughout the course of infection. At set times post infection, mice were sacrificed and organs aseptically removed. Organs were frozen in plastic weigh boats using dry ice and stored at -80°C until analysis.

MALDI IMS of Mouse Lungs

Frozen lungs were identically oriented based on histological ink and sectioned at -20°C to 10 µm thickness using a Leica CM3050S cryostat (Leica Microsystems, Bannockburn, IL, USA). Tissue sections were thaw-mounted onto indium-tin oxide (ITO) coated glass slides (Delta Technologies, Loveland, CO, USA). Excess lipids and salts were removed by washing the slides in sequential 30 second washes of chilled 70, 90, and 95% ethanol. Sinapinic acid matrix was prepared at a concentration of 20 mg/ml in 60% acetonitrile with 0.1% TFA. A Portrait 630

(Labcyte, Sunnyvale, CA, USA) acoustic robotic microspotter was used to apply matrix to samples. The microspotter was operated in flyby mode at 300 μm lateral resolution. Technical replicates were performed at 500 μm lateral resolution. Matrix was applied in four passes of 15 droplets, with each droplet having an approximate volume of 170 pL.

Samples were analyzed using a Bruker AutofleX Speed time-of-flight mass spectrometer with a modified Swiss Cross source (Bruker Daltonics, Billerica, MA, USA) equipped with a SmartBeam™ laser (Nd:YAG, 355 nm) in linear positive–ion mode. Two hundred laser shots were collected at each matrix spot in 50 shot increments with a random walk pattern within the spot. The laser repetition rate was 1,000 Hz; extraction and acceleration voltages were 19.67 kV and 18.22 kV, respectively, with a delayed extraction time of 350 ns and a lens voltage of 8.5 kV. The measured mass range was from *m/z* 3,000- 25,000. Within each trial, lungs were imaged at the same time in a random order selected by an unaffiliated and unbiased researcher. Images were collected at 300 μm lateral resolution. Technical replicates were performed at 500 μm lateral resolution to reduce data size and to show similar spatial distributions from additional sections. Images were viewed using flexImaging 3.0 Software (Bruker Daltonics) and were normalized to total ion current. Ion intensity maps were extracted and scaling was constant for each ion of interest. To assess differences in images, regions of interest were selected from areas of inflammation and correlating control tissue using flexImaging. Spectral filter data were exported and average pixel intensity was calculated.

MALDI IMS of Mouse Kidney

Frozen mouse kidneys were oriented in the same manner and sectioned at 10 μm spatial resolution using a Leica CM3050S cryostat (Leica Microsystems, Bannockburn, IL, USA). Tissue

sections were thaw-mounted onto ITO coated glass slides (Delta Technologies, Loveland, CO, USA). Serial sections were obtain for histological analysis. Slides were washed to remove any excess interfering lipids and salts. Slides were washes in a glass petri dish by sequential washes of 70% ethanol (30 seconds,) 100% ethanol (30 seconds,) Carnoy solution (6:3:1 Ethanol:chloroform:acetic acid for 120 seconds,) 100% ethanol (30 seconds,) Water with 0.2% TFA (30 seconds,) and 100% ethanol (30 seconds.) After sections were dry, a mixed matrix of 15 mg/mL dihydroxybenzoic acid and 5 mg/mL α-cyano-4-hydroxycinnamic acid were prepared in 90% acetonitrile with 0.2% TFA. This solution was homogeneously sprayed onto the surface of mouse kidneys using a HTX TM Sprayer. The TM sprayer was operated at a speed of 1100 mm/min with 2 mm track spacing between rows. The nozzle was heated to 90°C and 90% acetonitrile was used as a pushing solvent at a rate on 0.2 mL/minute. Six passes of matrix were applied in a criss-cross pattern. After matrix was applied, the sample was rehydrated similarly to previously described.[120] The slide was warmed for 2 minutes at 85°C before it was suspended over a solution of 10% acetic acid for 3 minutes.

MALDI IMS analysis was performed using a Bruker AutofleX Speed TOF/TOF operated in linear ion mode with conditions similar to those described above. The analysis was performed at 75 micron spatial resolution. There were 20,253 positions interrogated leading to a 7 gigabyte file that was collected in ≈ 6.5 hours.

Histological Analysis of Mouse Lungs

For each section analyzed using MALDI IMS, a serial section was collected for histological analysis. Serial sections were hematoxylin and eosin (H&E) stained. Slides were scanned using a MIRAX Scan slide scanner (Carl Zeiss MicroImaging, Gŏttingen, Germany) in manual bright field

mode and optical images were generated using MIRAX Viewer version 1.11.22.0 (Carl Zeiss MicroImaging.) Forty times magnification images were generated by an experienced pathologist to assess biological and technical replicates for gross pathology and similarity. Images were obtained using an Olympus BX41 microscope (Olympus, Melville, NY, USA) equipped with a Spot Insight Camera (Diagnostics Instruments, Sterling Heights, MI, USA).

Histological Analysis of Mouse Kidney

Serial sections of all kidney tissues analyzed using MALDI IMS was collected for histological analysis. In addition, post analysis matrix was washed away using ethanol baths and the same sections used in MALDI IMS were stained for histological analysis. Slides were scanned using a Leica SCN400 Brightfield Scanner at 20x magnification.

Protein Purification

Tissue samples with high abundance of S100A8 and S100A9 (samples from 48 hpi) were used for protein identification. Adjacent sections of tissue from those imaged were collected and homogenized using Tissue Protein Extraction Reagent (T-PER). Extracts were fractionated by reversed phase high performance liquid chromatography (HPLC) using a Waters 2690 Separations Module and C8 column (VYDAC, Grace Davison Discover Sciences). Proteins were eluted over 75 minutes using the following gradient: initial flow of 95% solvent A (0.1% TFA), 5% solvent B (acetonitrile, 0.1% TFA), ramped to 25% B over 15 minutes, ramped to 60% B over 50 minutes, ramped to 95% B over 10 minutes, held for 5 minutes, ramped down to 5% B over 10 minutes and held for 20 minutes. Fractions were collected each minute at a rate of 0.5 mL/min. MALDI spectra were collected from each fraction to determine fractions of interest.

LC-Coupled Tandem Mass Spectrometry

Fractions corresponding to S100A8 and S100A9 were dried down and reconstituted in 100 mM ammonium bicarbonate, pH 8.0. Aliquots corresponding to 2 μg of protein (measured using a Bradford assay) were digested with endoproteinase trypsin (Promega Madison, WI) at 1:20 enzyme: protein ratio overnight at 37°C. The resulting peptides were acidified and bomb-loaded onto a self-packed pre-column (4 cm x 0.1 mm, Jupiter 5 μm, 300 Å, C18) (Phenomenex, Torrance, CA) fritted with an M520 inline microfilter union (IDEX, Lake Forest, IL). Following equilibration, this column was attached to a self-packed analytical column (20 cm x 0.1 mm, Jupiter 3 μm, 300 Å, C18) (Phenomenex, Torrance, CA) equipped with a laser-pulled, 1 μm nanospray emitter tip (P-2000, Sutter Instruments, Novato, CA) and coupled directly to an LTQ mass spectrometer (Thermo Scientific, Waltham, MA) with a nanoelectrospray source.

Peptides were eluted over 75 minutes using a nanoAcquity UPLC system (Waters, Manchester, UK) using the following gradient: initial flow of 98% solvent A (0.1% formic acid), 2% solvent B (acetonitrile, 0.1% formic acid), ramped to 25% B over 45 minutes, ramped to 90% B over 15 minutes, held for 5 minutes, ramped down to 2% B over 2 minutes and held for 8 minutes. Throughout the entire run, a full scan was taken followed by five data-dependent collision activated dissociation (CAD) MS/MS scans with dynamic exclusion enabled with a repeat count of 1, a repeat duration of 30 seconds, and an exclusion duration of 60 seconds. The resulting MS/MS spectra were searched via SEQUEST against a UniprotKB database of canonical mouse proteins. Identifications were filtered and collated at the protein level using Scaffold (Proteome Software, Portland, OR). Peptide hits corresponding to S100A8 and S100A9 were manually verified at both the full MS level and MS/MS level using Xcalibur software (Thermo Scientific, Waltham, MA).

CHAPTER III

PROTEINS THAT ACCUMULATE AT INFECTIOUS FOCI ARE TARGETS OF OXIDATIVE DAMAGE

A version of the following chapter was previously published and has been adapted from Spraggins, Rizzo, Moore et al, *Journal of the American Society for Mass Spectrometry*,

Overview

MALDI IMS is a highly sensitive tool for providing spatial information about the pathogen-host interface. Traditional TOF analysis has limited mass accuracy and resolving power, which hinders both identification and the ability to resolve modified forms of proteins. Using MALDI FTICR IMS solves these problems by providing both mass accuracy and high resolving power, which enables the differentiation of post translational modification of proteins at the pathogen-host interface.

Introduction

Oxidative Modifications to Proteins

Staphylococcus aureus is a Gram-positive pathogen that has the ability to infect virtually any organ.[64] A hallmark of *S. aureus* infection is the formation of purulent infectious foci, called abscesses. Abscess formation has been studied extensively using histologically methods and is

characterized by the robust accumulation of neutrophils and macrophages. These host immune cells are equipped with a range of antimicrobial strategies[89], including the ability to induce oxidative stress in an attempt to kill pathogens.[90, 91, 121, 122] Reactive oxygen species (ROS) generated in response to pathogens can have bystander effects to host cells, sometimes causing irreparable damage and cell death.

Of particular interest is the host protein calprotectin, which accounts for an estimated 40-60% of the cytosolic content of neutrophils.[73] Calprotectin is a metal-chelating heterodimer consisting of the protein subunits S100A8 and S100A9.[123] Bacterial pathogens proliferating within vertebrates must obtain nutrient metals from their hosts to survive and cause disease. In response, vertebrates sequester these elements from pathogens, a process known as nutritional immunity.[65, 69] Previous IMS experiments have shown that the subunits S100A8 and S100A9 have a high relative concentration at infectious foci. At these foci, calprotectin is in close proximity to other proteins known to generate ROS. However, oxidative damage to calprotectin by ROS has not been extensively characterized.[124-126] Imaging proteins with MALDI FTICR MS provides the performance necessary to spatially describe this important family of proteins including their many proteoforms.

Calprotectin has been shown via IMS to be a temporally transient protein- it aggregates at sites of active infection and is cleared when the immune stimulant is no longer a threat.[100] Accumulation at infectious foci is not without risk to the protein; these regions are under significant oxidative stress from other neutrophils attempting to kill pathogens.[80, 87] This supports hypotheses that proteins accumulating at these foci could be targets of oxidative damage. However, traditional protein imaging using MALDI TOF MS does not provide the resolving power to distinguish proteoforms from within tissue, particularly oxidations, which cause a mass shift of

+15.99 on large proteins. This is also applicable for downstream identification confidence using indirect methods; in order to correlate IMS data to proteomics data with confidence, the mass accuracy of a high performance instrument is paramount. Mass accuracies from MALDI TOF imaging experiments have particular bias when collecting mass spectra directly from tissue, where differences in sample height can introduce surface charging due to the insulating nature of the tissue. The practical mass accuracy of a MALDI TOF protein experiment is limited to 20-100 ppm from tissue. This makes identification of analytes from tissue quite challenging

Amino Acid	Selected Modification
Cysteine	Sulfoxide, Sulfone, Disulfide bonds, Nitrosylation, S-Nitroglutathione, Chlorination
Methionine	Sulfoxide, Sulfone
Tyrosine	Dityrosine, 2-Hydroxytyrosine, 3-Hydroxytyrosine, 3-Nitrotyrosine, 3-Chlorotyrosine, 3-Bromotyrosine
Tryptophan	Hydroxytryptophan, Nitrotryptophan
Histidine	2-oxo-Histidine
Lysine	3-Hydroxylysine, Chlorolysine, Protein Carbonyls
Proline	Hydroxyproline, Protein Carbonyls
Arginine	Protein Carbonyls
Threonine	Protein Carbonyls

Table 3.1: Common Oxidative Modifications

Table 3.1 lists common oxidative modifications and the amino acids they affect. It was adapted from Free Radical Biology and Medicine, 41, 10. Schoneich et al, "Mass Spectrometry of Protein Modifications by Reactive Oxygen and Nitrogen Species." 2006 with permission from Elsevier.[127]

Oxidative modifications can alter many amino acids, with the most common targets detailed in Table 3.1. The most abundant proteins in neutrophils have been reported to be oxidatively modified. S100A8, a subunit of calprotectin, can have many modifications at cysteine residues induced *in vitro*, including S-nitrosylation, glutathionylation, and conversion to sulfenic and sulfonic acids.[128] Additionally, methionine residues in S100A8 can oxidize to sulfoxides.[125] Alteration of easily oxidized residues has shown some changes to biological function. It has been

proposed that native calprotectin is anti-inflammatory, but calprotectin under oxidative stress is more antimicrobial.[129] Mutation of S100A8 cysteine 42 to alanine caused a lack of the dimer's activity and mutation of S100A9 methionine residues at positions 63 and 83 decreased antifungal activity.[129] These examples highlight the need to study the biological role of oxidative modifications to proteins in infection. Such modifications and their biological impact have remained largely unstudied and could present a new area of focus for antimicrobial strategies.

In this work, we propose to explore oxidative modifications on host and bacterial proteins spatially localized to the pathogen-host interface. With a focus on calprotectin as a model protein, this work intends to analyze the spatial distribution of oxidized calprotectin at infectious foci.

Neutrophil Extracellular Traps

Neutrophils are the most abundant innate immune cell. Representing the first line of defense for the immune system, they come with an arsenal of antimicrobial compounds. When presented with pathogens, neutrophils have three main modes of attack. First, they can use phagocytosis to destroy the pathogen intercellularly. Second, they can generate ROS extracellularly by degranulation.[83] The final method is a novel form of cell death that leads to the generation of neutrophil extracellular traps, or NETs.[130] Much like their acronym, NETs are net-like structures formed with a backbone of chromatin and histones. NETs contain all the antimicrobial arsenal of the neutrophil and can bind and kill microorganisms.[130] Interestingly, the formation of NETs requires that ROS be generated; cells lacking NADPH oxidase are unable to form NETs.[130] A proteomic study a NETs identified 24 NET-associated proteins, including calprotectin.[83] Additionally, histones were identified as the backbone of the structure as well as several proteins that are known to localize to granules. Table 3.2 shows the proteins identified by

Urban et al.[83] Since these proteins are trapped on the actual NET, they are immobilized at regions of intense pathogen-host interactions. Since other neutrophils spatially localized to this regions are generating ROS extracellularly in attempts to kill the pathogen, it is hypothesized that the host proteins in Table 3.2 might also be targets of oxidative damage. Microorganisms have also developed novel mechanisms to escape NETs. The ability to degrade the chromatin backbone of the structure has allowed many microorganisms to escape this antimicrobial strategy. For example, Group A *Streptococcus* expresses a DNase that allows the degradation of the NET and the bacteria to escape its killing mechanisms.[131]

Cellular Localization	Protein	Gene
Granules	Leukocyte Elastase	ELA2
	Lactotransferrin	LTF
	Azurocidan	AZU1
	Cathepsin G	CTSG
	Myeloperoxidase	MPO
	Leukocyte Proteinase 3	PR3
	Lysozyme C	LYZ
	Neutrophil Defensin 1 and 3	DEFA-1, DEFA-3
Nucleus	Histone H2A	H2A
	Histone H2B	H2B
	Histone H2B-Like	H2B
	Histone H3	H3
	Histone H4	H4
	Myeloid Cell Nuclear Differentiation Antigen	MNDA
Cytoplasm	S100A8	S100A8
	S100A9	S100A9
	S100A12	S100A12
Cytoskeleton	Actin	ACTB, ACTG1
	Myosin-9	MYH-9
	Alpha-actinin	ACTN1, ACTN4
	Plastin-2	LCP1
	Cytokeratin-10	KRT-10
Peroxisomal	Catalase	CAT
Glycolytic	Alpha-Enolase	ENO1
Enzymes	Transketolase	TKT

Table 3.2: Proteins that Localize to NETs

Proteins that localize to NETs. Proteins are organized by their localization in unstimulated neutrophils. Reprinted from PLoS Pathogens, 5, 10, Urban et al. "Neutrophil Extracellular Traps Contain Calprotectin, a Cytosolic Protein Complex Involved in Host Defense against *Candida albicans*" 2009 distributed under the terms of the Creative Commons Attribution License.

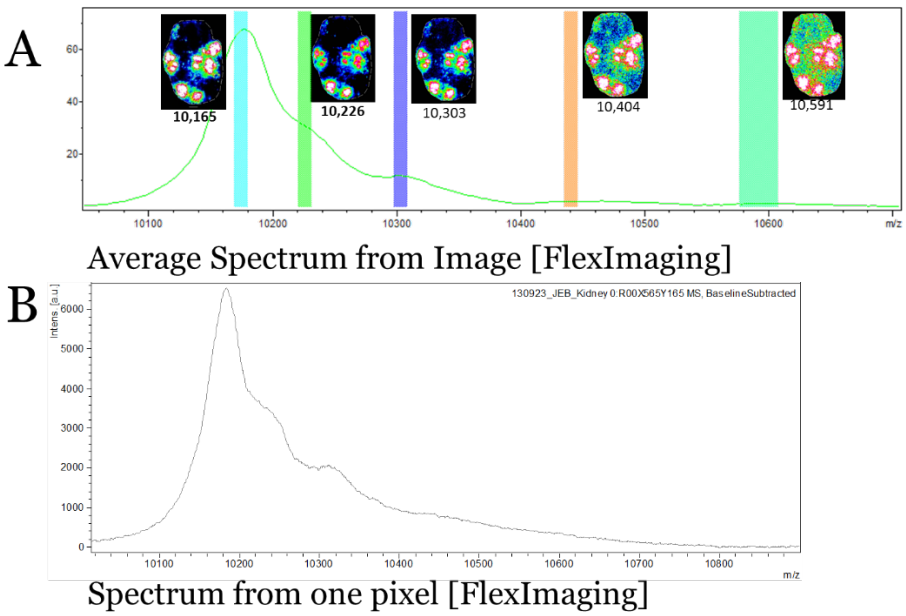

Figure 3.1: Time-of-Flight MS Does Not Resolve Peaks

Time-of-flight mass spectrometers lacked the resolving power to differentiate peaks surrounding S100A8. A representative spectrum is shown in A) taken from the overall averaged spectrum. Insets show MALDI IMS ion intensity maps selected from within the spectral region. These ion intensity maps share similar spatial resolution, suggesting that they could be related proteins. B) is a representative spectrum taken from a single pixel from within the aggregated neutrophils of the abscess.

Results and Discussion

TOF MS Lacks the Resolution to Resolve Post-Translational Modifications of Proteins

Traditional MALDI IMS experiments have been performed on TOF instruments, which have limited mass resolving power. This proves problematic for modified protein isoforms. It was hypothesized that the proteins in Table 3.2, which are associated with NETs and unable to escape the ROS generated by other leukocytes, would be targets of oxidative damage. Two of these proteins are S100A8 and S100A9, the subunits of calprotectin. These proteins are abundantly recruited to sites of infection in kidney tissue from mice infected with *S. aureus.* Figure 3.1 shows

a typical MALDI TOF MS spectrum from an on-tissue imaging experiment. Figure 3.1A shows the overall averaged spectrum while Figure 3.1B shows a spectrum taken from a single pixel in the analysis. It is apparent that there are multiple species represented and that the instrument lacks the resolving power to differentiate these species. In order to further study these species and their potential biological role, a high mass resolving power instrument was used.

FTICR MS Reveals Post-Translational Modifications of Proteins

MALDI FTICR MS has the capability to address the lack of resolving power in the previous analysis. Figure 3.2 displays the spectral complexity of MALDI FTICR IMS data of intact proteins from kidney tissue taken 9 dpi with Strain Newman *S. aureus*. The overall averaged spectrum is shown in Figure 3.2A. Figure 3.2B expands the y axis (intensity) to highlight the quality of the data and the ability of high mass resolution instrumentation to differentiate the charge state of individual analytes, further aiding downstream protein identification strategies. These data were collected at a resolving power of ~75,000 at *m/z* 5,000 providing isotopic resolution and allowing multiple potential isoforms of S100A8 to be distinguished in Figure 3.2C. In this robust data set, 2,552 peaks detected between *m/z* 2,000 – 12,000 with S/N > 20.

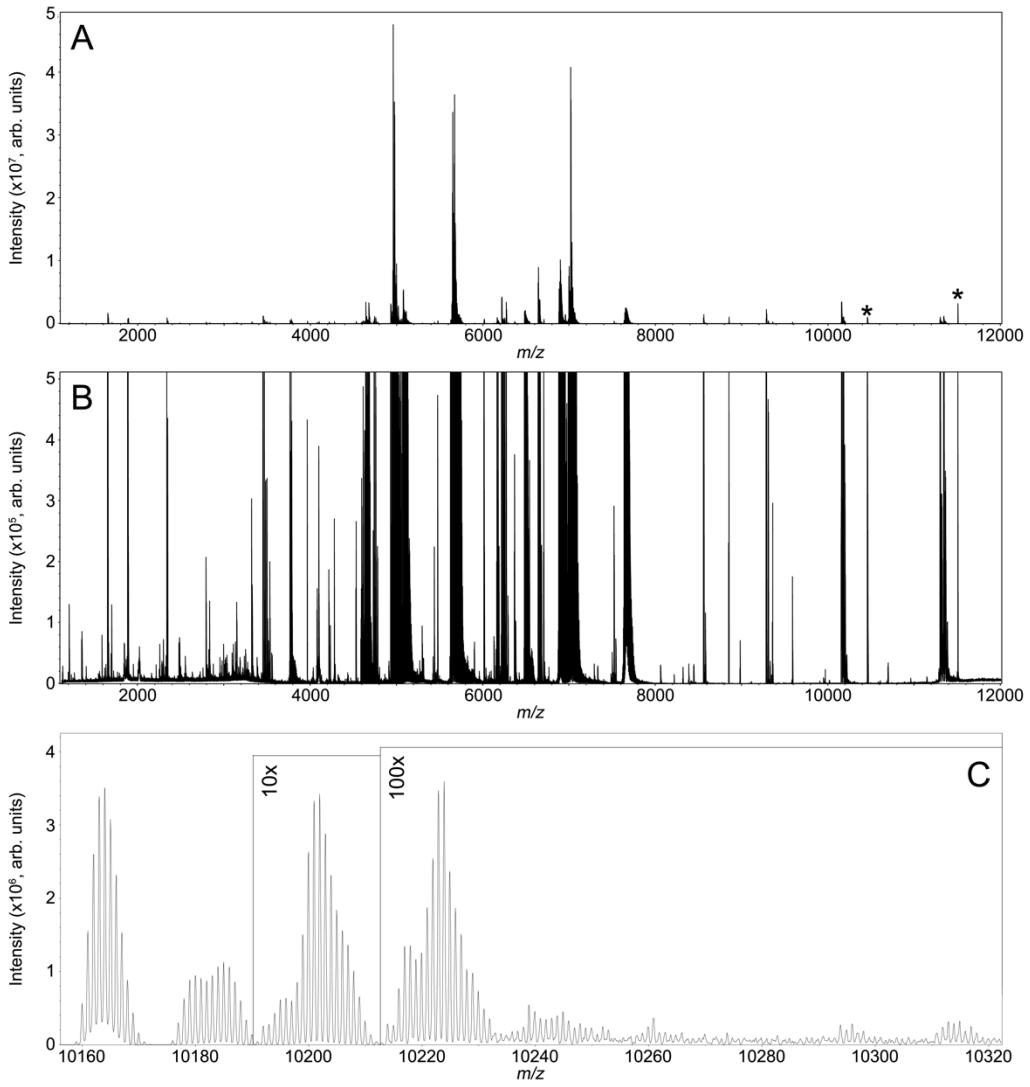

Figure 3.2: FTICR MS Reveals Multiple Proteins

"MALDI FTICR IMS of intact proteins from kidney tissue from a mouse infected with *S. aureus*. The average spectrum of the entire imaging data set is shown in panel A. Expanding the intensity scale (B) highlights the overall quality of the data with singly and doubly charged protein signals detected between *m/z* 1,000 – 12,000. Data were collected with a resolving power of ~75,000 at *m/z* 5,000 providing isotopic resolution and allowing multiple isoforms of S100A8 to be distinguished (Panel C). Electronic noise peaks are labeled (*). Reprinted from the Journal of the American Society for Mass Spectrometry, 26, "MALDI FTICR IMS of Intact Proteins: Using Mass Accuracy to Link Protein Images with Proteomics Data." Spraggins, Rizzo, and Moore et al. 974-985. 2015 with permissions from Springer.[30]

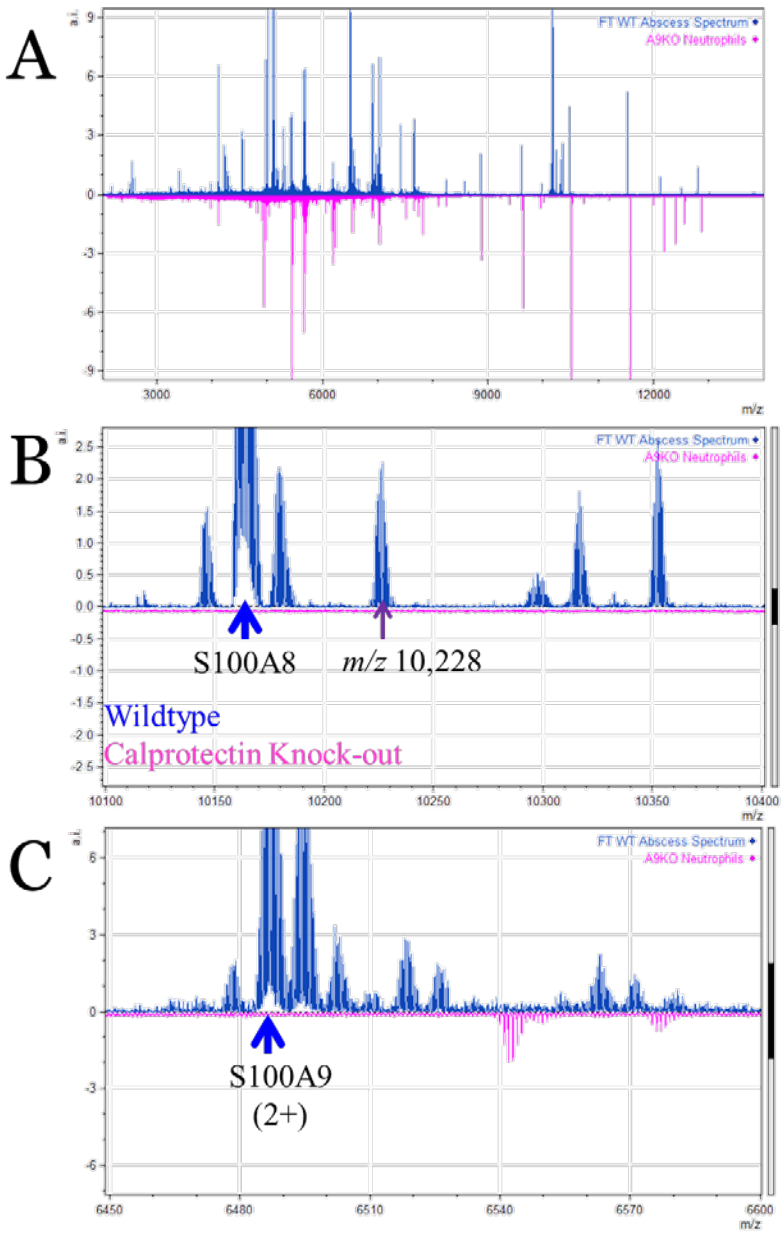

Figure 3.3: FTICR Reveals Peaks Not Present in Calprotectin Knock-out Mouse
In order to support the idea that peaks surrounding S100A8 and S100A9 could be isoforms of calprotectin, they were compared to spectra taken from the lesions of a calprotectin knock-out (CPKO) mouse. The spectrum from the wildtype mouse is shown in blue while the knockout mouse is shown in pink. The CPKO spectrum is falsely inverted on the axis strictly for display purposes. A) shows the full spectrum, revealing robust data from each animal and confirming that a lack of signal in the CPKO was not due to a poor quality analysis. B) shows a magnification of the spectrum around the mass of S100A8, with many peaks present in the WT that are absent in the CPKO. C) shows similar data for S100A9, which was best detected in a 2+ charge state. Taken together these data support the idea that the peaks could represent modified forms of calprotectin.

In order to support the idea that the peaks in Figure 3.2C might be isoforms of S100A8, an additional analysis was performed on a calprotectin knock-out (CPKO) mouse. This mouse lacks the ability to produce S100A9, but because of this genetic alteration does not express S100A8 either. Figure 3.3 shows spectra from lesions of either wildtype or CPKO mice collected on a 15T FTICR MS. Figure 3.3A shows the robust spectra collected from both lesions taken at 9 dpi with strain Newman *S. aureus*, with the spectra from wildtype abscess in blue and the CPKO abscess in pink. The CPKO spectrum is inverted for comparison purposes only. However, Figure 3.3B shows a dramatic difference in the spectra surrounding the peak for S100A8 and Figure 3.3C shows peaks surround S100A9 in a 2+ charge state. A number of peaks appear in the wildtype (blue) spectrum that are absent entirely from the CPKO (pink, inverted) spectrum. It is hypothesized that these peaks represent modified forms of S100A8 and S100A9. Although not fully resolved, the data suggest there are ~12 species within the highlighted mass window in Figure 3.2C and 3.3B, all likely unique proteoforms of S100A8.

Top Down Sequencing Identifies Proteoforms of S100A8

The protein S100A8 was detected at *m/z* 10,164.03 ($[M+H]^{1+}$, -2.1 ppm) in the MALDI mass spectrum using a 15T FTICR MS. This peak was subsequently identified using top-down fragmentation. Figure 3.4 shows data obtained using LC-MS/MS to isolate and sequence this ion of interest. Figure 3.4A shows the full MS of the parent ion, with the charge state selected for sequencing annotated in red. Figure 3.4B shows an annotated MS/MS spectrum obtained by top-down fragmentation using an ETD-enabled Thermo Scientific LTQ Orbitrap Velos.

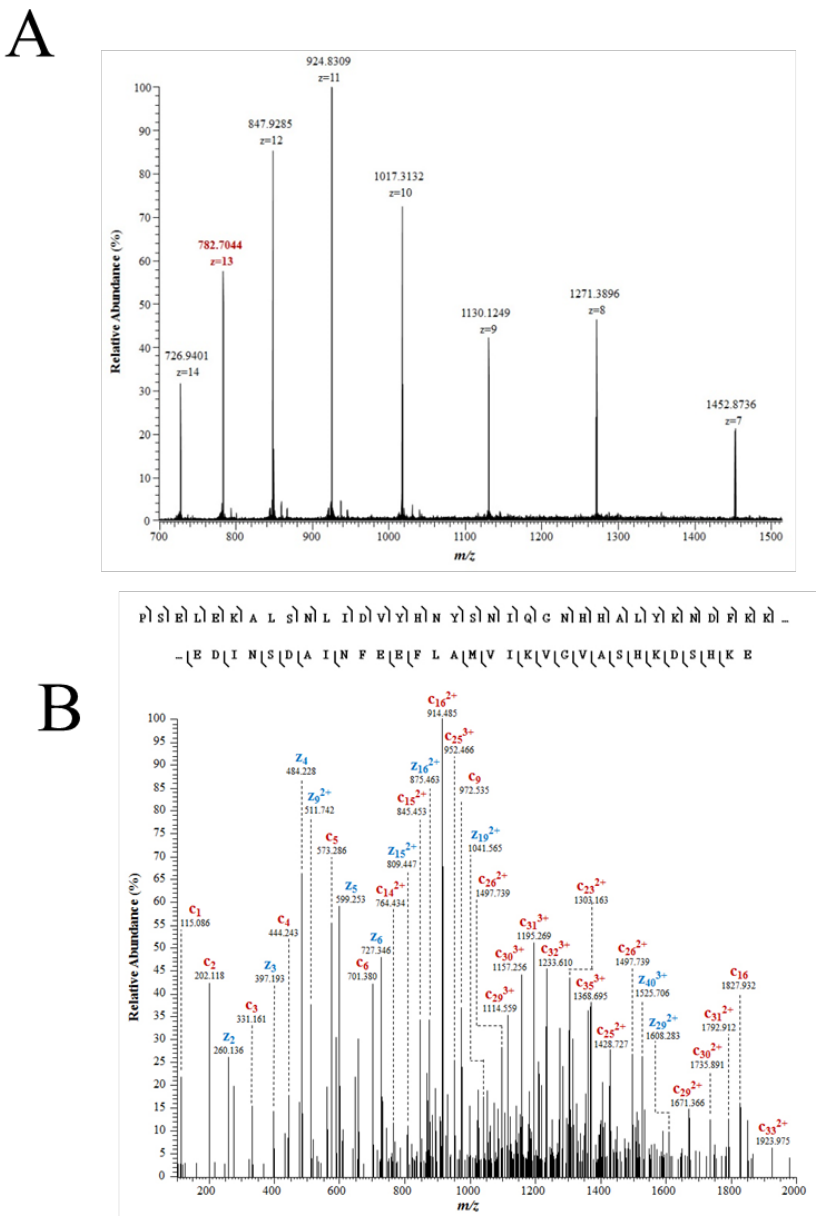

Figure 3.4: ETD Sequencing of S100A8

ETD LC-MS/MS data for S100A8. The charge state distribution is shown in the top panel with the specific charge state selected for MS/MS highlighted in red. ETD fragmentation data is shown in the bottom panel including selected c (red) and z (blue) ion annotations. A summary of the observed fragments and sequence coverage is also included. Reprinted from the Journal of the American Society for Mass Spectrometry, 26, "MALDI FTICR IMS of Intact Proteins: Using Mass Accuracy to Link Protein Images with Proteomics Data." Spraggins, Rizzo, and Moore et al. 974-985. 2015 with permissions from Springer.[30]

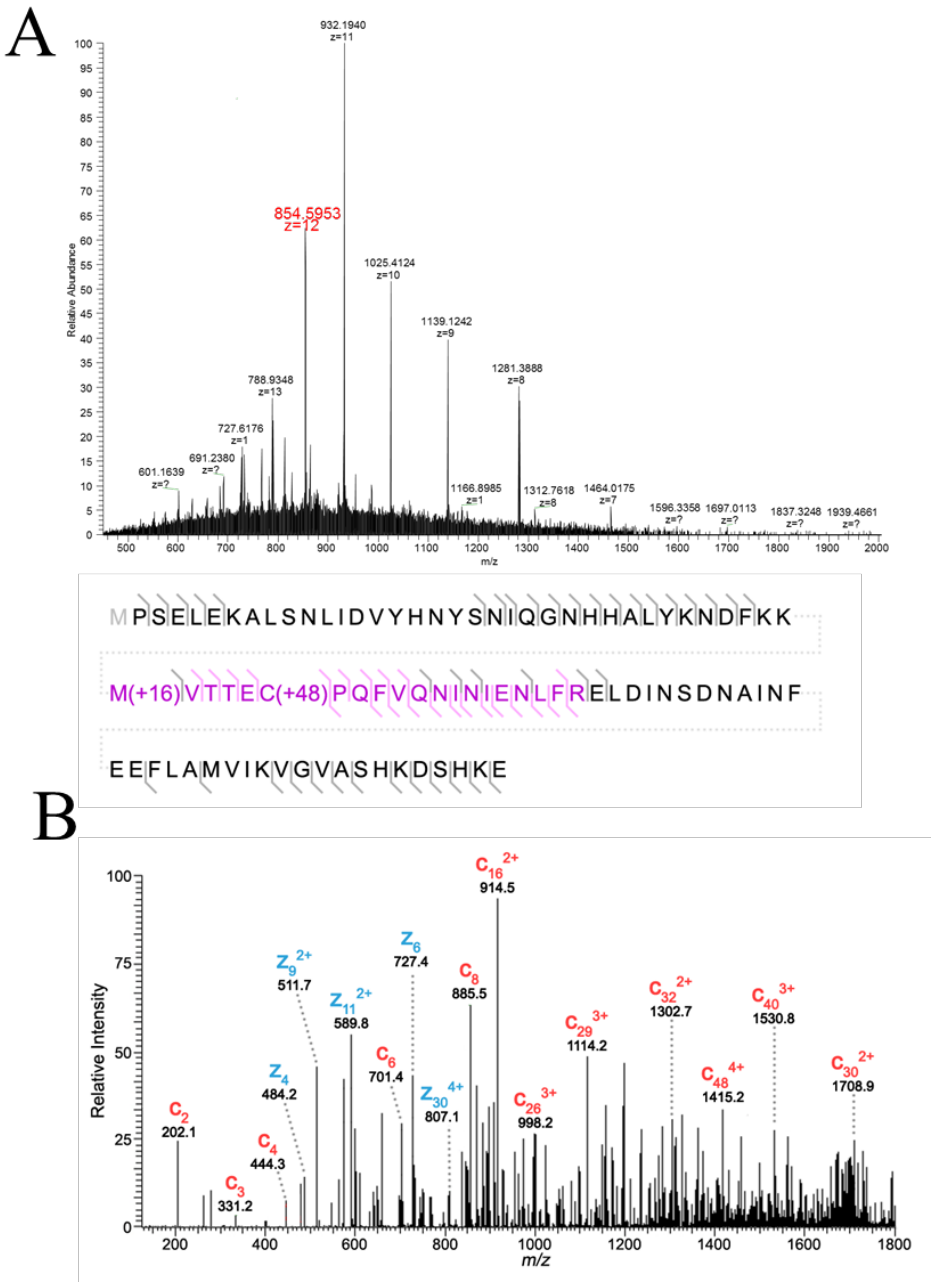

Figure 3.5: ETD Sequencing of Modified S100A8

ETD LC-MS/MS data for modified S100A8. The charge state distribution is shown in A) with the specific charge state selected for MS/MS highlighted in red. ETD fragmentation data is shown in B) including selected c (red) and z (blue) ion annotations. A summary of the observed fragments and sequence coverage and modifications is also included. Reprinted from the Journal of the American Society for Mass Spectrometry, 26, "MALDI FTICR IMS of Intact Proteins: Using Mass Accuracy to Link Protein Images with Proteomics Data." Spraggins, Rizzo, and Moore et al. 974-985. 2015 with permissions from Springer.[30]

Identification was also attempted on the masses that corresponded to the potential proteoforms of S100A8. One in particular, appearing at *m/z* 10,228.00 was extensively purified for top-down sequencing to both identify the protein and the residues that were altered or modified. MS/MS data are shown in Figure 3.5. The parent spectrum is shown in Figure 3.5A with the charge state selected for MS/MS analysis annotated in red. Figure 3.5B shows both the MS/MS spectrum and sequence coverage of the protein. This determined a mass shift of +48.00 on cysteine residue 42, consistent with a trioxidation of cysteine to cysteic acid. There was also a mass shift of +15.99 on methionine 37, consistent with an oxidation. In order to confirm these post-translational modifications, a bottom-up protein identification strategy was employed. After tryptic digestion, the peptide containing the modification, annotated in Figure 3.5B by pink text, was fragmented using HCD on a Thermo Q Exactive Orbitrap MS. The annotated peptide fragmentation spectrum is shown in Figure 3.6. Bottom-up fragment ions of particular importance for making this identification included the b_2+16 fragment showing the addition of oxygen to methionine 37 and the b_5+16 and b_6+64 fragment ions that result from three oxygen atoms being added to cysteine 42. Oxidation of S100A8 has been hypothesized to play a critical role in the protein's antimicrobial activity.[132]

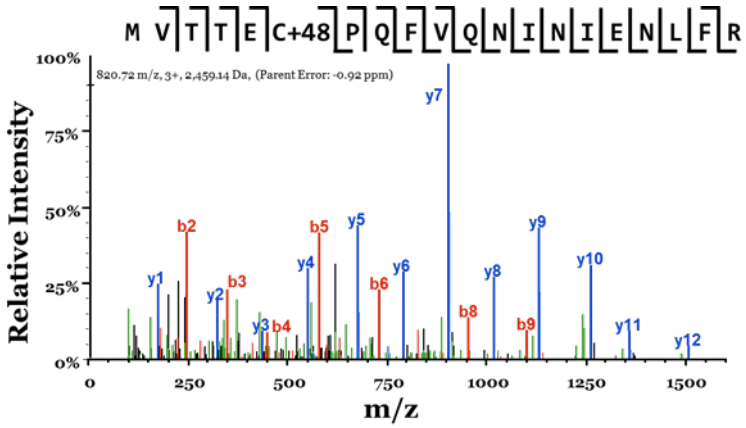

Figure 3.6: MS/MS sequencing at a Peptide Level Confirms PTMs
An aliquot of the sample in Figure 3.5 was subjected to tryptic digestion to confirm the modification at a peptide level. The pink peptide annotated in Figure 3.4 containing the modified cysteine residue to sequenced here.

Proteoforms of S100A8 are Differentially Localized in Staphylococcal Lesions

Understanding the impact of oxidative damage to S100A8 on its function during the host-pathogen interaction is of great importance. In order to study this, MALDI IMS was used to spatially localize these identified proteoforms. An abscessed mouse kidney was subjected to MALDI IMS experiments using a 15T FTICR. The resulting images are shown in Figure 3.7. Figure 3.7 highlights the high quality of these data and the ability to generate many ion intensity maps from a single analysis. This also allows for the annotation of charge states of the ions, which will greatly aid downstream protein identification strategies by allowing accurate mass measurements. Figure 3.8 features selected ion images for a proposed series of oxidative modifications to S100A8. MALDI FTICR images of acetylated $T\beta_{10}$ ($T\beta_{10}$-AC, $[M+H]^{1+}$, 1.2 ppm) and acetylated $T\beta_4$ ($T\beta_4$-AC, $[M+H]^{1+}$, 1.6 ppm) were included for comparison. Labeled ions (*) are only tentatively identified based on mass accuracy. Both thymosins were found to

localize primarily to non-abscessed tissue, whereas S100A8 and the oxidation products S100A8+O (*m/z* 10,180.07, $[M+H]^{1+}$, 2.3 ppm), S100A8+2O (*m/z* 10,196.07, $[M+H]^{1+}$, 3.0 ppm), and S100A8+4O (*m/z* 10,228.00, $[M+H]^{1+}$, -2.6 ppm) were all specifically detected with greater intensity at infectious foci. An interesting observation is that oxidation seems to occur at a greater rate near the center of abscesses leading to more advanced oxidation products at these locations. This is particularly noticeable when comparing the MALDI FTICR IMS data to an H&E stained micrograph of a serial tissue section (Figure 3.8B). Abscesses are clearly distinguished as darker stained regions in the microscopy image and a zoomed-in view of one particular abscess highlights a staphylococcal microcolony that can be found at the center of these infectious foci. In comparing the histological images to overlays of ion images (Figure 3.8C), advanced oxidation products are found to co-localize to regions where the staphylococcal microcolonies are found. The overlay displayed on the left side of Figure 3.8C shows S100A8 is localized to the infectious foci, however, the unmodified form of the protein seems to be of lower abundance at the center of the highlighted abscess. On the other hand, the S100A8+4O oxidation product, shown on the right side of Figure 3.8C, is found in the center of this particular abscess suggesting oxidative processes are occurring specifically at the host-pathogen interface.

The ability to differentiate modified proteins with high confidence in MALDI FTICR IMS experiments with high resolution and mass accuracy is important to infection biology because protein oxidation can generate new proteoforms, which are hypothesized to elicit both innate and adaptive immune responses.[132] For calprotectin, which has extensive downstream effects as both an initiator of inflammation and a signaling molecule, defining the biologically relevant form of the protein becomes very important.[133] Oxidized proteoforms of S100A8 and S100A9 have previously been hypothesized to suppress inflammation.[125, 134] Given the important biological role

of calprotectin both as a major component of nutritional immunity and as a mediator of inflammatory response, IMS analyses such as these stand to greatly enhance our knowledge of calprotectin's oxidative forms at infectious foci.

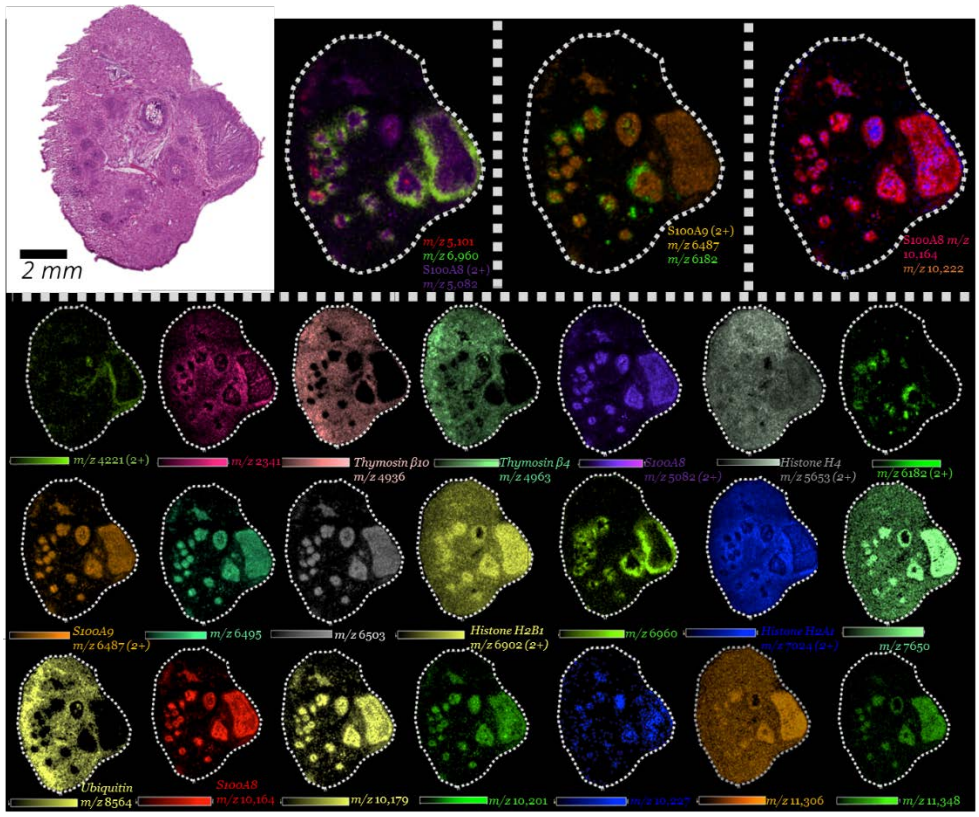

Figure 3.7: MALDI IMS Data Generated from FTICR IMS of 9 DPI Kidney
MALDI FTICR IMS performed on a mouse kidney taken 9 days post infection. The top panels shows histological staining as well as several ion intensity maps overlaid to generate molecular maps marking histological features associated with infection. The bottom panels show a selected series of ions that have interesting distributions throughout this biology as an example of the power of MALDI IMS experiments for discovery-based analyses. Ions given protein identities in this analysis were determined using accurate mass measurements only.

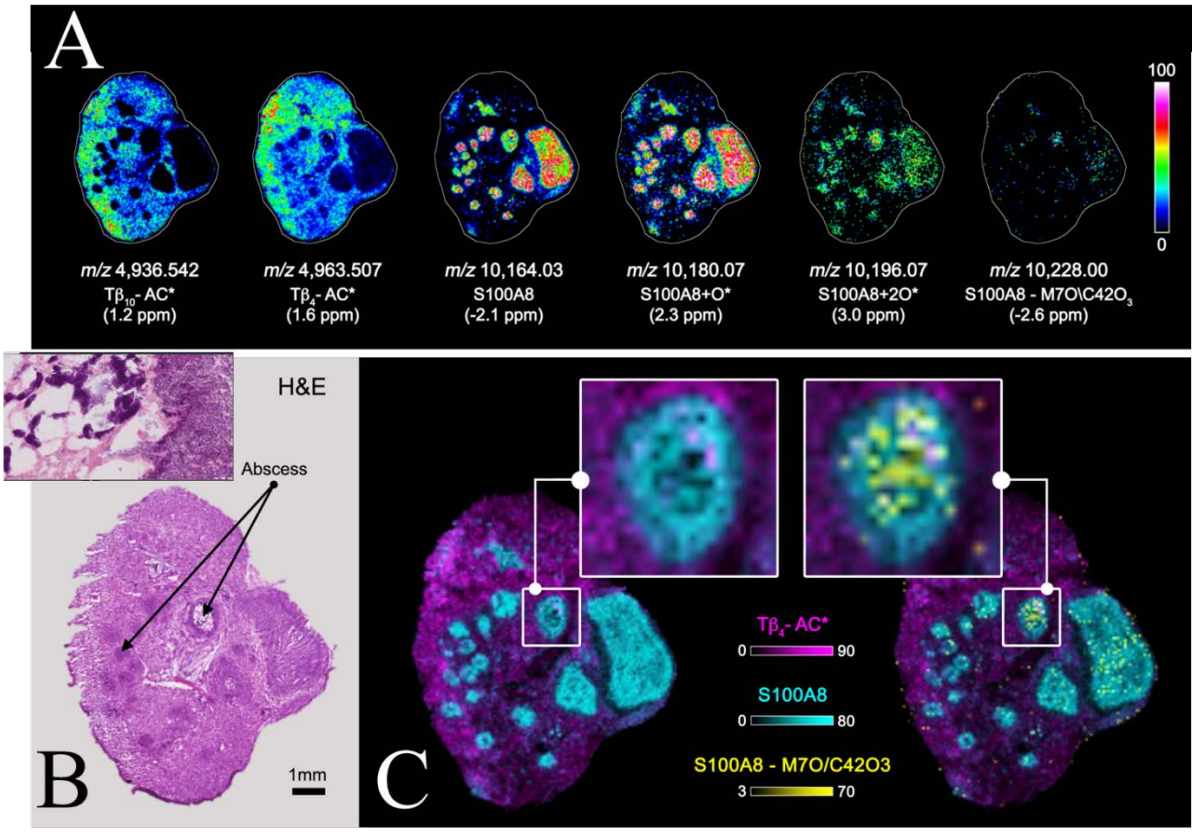

Figure 3.8: Proteoforms of S100A8 are Differentially Localized to Staphylococcal Lesions Selected ion images of intact proteins from kidney tissue from a mouse infected with *S. aureus* collected using MALDI FTICR MS (**A**). Ions were identified using mass accuracy to correlate imaging results with separate top-down proteomics experiments. For comparison, a serial tissue section was H&E stained (**B**). Ion image overlays show the advance oxidation product S100A8 – M7O/C42O$_3$ is localized specifically to the center of infectious foci (**C**). Italicized ions were tentatively identified by mass accuracy only" Reprinted from the Journal of the American Society for Mass Spectrometry, 26, "MALDI FTICR IMS of Intact Proteins: Using Mass Accuracy to Link Protein Images with Proteomics Data." Spraggins, Rizzo, and Moore et al. 974-985. 2015 with permissions from Springer.[30]

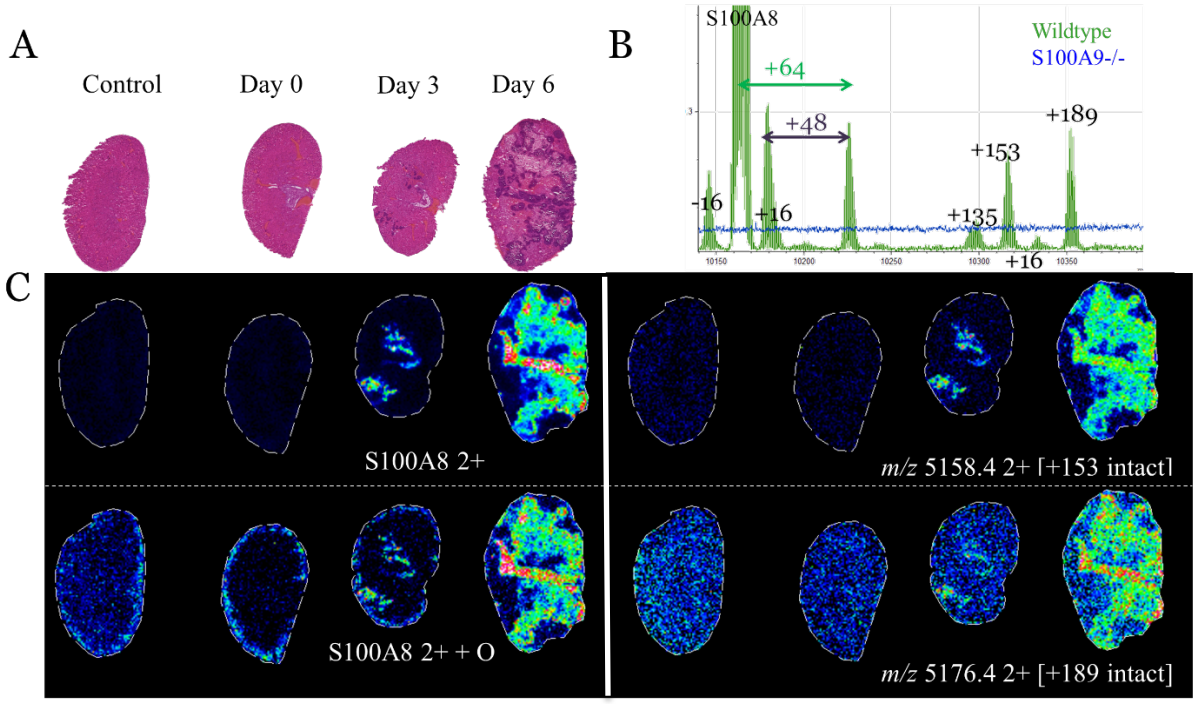

Figure 3.9: Neutrophils Accumulate at Infectious Foci as Infection Progresses
As systemic bacterial infection progresses without treatment, large inflammatory foci and tissue necrosis occur, as shown in A. These foci develop oxidative modifications not present in a CPKO mouse, shown in panel B. The spectrum taken from the wildtype lesion is shown in green while the spectrum from the CPKO lesion is shown in blue. Mass differences are annotated. Ion intensity maps showing such shifts and how they accumulate over the time course are shown in panel C.

Accumulation of Neutrophil Extracellular Traps at Infectious Foci leads to Post-Translational Oxidation

The previous analyses utilized animals from a late time point in the sepsis model- 9 dpi. This allowed oxidative modifications to build with time and disease progression. However, in order to study the formation of these proteoforms, a time course model of abscess formation was studied. Here, both control and animals at 0, 3, 6 dpi were analyzed using MALDI FTICR IMS. Figure 3.9 highlights the formation of modified S100A8 detected during this time course of infection. Figure 3.9A shows histological staining for orientation. Figure 3.9B represents a

MALDI FTICR mass spectrum taken from a 9 dpi wildtype and CPKO mouse with mass shifts from parent S100A8 annotated to the nearest whole value. Modified forms are not detected before 3 dpi, when lesions are small but well-formed. By 6 dpi, when lesions are large and surrounded by necrosis, several modified forms of S100A8 are detected, including those with mass shifts of +153 and +189, which are still unidentified. Interestingly, the ion at *m/z* 10,228 representing a methionine oxidation and cysteine trioxidation was not detected in this analysis. This could indicate that such a product is only formed later, when the host has undergone long time periods under oxidative stress, consistent with sepsis progression to severe sepsis or septic shock.

Oxidation of S100A8 Occurs in Acute Infection Models

The ability of MALDI IMS to detect multiple proteoforms during bacterial infection is very analytically powerful. A model of severe infection was an ideal model for this technology, where one would expect the disease to progress until it overtakes the host, causing extensive oxidative damage to proteins in the process. However, this also prompted us to consider oxidative modifications in acute infection models, where the infection is resolved by the host. This would reveal whether such oxidative modifications lead to long-term tissue damage or if they are easily resolved by the host once the infection is resolved.

During initial TOF MS imaging analyses from Chapter II, a time course of *A. baumannii* pulmonary infection was utilized to monitor infection over time. This infection begins to resolve at 24-36 hpi with a marked decrease in bacterial burden that is below the limit of detection by 96 hpi. The signal from calprotectin subunits S100A8 and S100A9 was a bit longer lived, with signal still present at 144 hpi but resolving by 192 hpi. By this time [8 days post infection] the mice have

regained weight to be comparable to pre-infection weights. Though Chapter II only showcased ion intensity maps from a few selected ions, there are a plethora of other signals present in these

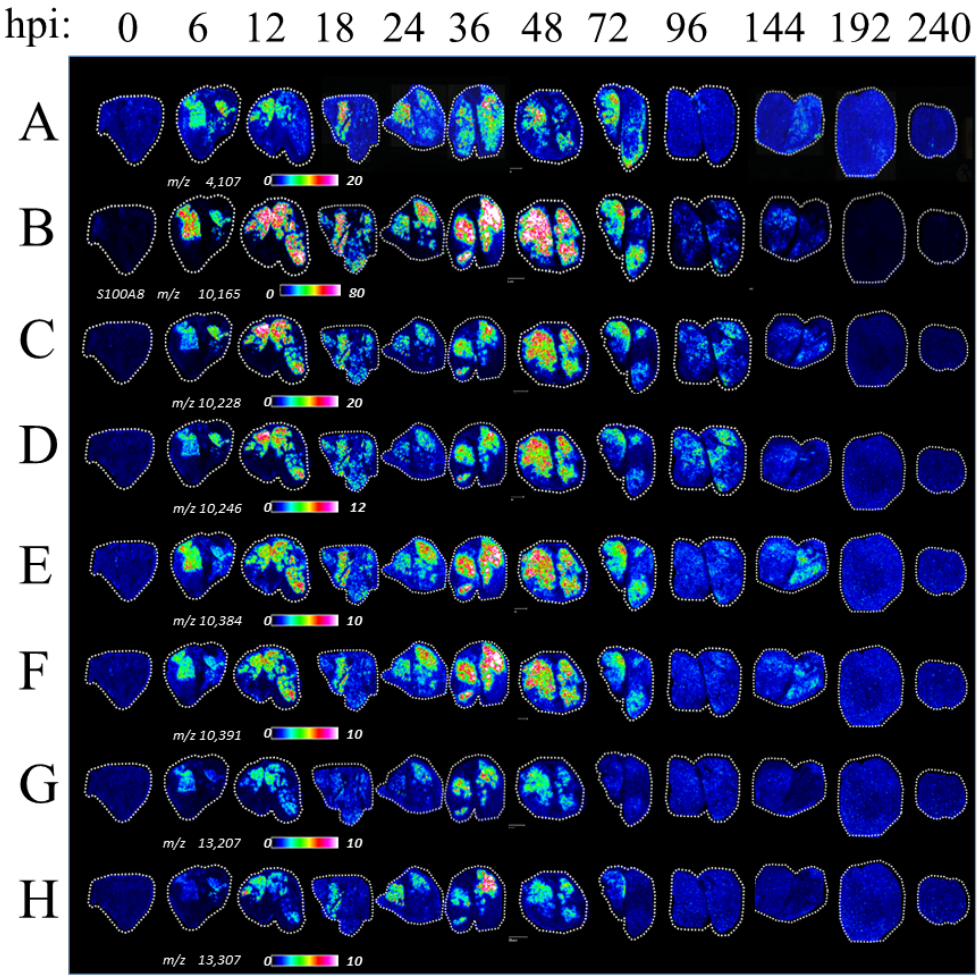

Figure 3.10: Unresolved Modifications are Present in an Acute Model of Infection
Initial time-of-flight analyses of an acute model of *A. baumannii* pneumonia revealed a number of peaks with spatial distribution patterns that closely followed S100A8, shown in B. Many of these peaks had *m/z* ratios that were consistent with oxidative modifications that had been observed in staphylococcal lesions. . Reprinted from *Proteomics,* 14, 0, "Imaging Mass Spectrometry for assessing temporal proteomics: Analysis of calprotectin in *Acinetobacter baumannii* pulmonary infection." Moore et. al, 2014, 820-828 with permission from John Wiley and Sons.[100]

analyses. Revisiting these data for patterns similar to S100A8 and S100A9, which rise with infection and disappear when infection resolved yielded many analytes of interest. Figure 3.10

shows other signals of interest and potentially represents other proteins involved in response to bacterial infection. Several of these signals were similar to those detected in high resolving power analyses presented here. Additional analyses were required to confirm this, since it is difficult to determine an accurate mass from a peak that is not resolved from neighbors in TOF analyses.

To determine this, an abridged time course of *A. baumannii* pulmonary infection was analyzed using MALDI FTICR IMS. Figure 3.11 shows two ion intensity maps- one for S100A8 and one for S100A8 with a mass shift of +15.99, representing the oxidized form of S100A8. These two ions seem to have drastically different spatial localization within the inflamed lung. Consistent with previous analyses, calprotectin is not detected at 0 hpi but has robust signal at 6 hpi, when the host has detected the pathogen. At 36 hpi, when the host is beginning to decrease bacterial burdens, there is still signal from both S100A8 and oxidized S100A8. There is a bit of detectable signal at 192 hpi as well, though for the most part signal from both S100A8 and oxidized S100A8 has resolved. In an attempt to understand why S100A8 and oxidized S100A8 would exhibit different spatial localizations, more in depth histological analyses were performed on these tissues. Figure 3.12 shows a more in depth histological look at the lung from 36 hpi, which shows robust neutrophil recruitment to airways. Figure 3.12A shows the section of lung at 36 hpi with two regions annotated for histological analysis. The grey box annotates the MALDI IMS ion intensity maps that are shown at a larger magnification in Figure 3.12B. Areas of immune cell recruitment, which stain darker purple in Figure 3.12A, have robust signal in the MALDI IMS data. Focusing on one airway from the lung, annotated in Figure 3.12A with a blue box, a side by side comparison of both histological and MALDI IMS data can be seen in Figure 3.12C and D, respectively. Here robust neutrophil recruitment can be visualized in the airways of Figure 3.12C. Figure 3.12D shows that the oxidized calprotectin seems to be localized to the center of affected airways, where

we would expect bacteria to be localized. This analysis was carried out at 200 micron spatial resolution, and therefore image reconstruction will fill in a 200 by 200 micron region for each pixel. To fully understand if calprotectin is secreted into the airways where it is oxidized, higher spatial resolution analyses are necessary. These data support the idea that calprotectin is oxidized even in cases of acute infection, and support the idea that the host can clear oxidized calprotectin similarly to the native form.

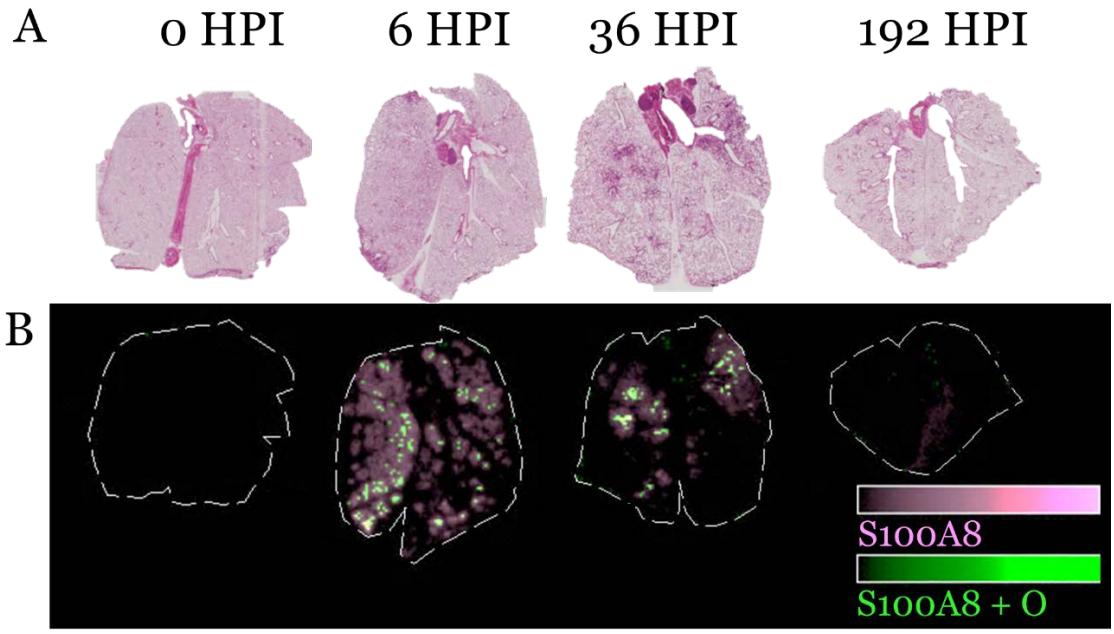

Figure 3.11: FTICR IMS Reveals Oxidations in Acute Model of Infection
High Mass resolution IMS experiments of mouse lungs at various time points post infection. A) shows selected time points, which are representative of the time course presented in Chapter II. Infectious foci are clearly visible at 6 and 36 hours post infection. B) shows high mass resolution MALDI IMS data of two ions of interest, S100A8 and an oxidized form of S100A8 containing a single oxidation. Oxidative forms of S100A8 seem to have colocalization patterns in the middle of the native form.

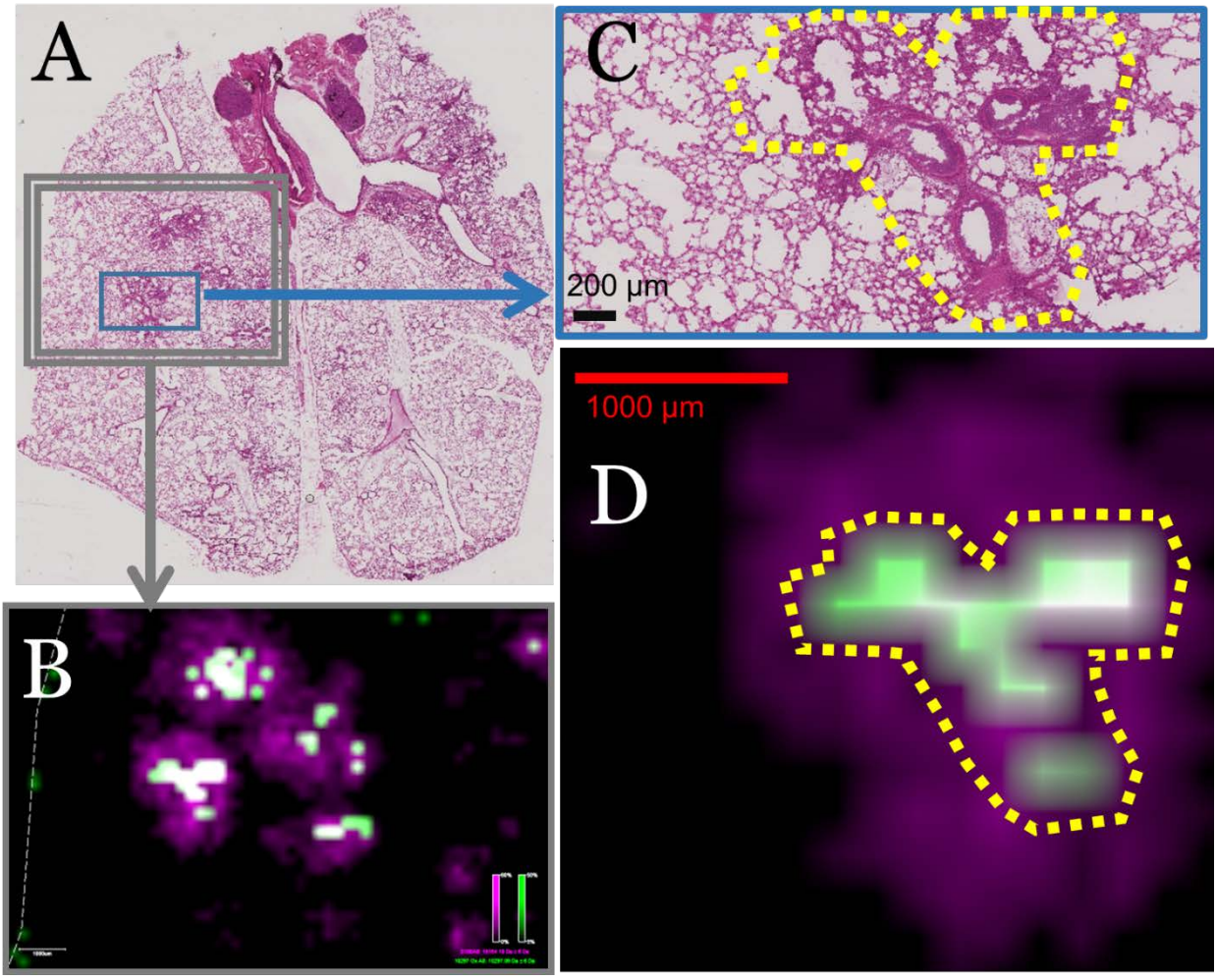

Figure 3.12: Magnification of 36 HPI lung reveals oxidations localize to airways
In order to explore to spatial localization pattern of S100A8 and oxidized S100A8, additional analyses of the lung from 36 hpi were performed. A) shows histological analysis of the lung with two insets enhanced. MALDI IMS data from the grey double box is shown in B. Areas of dark histological staining in A are marked with robust signal of S100A8 (pink) with small centers of oxidized S100A8 (green.) A more in depth analysis of a single bronchi, marked with a blue box in panel A, was performed. Histologically, Figure C shows that this region is marked with robust neutrophil aggregation in a series of airways. Interestingly, in these airways, Oxidized calprotectin (green) co-localizes in panel D.

Methods

Bacterial Strains and Infection

All in-house animal experiments were performed with approval by the Vanderbilt Institutional Animal Care and Use Committee.

Female 6-8 week old C57bl/6 mice (Jackson Laboratories) were infected using a retro-orbital intravenous injection of the clinical isolate Strain Newman *S. aureus.*[119] Inoculae were prepared as detailed in Chapter II. Mice were anesthetized using Avertin (2-2-tribromoethanol) and injected with 100 µL of inoculum in PBS. Mice were monitored as they recovered from anesthesia and were provided free access to food and water throughout the course of infection. Control mice were retro-orbitally injected with PBS only. The infection was allowed to progress up to 9 dpi. At set times post infection, (0, 3, 6, and 9 dpi) mice were sacrificed and organs aseptically removed. Moribund mice were sacrificed immediately when found. Organs were frozen in plastic weigh boats using dry ice and stored at -80°C until analysis.

A mouse model of pulmonary infection was used as described in Chapter II. [81, 118] Briefly, Strain Ab17978 *A. baumannii* was grown in LB medium, washed, and resuspended in PBS. Seven week old female Swiss Webster mice (Charles River Laboratories) were anesthetized using avertin and infected intranasally with 30 µL of bacteria suspended in PBS. Mice were euthanized at set time points post infection and lungs were perfused with 1 mL of 1:1 OCT:water. Lungs were then marked using histological dye, snap frozen, and stored at -80°C until analyzed.

MALDI IMS of Mouse Kidney

Frozen tissue was sectioned to 10 microns at -20°C using a Leica CM 3050S Cryostat (Leica Microsystems, GmbH, Wetzlar, Germany). Sections were mounted onto conductive Indium-tin-oxide coated slides (Delta Technologies). Tissue was washed to remove interfering lipids and salts in sequential washes of 70% ethanol (30 seconds), 100% ethanol (30 seconds), Carnoy fluid (6:3:1 ethanol: chloroform: acetic acid) (2 minutes), 100% ethanol (30 seconds), water with 0.2% TFA (30 seconds), and 100% ethanol (30 seconds). Slides were stored at -80°C until IMS analysis was performed. Matrix was applied using a TM Sprayer (HTX Technologies, Carrboro, NC, USA) with a 15 mg/mL DHA in 8:1:1 acetone:water:acetic acid matrix solution or 15 mg/mL DHA in in 9:1 acetonitrile:water with with 0.2% TFA. Other instrument parameters include a flow rate 0.15 mL/min, nitrogen flow of 10 psi, spray temperature of 30°C, 4 passes with offsets and rotations, a spray velocity of 1300 mm/min, and 90% acetonitrile as the pushing solvent.

Imaging experiments were performed using a 15T Bruker SolariX MALDI FTICR mass spectrometer (Bruker Daltonics, Billerica, MA, USA). The instrument is equipped with an Apollo II dual MALDI/ESI ion source and a Smartbeam II 2kHz Nd:YAG (355nm) laser. All images were collected using the small laser setting (~50 μm) with a pixel spacing of 75 μm in both x and y dimensions unless otherwise noted. Data were collected from *m/z* 1,000 – 15,000 with a resolving power of ~75,000 at *m/z* 5,000 for 9 dpi kidney analyses. Special tuning of the Funnel RF amplitude (190 Vpp), accumulation hexapole (1.4 MHz, 1200 Vpp), transfer optics (1 MHz, 310 Vpp), time-of-flight delay (2.5 ms), and ICR cell (Sweep excitation power: 43%) were required for high *m/z* analysis. External calibration was performed prior to analysis using CsI clusters. FlexImaging 4.1 (Bruker Daltonics, Billerica, MA, USA) was used to visualize ion

images. For comparison, linear MALDI-TOF data were collected using a Bruker AutofleX Speed (Bruker Daltonics, Billerica, MA, USA).

Protein Purification

Kidneys of *S. aureus* infected animals were homogenized using 1 mL of phosphate buffered saline and a rolling pin. Cells were lysed by adding 0.5 mL of 50% trifluoroethanol and centrifuged for 10 minutes at 9g using Eppendorf Centrifuge 5415c. Protein was extracted from homogenates using 0.5 mL of 60% acetonitrile and centrifuged for 10 minutes at 9g. Supernatants from the extraction were saved and proteins were quantified using a Bradford Assay (Thermo Scientific Pierce, Rockford, IL, USA). Extracted proteins were further fractionated by reversed-phase HPLC using a Waters 2690 Alliance Separations Module (Waters Milford, MA, USA) and a Vydac 218 250 mm C18 5 micron column (Vydac Grace Columbia, Maryland, USA.) The column was heated to 40 degrees C and proteins were eluted at flow rate of 0.2 mL/min over a 120 minute gradient of 0.2%TFA in acetonitrile (solvent A) and 0.2%TFA in water (Solvent B.) The gradient consisted of 95-70% B in 20 minutes, followed by 70-40% B in 60 minutes and 40-20% B in 20 minutes. Fractions were collected every 1.5 minute using an offline fraction collector. The separation was performed three times and combined. Fractions were dried using a Savant SPD131DDA Speedvac Concentrator (Thermo Scientific, Rockford, IL, USA) and reconstituted in 30µL of 40% acetonitrile. One µL of each fraction was spotted for analysis by MALDI MS. Wells containing protein of interest were targeted for top-down analysis.

LC-Coupled Tandem Mass Spectrometry

For identification of modified S100A8, the purified fraction of interest was diluted 15-fold in 0.1% formic acid. Five µL of diluted sample were loaded for each analysis as described previously. Sequencing modified S100A8 was performed similarly to above, but the instrument method was customized with targeted scan events to assure ETD MS/MS acquisition of $[M+11H]^{+11}$ and $[M+12H]^{+12}$ charges states of modified S100A8. An isolation width of 4 *m/z* and an ETD reaction time of 70ms were used for MS/MS spectra. The MSn AGC target value in the Orbitrap was set to $7.5x10^5$, and MS2 spectra were acquired 15000 resolution. Theoretical fragmentation data of mouse S100A8 (P27005) were generated using Protein Prospector MS-Product (v 5.12.4 http://prospector.ucsf.edu/). MS/MS spectra acquired over an 18-second time range (retention time 68.23-68.53 minutes) were averaged and *de novo* sequenced to determine modifications. Modifications were confirmed at the peptide level following LC-MS/MS analysis of a tryptic digestion of the S100A8 fraction. An aliquot of the HPLC fraction was digested with mass-spectrometry grade endoproteinase trypsin (Promega Coorperation, Madison, WI, USA.) Peptides were acidified and bomb-loaded onto a self-packed trap column (360µm OD x 100µm ID) packed with 4 cm of C18 reverse phase material (Jupiter C18, 5 µm beads, 300Å, Phenomenex). An M-520 microfilter union (IDEX Health & Science) was used to connect the trap column to a capillary analytical column (360µm OD x 100µm ID), equipped with a laser-pulled emitter tip and packed with 18 cm of C18 material (Jupiter, 3 µm beads, 300Å, Phenomenex). Using an Eksigent NanoLC Ultra HPLC, peptides were gradient-eluted at a flow rate of 500 nL/min, and the mobile phase solvents consisted of 0.1% formic acid, 99.9% water (solvent A) and 0.1% formic acid, 99.9% acetonitrile (solvent B). A 90-minute gradient was performed, consisting of 2-40% B in 70 min, followed by 45-95% B in 5 min. Upon gradient elution, peptides

were mass analyzed on a Q Exactive mass spectrometer. The instrument method consisted of MS1 acquisition (R=70,000) followed by up to 18 MS/MS scans (R=17,500) of the most abundant ions detected in the preceding MS scan. The MS2 AGC target value was set to 2 x 10^5 ions, with a maximum ion time of 150 ms and a 4% underfill ratio. HCD collision energy was set to 28, dynamic exclusion was set to 10s, and peptide match and isotope exclusion were enabled. Resulting MS/MS spectra were searched against a *Mus musculus* subset database of the UniprotKB protein database using a custom version of SEQUEST (Thermo Scientific) operating on the Vanderbilt ACCRE computing cluster. Search parameters included variable modifications of oxidation (+15.9949) on methionine and oxidation of cysteine to cysteic acid (+47.9847). Search results were assembled using Scaffold 4.0 (Proteome Software, Porland, OR, USA).

MALDI IMS of Mouse Lung

Mouse lungs were prepared and frozen as described in Chapter II. Lungs were oriented identically and sectioned at 10 micron thickness using a Thermo Scientific Cryostar NX70 cryostat. Sections were thaw-mounted onto chilled Indium-tin-oxide slides (Delta Technologies.) Tissue was washed to remove interfering lipids and salts in sequential washes of 70% ethanol (30 seconds), 100% ethanol (30 seconds), Carnoy fluid (6:3:1 ethanol: chloroform: acetic acid) (120 seconds), 100% ethanol (30 seconds), water with 0.2% TFA (30 seconds), and 100% ethanol (30 seconds).

2,6-dihydroxyacetophenone (DHA) was used as a matrix and applied via sublimation similarly to previously described.[120] Briefly, a sandbath was heated to 105°C. DHA was placed in the bottom of the sublimation apparatus and samples were suspended above the matrix by taping them to a cold finger. The chamber was evacuated to 50 mTorr and the sublimation was allowed

to occur for 5 minutes. Samples were rehydrated before analysis using a rehydration chamber described by Yang et al.[120], only using 1 mL of 50 mM acetic acid as the rehydration solvent. Rehydration was carried out at 85°C for 1 minute. Samples were analyzed using a Bruker 15T SolariX FTICR MS equipped with an Apollo II dual MALDI/ESI ion source and a Smartbeam II 2kHz Nd:YAG (355nm) laser. High mass resolution images were collected with instrumental parameters similar to those reported for kidney analysis. Pixel spacing was 200 microns in both the x and y direction. FlexImaging 4.1 (Bruker Daltonics, Billerica, MA, USA) was used to visualize ion images.

CHAPTER IV

METAL SEQUESTRATION AT SITES OF INFECTION AFFECTS BACTERIA

A version of the following chapter was previously published and has been adapted from Kehl-fie, Zhang, Moore et al., *Infection and Immunity,* Copyright 2013 by the American Society for Microbiology[135] and from Cassat, Moore et al., A Multi-Modality Imaging Platform for Identifying Molecular Alterations at the Host-Pathogen Interface., in progress

Overview

Nutritional immunity is the basis of calprotectin's antimicrobial activity- through the sequestration of nutrients from invading pathogens, the pathogens are limited in their ability to replicate and cause disease. Though MALDI IMS has greatly enhanced our knowledge of host response to bacterial infection, it has historically lacked the spatial resolution to resolve bacterial signals from those of the host. Additionally, the introduction of LA-ICP-IMS allows for the spatial distribution of metals to be determined from within biological samples. This allows for the unprecedented study of the metalloproteome, with proteins and metals analyzed in serial sections of tissues. This work intends to utilize high spatial resolution MALDI IMS and LA-ICP-IMS to uncover how bacteria are responding to calprotectin-mediated nutritional immunity during active infection in both tissue sections and whole organ systems.

Introduction

Nutritional Immunity and Bacteria

Metals are essential for all forms of life; they are important for many reasons, including enzymatic functions as cofactors or as critical components of tertiary protein structure. [71, 136-138] Nutritional immunity is the term given to the process of vertebrate hosts sequestering metals from invading pathogens. [71, 139] Previous studies utilizing laser ablation inductively coupled plasma imaging mass spectrometry (LA-ICP-IMS) revealed that staphylococcal lesions were manganese and zinc depleted.[140]

For pathogens to cause disease in hostile host environments, they must evolve ways to obtain nutrients despite host efforts. The most successful pathogens have evolved mechanisms to circumvent nutritional immunity, including the secretion of small molecules with high affinity for metals, called siderophores, and dedicated metal uptake machinery. Mn and Zn uptake systems contribute to the pathogenesis of a number of bacterial species including *Campylobacter jejuini*, *Salmonella enterica*, *Haemophilus ducreyi*, uropathogenic *Escherichia coli*, *Brucella abortus*, *Yersinia pestis*, *Streptococcus pneumoniae,* and *Streptococcus pyogenes.* [141-156] It is notably difficult to study metal uptake systems in the context of pathogenesis because it is difficult to distinguish whether such systems that work *in vitro* are also working within the vertebrate host.

Analysis in 3D

Determining the nuances of nutritional immunity in an organ system is not a trivial task. This is especially true for discovery-based approaches that do not have *a priori* knowledge of analytes so that specialty reagents such as antibodies or probes can be developed. To fully understand how metal is sequestered from within the kidney of mice during staphylococcal sepsis,

a 3D analysis strategy was implemented. This was partially to study intra-lesion heterogeneity, but also to study changes within a single lesion. Figure 1.4 outlined the anatomy of an abscess, where a bacterial population occupies only a small niche of the lesion, surrounded by inflammatory cells, necrosis, and in some cases completely healthy tissue.

In order to further characterize bacterial-host interactions in abscessed tissue, a multi-modality imaging strategy was developed that would combine bioluminescence, MALDI IMS, and LA-ICP-IMS. This strategy was applied to a murine model of disseminated *S. aureus* infection. Initial experimental planning focused on iron as it is a well-studied essential metal critical to host-pathogen interactions and virulence. Iron acquisition is critical for *S. aureus* pathogenesis, and also serves as one of the most powerful and well-studied signals to bacterial pathogens signifying a change in environment as they invade host tissues.[157] Iron levels vary considerably across host tissues, and to date it has been technically challenging to determine the abundance and spatial distribution of iron and other elements within a particular tissue. To answer this and other important biological questions, there was a need to successfully integrate 3D MALDI IMS, LA-ICP-IMS, and bioluminescence data sets. This task required a computational platform capable of accurate co-registration within the 3D volume. This necessitated additional imaging modalities to provide registration. To accomplish this, magnetic resonance imaging (MRI) and optical blockface imaging were including in the strategy.

This work reports the integration of whole animal bioluminescent and blockface optical imaging, magnetic resonance imaging, MALDI IMS, and LA-ICP-IMS as a multi-modality platform for identifying the abundance and spatial distribution of host and bacterial molecules in intact, infected tissues. We focus specifically on the struggle for nutrient metal between host and pathogen as a paradigm for innate immune responses to invading bacteria. By combining the multi-

modality imaging platform with top-down and bottom-up proteomics, we successfully identify host proteins involved in the innate immune responses to *S. aureus*, as well as bacterial proteins that specifically mark the bacterial nidus within tissue abscesses.

Results and Discussion

LA-ICP IMS Reveals Dramatic Rearrangement of Metal Distribution in Tissues

Bacteria sometimes exhibit preferential colonization of one organ over another. Since the ability to secure nutrient metals is so important for survival and dissemination, it is sensible to explore metal levels in varying organs. Previous work in our laboratory showed that in areas of infection, metal levels are dramatically altered at infectious foci.[28] To explore whether the amount of metal available in organs varies, bulk analysis of both WT and CPKO mice was performed. Kidneys and livers of infected and control animals were digested for total metal content, shown in Figure 4.1. In the case of total metal analysis, liver tissues contained much more Mn and Zn per gram total tissue than kidney. Interestingly, upon infection, the metal levels of kidney were relatively unchanged. Figure 4.1A shows that Mn levels dropped significantly in liver tissues when infected, while the change was not significant in kidneys. Zn levels also remained the same in infected kidneys, as shown in Figure 4.1B; however, total Zn levels appear to rise in the liver when infected. All measured metal levels from the bulk analysis are shown in Table 4.1.

Metal	Uninfected Liver	Infected Liver	Uninfected Kidney	Infected Kidney
Magnesium	240 ± 37	294 ± 7	95 ± 19	100 ± 15
Phosphorus	3,240 ± 466	3,855 ± 118	1,658 ± 370	1,657 ± 305
Calcium	49 ± 8	99 ± 5	30 ± 6	45 ± 7
Manganese	1.4 ± 0.2	0.9 ± 0.1	0.7 ± 0.2	0.6 ± 0.1
Iron	193 ± 37	253 ±8	51 ± 10	52 ± 8
Copper	4.4 ± 0.6	6.1 ± 0.4	2.0 ± 0.4	1.8 ± 0.3
Zinc	29 ± 3	57 ± 3	8 ± 2	9 ± 1

Data are results = ± SEM given in µg/gram tissue (n= 5 to 10)

Table 4.1: Total Metal Content in Organs

Reprinted from *Infection and Immunity,* 91, 9 "MntABC and MntH contribute to systemic *Staphylococcus aureus* infection by competing with calprotectin for nutrient manganese." Kehl-fie, Zhang, Moore et al. 2013 with permission from The American Society for Microbiology.[135]

Previous LA-ICP-IMS experiments had focused on lesions in the liver. The data presented in Figure 4.1 showed that liver lesions might not be comparable to those in the kidney, since the total metal content varied so greatly. To address this, LA-ICP-IMS was used in addition to MALDI IMS to measure both proteins and metals at sites of infection. The distribution of metal and protein was measured in both wildtype C57CL/6 and CPKO mice in animals uninfected and infected with strain Newman *S. aureus.* Figure 4.2 shows data from this analysis.

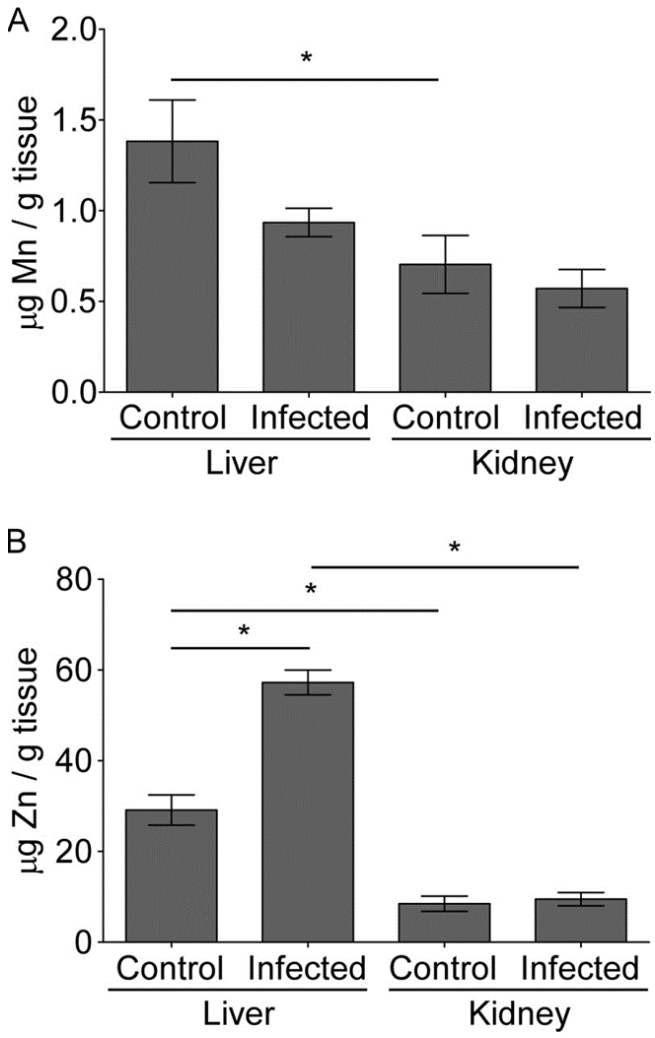

Figure 4.1: Manganese and Zinc Levels in Infected Organs

"Total tissue Mn and Zn levels vary by organ and are influenced by infection. To assess the impact of infection on bulk metal availability, 9-week-old C57BL/6 mice were infected with wild-type *S. aureus* or mock-infected with PBS. Following 4 days of infection, livers and kidneys were harvested, and total Mn (A) and Zn (B) content was assessed by inductively coupled plasma mass spectrometry. *, $P = 0.05$ via one-way ANOVA with Bonferroni's posttest. Error bars indicate SEM ($n = 5$ to 10)" Reprinted from *Infection and Immunity,* 91, 9 "MntABC and MntH contribute to systemic *Staphylococcus aureus* infection by competing with calprotectin for nutrient manganese." Kehl-fie, Zhang, Moore et al. 2013 with permission from The American Society for Microbiology.[135]

In Figure 4.2 A, hematoxylin and eosin stains of serial sections are shown for orientation. Staphylococcal lesions are the darker staining areas within infected tissues. Figure 4.2B shows

selected MALDI IMS data acquired at 100 micron spatial resolution. The ions representing S100A8 and S100A9 are shown to co-localized in the WT infected lesions, but are absent in the CPKO lesions. Figure 4.2 C highlights the LA-ICP-IMS data on serial tissue section. In both WT and CPKO lesions, calcium is increased, consistent with the recruitment of immune cells. A slight increase in calcium is also detected in bulk analysis, but the IMS data reveals that this slight increase is spatially localized to infectious foci. Manganese and zinc levels were largely unchanged in the kidney (Figure 4.1.) Interestingly, Figure 4.2C shows that both the WT and CPKO lesions are depleted of manganese. This suggests that there might be compensatory mechanisms or mechanisms other than calprotectin responsible for removing this nutrient from infectious foci. Figure 4.2C also suggests WT lesions have reduced zinc while the CPKO lesions appear to have an increase in zinc. This demonstrates that although there are relatively low zinc and manganese levels in the bulk analysis of the kidney (Table 4.1) their spatial distribution is remarkable changed upon infection. Such studies highlight the necessity of metal-protein co-localization analyses to study nutritional immunity; it is clear that the vertebrate host is sequestering metals in response to infection. However, this analysis considers only one plane of a kidney. To fully define how metal and protein interact throughout lesions in a kidney, and how they interact with bacteria, more in depth analysis is necessary.

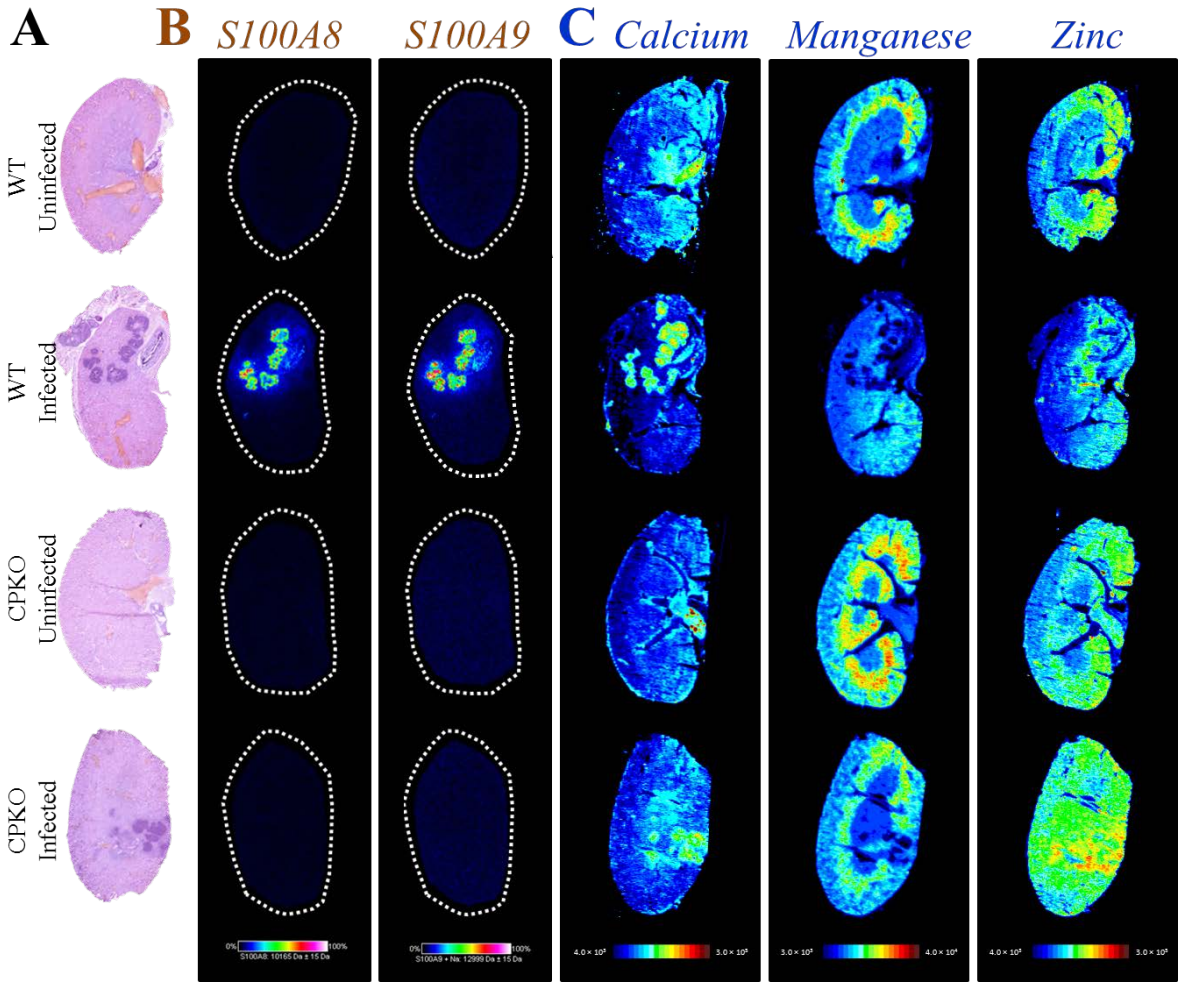

Figure 4.2: IMS Reveals Localization Changes of Metals and Proteins in Infection
In tissues with relatively low basal levels of Mn and Zn, access to these metals is further restricted during infection. To assess the distribution of Mn and Zn within the kidney during infection, C57BL/6 or CP-deficient (S100A9−/−) mice were infected with wild-type *S. aureus* or mock-infected with PBS. Following 4 days of infection, the tissues were harvested and analyzed by H&E staining (A), MALDI IMS for CP distribution (B), and LA-ICP-MS for calcium, manganese, and zinc distribution (C). (B) Scale represents percent maximal ion intensity. To assess the distribution of S100A8, a mass of 10,165 Da was mapped. For S100A9, a mass of 12,999 Da was mapped, which corresponds to S100A9 in complex with a sodium ion. (C) Scale represents absolute ion intensity for the indicated metal. Images are representative of two independent experiments.)" Reprinted from *Infection and Immunity*, 91, 9 "MntABC and MntH contribute to systemic *Staphylococcus aureus* infection by competing with calprotectin for nutrient manganese." Kehl-fie, Zhang, Moore et al. 2013 with permission from The American Society for Microbiology.[135]

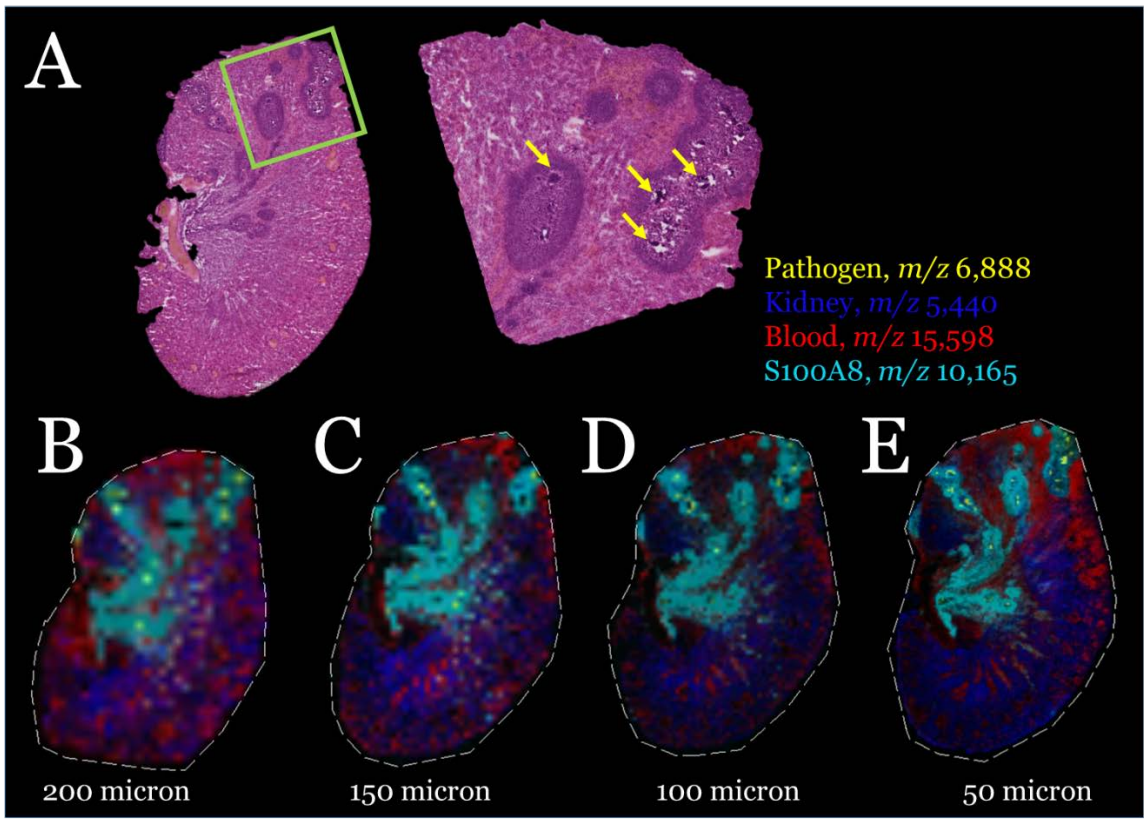

Figure 4.3: IMS Spatial Resolution and Staphylococcal Communities
Spatial resolution is important in MALDI IMS to define anatomical features of interest. A) An H&E stain of a staphylococcal abscess in a mouse kidney. The inset shows the anatomy of the abscess, with staphylococcal colonies residing in the center. B-E) Serial sections of the mouse kidney analyzed at increasing spatial resolutions. B, C, D, and E were interrogated at 200, 150, 100, and 50 µm spatial resolution. A signal co-localizing with the bacterial colony is displayed in yellow. At increasing spatial resolution, it is much easier to distinguish this signal from surrounding host tissues. Reprinted from *Proceedings of the NATO Advanced Study Institute in Rapid Threat* Detection, 2017, *Imaging Infection*, with permission from Springer Publishing Company.[3]

High Spatial Resolution MALDI IMS reveals Bacterial Signals

Early studies of infection were at relatively low spatial resolution, typical around 200-250 microns between each spectrum. When considering staphylococcal microcommunities within lesions, this sampling capability was only able to detect signals associated with host immune

response and not from the pathogen. Therefore, recent efforts both in sample preparation and in instrument development have focused on making higher spatial resolution analyses a capability. Figure 4.3 shows how anatomical features of a staphylococcal lesion are defined with increasing spatial resolution. Figure 4.3A shows a hematoxylin and eosin stain of a mouse kidney infected with *S. aureus*. The green box shows a magnification of a lesion. At the center of the lesion is the staphylococcal community, which is annotated with a yellow arrow. Four serial sections of this kidney were analyzed at increasing spatial resolutions: 200, 150, 100, and 50 microns. As the spatial resolution increases, signals marking anatomical features, such an aggregated neutrophils, blood vessels, and even staphylococcal communities can be distinguished with molecular data. At 50-100 micron spatial resolution, signals co-localizing to staphylococcal communities within the center of abscesses can be determined. MALDI IMS experiments can be performed at very high spatial resolution. Figure 4.4 features a staphylococcal abscess analyzed at 10 micron spatial resolution. A cartoon schematic of cell types and a hematoxylin and eosin stain of the section post analysis are shown in Figure 4.4A. Figure 4.4B highlights the quality of the MALDI IMS data at such high spatial resolutions. Here signals belonging to bacterial colonies can be clearly differentiated, as well as signals marking heterogeneities within the actual bacterial colony. For example, an ion at *m/z* 5522 is co-localized with the bacteria, while *m/z* 6422 is localized in the necrotic area immediately surrounding the colonies. This type of spatial resolution allows us to clearly isolate and differentiate the pathogen-host interaction by detecting signals from both pathogen and host, and could provide novel information about microbial pathogenesis.

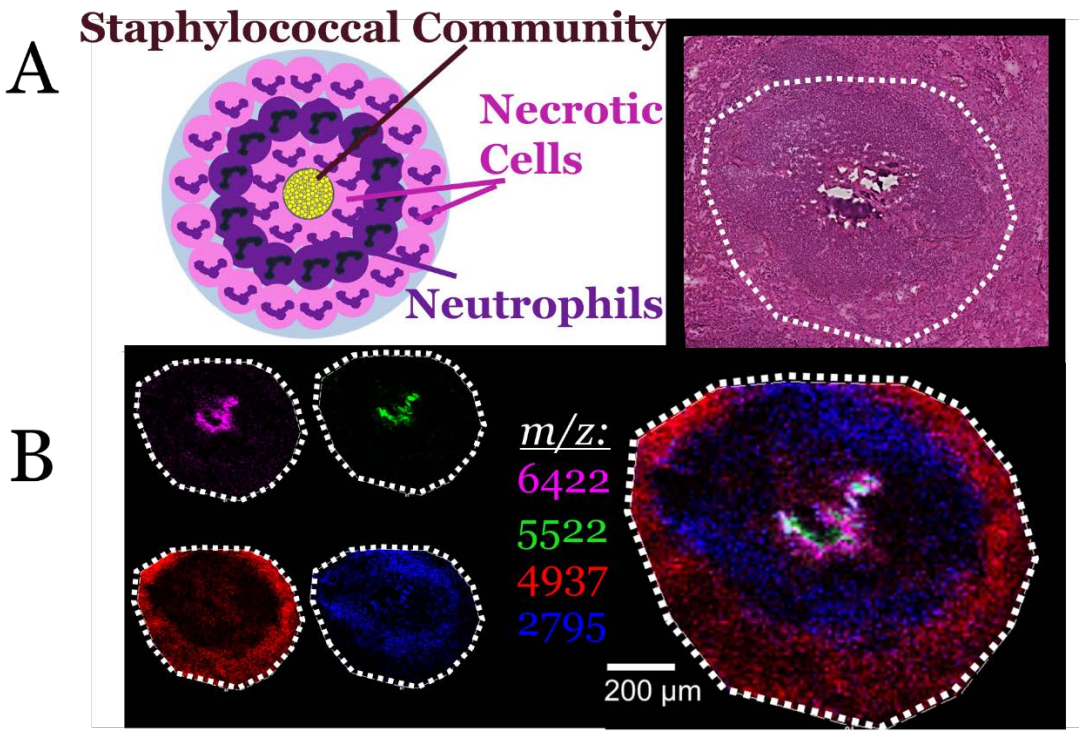

Figure 4.4: High Spatial Resolution IMS Reveals Heterogeneities within Staphylococcal Communities

MALDI IMS was performed on a staphylococcal abscess at 10 micron spatial resolution. H&E staining of the tissue post MALDI IMS analysis is shown in A. A simplified schematic of the histology of the staphylococcal lesion is also shown. B shows data from IMS at 10 microns. An ion at *m/z* 2,795 marks aggregated neutrophils and is shown in blue while an ion at *m/z* 4,937 marks surrounding host epithelial tissue and is shown in red. Of great interest are the ion at *m/z* 6,422 (pink) and *m/z* 5,522 (green). Both of these ions are co-localized within the center of the abscess, but have different spatial distributions. The green ion seems to directly co-localize with the colony while the pink ion is in the region directly outside of the colony.

Though high spatial resolution IMS experiments provide novel molecular information about pathogen-host interaction, there is a trade-off for such analyses. First, they tend to be large data sets, making file storage cumbersome and expensive. Second, they are time consuming, requiring large amounts of instrumental time for data acquisition. These considerations make high

spatial resolution analyses not feasible for 3D analysis of abscess lesions. In order to characterize a kidney abscess in 3D, analyses were performed at 50 micron spatial resolution.

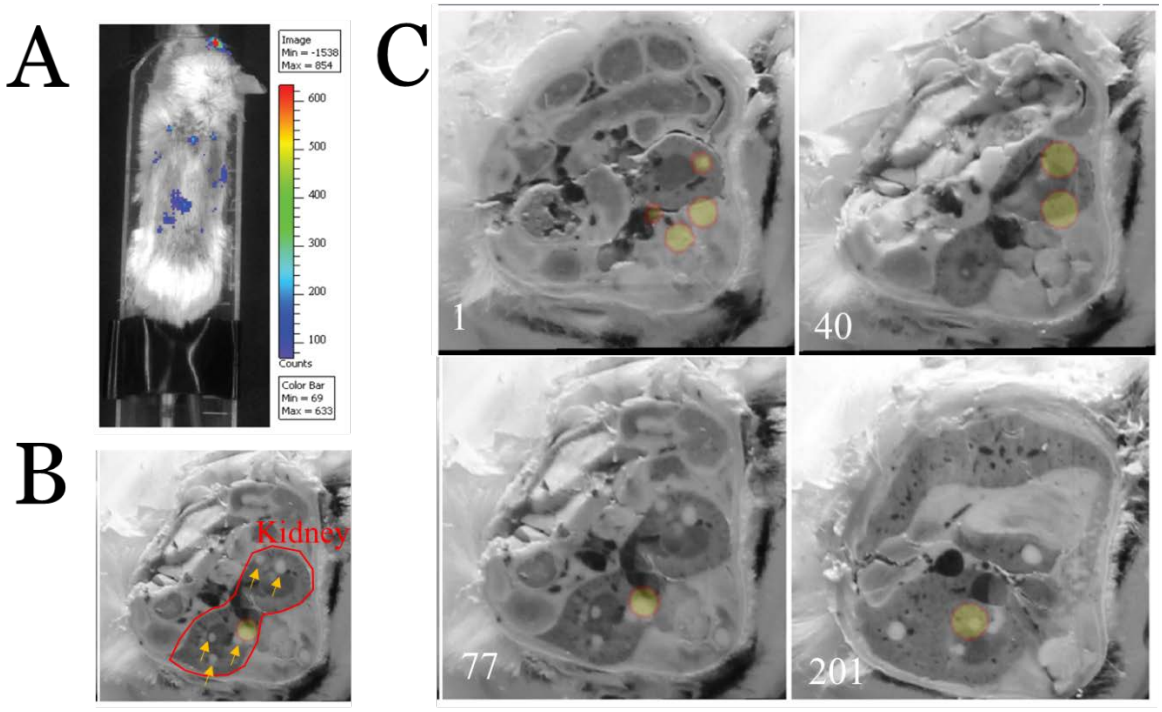

Figure 4.5: Bioluminescent Imaging Reveals Metal-Starved Bacteria within Host
Bioluminescent Analyses of a mouse shows regions of bacterial colonization that are experiencing metal starvation. A) shows the mouse within IVIS being analyzed. After sacrifice, the bioluminescent data was overlaid with blockface images taken during sectioning. B shows gross morphology of the mouse during sectioning with kidneys circled in red and abscessed regions shown with yellow arrows. C shows four different planes of the analysis throughout sectioning the mouse, 1, 40, 77, and 201. Abscesses appear as white circular foci on internal organs. In some cases, like section 40, all abscesses within the plan have signal. In others, such as plane 77 and 201, only certain lesions have signal.

3D Bioluminescent Analysis Determines Iron Starvation of S. aureus *within Lesions*

To determine how metals and proteins change throughout organ systems, we established a model to perform analysis of biomolecules in 3D. Iron is one of the most studied metals in the field of nutritional immunity. Iron withholding is therefore an ideal system to probe iron starvation of bacteria within host. If staphylococcal lesions are heterogeneous within an organ system, we would expect varying levels of iron starvation throughout the organ. In order to test this hypothesis, mice were intravenously infected with a strain of *S. aureus* (Newman p*isdI.Xen1*) containing an iron-responsive luminescent construct, in which the promoter of the iron-regulated surface determinant gene *isdI* is fused to a *luxABCDE* operon. When these bacteria are iron-starved, we expect that they will luminesce. Previous studies revealed that this promoter is active *in vivo* in response to iron limitation [158]. The infection was allowed to progress for 96 hours (4 dpi) at which time the mice were anesthetized and subjected to bioluminescent imaging (BLI) using an IVIS 200 platform. Figure 4.5 shows data collected from BLI experiments. Figure 4.5A shows the BLI from the animal chosen for 3D imaging analysis. Recorded foci of light production are recorded throughout the mouse, consistent with a disseminated sepsis infection. The bacteria causing this light production are under iron starvation. This mouse was subjected to further 3D BLI to more accurately determine the origin of the luminescent signal. This allowed for better registration throughout the 3D volume by clarifying the location of bacteria undergoing iron starvation, as well as the extent of the foci exhibiting bioluminescent signal. Figure 4.5B shows a blockface image obtained during sectioning with the kidneys annotated in red and the abscesses annotated with yellow arrows. Figure 4.5C shows four blockface images from different depths of the 3D volume. These were taken at sections 1, 40, 77, and 201. Staphylococcal lesions appear as small white circular structures in the blockface images. When overlaid with BLI, it is apparent that not all

abscesses are experiencing comparable iron starvation. Since bacteria express metal acquisition systems to combat host-imposed nutritional immunity, it is reasonable to assume that not all bacteria residing within lesions will be iron-starved and therefore would not express signal detectable using BLI. Alternatively, the lack of light production in tissue abscesses may result from insufficient bacterial burdens in a single abscess, reflecting the absence of suitable numbers of bacteria to reach the detection threshold for bioluminescent imaging.

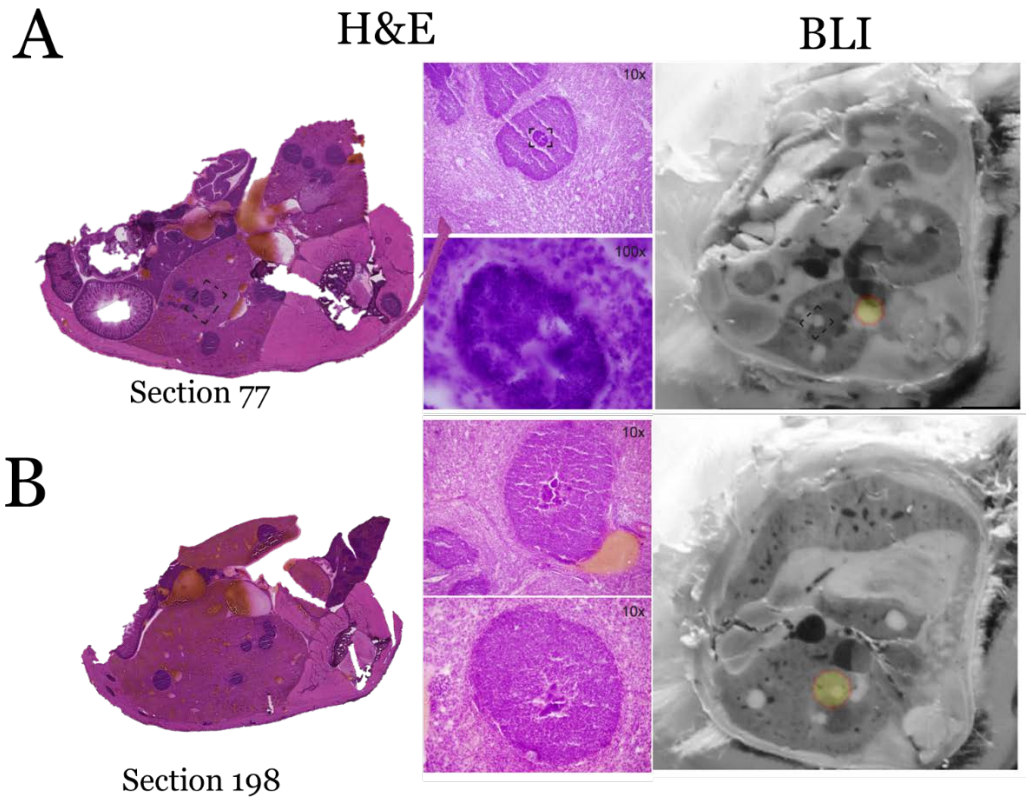

Figure 4.6: Histological Analysis Reveals Lesions without Bioluminescent Signal Contain Bacteria

To ensure that lesions lacking bioluminescent signal were not void of bacteria, histological analysis was performed. Two planes of analysis are shown above: section 77 in A and section 198 in B. Section 77 represents a lesion where bacteria are visibly present via microscopic analysis but do not seem to be iron starved. Section 198 features a lesion with bacteria in the plane that has signal in bioluminescence analysis, suggesting that this lesion is iron starved.

Magnetic Resonance Imaging, Iterative Blockface Imaging, and Histological Staining Define Tissue Architecture

To study each lesion individually required further definition of the tissue architecture to determine how lesions were distributed throughout the 3D volume. To facilitate high-resolution MRI and other downstream applications, the mouse was secured to a rigid restraint device prior to BLI. Immediately after BLI, MRI was performed using a Varian 9.4T horizontal bore imaging system and included the portion of the mouse encompassing the kidneys, a site of maximal pathology in the *S. aureus* disseminated infection model.[121] BLI data was manually co-registered with MRI data using an iterative closest point algorithm.[159] The coordinated imaging data set revealed the presence of multiple kidney abscesses. Previous studies have shown that *S. aureus* exists as a microcolony or "staphylococcal abscess community" in mature tissue abscesses.[63] However, such small bacterial structures are not visible on MRI, necessitating additional analyses to pinpoint the bacterial niche. Further high resolution analysis of tissue might also delineate the source of bioluminescent heterogeneity in tissue abscesses.

At the completion of MRI, the infected mouse was euthanized and carefully flash-frozen in liquid nitrogen, minimizing movement from the initial imaging position. The middle third of the frozen mouse was then transversely sectioned at 30 μm increments to include both kidneys in their entirety. Adjacent sections were digitally imaged, and then utilized alternatively for hematoxylin and eosin (H&E) staining or downstream imaging analyses. Digital blockface imaging of adjacent sections was archived as a volume and then manually co-registered to the BLI data set. To determine if this heterogeneity in BLI signal was due to fluctuating metal availability or the absence of bacteria, adjacent tissue sections were stained with H&E and scanned at high resolution. Staphylococcal microcolonies could be visualized in many abscesses throughout the

infected kidneys, including those without bioluminescent signal. Figure 4.6 shows histological stains adjacent to BLI data. Figure 4.6A was taken from section number 77. The dotted box surrounds a lesion that was optically analyzed at higher magnification. The dark purple regions in the center of the lesion are staphylococcal microcolonies. When compared to the BLI imaging on the far right, it is apparent that there is no luminescence from these bacteria. Figure 4.6B provides another example of aligning histological data with BLI data, taken from section 198. Here, the lesion highlighted with dotted boxes is shown at 10x magnification and contains bacteria. The panel at the far right shows robust signal from BLI, further strengthening the idea that certain bacteria within lesions are experiencing different levels of metal starvation. It is interesting to note that both of these lesions have similar histopathological appearance, defining the need for advanced imaging modalities to study nutritional immunity. This showcases the power of co-registered volumes of BLI, MRI, and blockface imaging data but also highlights the need for more molecular information for the analysis of bacterial stress responses.

Staphylococcal Lesions are Molecularly Defined by MALDI IMS

The creation of a 3D volume of MRI and blockface data provides a framework onto which additional imaging modalities may be co-registered. Because the BLI analyses revealed heterogeneity in staphylococcal communities throughout the organ system despite histological similarity, it was clear that additional molecular information was needed to more fully study abscess formation and bacterial proliferation. In order to analyze both host and bacterial proteins involved in the pathogen-host interaction, MALDI IMS analyses were performed at 50 micron lateral spatial resolution every 150 microns throughout the sections encompassing the kidney. These analyses intended to define host proteins that respond to pathogens and potentially isolate

staphylococcal proteins marking lesions. Figure 4.7 highlights the ability of MALDI IMS to differentiate different tissues within a section of mouse. Figure 4.7A represents the nearest H& E, taken from section 77. Figure 4.7B shows MALDI IMS data analyzed using a 15T SolariX MALDI FTICR MS. A composite image of several ions is shown. The ion at *m/z* 3,006.646 is displayed in yellow, and co-localizes with bacterial colonies. Surrounding these bacterial signals is *m/z* 5082.547, the ion representing S100A8 (2+,) displayed in pink. This ion is co-localized with aggregated neutrophils and surrounds the signal representing the bacterial colonies. The ion at *m/z* 3,454.771 is shown in teal and marks the medulla of the two kidneys in the plane of analyses. The ion displayed in green, *m/z* 4,116.946 is marking the intestinal tract while *m/z* 5,921.093 marks liver. Finally, displayed in dark blue is *m/z* 5,653.720, an ion belonging to Histone H4 (2+), which is detected throughout the mouse tissues.

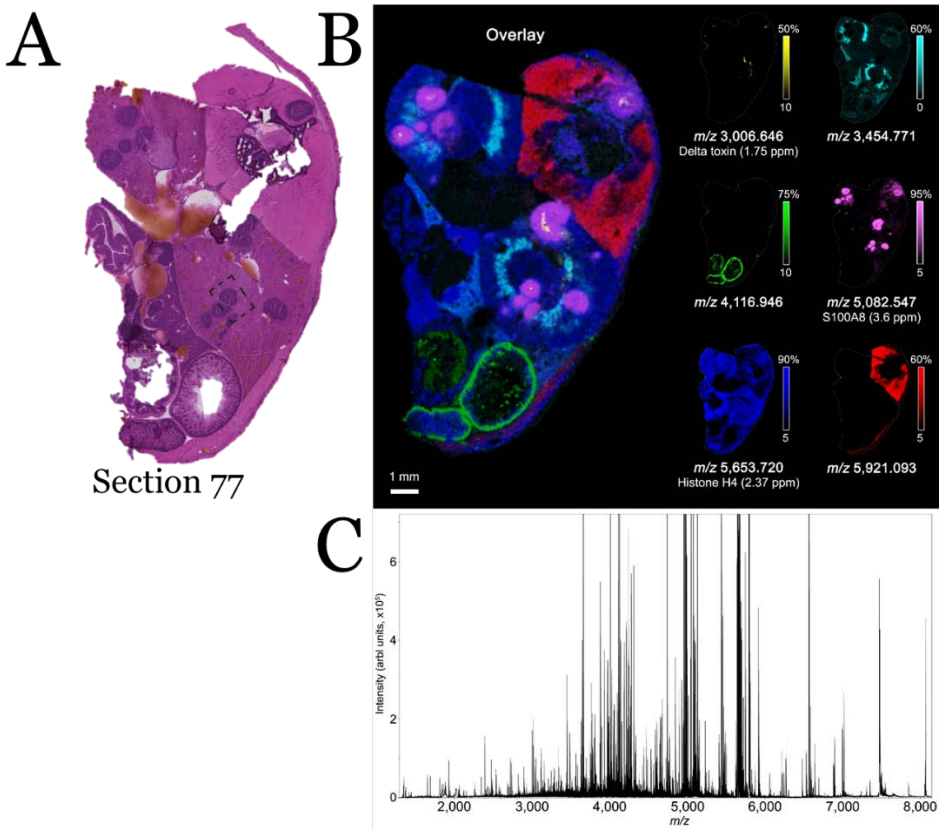

Figure 4.7 MALDI IMS Molecularly Defines Tissue Architecture
A section serial to that used in the 3D analysis was analyzed for high mass resolution MALDI IMS to aid in the identification of analytes. A shows the nearest H&E for the analysis. Both kidneys, liver, and some intestines are present in this analysis. B shows an overlay of several ions to recreate the tissue morphology with molecular data. Individual ions and their *m/z* values are shown to the right. C shows the overall averaged spectrum from the analysis, highlighting the robust nature of these data and the number of analytes identified in this analysis.

Identification of Bacterial Signals from MALDI IMS Experiments

In addition to the signals at *m/z* 3,006, a signal at *m/z* 6,888 also seemed to exhibit a localization pattern consistent with staphylococcal microcolonies. Because of these strong co-localization patterns and the possibility that these ions could represent microbial proteins, protein identification was necessary. In order to enhance these signals for extraction and downstream

MS/MS sequencing, tissues from additional mice were used for protein purification. Infection of additional mice was allowed to progress for 9 dpi in order to generate larger abscesses. Microextraction techniques directly from visible staphylococcal abscess communities paired with top-down proteomics yielded the identification of *m/z* 6,888 as NWMN_0783, a CsbD-like superfamily protein. Figure 4.8 shows the data supporting this identification. The full scan is shown in Figure 4.8A, with the charge state selected for MS/MS analysis annotated in red. The +10 charge state at *m/z* 689.6499 was selected for ETD fragmentation, with MS/MS data shown in Figure 4.8B. This data was manually *de novo* sequenced and searched against the *Staphylococcus aureus* strain Newman Uniprot database. Sequence coverage is notated in Figure 4.8B, with MS/MS data representing 89% coverage of the protein. To confirm this finding, the infection was repeated using a strain of *S. aureus* with NWMN_0783 knocked out. This strain of bacteria still formed abscessed with staphylococcal abscess communities visible by microscopy. Figure 4.9 shows these data. A lesion caused by *S. aureus* strain Newman is shown in Figure 4.9A while a lesion caused by strain Newman Δ NWMN_0783 is shown in Figure 4.9B. The robust signal at *m/z* 6,888 shown in Figure 4.9A is absent in the lesion caused by the knock-out strain, further reinforcing this identification. The role of NWMN_0783 in staphylococcal physiology is unknown, but CsbD-like proteins have been proposed to have roles in stress responses and metal starvation.[160, 161]

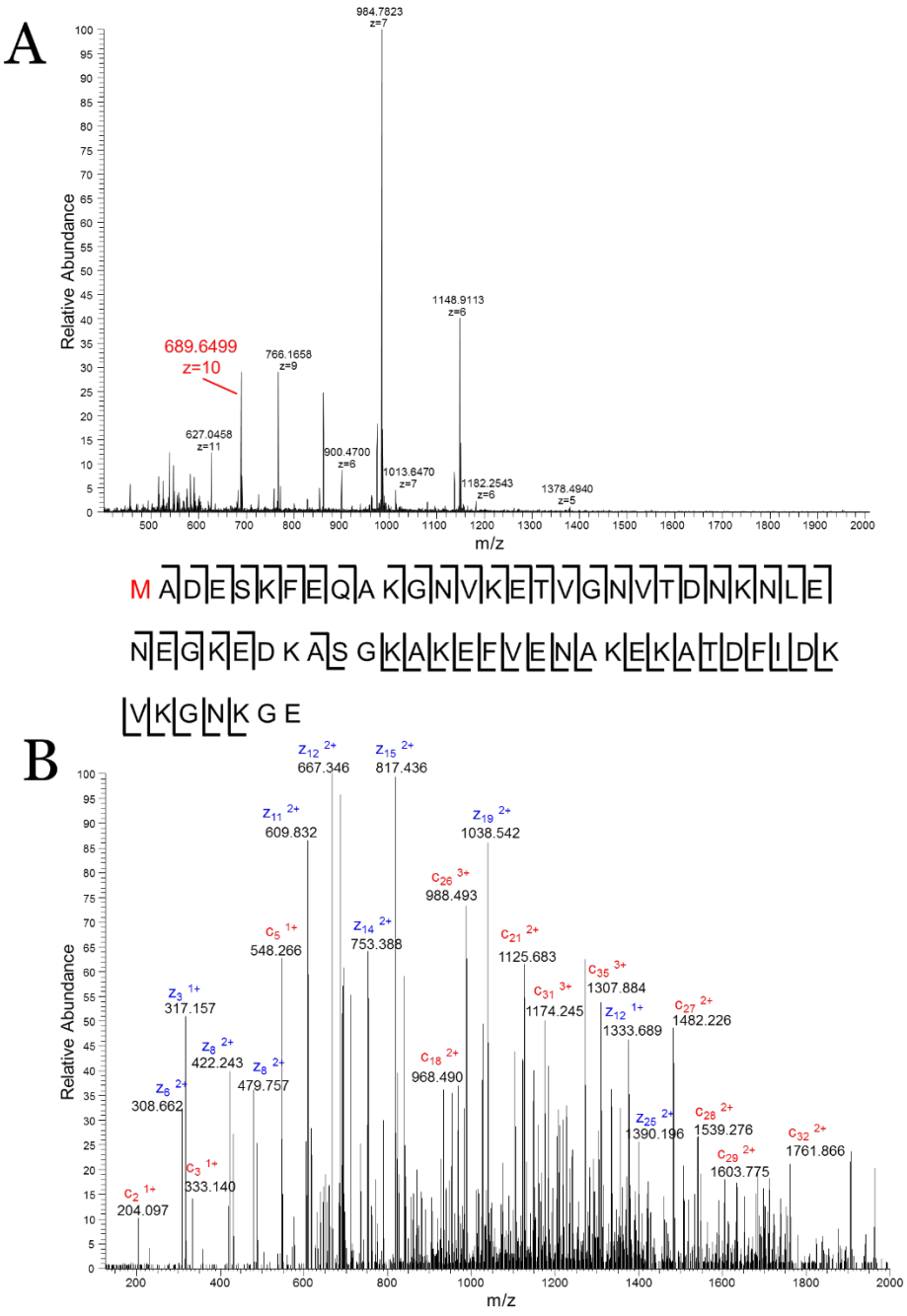

Figure 4.8: Top down Identification of NWMN_0783

ETD LC-MS/MS data for NWMN_0783. The charge state distribution is shown in A) with the specific charge state selected for MS/MS highlighted in red. ETD fragmentation data is shown in B) including selected c (red) and z (blue) ion annotations. A summary of the observed fragments and sequence coverage is included.

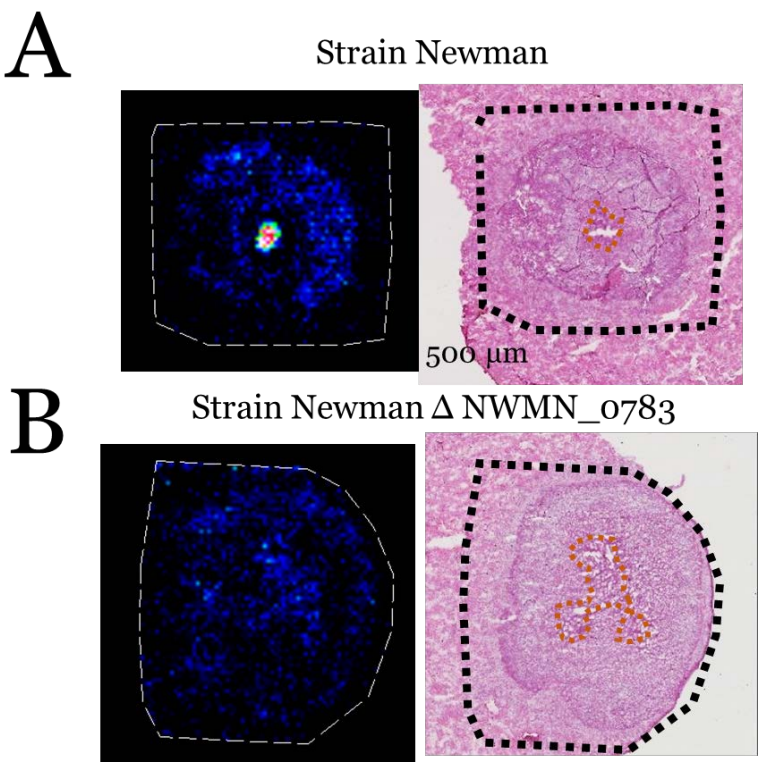

Figure 4.9: Infection with a knock-out strain of *S. aureus* confirms the Identification
To confirm the identity of *m/z* 6,888 as NWMN_0783, an infection was repeated with both strain Newman *S. aureus* (A) and strain Newman Δ NWMN_0783. Staphylococcal colonies are present in both sections and are annotated with orange lines. The signal at *m/z* 6,888 is present in strain Newman (B) but absent in the knock-out strain, further confirming this identification.

Identification of the signal at *m/z* 3,006 proved more challenging, as it was not successfully sequenced using top-down proteomics approaches. In order to identify this species of interest, the small protein was extensively purified using offline HPLC and a fraction collector. Fractions were analyzed using MALDI MS to determine where the protein of interest eluted. Top-down analysis of the purified protein was also unsuccessful. In order to have more material to work with, *S. aureus* was cultured to stationary phase under moderately hypoxic conditions. These bacteria also robustly expressed the signal of interest at *m/z* 3,006. Figure 4.10 shows the purification of this analyte of interest. Figure 4.10A shows an intact cell MALDI mass spectrum taken from an *S.*

aureus pellet. Figure 4.10B shows a mass spectrum from the same sample after proteins were extracted and purified using HPLC with offline fraction collection. Figure 4.10C is a mass spectrum taken from a protein extract from mouse kidney sacrificed at 9 dpi after being fractionated using the same HPLC method. Both 4.10 B and C shared the same retention time, strengthening the hypothesis that this protein was bacterial. In order to sequence this small protein, a tryptic digestion was attempted to further simplify the protein and increase the chances of identification by peptide sequencing. This proved to be effective, and *m/z* 3,006 was identified as NWMN_2624 encoding for the virulence factor delta hemolysin. Figure 4.11 shows MS/MS sequence data for the peptide WIIDTVNK. A targeted MS/MS analysis was used to include a scan of *m/*z 497.77, which represented the $[M+2H]^{2+}$ ion of this particular tryptic peptide and to increase the likelihood of strong fragmentation data. Figure 4.11A shows the MS/MS spectrum purified from *S. aureus* pellet while Figure 4.11B shows the MS/MS spectrum purified from 9 dpi mouse kidney. The sequence for delta hemolysin is shown, with the peptide of interest annotated in red.

Delta hemolysin is a well-characterized and broadly conserved virulence factor in *S. aureus.*[162] A member of the phenol-soluble modulin class of secreted toxins in *S. aureus*, delta hemolysin is an amphipathic peptide capable of lysing host cells and contributing to mortality during experimental septicemia.[163, 164] Collectively, these data reveal the power of MALDI IMS, when part of a multi-modality imaging platform, to identify host and bacterial proteins involved in the pathogenesis of invasive infection. Additionally, by identifying bacterial proteins that mark the infectious niche during invasive infection, this imaging platform provides a potential mechanism for the label and culture-free diagnosis of *S. aureus* infection in pathologic specimens.

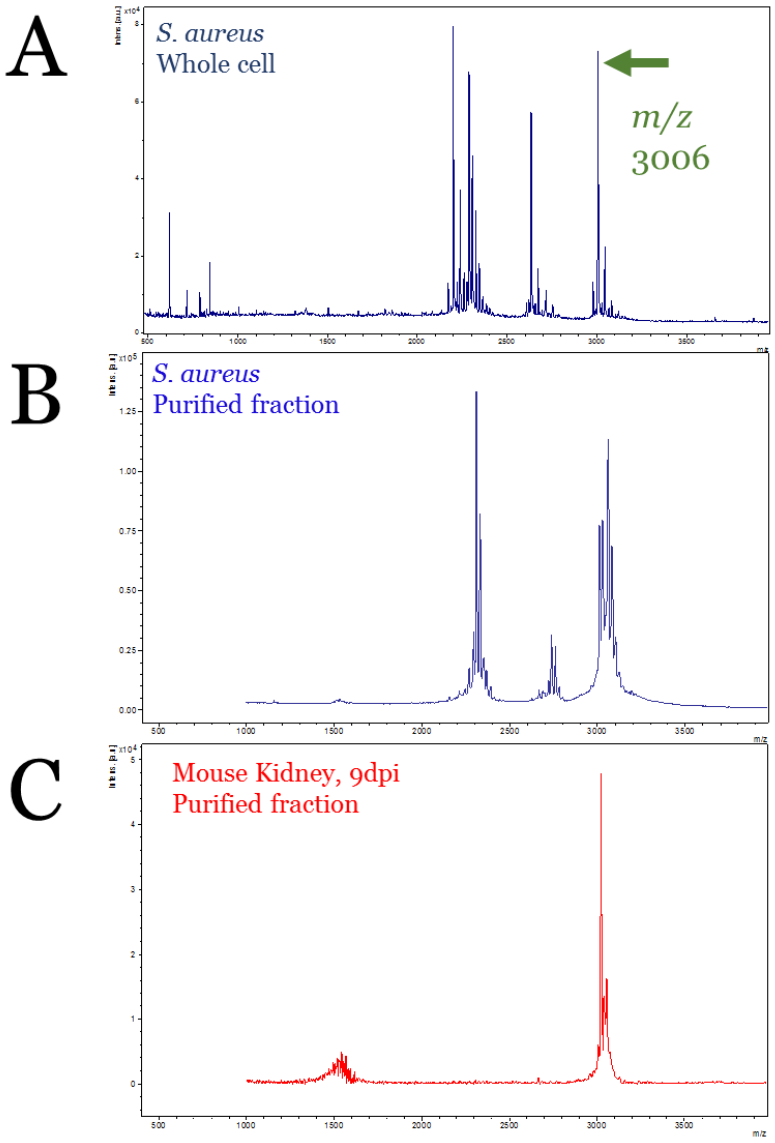

Figure 4:10 Purification of *m/z* 3,006

The target at *m/z* 3,006 required extensive purification for successful identification. To attempt this, *S. aureus* was cultured to stationary phase under moderately hypoxic conditions. Whole cell MALDI MS analysis of the cell pellet revealed the target of interest, shown in A. Both a protein extract from this *S. aureus* pellet and from a mouse extract at 9 days post infection were purified using HPLC with offline fraction collection and the analyte of interest was discover at the same retention time from both the *S. aureus* pellet (B) and kidney extract (C).

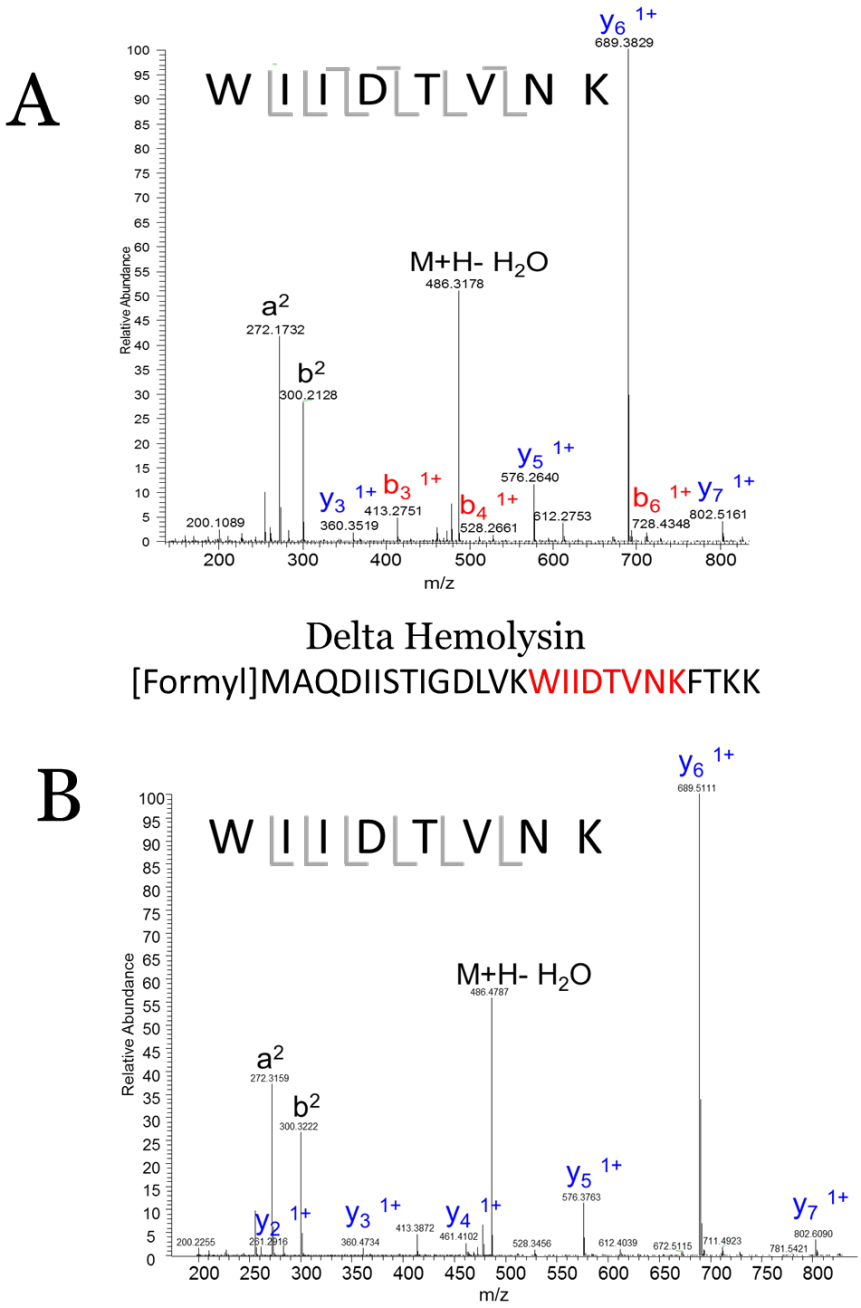

Figure 4.11: Identification of *m/z* 3006 as Delta Hemolysin

Purified protein from Figure 4.10 was subjected to tryptic digestion and MS/MS sequencing at the peptide level. This identified the protein of interest as delta hemolysin. A) shows the MS/MS of the peptide from *S. aureus* pellet while B) shows the MS/MS from mouse kidney. The signals are the same, confirming the identity as delta hemolysin. The sequence of the peptide is shown in red from the overall sequence.

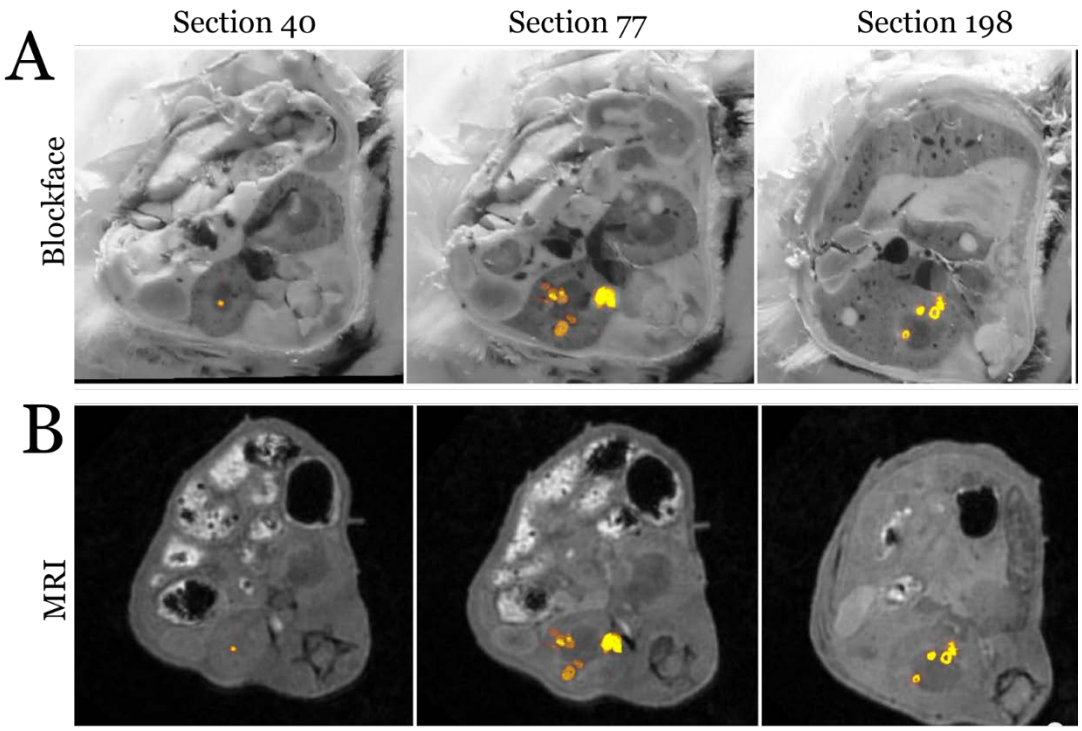

Figure 4.12: Co-registration of MALDI IMS data with Blockface and MRI Data
Co-registration of the MALDI IMS ion intensity maps of *m/z* 10,164, representing the S100A8 subunit of calprotectin, to either blockface (A) or MRI (B) data.

Integration of MALDI IMS and LA-ICP-IMS Characterizes Metal and Protein Distributions Associated with Infection

Because the 3D volume of MRI and blockface data provides a framework onto which additional imaging modalities may be co-registered, MALDI IMS and LA-ICP-IMS data can be overlaid to explore changes in distribution in 3D. Figure 4.12 highlights this ability by showing the co-registration of the MALDI IMS ion intensity maps of *m/z* 10,164, representing the S100A8 subunit of calprotectin, to either blockface (Figure 4.12A) or MRI (Figure 4.12B) data. Signal for S100A8 directly co-localized with abscesses, showing the robust nature of MALDI IMS to molecularly represent anatomical features. Figure 4.13 represents these data in the 3D volume, where images in Figure 4.13 sequentially step through the entirety of the kidney and show these

data in 3D space. Figure 4.14 overlays the MALDI IMS data for the two bacterial proteins, CsbD and Hld, onto two blockface images serial to H&E sections contain bacterial colonies. Section 157 (Figure 4.14A) and section 220 (Figure 4.14B) both show strong co-localization of MALDI IMS data with bacterial colonies. Co-registration of both MRI and blockface imaging with MALDI-IMS revealed bacterial and vertebrate proteins associated with the host-pathogen interface.

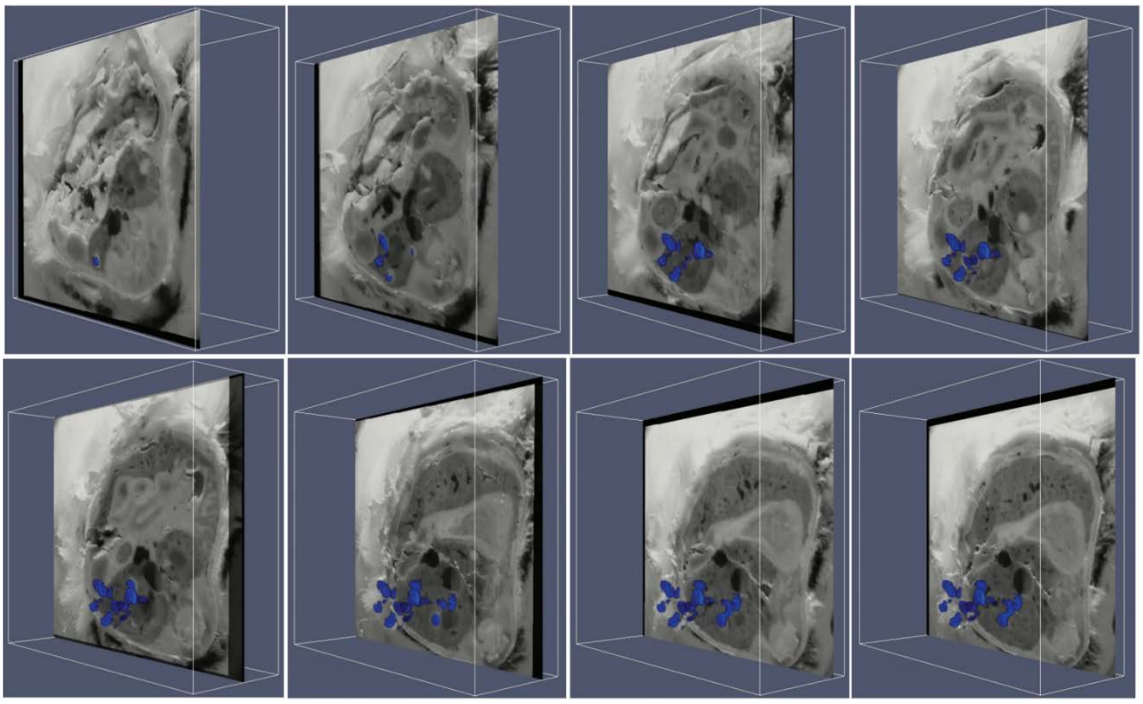

Figure 4.13: Registration of MALDI IMS data creates 3D Ion Maps of S100A8
Co-registration of MALDI IMS data to MRI and blockface images is continued throughout the entirety of the collected data. This allows for MALDI IMS data to be presented in 3D. Eight stills selected from throughout the 3D volume are shown above with blue signal representing the signal for S100A8.

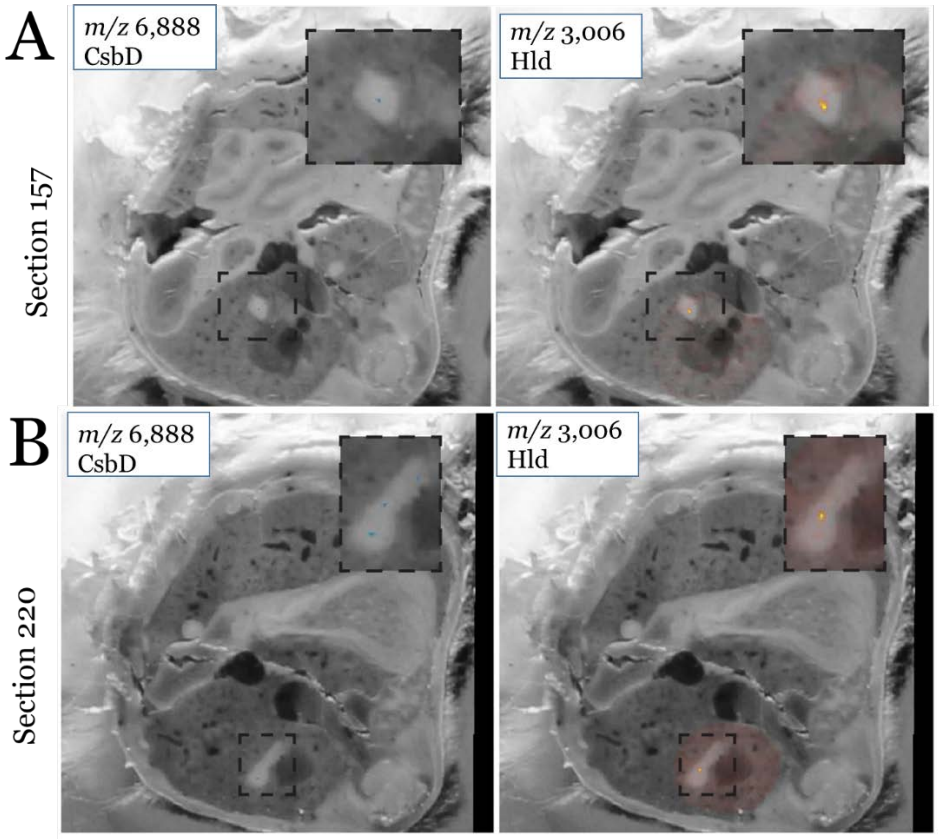

Figure 4.14: Bacterial Proteins Overlaid with Blockface Volume
The two signals identified as bacterial proteins were co-registered to this 3D volume. Presented here are two sections, 157 (A) and 220 (B). Microbial colonies were detected in each of these sections by histological staining. This presents strong co-localization of both the signal for CsbD and Hld with bacterial colonies.

This approach was also used to more globally define shifts in elemental availability during invasive staphylococcal infection using LA-ICP-IMS. LA-ICP-IMS is capable of determining the relative abundance and spatial distribution of elements in a two-dimensional tissue sections. LA-ICP-IMS was performed at 100 micron lateral resolution every 150 microns throughout the mouse to create a three-dimensional volume of elemental abundance and distribution throughout an entire kidney for inclusion in our multi-modality platform. Tissue distribution of calcium, phosphorous, manganese, zinc, magnesium, copper, and iron were determined in this manner, and the resultant elemental maps were co-registered to MRI and blockface volumes, as well as to the MALDI IMS

data set. Figure 4.15 provides an example of elemental IMS data co-registered to a single blockface image, section 224. Tissue abscesses were determined to be rich in calcium and relatively devoid of manganese, iron, and zinc. Copper was also largely excluded from tissue abscesses. Magnesium and phosphorus, on the other hand, were present in abscessed tissues. This data can be compared to the BLI data, where *S. aureus* bioluminescent signal is indicative of iron starvation. LA-ICP-IMS confirmed that bacterial iron starvation signals corresponded to areas relatively devoid of iron.

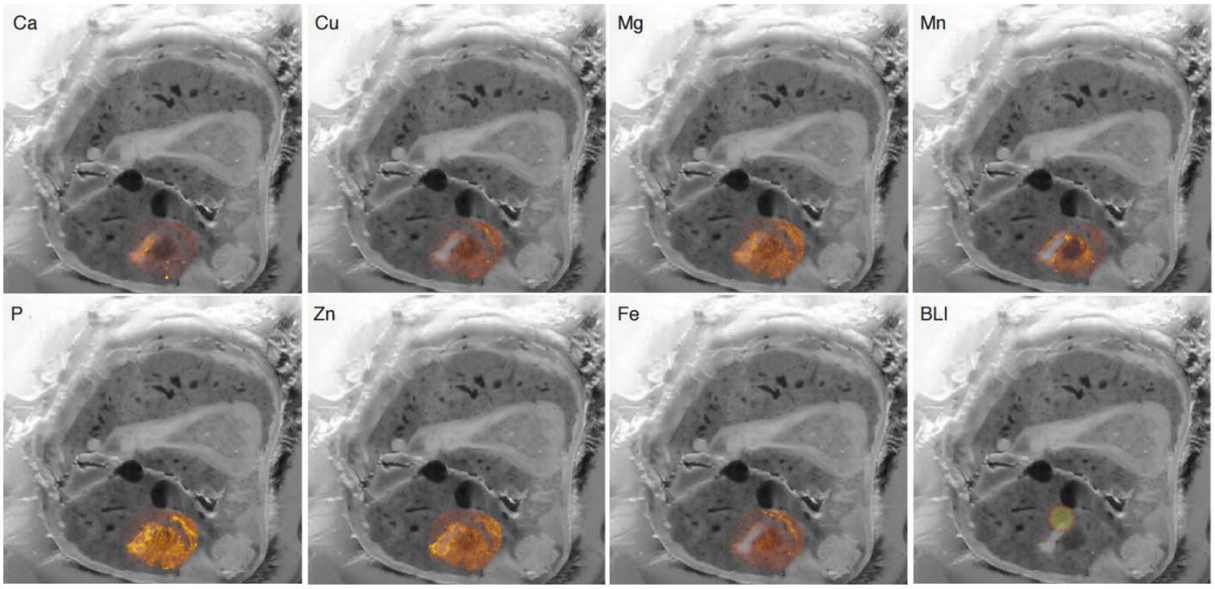

Figure 4.15: LA-ICP-IMS data are Registered to the 3D Volume
Generated metal IMS data can be co-registered to this 3D volume. One section, 224, is shown as an example. Bioluminescence data from this section is shown in the lower right corner to highlight the power of this analysis for comparing BLI to elemental iron analysis.

Co-registration of MALDI IMS and LA-ICP-IMS further characterizes factors involved in nutritional immunity and the host-pathogen interface by revealing protein signals that are spatially associated with nutrient metal distribution. Figure 4.16 shows MALDI IMS data for *m/*z 10,164, representing the subunit S100A8 of the protein calprotectin, a known calcium-binding protein.

Figure 4.16A shows co-localization with calcium throughout four sections of tissue, sections 61, 122, 205, and 227. Calprotectin generally co-localized with calcium throughout the infected organ. Calprotectin signal was inversely localized with manganese and zinc, Figure 4.16 B and C. This supports the idea that calprotectin has a role in chelation and removing these metals from infectious foci.

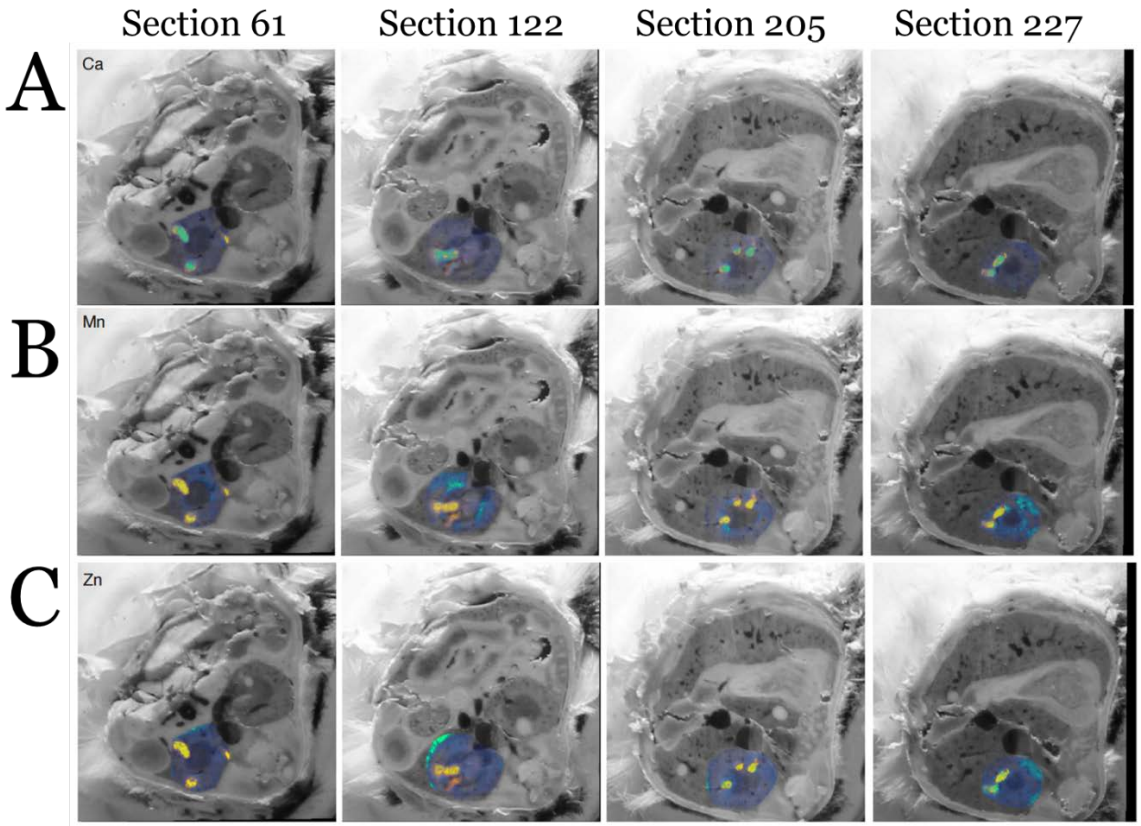

Figure 4.16: S100A8 signal is co-registered to Ca, Mn, and Zn

Calprotectin is known to bind calcium, manganese, and zinc. To explore this, MALDI IMS data for S100A8 was co-registered to calcium (A,) manganese (B,) and zinc (C.) S100A8 is displayed in orange while metals are shown in blue. Data from four sections selected from the 3D volume is displayed here. There were sections 61, 122, 205, and 227.

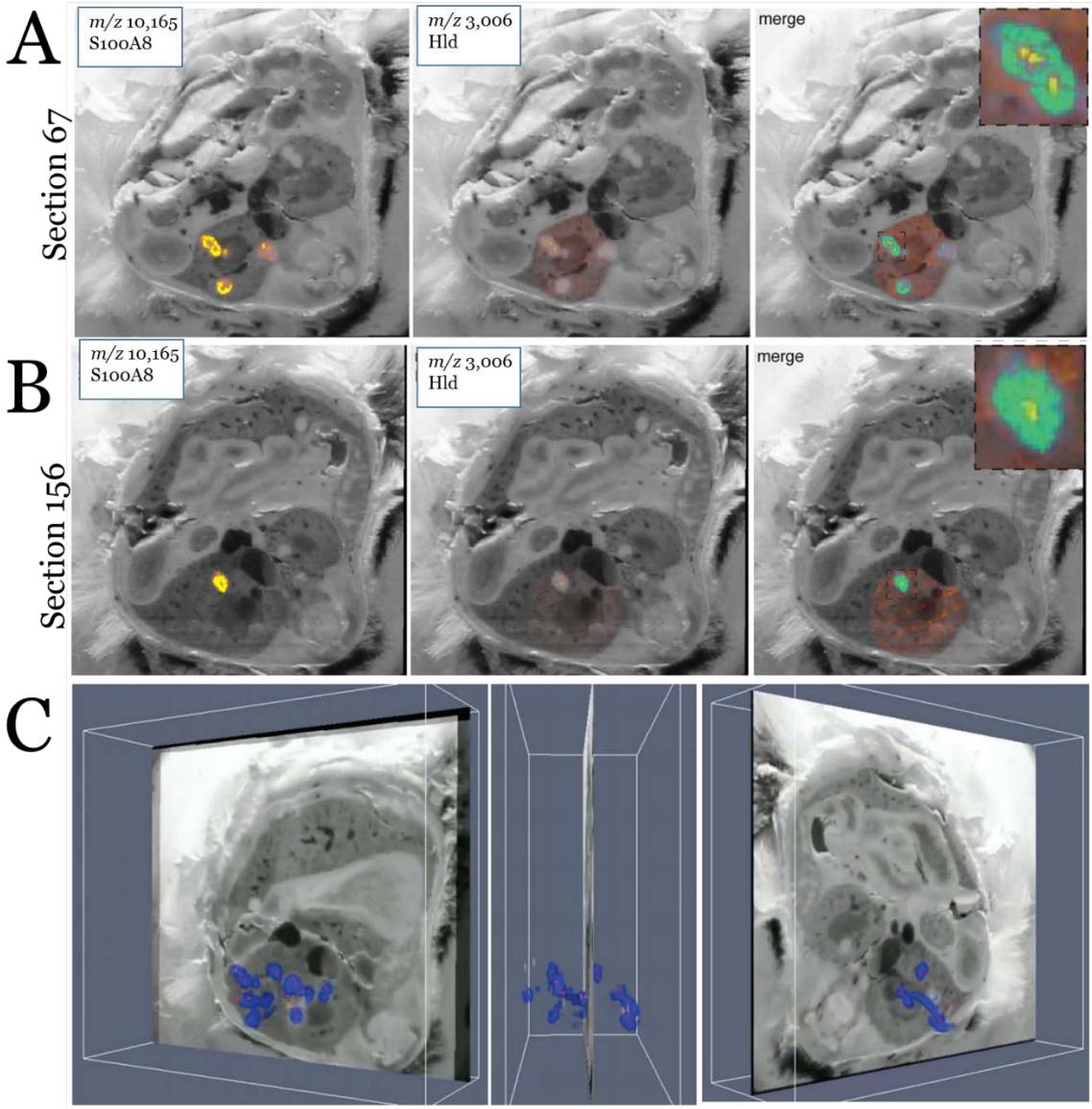

Figure 4.17: 3D Volume of S100A8 and Delta Hemolysin

To study the interaction of pathogen and host, a 3D volume was created that overlaid both S100A8, a robust marker of host neutrophils, and the newly identified signal for delta hemolysin, a known *S. aureus* virulence factor. Stills from two representative sections are shown: section 67 (A) and section 156 (B.) The panels display signal from S100A8 and delta hemolysin individually and then overlaid in the third panel. S100A8 is displayed in green while delta hemolysin is yellow. Insets show magnification of these signals. Panel C shows these ions displayed in the entire 3D volume, which highlights spheres of calprotectin signal with hollow centers that are occupied by delta hemolysin signal.

When comparing calprotectin signal with the identified bacterial signals, shown in Figure 4.17, there is a general lack of calprotectin signal in the center of the abscess, where the staphylococcal communities are residing. Figure 4.17 A and B provide two examples of this in two sections, 67 and 156, respectively. The phenomenon is also recapitulated throughout the entire 3D volume, shown in Figure 4.17C. Additionally, this phenomenon can explored over time, throughout a time course of bacterial infection, and is shown in Figure 4.18. Delta hemolysin is detectible as early as 3 dpi, when staphylococcal lesions are formed. The mutual exclusion of bacterial and calprotectin protein signals may suggest mechanisms of calprotectin degradation or exclusion in the staphylococcal microcolony *in vivo*, providing a partial explanation for how bacteria persist in the presence of a host protein that severely limits bacterial growth *in vitro*. Alternatively, additional high mass resolution IMS experiments on late-stage lesions in a time course of infection reveal a number of signals similar to the *m/z* observed for delta hemolysin, shown in Figure 4.18 C-F. Continuing with the themes explored in Chapter III, it is possible that these *m/z* values represent post translationally modified forms of the protein. If true, this could help visualize not only bacterial degradation of host proteins, but also host-imposed oxidation of bacterial toxin. Whether or not such PTMs and oxidative modification affect the virulence and toxicity of delta hemolysin remains unstudied, but presents another strong example of how MALDI IMS provides unprecedented molecular information about pathogen-host interactions.

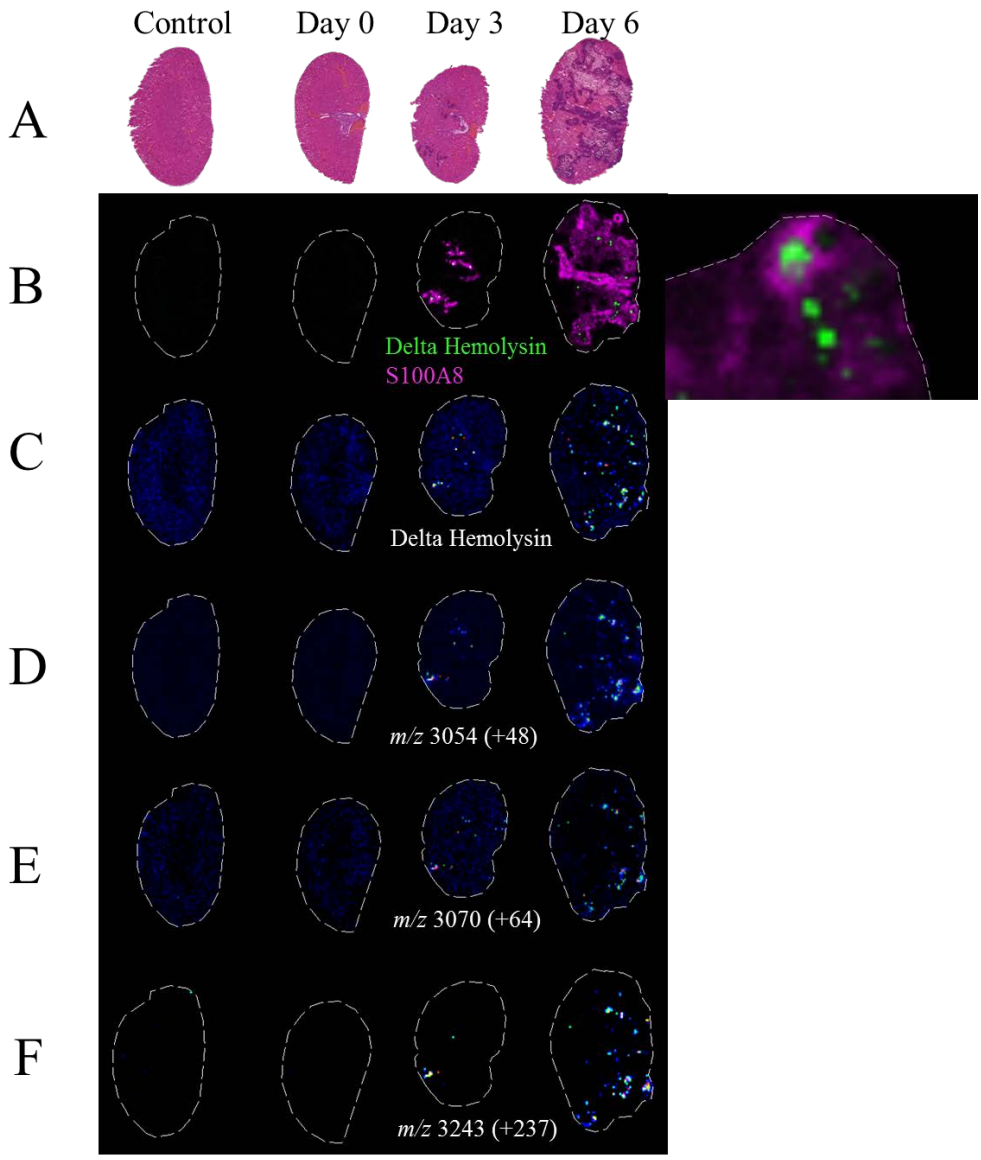

Figure 4.18: Potential Modifications of Delta Hemolysin

The *m/z* 3,006 was identified as delta hemolysin, a staphylococcal virulence factor known to lyse host cells. There are several other peaks around this *m/z* present in high mass resolution analysis. Interestingly, some of these *m/z* shifts are consistent with extensive oxidations (D, +4O, E, 5O,) and some with unknown modification (F, +237.)

Methods

Bacterial Strains and Infections

The *S. aureus* clinical isolate Newman served as the genetic background for all experiments unless otherwise noted.[119] Newman p*isdI.Xen1* was previously described.[158] A Newman *csbD* transposon mutant was created by φ85-mediated transduction of the *csbD::erm* allele from strain NE946, which was obtained from the Network on Antimicrobial Resistance in *Staphylococcus aureus* (NARSA) transposon library at BEI Resources. This csbD mutant strain was used for subsequent proteomic analyses (see below). Bacteria were grown in tryptic soy broth (TSB) at 37°C with 180 rpm shaking. Chloramphenicol was added to the media at a final concentration of 10 μg/ml where indicated. To prepare inoculae for the disseminated infection model, overnight cultures were back-diluted 1:100 and grown for an additional 3 hours, after which time the bacteria were harvested by centrifugation and washed in PBS. Washed bacteria were resuspended to a final concentration of approximately 5 x 10^8 colony forming units (CFU) per milliliter, and kept on ice until used for retro-orbital injection.

All experiments involving animals were reviewed and approved by the Institutional Animal Care and Use Committee of Vanderbilt University. All experiments were performed according to NIH guidelines, the Animal Welfare Act, and U.S. Federal law. Disseminated infection was induced in 6-8 week BALB/cJ (imaging) or C57BL6/J (proteomic identification) female mice by intravenous injection of *S. aureus*. Briefly, mice were anesthetized with 2-2-tribromoethanol (Avertin) and then subjected to retro-orbital injection of 5x10^7 CFU of *S. aureus* in 100 μl PBS. Upon recovery from anesthesia, the mice were returned to the animal housing facility and provided food and water *ad libitum*. At 4 days post-infection, the mice were subjected to the imaging

procedures below. For proteomic identification of proteins imaged by MALDI IMS, infection was allowed to proceed for 9 days. For imaging mass spectrometry-based analysis on individual organs, organs were flash-frozen in a slurry of dry ice and technical grade hexanes (Sigma Aldrich, St. Louis MO) and then stored at -80˚C.

Total Tissue Elemental Analysis

Quantitative analysis was performed on a Thermo Element 2 high resolution sector field inductively coupled plasma mass spectrometer (Thermo Fisher Scientific, Bremen, Germany). Following harvest, the samples were placed in Optima grade nitric acid and sulfuric acid (Sigma Aldrich, St. Louis MO), then heated to promote digestion. After digestion, the samples were diluted using ultrapure water. The introduction of diluted acid-digested samples were conducted by an ESI auto sampler (Elemental Scientific, Omaha, NE) via 0.50 mm ID sample probe and sample capillary in self-aspiration mode. The sample capillary was directly connected to a PFA microflow nebulizer (Elemental Scientific, Omaha NE) followed by a double channel spray chamber (at room temperature). The fine sample aerosol formed in the spray chamber was then transported by argon gas to hot plasma for vaporization, atomization, and ionization. Then all analyte ions were filtered and separated by magnetic sector and electric sector for the selected element isotopes. Each sample was analyzed 10 times, and the following isotopes were monitored: ^{25}Mg, ^{31}P, ^{44}Ca, ^{55}Mn, ^{56}Fe, ^{63}Cu, ^{66}Zn. The instrument was operated in medium resolution mode with an RF power of 1250 W. Samples gas was set to a flow rate of 0.97 L/min with a cooling gas at a flow rate of 16.00 L/min. Auxiliary gas was set to 0.8 L/min.

Bioluminescent Imaging

Bioluminescence imaging was performed using an IVIS 200 optical imaging system (PerkinElmer, Waltham, MA). Mice were anesthetized with 2% isoflurane, shaved, secured to a rigid restraint device, and placed in the imaging chamber of the IVIS 200 system. Spectral imaging was obtained by imaging bacterial luciferase emission through four 20 nm band pass filters at wavelengths from 560 to 620 nm. The surface topography of the mouse was generated using a structured light image. Tomographic source reconstruction was performed using the Living Image Software 3D Analysis software package (PerkinElmer, Waltham, MA). The emission spectrum of bacterial luciferase and tissue optical properties of muscle were used for reconstruction. An emission lower threshold of 2000 photons/sec was used. Final reconstructed source voxel size was 2 mm.

Magnetic Resonance Imaging

Following bioluminescent imaging, mice were maintained under anesthesia in the rigid restraint device and carefully transported to the MRI area. Mice were subsequently secured in the prone position in a 38-mm inner diameter radiofrequency (RF) coil and placed in a Varian 9.4T horizontal bore imaging system (Varian Inc, Palo Alto, CA) for data collection. Respiration rate and internal body temperature were continuously monitored. A constant body temperature of 37°C was maintained using heated airflow. Scout images were collected in all three imaging planes for localization of the kidneys, using a gradient echo sequence with repetition time (TR) = 75ms, echo time (TE) = 5ms, slice thickness = 2mm, flip angle = 35, and an average of 4 acquisitions. Additional parameters include field of view (FOV) = 32mm x 32mm and data matrix = 128 x 128.

Following localization of the kidneys, three dimensional multiple gradient echo imaging data was acquired with FOV = 25.6mm x 25.6mm x 25.6mm, TR = 40ms, echo spacing = 1.7ms, echo train length = 7, flip angle = 25 degrees, data matrix = 128 x 128 x 128, with 4 acquisitions per phase encode step, for a total acquisition time of approximately 43 minutes per animal. The acquired data were zero padded and reconstructed using Matlab 2014a (The Mathworks, Inc., Natick, MA) at 256 x 256 x 256 matrix using an inverse Fourier transform, resulting in a nominal isotropic resolution of 100 microns. Following imaging, the mice were sacrificed with a 5% isoflurane overdose, and then submerged for approximately thirty seconds in liquid nitrogen. Care was taken to avoid movement of mice within the rigid restraint device. The samples were then stored in a -80 C freezer until removed for sectioning, blockface imaging, and MALDI IMS / LA-ICP-IMS.

Sample Preparation of 3D Mouse

The frozen mouse body was manually truncated by removing both the head and tail regions and leaving an approximately 2-3 inch piece of the torso containing both kidneys. The posterior side was affixed to a cryostat chuck with Optimal Cutting Temperature Polymer (Tissue-Tek, Sakura Finetek, Torrance, CA). Transverse 30-µm thick sections were acquired throughout the length of the kidney using a Leica CM 1900 cryostat (Leica Microsystems, Bannockburn, IL. Digital images of the remaining blockface were acquired after every section using a digital camera (Canon EOS 60D SLR digital camera, Canon, New York, NY). Sectioning was performed by collecting serial tissue sections in batches of 5 onto the following types of slides (in order, labeled A through E): A) Gold-coated stainless steel plate for MALDI IMS; B) Glass slide for histological analysis; C) Nitric-acid washed poly(L)lysine-coated vinyl slides (Electron Microscopy Sciences,

PA) for LA-ICP MS imaging; D) Gold-coated stainless steel plate for MALDI IMS backup; and E) Nitric-acid washed poly(L)lysine-coated vinyl for LA-ICP MS imaging backup. This set of 5 serial tissue sections (A through E) constitutes a single 'voxel' in 3D image reconstruction. As the tissue was sectioned at 30-µm thickness, a single voxel transverses 150 µm, resulting in a z-dimension spatial resolution of 150 µm. A total of 240 sections were ultimately collected, or 48 voxels. For the MALDI analyses, two sections were collected onto a single gold plate (i.e., voxel 1, section A and voxel 2, section A were collected together).

Sections obtained for MALDI analysis (A and D) were thaw-mounted on gold-coated stainless steel MALDI target plates for 30 sec. All plates for MALDI IMS analyses were washed to remove interfering lipids and salts as previously described.[30, 120] Briefly, sections were sequentially washed in 70% ethanol for 30 sec; 100% ethanol for 30 sec; Carnoy's fluid (60% ethanol, 30% chloroform, and 10% acetic acid) for 2 min; 100% ethanol for 30 sec; water for 30 sec; and 100% ethanol for 30 sec. The plates were allowed to dry in a fume hood before being placed in Petri dishes, flooded with nitrogen gas, sealed, and placed in a -80°C freezer until analysis.

The slides for histological analysis (B) were stained with hematoxylin and eosin. Optical images of stained sections were obtained at 20x magnification using a Leica SCN400 Brightfield Slide Scanner (Leica Microsystems, Bannockburn, IL).

Sections obtained for LA-ICP MS analysis (C and E) were thaw-mounted onto nitric-acid washed poly(L)lysine-coated vinyl slides as previously described. [29, 135, 165] Slides were placed in a slide box and stored at -80°C until analysis.

MALDI IMS of Single Organs

Serial sections denoted for MALDI IMS were washed to remove excess lipids and salts. Slides were sequentially washed in 70% ethanol for 30 seconds, 100% ethanol for 30 seconds, Carnoy's fluid (6:3:1 ethanol: chloroform: acetic acid) for 2 minutes, 100% ethanol for 30 seconds, 0.2% trifluoracetic acid (TFA) for 30 seconds, and 100% ethanol for 30 seconds. Slides were allowed to dry before matrix was applied. For the matrix in Figure 4.2, a 5 mg/ml solution of sinapinic acid matrix was prepared in 60% acetonitrile with 0.1% TFA and sonicated for 5 minutes to ensure that the matrix was completely dissolved. Matrix was applied using a TM-Sprayer (HTX Imaging, Carrboro, NC) heated to 90°C in 8 passes at a rate of 1050 mm/minute with a 2 mm spacing. The spray pattern was spatially alternated at a 90° angle and offset by 1 mm to ensure uniform sample coverage. After matrix application, samples were rehydrated at 85°C in an oven (Thermolyne Oven Series 1297, Dubuque, IA). Samples were fixed to the lid of a petri dish using conductive tape and preheated in the oven for 2 minutes. Following this, 1 ml of water and 100 µL of acetic acid were pipetted onto filter paper in the petri dish bottom. The petri dish was reassembled to form a rehydration chamber and was heated at 85°C for an additional 3.5 minutes. The rehydrated slide was allowed to dry at room temperature before analysis. Trifluoracetic acid (TFA) and sinapinic acid were purchased from Sigma-Aldrich (St. Louis, MO). HPLC-grade acetonitrile, ethanol, chloroform, glacial acetic acid, and technical grade hexanes were purchased from Fisher Scientific (Pittsburgh, PA, USA).

For Figures 4.3 and 4.4, 2,6-dihydroxyacetophenone (DHA) was used as a matrix and applied via sublimation similarly to previously described.[120] Briefly, a sand bath was heated to 105°C. DHA was placed in the bottom of the sublimation apparatus and samples were suspended above the matrix by taping them to a cold finger. The chamber was evacuated to 50 mTorr and the

sublimation was allowed to occur for 5 minutes. Samples were rehydrated before analysis using a protocol similar to above, only using 1 mL of 50% acetic acid as the rehydration solvent. Rehydration was carried out at 37°C for 3.5 minutes.

Following rehydration, the tissue was analyzed using a Bruker AutofleX Speed TOF(/TOF) mass spectrometer (Bruker Daltonics, Billerica, MA, USA) equipped with a Gaussian beam profile laser (Nd:YAG, 355 nm) in linear positive–ion mode at 75 μm spatial resolution. One hundred laser shots were collected at each position in a random walk pattern in 25 shot step increments, with a laser repetition rate of 1000 Hz. Extraction and acceleration voltages were 19.5 kV and 18.0 kV, respectively, with a delayed extraction time of 340 ns and a lens voltage of 7.5 kV. The measured mass range was from *m/z* 3,000-30,000, with a deflection mass of 3,000. Images were viewed using flexImaging 3.0 Software (Bruker Daltonics) and were normalized to total ion current. Ion density maps were extracted and scaling, relative to total ion current, was constant for each ion of interest.

3D MALDI IMS

Plates for MALDI IMS were removed from the -80°C freezer and allowed to warm up to room temperature for 30 min prior to opening the sealed Petri dish in order to minimize water condensation on the samples. After warming, digital images of each plate were acquired on a desktop scanner at 2400 dpi. 2,5-dihydroxyacetophenone (DHA) MALDI matrix was prepared at a concentration of 15 mg/mL in 90% acetonitrile with 0.2% trifluoroacetic acid. Matrix was applied to the plate robotically using a TM Sprayer (HTX Technologies, Carrboro, NC, USA.) The sprayer was operated at a flow rate of 0.2 mL/min with a 10-psi nitrogen flow gas and a nozzle temperature of 85°C. Samples were sprayed at a velocity of 1100 mm/min and a track spacing of

2 mm. Six total spray passes were applied to sections, rotating and offsetting every other pass by 1 mm to ensure even coverage of matrix. Just prior to MS analysis, the plates were rehydrated by first heating the plate to 37°C in a lab oven for 2 min, followed by 3 min at 37°C in a Petri dish with 1 ml of 50 mM acetic acid. [2, 120]

Sections for 3D analysis were analyzed on a MALDI TOF MS (SimulTOF 200 Combo, SimulTOF Systems, Sudbery, MA) in positive ion linear mode. This system is equipped with a 349 nm, diode-pumped, frequency-tripled Nd:YLF laser (Spectra-Physics, Santa Clara, CA). Ion images were acquired in typewriter mode (*i.e.*, acquisition in one lateral direction only) using continuous raster sampling at a 50-µm calculated horizontal spatial resolution and a 50-µm vertical step. [17, 166] For most sections, only a region encompassing the kidney was analyzed. Sections were analyzed using 2000-kHz laser repetition rate, 2-mm/s stage speed, and 50 hardware averages for a 40-Hz digitizer acquisition rate. The effective pixel rate is slightly slower due both to the time required to return the stage to the beginning of the next raster line and to a built in delay to flush acquired spectra from the acquisition card to the hard disk at the end of each line scan. Over the 48 plains of analysis, 930,398 pixels were acquired in just 22.2 hours of instrument time (for an effective pixel rate of ~11.6 Hz). On more conventional imaging platforms, which are capable of 1-2 Hz acquisition rates, this same analysis would have required 5-11 days of instrument time.

Following data acquisition, all spectra were preprocessed for baseline subtraction, intensity normalization, and *m/z* alignment. All 48 individual 2D IMS data sets were concurrently loaded into MATLAB to establish a single 3D IMS data set. Each 2D data set consists of spectra that contain around 30,000 *m/z* bins, each describing a range from *m/z* 600 to 49,000. Given that each 2D IMS experiment reports its own *m/z* axis, and subsequent preprocessing algorithms need to approach the spectra that were collected over all cutting depths as a single (3D) IMS data set with

a single *m/z* axis, the spectra of all 2D data sets were resampled to a single consensus *m/z* axis. The *msresample()* function from the Bioinformatics Toolbox of MATLAB (The Mathworks Inc., Natick, MA) was used to resample uniformly. To reduce the size and dimensionality of the overall data set, this step was also used to down-sample the number of bins per spectrum to 7,944. The resampling step ensures that the spectra collected across different 2D experiments can be directly compared along the chemical (*m/z*) domain. To ensure that ion intensity values can be compared along the (inter-experiment) z dimension as well as along the (intra-experiment) x and y dimensions, all spectra across the different cutting planes were preprocessed as one all-encompassing data set. Although this induces an increased computational and memory resource cost over preprocessing 2D IMS data serially on a plane-by-plane basis, it makes 3D ion volumes more robust and less susceptible to cutting plane-to-plane signal variation. The preprocessing steps entail normalization, baseline correction, *m/z* alignment, and peak picking. The spectra were normalized using common ion current as a reference, disregarding differential peaks. Baseline correction was accomplished using a spline approximation of the baseline at the 0.1-quantile of ion intensities per spectrum, employing a window size of 500 and a step size of 250. Furthermore, the spectra were aligned along the *m/z* axis to reduce peak drift, allowing a maximum *m/z* shift of 60. These steps were implemented using the *msbackadj()* function and the *msalign()* function provided by the Bioinformatics Toolbox of MATLAB (MathWorks). The subtraction of the baseline estimate can sometimes result in small negative intensity values in non-peak areas of the mass spectral profile when the estimate overshoots the true baseline. Such artifacts were removed by setting negative ion intensities to zero post-baseline correction. The *m/z* alignment was driven by five reference peaks that were present across the majority of cutting depths: *m/z* 5,653; 10,164; 11,306; 14,050; and 14,956. The preprocessing phase was finalized by a feature extraction step

that reduces the high-dimensional full profile spectra to distinct peaks, retrieving the corresponding peak intensities across all cutting depths. This peak-picking step employs the *mspeaks()* function provided by MATLAB and uses nearest neighbor interpolation to extract peak heights from each spectrum.[167]

High mass resolution and accuracy IMS data were collected on a 15T MALDI Fourier Transform Ion Cyclotron Resonance (FTICR) MS (Bruker Daltonics, Billerica, MA) from the kidney region of a single transverse tissue section (Section 13D). The instrument is equipped with an Apollo II dual MALDI/ESI ion source and a Smartbeam II 2kHz Nd:YAG (355nm) laser. Data were collected from *m/z* 900 – 18,000. Special tuning of the Funnel RF amplitude (190 Vpp), accumulation hexapole (1.4 MHz, 1200 Vpp), transfer optics (1 MHz, 310 Vpp), time-of-flight delay (2.0 ms), and ICR cell (Sweep excitation power: 40%) were required for high *m/z* analysis. Imaging data were collected using the small laser setting (~50 μm) with a pixel spacing of 75 μm in both x and y dimensions and 500 laser shots averaged per pixel. External calibration was performed prior to analysis using CsI clusters and internally following analysis using a series of previously identified proteins. [2, 30] FlexImaging 4.1 (Bruker Daltonics, Billerica, MA, USA) was used to visualize ion images.

LA-ICP IMS

Trace element imaging was performed similarly to previously described.[29, 135] Briefly, samples were ablated using an LSX-213 laser ablation system (LA, CETAC, Omaha, NE USA) and analyzed using a coupled Element 2 high resolution sector field ICP-MS (Thermo Fisher Scientific, Bremen, Germany). Vinyl slides were placed into a sealed ablation chamber and were ablated in multi-line mode (line by line) at a rate of 30 μm/s using a focused Nd:YAG laser beam

(213 nm). The laser had a spot size of 100 µM with a laser shot frequency of 5 Hz. For most sections, only the region encompassing the target kidney was ablated. Helium gas was used to assist in laser ablation of the sample, and ablated sample particles were introduced online into the ICP-MS using helium gas to maximize sample transport efficiency at a flow rate of ~1 L/min. Particles were mixed with argon gas at a flow rate of ~1 L/min before online introduction to the ICP-MS. The mass spectrometer was operated in resolution mode. The following isotopes were detected: $^{44}Ca^{+}$, $^{55}Mn^{+}$, $^{56}Fe^{+}$, and $^{66}Zn^{+}$. Flow rates of carrier and sample gas were tuned for each sample to obtain the same signal response from a standard.

Histological Analysis

Serial sections collected for histological analysis were hematoxylin and eosin (H&E) stained. Stained slides were scanned using a MIRAX Scan slide scanner (Carl Zeiss MicroImaging, Gŏttingen, Germany) in manual bright field mode. Optical images were generated from the scans using MIRAX Viewer version 1.11.22.0 (Carl Zeiss MicroImaging).

Protein Identification

Selected protein ions of interest from the MALDI images were identified using an indirect strategy.[27, 30, 168] Briefly, common spatial localizations between an ion image acquired on the high mass resolution FTICR instrument and ion images acquired on the low mass resolution TOF instrument were used to link high mass accuracy measurements made on the FTICR to the protein ions observed in the TOF data. These exact mass measurements (<5 ppm) provided values to subsequently target for top-down LC-MS/MS proteomics.

For top-down proteomics, on-tissue protein microextractions were first performed on abscesses using a section containing clear infectious foci similarly to previously described.[27] Protein was extracted from abscesses using 0.5μL of 30% acetonitrile 0.1% TFA and microextracts from four sections were combined. A second extraction was performed sequentially on the same four sections using 0.5μL of 50% acetonitrile 5% formic acid.2 or 2.3 μL of microextract was diluted at least 10-fold in 0.1% formic acid and was bomb-loaded onto a reversed-phase capillary trap column using a helium-pressurized cell as previously described.[27, 30] Eluted proteins were mass analyzed using an ETD-enabled LTQ Orbitrap Velos mass spectrometer that was equipped with a nanoelectrospray ionization source (Thermo Scientific, San Jose, CA, USA) operated with a data-dependent method. A full scan spectrum of *m/z* 400–2000 (resolving power (RP): 60,000 at *m/z* 200) was acquired as the initial scan event per duty cycle. Following the full-scan, four data-dependent scan events were selected for fragmentation using ETD in the Velos ion trap using the four most abundant ions in each MS scan. Dynamic exclusion was enabled allowing a repeat count of 1 within 20 seconds. ETD tandem mass spectra were acquired sequentially using the LTQ Velos ion trap followed by the Orbitrap (RP: 15,000 at *m/z* 200) for mass analysis. An isolation width of 3 Da and an ETD reaction time of 90-100ms were used for MS/MS spectra. The MS^n AGC target value in the ion trap was set to 2×10^4, the MS^n AGC target for Orbitrap scan events was 8×10^5, and the ETD reagent ion (fluoranthene) AGC target was set to 1×10^5. Parent ions of interest were selected from the full-scan and matched ions detected in FTICR IMS data sets. Fragmentation spectra from these ions were manually *de novo* sequenced and searched using BLAST databases. Targets of interest isolated from data-dependent methods were targeted for fragmentation by customizing the instrumental method with targeted scan events to ensure ETD MS/MS of selected ions.

Further protein purification was needed to isolate certain targets of interest. In order to maximize the abundance of bacterial proteins in kidney abscesses, *S. aureus* infection was allowed to proceed for 9 days, after which time the kidneys were excised and homogenized in 1 mL of phosphate buffered saline using a rolling pin. To extract proteins, 1 ml of 2,2,2-trifluoroethanol and 2 mL of 50% acetonitrile was added to the homogenate. Kidneys were further homogenized using an ultrasonicator dismembrator Model 150E (Fisher Scientific). Extracts were centrifuged to remove particulates and were fractionated using a Waters 2690 Separations Module (Waters, Milford, MA, USA) equipped with an offline fraction collector. Proteins were fractionated using a Vydak 208TP 150 mm 5 μm C8 column (Vydac Grace, Columbia, Maryland) and an aqueous to organic gradient over 120 minutes. Fractions were collected every minute. The fractionation was performed four times and the fractions were combined. The fractionation was dried using a Savant SPD131DDA SpeedVac Concentrator (Thermo Scientific) and reconstituted in 20 μL of 50% acetonitrile with 0.1% TFA. One μL of each well was spotted onto a Bruker Anchorchip (Bruker Daltonics) with 1 uL of 15 mg/mL DHA matrix in 40% acetonitrile. A MALDI MS was obtained for each spot and fractions of interest were manually selected based on the presence of *m/z* values of interest. Fractions of interest were subjected to targeted MS/MS analysis as described above.

To identify HLD, a bottom-up proteomics approach was used. A purified fraction from above was subjected to overnight tryptic digestion. For analysis by LC-coupled tandem mass spectrometry (LC-MS/MS), peptides were loaded onto a capillary reverse-phase analytical column (360 μm o.d. × 100 μm i.d.) using an Eksigent NanoLC Ultra HPLC and autosampler. The analytical column was packed with 20 cm of C18 reverse-phase material (Jupiter, 3 μm beads, 300 Å, Phenomenex), directly into a laser-pulled emitter tip. Peptides were gradient-eluted over a 90-minute gradient at a flow rate of 500 nL/min. The mobile phase solvents consisted of water

containing 0.1% formic acid (solvent A) and acetonitrile containing 0.1% formic acid (solvent B). The gradient consisted of the following: 0-15 min (sample loading via autosampler onto column), 2% B; 15-65 min, 2-40% B; 65-74 min, 40-90% B; 74-75 min, 90% B; 75-76 min 90-2% B; 76-90 min (column equilibration), 2% B.

Peptides were sequenced using Q Exactive Oribtrap MS (Thermo Scientific.) The mass spectrometer collected one full scan followed by MS/MS fragmentation data for the top 12 ions. A mass range of *m/z* 300-2000 was collected per each scan. A targeted scan event was included to obtain MS/MS data for *m/z* 497.77, representing the $[M+2H]^{2+}$ ion for the tryptic peptides WIIDTVNK.

Imaging Reconstruction and Registration

As described above, care was taken not to move the mouse between optical imaging, MRI, and the freezing process. Thus, a rigid-body image registration was used to transform the MRI data into the blockface images' coordinate system.[159, 169] The resulting transformation was also applied to the optical data, resulting in the optical, MRI, and blockface data in a unified coordinate system.

Imaging the blockface data during tissue sectioning does not create intrinsically registered images. In order to reconstruct an aligned three-dimensional blockface dataset, the imaging data was aligned slice by slice through an image registration that maximizes a normalized mutual information metric using a rigid body transformation.[159, 169] This approach starts with the central blockface image and registers a neighboring slice in the same direction. Registration is continued for the entire volume by registering each successive slice to the proceeding slice until the initial image is reached. Once all blockface slices were aligned, they were combined into one three-

dimensional dataset, providing the base coordinate system to which all imaging data will be transformed.

To perform the optical to MR registration a full-body MRI dataset of the mouse was needed. However, due to limitations of the MRI coil two separate scans were required to obtain full coverage of the specimen. Thus, the upper and lower sections of the mouse were imaged separately with overlapping portions towards the middle of the body. Following acquisition, the overlapping data were used to combine the two scans to form one cohesive structural image using image registration.

The transformation between the optical imaging coordinate system and MRI coordinate system was calculated using a surface based registration. During acquisition the optical imaging system creates a 3D surface mesh of the mouse. A second mesh was created in the MRI coordinate system by manually segmenting the mouse body using the full body MRI. Once each surface mesh was created and manually reoriented to similar positions an iterative closest point algorithm was used to align the optical mesh in the MRI mesh coordinate system.[159] This provided the necessary transformation to move the raw optical data into the MRI coordinate system.

Once the 48 2D MALDI datasets were acquired, a single *m/z* bin was chosen with well-defined anatomical features for each slice. This image was manually registered to the corresponding blockface image. The resulting transformation was then applied to all ion images for this slice. These data were combined to form one 3D MALDI dataset for each of the defined *m/z* bins by inserting data into the appropriate location in an empty matrix of the same dimensions as the blockface data, and interpolating the missing data between slices using a weighted interpolation. This resulted in a 3D MALDI image for each of the selected *m/z* bins within the same coordinate system as the blockface.

Similar to the MALDI IMS to Blockface registration, a single element image from LA-ICP-IMS was chosen for each slice and manually registered to the corresponding blockface image. The resulting transformation was applied to the remaining element images for the similar slice. Once all data had been registered, the 2D data were inserted into the correct location in 3D space, and data between slices were interpolated. The result was a 3D LA-ICP-IMS dataset for each analyzed element in the same coordinate system as the blockface.

Statistical analysis

Statistical analysis was performed using Graph Pad Prism version 5.0 and the indicated statistical test.

CHAPTER V

CALPROTECTIN AFFECTS BACTERIAL BIOFILMS

A version of the following chapter was previously published and has been adapted from Wakeman and Moore et al., *Nature Communications*, Copyright 2016 by Springer Nature[29] and from Spraggins, Rizzo, Moore et al. *Proteomics*, Copyright 2016 by Wiley and Sons.[2]

Overview

Bacterial biofilms represent the physiologically relevant form of bacteria, both in pathogenic and non-pathogenic settings. It is known that biofilms contain differentiated bacterial populations, all performing different tasks within the community. However, very little is known about the factors driving that differentiation. Mass Spectrometry is a powerful analytical tool to understand biological systems. In this work, biofilms grown in a drip-flow reactor are subjected to MALDI IMS, LA-ICP-IMS, and shotgun proteomic analysis to further understand the factors that drive differentiation. Biofilms are subsequently challenged with the host protein calprotectin, an abundant innate immune protein responsible for the chelation of nutrient manganese and zinc at sites of infection. It was determined that calprotectin exposure promotes interactions between *Staphylococcus aureus* and *Pseudomonas aeruginosa*- two microbes that do not tolerate each other in culture, but are known to co-colonize humans with diseases hallmarked by chronic inflammation and calprotectin recruitment, such as cystic fibrosis.

Introduction

Bacterial Biofilms

Biofilms are multicellular microbial communities that represent the most common lifestyle of many microorganisms.[170] The unique architecture of biofilms allows these microbial structures to persist in a wide range of niches, including biotic and abiotic surfaces.[171, 172] A biofilm can originate from a single microbial species or from numerous and diverse microorganisms, potentially encompassing multiple domains of life.[170, 173] Even biofilms containing a single species exhibit distinct roles within the community, characterized by different gene and protein expression.[174, 175] The presence of these spatially-defined regions of differentiated cells gives a biofilm tissue-like properties in which different subpopulations of cells serve defined roles in the microbial community to promote the overall health of the biofilm.[176, 177] It is believed that nutrient gradients form as the biofilm thickens and that such gradients influence the physiology within the microbial structure.[175, 178]

Many infections are caused by biofilms arising from either a single species or a community of pathogens, making the study of biofilms important for human health and industry.[170] The role of nutrient metal fluctuations is particularly important in the context of infection because host cells attempt to sequester metals from invading pathogens as a major innate defense mechanism.[179] This process is known as nutritional immunity; some of the best studied strategies of nutritional immunity are the chelation of iron (Fe) through the action of host-derived proteins such as transferrin and lactoferrin as well as chelation of zinc (Zn) and manganese (Mn) by calprotectin.[157, 179]

Consistent with the theory that host-imposed nutrient starvation can affect microbial community structure, environmental iron levels impact the gross morphology of various types of single-species biofilms.[180, 181] iron levels also influence the composition of pathogenic polymicrobial communities.[182-184] For example, in response to iron depletion, *Pseudomonas aeruginosa* up-regulates production of alkyl-hydroxyquinolones (AQs) to lyse staphylococcal cells for use as an iron source.[182, 185]

These works supported new hypotheses that metal gradients within developing biomasses might cause dramatic shifts from the proteins expressed in certain bacterial populations. Techniques such as RNA fluorescence *in situ* hybridization (RNA FISH) and reporter gene fusions have been successfully employed in multiple studies to establish the existence of bacterial subpopulations within a biomass.[175, 186] However, these methods are limited by the number of differentially-expressed targets that can be assessed at one time and require prior knowledge of molecules of interest. In order to study the impact that metal distributions have on bacterial subpopulations, a multi-modality Imaging Mass Spectrometry (IMS) approach was utilized. Here we present a combination of matrix-assisted laser desorption/ionization (MALDI) IMS [187] and laser ablation inductively coupled plasma (LA-ICP) IMS to visualize heterogeneity of proteins, small molecules, and metals within a *P. aeruginosa* biofilm in intricate and unprecedented detail.

Pseudomonas aeruginosa

Pseudomonas aeruginosa is a Gram negative bacterium typically found in soil. The bacterium is quite adaptable and has been found to grow in soil, water, and other abiotic surfaces.[188] This is partially due to *P. aeruginosa*'s ability to form robust biofilms, leading this bacterium to be often used as a model organism for the study of biofilm formation.

P. aeruginosa will also adopt a pathogenic lifestyle and cause infections of most vertebrate niches. In addition to adept colonization of the host, this organism has high capabilities to resist antimicrobial strategies.[189] This is partially due to its genetic abilities to produce efflux pumps and other proteases that degrade antimicrobial compounds. It has also emerged as a major pathogen affecting immunocompromised patients. It is the third leading cause of hospital-acquired urinary tract infections, a major cause of swimmer's ear, and a major cause of nosocomial pneumonia.[189] Of particular interest is the ability of *P. aeruginosa* to colonize the airways of patients with cystic fibrosis.

Cystic Fibrosis

Cystic fibrosis (CF) is a genetic disorder affecting 1 in every 3,000 newborns. The disease is caused by mutations in the cystic fibrosis transmembrane conductance regulator protein, which is involved in homeostasis of epithelial sodium channels. This can cause dysregulation of sweat, gastrointestinal fluids, and mucus.[190] Hallmarked by long-term persistent bacterial colonization in the lungs, patients with late-stage lung disease develop thick mucus blocking airways and causing fibrosis, making it increasingly difficult for patients to breathe.[191] *Pseudomonas aeruginosa* is a known persistent colonizer of the CF lung.[192]

Results and Discussion

Biofilms Grown in a Drip Flow Reactor Have Distinct Structural Features

A drip flow reactor (DFR) generates robust bacterial biofilms.[193] In this system, a continuous influx of nutrients is supplied to a developing biofilm over the course of several days while the waste is removed by gravity flow to minimize shear force. Figure 5.1 shows a cartoon

schematic of a DFR. Figure 5.1A shows how fresh media is delivered at a constant flow over bacteria seeded in a chamber. The low-shear force flow is gravity-driven, so fresh media always flows down the slide toward the waste container. The biofilms in a DFR chamber form on a provided surface, such as a glass slide. After six days of growth in this system, *P. aeruginosa* develops a robust biofilm that is ~3 mm thick and capable of withstanding significant physical manipulation. An example biofilm is shown in Figure 5.1B.

P. aeruginosa biofilms that are grown in the DFR are visibly influenced by the flow of nutrients. The portion of the biomass that developed around the initial drops of medium entering the chamber formed a distinct pore, which is annotated in Figure 5.1B. As the medium flowed down the length of the slide, a pink-pigmented population of cells formed on this presumably nutrient-rich channel. The biomass forming on the edges of the glass slide with no direct access to the nutrients from the central channel relied on nutrient diffusion and was likely experiencing greater levels of starvation. Despite the visible differences in these distinct portions of the *P. aeruginosa* DFR biofilm, all regions of the biomass were composed of approximately equivalent ratios of live to dead cells as determined by live/dead staining confocal microscopy, shown in Figure 5.2. Additional Analyses by electron microscopy are shown in Figure 2 and further support the live/dead staining. This confirmed that the visual heterogeneities throughout the biomass were not simply due to cell death at the nutrient poor regions or from any contaminating microorganisms who were contributing to the heterogeneity.

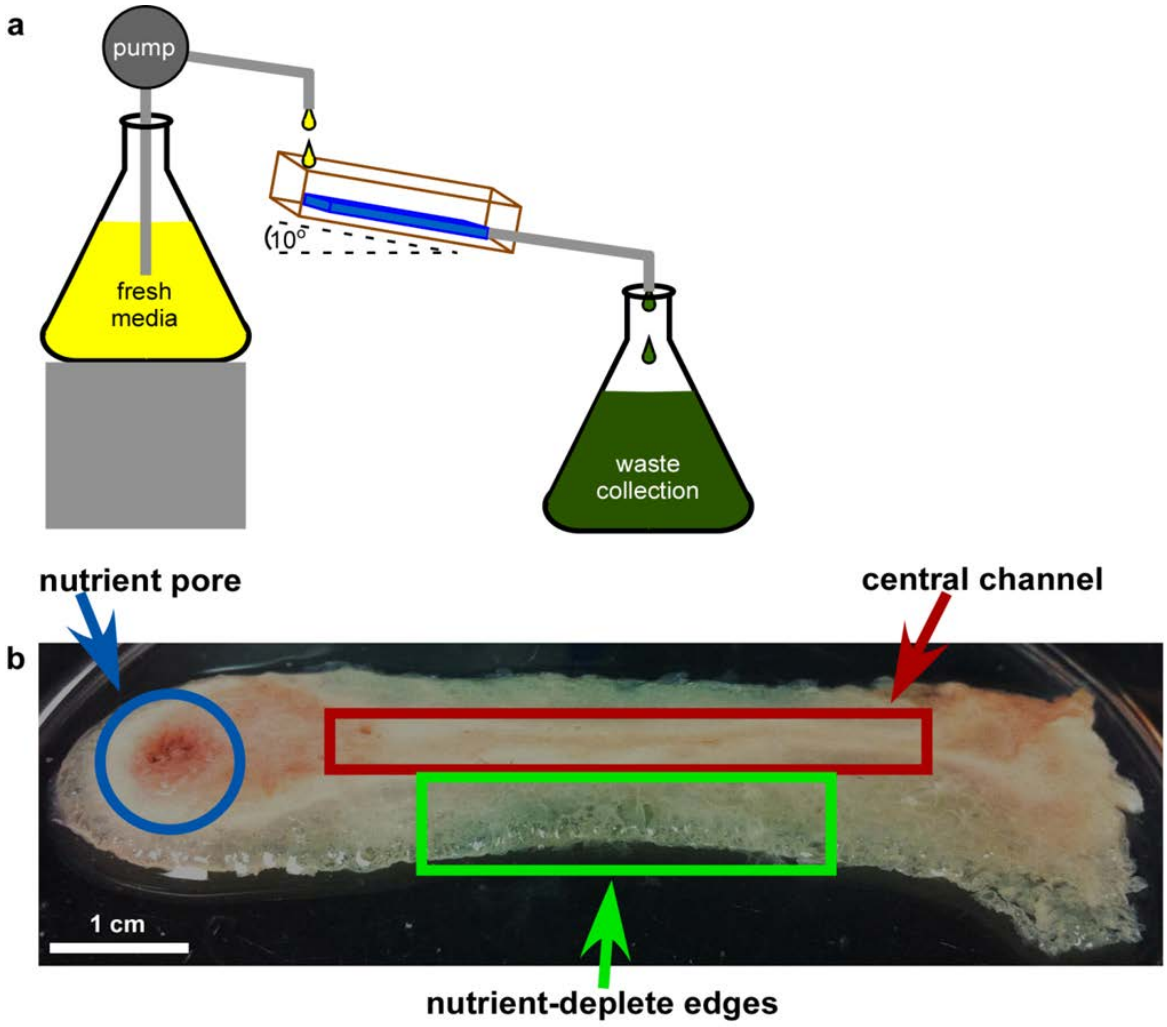

Figure 5.1: Drip Flow Reactor Biofilms

Panel A) shows a cartoon schematic of a drip flow reactor, where fresh media is dripped over bacteria in a chamber using a peristaltic pump. Waste leaves the chamber based on gravitational force, which results in low shear-force on the biofilms. *P. aeruginosa* biofilms grown in this manner are very robust, shown in panel B) Structural features of interest include a nutrient pore, formed at the point where media drips onto the slide. A pink central channel forms in regions where medium flows. Nutrients diffuse outward from the central channel, creating nutrient-depleted edges. Reprinted from *Nature Communications*, vol 7, Wakeman and Moore et al, from "The innate immune protein calprotectin promotes Pseudomonas aeruginosa and Staphylococcus aureus interaction" 2016 with permission from Nature Publishing Group under a Creative Commons license.[29]

IMS Reveals Heterogeneities in Bacterial Biofilms

In order to study protein distributions in an unbiased way throughout heterogeneous bacterial biofilms, a MALDI IMS analytical approach was implemented. To identify differential protein expression within the *P. aeruginosa* biofilm, various portions of the biomass both proximal and distal to nutrient influx were analyzed using MALDI IMS. This analysis revealed the presence of distinct subpopulations throughout the biomass by tracking unique mass to charge (*m/z*) ratios. These data are shown in in Figure 5.3. Interestingly, many of the ion intensity maps generated correlated with the nutrient gradients that were predicted from both visual and microscopic analyses.

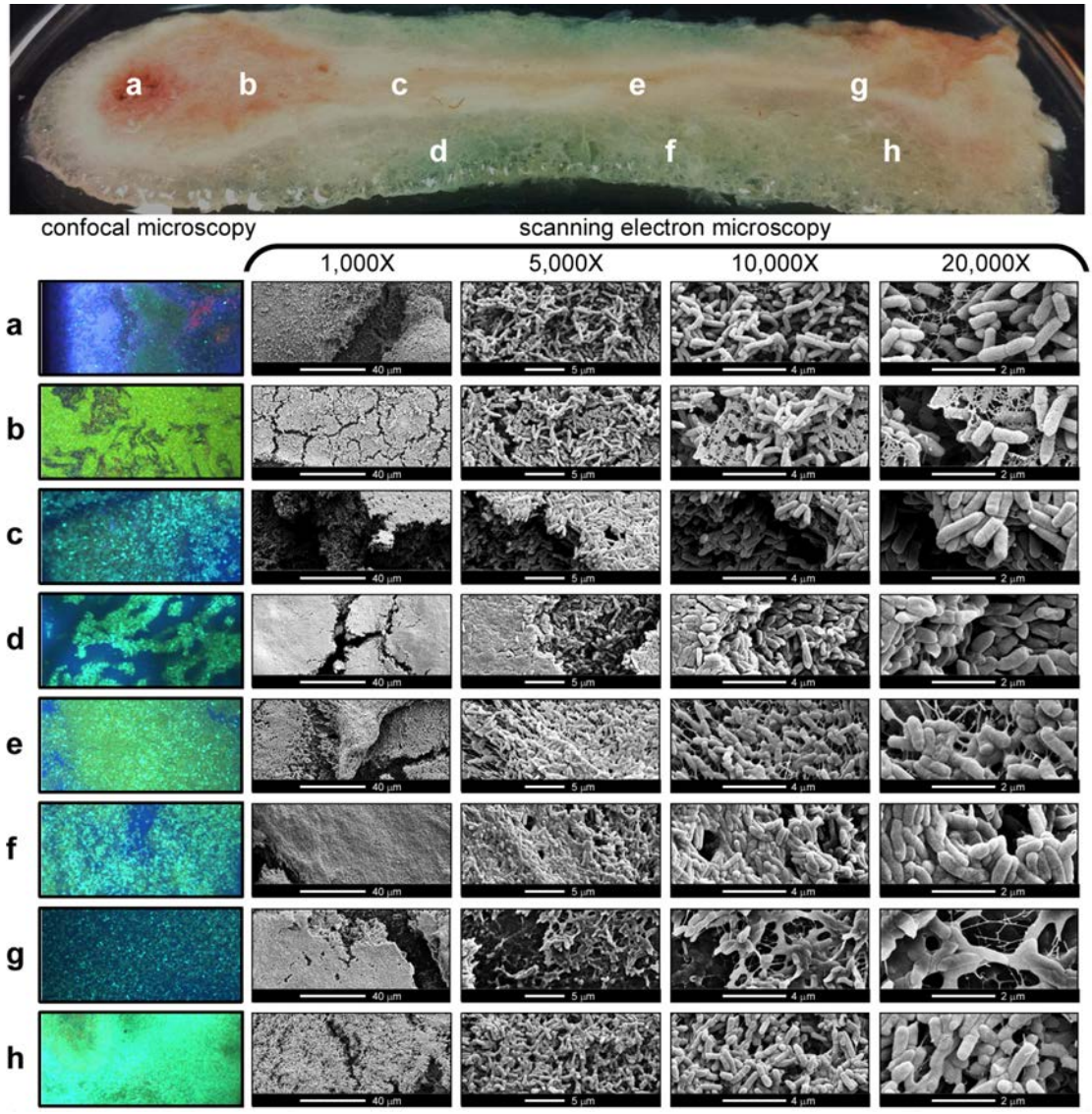

Figure 5.2: Biofilm Heterogeneity Revealed by Microscopic Analysis

Different portions of *P. aeruginosa* biofilms were analyzed by confocal and scanning electron microscopy to reveal the microscopic structural features unique to different regions of the biofilm. The letters adjacent to each picture correspond to the regions highlighted on the top biofilm image. In the confocal analysis, green stain (Syto 9) represents live cells, red stain (propidium iodide) denotes dead cells, and blue stain (calcofluor white) highlights carbohydrate-rich features. The electron micrograph images of each biofilm are shown at four different magnifications. Reprinted from Nature Communications, vol 7, Wakeman and Moore et al, from "The innate immune protein calprotectin promotes Pseudomonas aeruginosa and Staphylococcus aureus interaction" 2016 with permission from Nature Publishing Group under a Creative Commons license.[29]

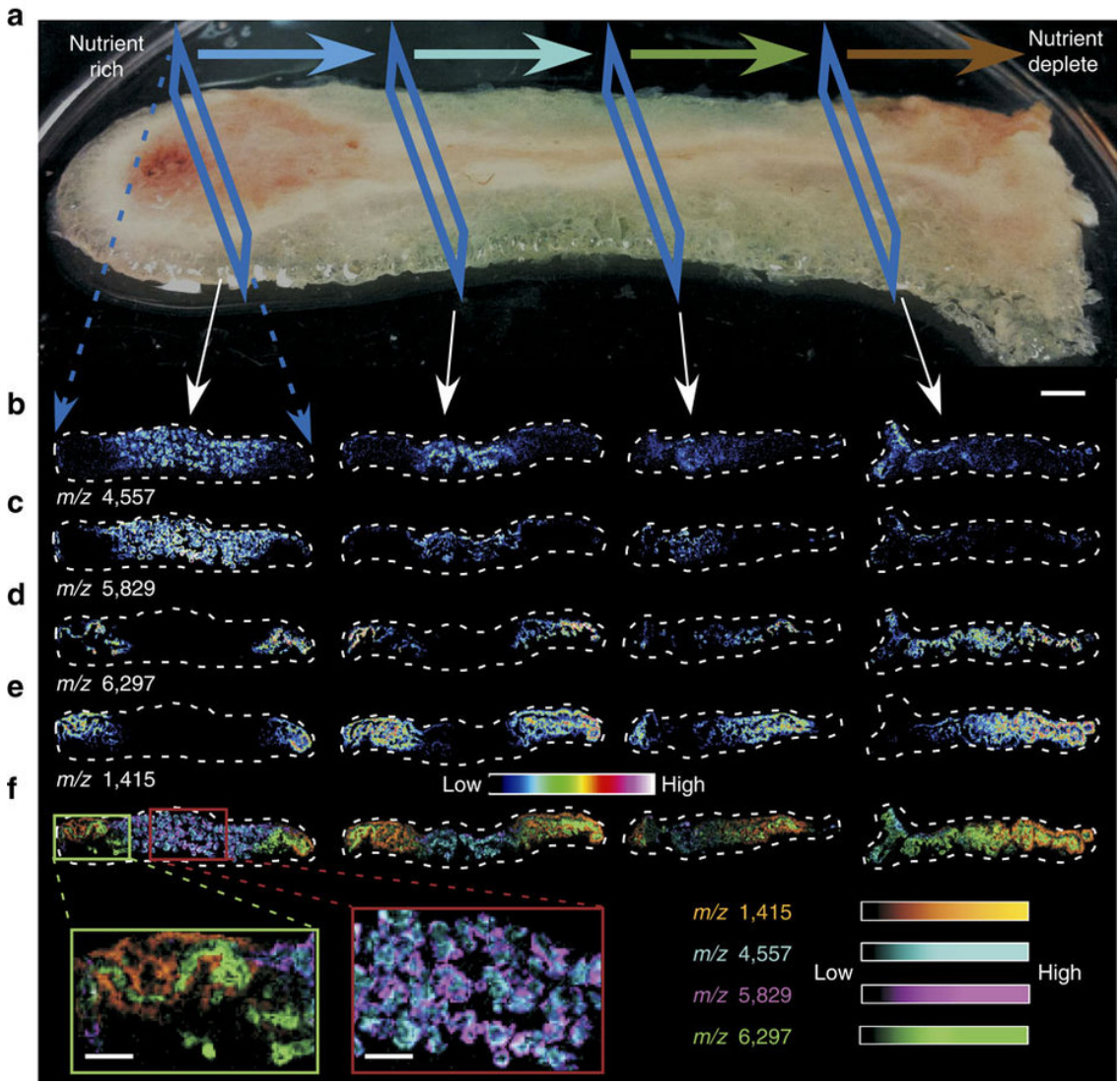

Figure 5.3: Heterogeneous structure of a *Pseudomonas aeruginosa* biofilm grown in a drip flow reactor (DFR)

(a) Representative image of a *P. aeruginosa* biofilm grown in a DFR. The flow of nutrients is depicted by the topmost arrows ranging in color from blue to brown. Blue boxes denote the approximate regions from which 12 µm thick sections were obtained for MALDI IMS analysis. (b-c) MALDI IMS signals with differential biofilm localization found primarily in portions of the biomass presumed to be nutrient-replete. (d-e) MALDI IMS signals primarily localized to portions of the biomass predicted to be nutrient-deplete. (f) Overlay of signals shown in b-e highlighting sublocalization of signals within the predicted nutrient-replete and nutrient-deplete niches with zoomed insets highlighted. Scale bar = 3 mm . . Reprinted from Nature Communications, vol 7, Wakeman and Moore et al, from "The innate immune protein calprotectin promotes Pseudomonas aeruginosa and Staphylococcus aureus interaction" 2016 with permission from Nature Publishing Group under a Creative Commons license.[29]

As nutrients are introduced to the chamber and flow towards the waste, access to fresh media is reduced. Many molecules that were abundant in biofilm sections proximal to the influx of nutrients were virtually absent in distal sections. This is displayed in Figure 5.3B and 5.3C. Other ions, like those in Figure 5.3D and 5.3E, exhibit a reciprocal ion intensity map. These molecules are relegated to the edges of the presumably nutrient-poor regions and are enriched in the distal portions of the biomass. When differentially-expressed *m/z* signals were overlaid, there were distinct subpopulations within the nutrient-rich and nutrient-deplete portions of the biofilm, indicating MALDI IMS is capable of uncovering biofilm heterogeneity extending beyond that intuitively dictated by nutrient gradients. These data are shown in Figure 5.3F. Intricate details in biofilm architecture revealed by MALDI IMS include a heterogeneous population of cells within the central channel (*m/z* 4,557 and 5,829,) and the nutrient-deplete edges (*m/z* 1,415 and 6,297). Figure 5.4 shows additional signals from MALDI IMS data with surprising localization patterns. A small population of cells residing at the interface of the central channel and nutrient-deplete edges was also isolated (*m/z* 9,731). Additional signals were found primarily at the air-exposed surface of the biofilm while others were only present deep within the portions of the biomass adhered to the glass slide. These trends in biofilm heterogeneity may be influenced by oxygen availability as oxygen might not efficiently diffuse throughout the ~3 mm thick biomass (*m/z* 5,867 and 11,701, Figure 5.4). This finding is consistent with similar results identifying differential gene expression within anoxic regions of biofilms.[174, 186, 194] In total, these results demonstrate that MALDI IMS is a useful tool to study biofilm heterogeneity, capable of determining the spatial localization of hundreds of proteins in a single experiment.

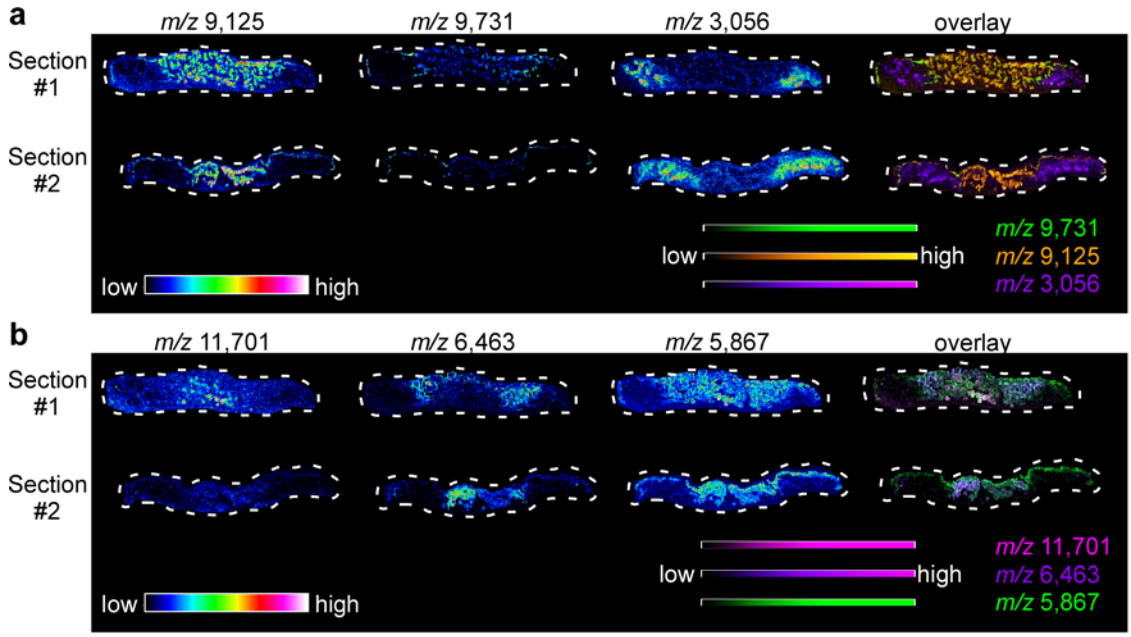

Figure 5.4: Additional Heterogeneously-expressed Signals Revealed by MALDI IMS
Biofilm sections #1 and #3 represent the two sections most proximal to nutrient entry highlighted in Figure 5.1. (a) A peak at *m/z* 9,731is enriched at the interface between the nutrient-replete center (marked by *m/z* 9,126) and the nutrient-deplete edge (marked by *m/z* 3,056.) (b) A peak at *m/z* 11,701 is found only in the anoxic portion of the most nutrient-deplete biofilm section, whereas a peal at *m/z* 6,463 which localizes with nutrient-replete regions of the biomass is excluded from the anoxic portion. A peak at *m/z* 5,867 is found abundantly throughout the nutrient rich portions of the biofilm but appears further enriched at the oxygen-exposed surface. Reprinted from Nature Communications, vol 7, Wakeman and Moore et al, from "The innate immune protein calprotectin promotes Pseudomonas aeruginosa and Staphylococcus aureus interaction" 2016 with permission from Nature Publishing Group under a Creative Commons license.[29]

MALDI IMS analysis of replicate biofilms revealed numerous ions with consistent and reproducible patterns within the biomass. These *m/z* species were targeted for identification using bottom-up proteomics approaches. Initial identification strategies revealed a number of small ribosomal proteins, RpmC, RpmD, and RpsP, are either enriched in the central channel or the putatively nutrient-deplete edge of the biofilm (Figure 5.5). Ribosomal proteins can be regulated in response to Zn levels[195]; therefore, it is possible these ribosomal proteins are differentially-regulated in response to nutrient gradients occurring within the biomass. Proteins of unknown

function, including the proteins PA14_19610 and PA14_50750, as well as proteins related to general stress, such as cold shock protein Csp were also identified. Additionally, general metabolic proteins were detected, including cytochrome cbb oxidase CcoQ and DNA-binding protein HupB. Many of these signals appeared to be distributed relatively evenly throughout the biomass with subtle decreases in signal intensity in the biofilm edge, likely attributed to decreased cell density in regions with limited nutrient access. These results demonstrate MALDI IMS signals can be identified using bottom-up proteomic approaches.

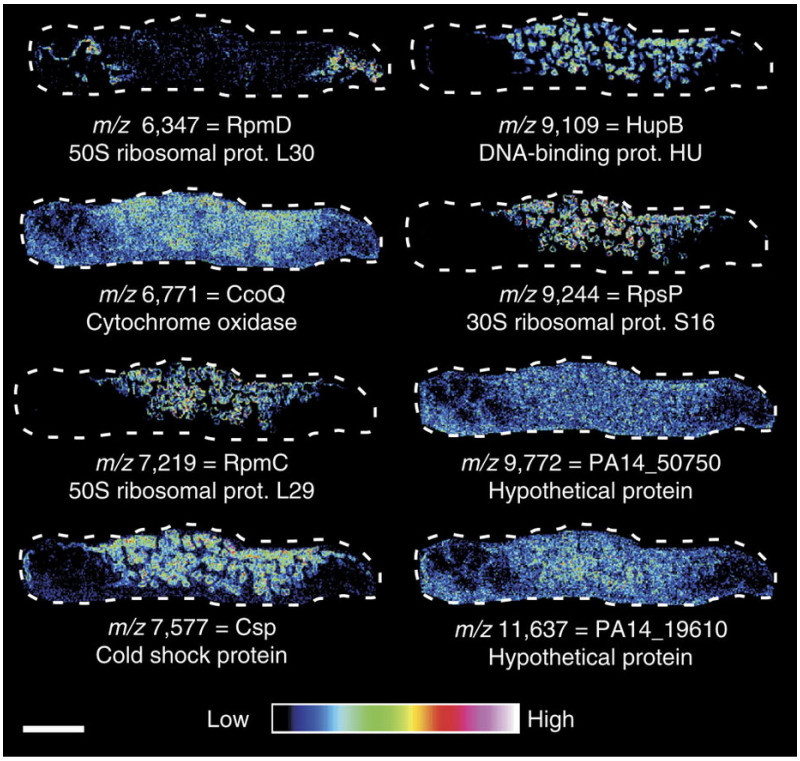

Figure 5.5: MALDI IMS signals identified using bottom-up proteomics.
m/z values and associated protein designations are included adjacent to MALDI IMS images of the biofilm section proximal to the nutrient pore highlighted in Fig. 1. These identifications derive from signals that were reproducibly detected during the analysis of 15 replicate DFR biofilms. . Reprinted from Nature Communications, vol 7, Wakeman and Moore et al, from "The innate immune protein calprotectin promotes Pseudomonas aeruginosa and Staphylococcus aureus interaction" 2016 with permission from Nature Publishing Group under a Creative Commons license.[29]

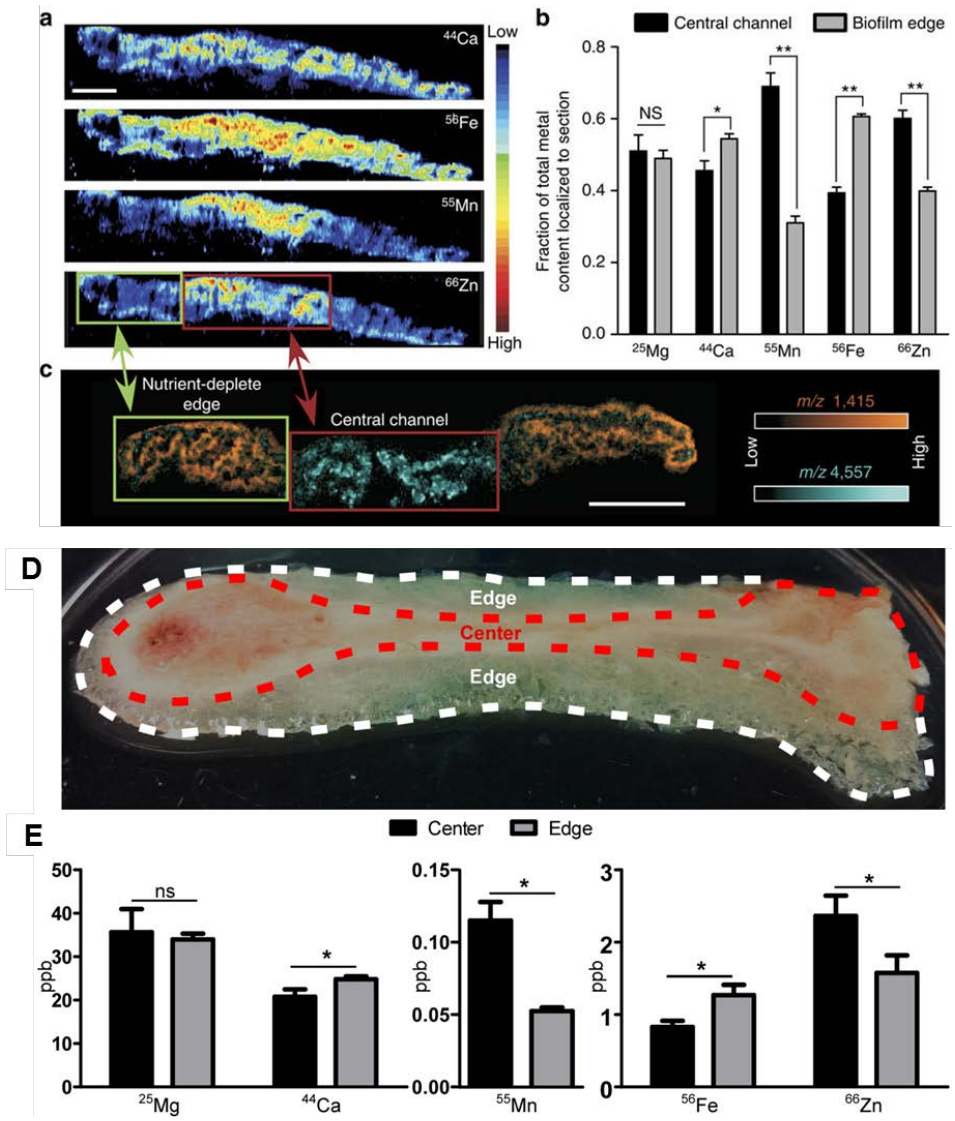

Figure 5.6: Metal Distribution Patterns Revealed by LA-ICP IMS Correlate with Differential Protein Localization within the Biofilm.

(a) LA-ICP IMS analysis of a biofilm section containing a defined "central channel" and "nutrient-deplete edge." (b) ICP-MS quantification of metal levels within distinct portions of the biofilm. Error bars represent s.d. of data derived from triplicate biofilms. * designates $p<0.05$, ** designates $p<0.002$ as determined by a Student's *t*-test. (c) MALDI IMS analysis highlights the presence of differential protein distribution patterns that follow similar trends to the metal localization patterns. (d) shows approximate section dissected from DFR biofilms for analyses. (e) Raw ICP-<S data acquired from triplicate DFR biofilms. Biofilm homogenates were normalized to total protein content prior to analysis by ICP-MS. Error bars represent SD of triplicate samples. Reprinted from Nature Communications, vol 7, Wakeman and Moore et al, from "The innate immune protein calprotectin promotes Pseudomonas aeruginosa and Staphylococcus aureus interaction" 2016 with permission from Nature Publishing Group under a Creative Commons license.[29]

Calprotectin Alters Nutrient Availability in Bacterial Biofilms

Alterations in metal availability have been shown to influence overall biofilm architecture.[180, 181] In an effort to determine which metals are restricted in the nutrient-deplete edges of the *P. aeruginosa* DFR biofilm, a section of biomass was analyzed using LA-ICP IMS. This analysis revealed that not all metals were equally depleted within the biofilm edges. Zn and Mn were found in low levels in the biofilm edge; however, Fe and Ca were distributed throughout the biomass as displayed in Figure 5.6A. To verify that the visibly distinct edges of the *P. aeruginosa* biofilm corresponded to regions experiencing Zn and Mn deprivation, the nutrient-deplete edges of the DFR biofilm were dissected away from the central channel. Separated regions are shown in in Figure 5.6D. These samples were homogenized, digested, and subjected to ICP-MS analysis to determine total metal concentration, revealing that the nutrient-deplete edges of the DFR biofilm indeed correspond to areas of low Zn and Mn levels. Figure 5.6 B shows metal levels adjusted to total protein content. Figure 5.6E shows raw values, in ppb. Interestingly, when the measured metal concentrations were adjusted to total protein content of the sample, an apparent increase in Fe and Ca was observed in the biofilm edge. These metal localization patterns correspond well with regions of differential protein production (Figure 5.6C). These results indicate nutrient metals differentially diffuse throughout the bacterial biomass.

Proteomic Analysis of Biofilms Reveals Changes in Proteome Due to Nutrient Limitation

The dissected biofilm samples from Figure 5.6D were submitted for bottom-up proteomic analysis to augment the MALDI IMS studies and to identify overall protein changes that occur in response to the nutrient metal-depletion found in the biofilm edge. Overall, the detected proteins in the biofilm edge and central channel were largely similar with several distinct changes in

abundance (data available online using the Pride Repository PXD004081). One trend of note was the suppression of several well-studied biosynthetic enzymes of *P. aeruginosa* in the nutrient-deplete biofilm edge, shown in Figure 5.7. The *hcn*, *phz*, and *pqs* genes control production of hydrogen cyanide, pyocyanin, and alkyl hydroxyquinilones (AQs), respectively. Each of these molecules has antimicrobial capabilities that enable *P. aeruginosa* to outcompete surrounding bacterial species.[196] *S. aureus*, an organism commonly found in polymicrobial infections involving *P. aeruginosa*, is particularly susceptible to these products. These biosynthetic operons are regulated by quorum sensing (QS).[197]

However, overall QS capabilities were not inhibited in the biofilm edge as the QS-activated enzyme LasA was dramatically up-regulated in this niche while other QS-regulated proteins, such as RmlC, were unchanged throughout the biomass (Figure 5.7). In addition to QS-based regulation, the anti-staphylococcal activity of *P. aeruginosa* is increased under Fe-limiting conditions.[182] However, in the Zn and Mn-limited portion of the biofilm, *P. aeruginosa* appears to repress the production of these factors. The repression of anti-staphylococcal factor production in the biofilm edge contrasts with other proteins known to be activated under Fe-limitation such as the pyoverdine receptor FpvA[198] which was enriched in the biofilm edges, or the Fe-regulated succinate dehydrogenase SdhA[199] which was constitutively detected throughout the biomass (Figure 5.7). Because FpvA was enriched and HcnB, PhzS, and PqsB were repressed in a Zn and Mn-deplete yet Fe-replete portion of the biofilm, it is possible that a subset of characterized Fe-regulated genes is responsive to multiple metal ions.

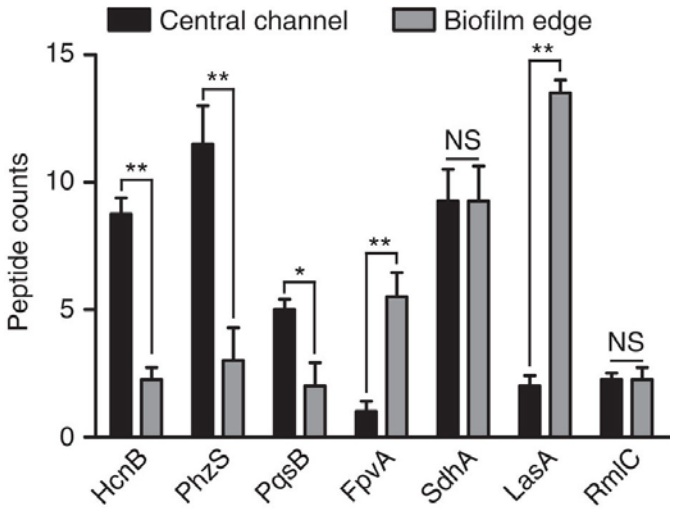

Figure 5.7: Bottom-up Proteomics Reveals Repression of Anti-staphylococcal Biosynthetic Proteins

HcnB, PhzS and PqsB are components of various anti-staphylococcal biosynthetic pathways that were found in lower abundance in the biofilm edge. While expression of the corresponding genes has been shown to be both Fe and quorum sensing (QS)-regulated, the proteins' distribution profiles did not correlate with those of known Fe-responsive proteins such as FpvA and SdhA or proteins encoded by known QS-responsive genes such as LasA and RmlC. Error bars are s.e.m. derived from biological triplicate samples processed in four technical replicates per biofilm. '*' denotes $P<0.05$, '**' denotes $P<0.02$ as determined by a Student's t-test. NS, not significant. Reprinted from Nature Communications, vol 7, Wakeman and Moore et al, from "The innate immune protein calprotectin promotes Pseudomonas aeruginosa and Staphylococcus aureus interaction" 2016 with permission from Nature Publishing Group under a Creative Commons license.[29]

Calprotectin Causes a Repression in P. aeruginosa Anti-Staphylococcal Factors

To determine which of the various genetic changes observed in the nutrient-deplete biofilm edge can be specifically attributed to Zn and/or Mn deprivation, *P. aeruginosa* biofilms were treated with calprotectin to induce Zn and Mn starvation throughout the biomass and to recapitulate conditions the biofilm might encounter within a vertebrate host. Calprotectin is an abundant innate immune protein with antimicrobial activity deriving from its ability to sequester transition metals away from invading pathogens.[65, 140] Proteomic analyses indicated that calprotectin diffusion

throughout the biomass was incomplete, likely owing to the protective features of the biofilm (Figure 5.8A). This was also shown with MALDI IMS data, shown in Figure 5.8B. Here a calprotectin-treated and untreated biofilm were both analyzed. Several ions did not change despite treatment with calprotectin. Calprotectin itself clearly does not fully penetrate the biofilm when administered in a DFR. However, these studies identified a subset of differentially-localized proteins that were constitutively expressed or repressed throughout the biofilm upon calprotectin treatment (Figure 5.9). This subset of proteins, which included many of the anti-staphylococcal biosynthetic enzymes, may represent the targets most responsive to calprotectin-induced metal starvation. However, the incomplete diffusion of calprotectin throughout the biomass indicated there may be additional calprotectin-dependent responses undetected in this experiment. Therefore, we sought to determine if these metal-dependent responses could be recapitulated in planktonic culture.

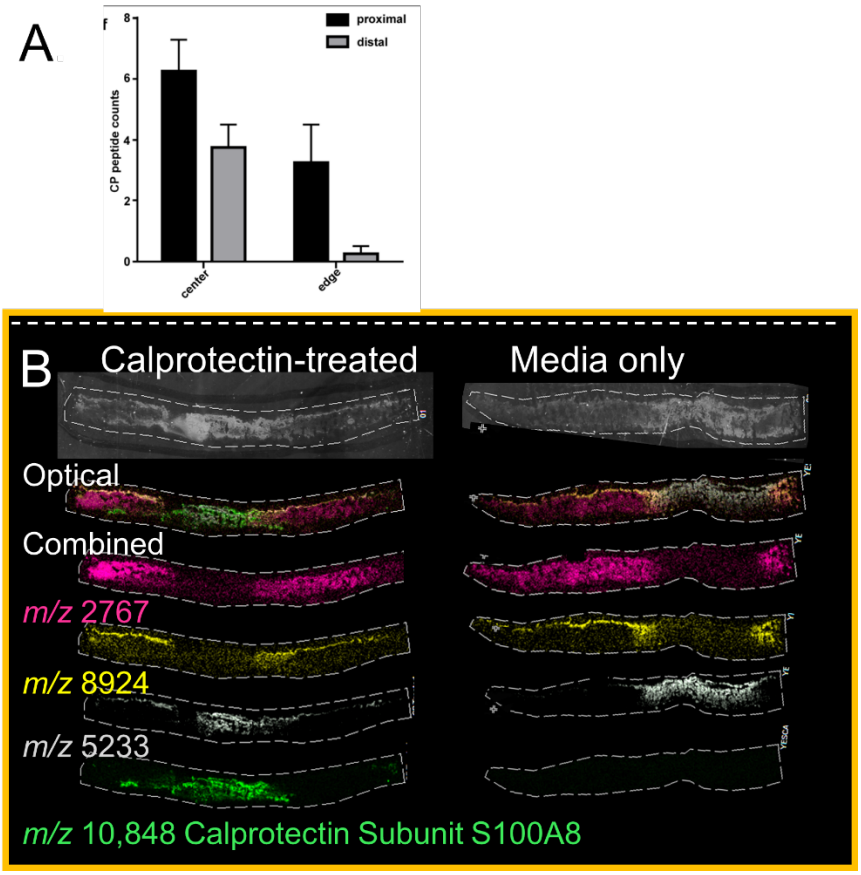

Figure 5.8: Calprotectin does not Penetrate the DFR Biofilms

The protective nature of the biofilm does not allow calprotectin to fully penetrate the biofilm. A. shows peptide counts taken from the center and edge of DFR biofilms both proximal and distal to the nutrient pore, which represents the point of treatment. Panel B explores a series of ion intensity maps in section 3 of both a calprotectin-treated and untreated biofilm. Several ions did not change due to calprotectin. The ion intensity map of calprotectin subunit S100A8 is also displayed to show that the biofilm is not fully exposed to the protein.

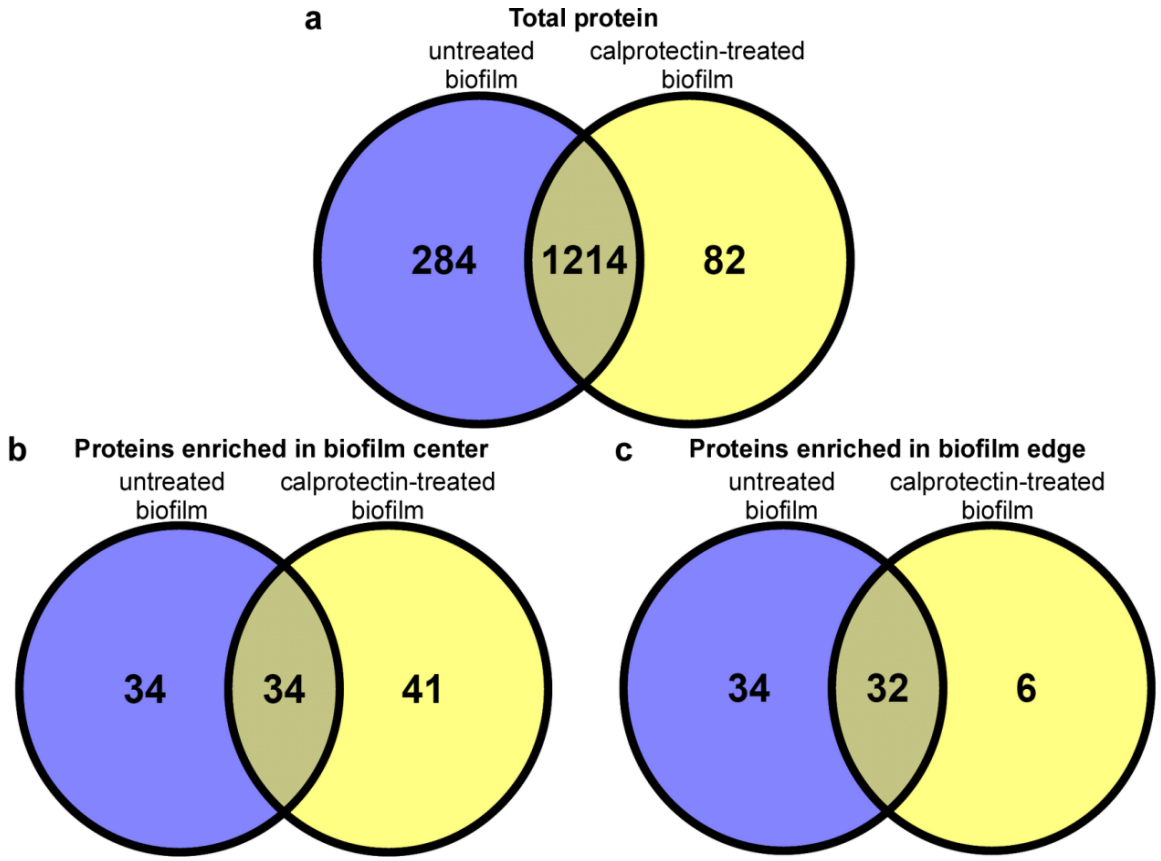

Figure 5.9: Venn Diagram Summary of Shotgun Proteomics Data

(a) The total number of protein identified from shotgun proteomics of untreated and calprotectin-treated biofilms reveals that the bulk of proteins in both data sets are identical. (b) Approximately half of the proteins found to be enriched in the central channel of untreated biofilms were also enriched in the central channel of calprotectin-treated biofilms. (c) Approximately half of the proteins found to be enriched in the edge of the untreated biofilms were also enriched in the edge of the calprotectin-treated biofilm. Reprinted from Nature Communications, vol 7, Wakeman and Moore et al, from "The innate immune protein calprotectin promotes Pseudomonas aeruginosa and Staphylococcus aureus interaction" 2016 with permission from Nature Publishing Group under a Creative Commons license.[29]

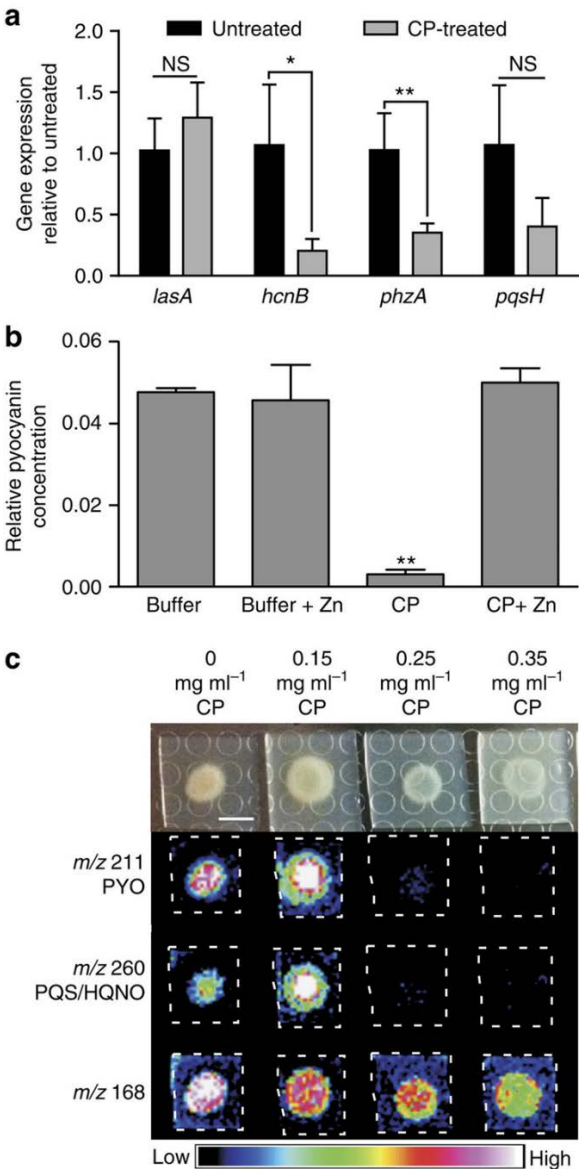

Figure 5.10: Calprotectin (CP)-treatment Represses P. aeruginosa Biosynthetic Genes Responsible for Production of Numerous Anti-staphylococcal Factors

(a) qRT-PCR quantification of anti-staphylococcal biosynthetic gene transcripts in the presence or absence of 0.25 mg/mL CP. (b) Quantification of pyocyanin in cultures grown in the presence or absence of 0.25 mg/mL CP and/or 10 µM Zn. * designates $p<0.05$, ** designates $p<0.002$ as determined by a Student's t-test. Error bars represent s.d. of triplicate samples. (c) MALDI IMS detection of secondary metabolites, pyocyanin (PYO) and the alkyl hydroxyquinolones PQS and HQNO, as well as a control ion at m/z 168 on media embedded with increasing CP concentrations. Reprinted from Nature Communications, vol 7, Wakeman and Moore et al, from "The innate immune protein calprotectin promotes Pseudomonas aeruginosa and Staphylococcus aureus interaction" 2016 with permission from Nature Publishing Group under a Creative Commons license.[29]

RNA-seq analysis of planktonic cultures grown in the presence or absence of calprotectin revealed additional metal-dependent genetic responses. qRT-PCR quantification of anti-staphylococcal biosynthetic gene expression revealed significant repression of pyocyanin and hydrogen cyanide biosynthetic genes upon calprotectin exposure in planktonic culture with trends towards decreasing levels of PQS biosynthetic gene expression (Figure 5.10A). The unchanging levels of *lasA* transcription provided evidence that these responses did not result from decreased QS capacity of the culture. These transcriptional responses corresponded with a dramatic reduction in pyocyanin production that was reversed by the addition of exogenous Zn to the cultures (Figure 5.10B). The metal-dependent regulation of anti-staphylococcal secondary metabolites was also visualized using MALDI IMS of bacteria grown on agar plates infused with increasing levels of calprotectin. MALDI IMS identified signals with *m/z* ratios corresponding to pyocyanin and the AQs, PQS and 4-hydroxy-2-heptylquinoline-*N*-oxide (HQNO), which decreased with increasing calprotectin concentrations (Figure 5.10C). These signals were confirmed to be pyocyanin and HQNO/PQS as they were absent in strains with mutations in these biosynthetic operons (Figure 5.11, A-C). In total, these data demonstrate that calprotectin-induced metal deprivation significantly reduces anti-staphylococcal factor production under multiple growth conditions in both biofilm and planktonic states.

Calprotectin Promotes P. aeruginosa *and* S. aureus *Co-culture*

The biological impact of the metal-dependent regulation of *P. aeruginosa* anti-staphylococcal factors was tested in co-culture experiments with *S. aureus* under multiple types of growth conditions. In agar-based assays, a lawn of *S. aureus* cells was plated onto the surface of LB agar infused with either calprotectin or calprotectin-free buffer, and *P. aeruginosa* culture was

spotted onto discs positioned on the agar surface (Figure 5.12A). On calprotectin-free medium, a characteristic zone of clearance in the staphylococcal lawn formed around *P. aeruginosa*. However, in the presence of calprotectin, this zone of clearance was dramatically diminished. In a titration of calprotectin concentrations, maximal inhibition of *P. aeruginosa* anti-staphylococcal activity was shown to occur in the presence of 0.25 mg/mL calprotectin on both agar plates and in liquid culture. This supported the idea that calprotectin might promote the interactions between *S. aureus* and *P. aeruginosa.*

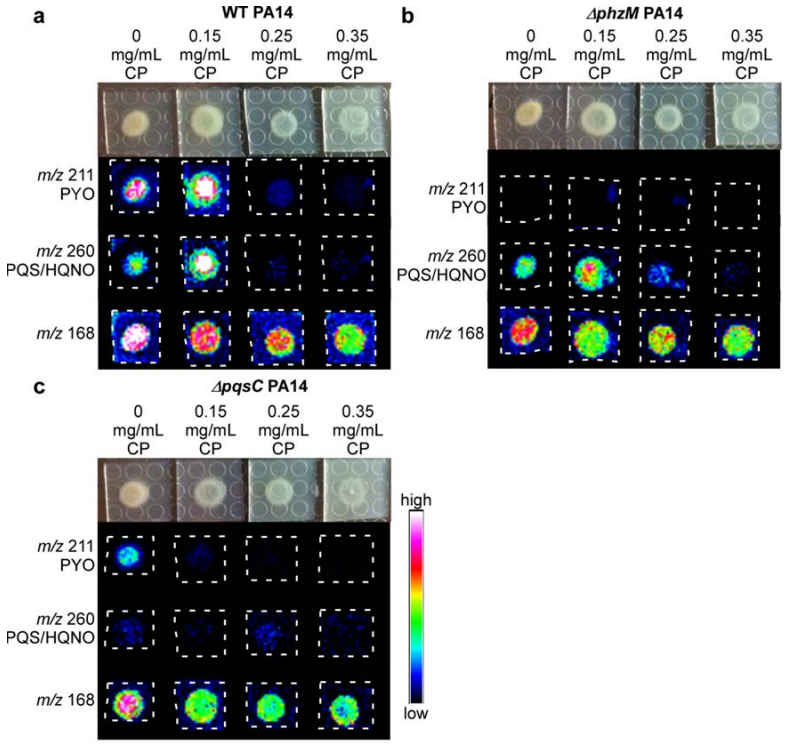

Figure 5.11: MALDI IMS Comparison of WT PA14 and Biosynthesis Mutants
(a) MALDI IMS detection of secondary metabolites, pyocyanin (PYO) and the alkyl hydroxyquinolones PQS and HQNO, as well as a control ion at *m/z* 168 in media embedded with increasing calprotectin (CP) concentrations. (b) A Δ*phzM* mutant on PA14 in unaffected in PQS/HQNO production as well as *m/z* 168. However, PYO signal is completely absent. (c) A Δ*pqsC* mutant of PA14 exhibits only background signal at the PQS/HQNO peak and also produces decreases levels of PYO because PYO levels are regulated by PQS levels. Reprinted from Nature Communications, vol 7, Wakeman and Moore et al, from "The innate immune protein calprotectin promotes Pseudomonas aeruginosa and Staphylococcus aureus interaction" 2016 with permission from Nature Publishing Group under a Creative Commons license.[29]

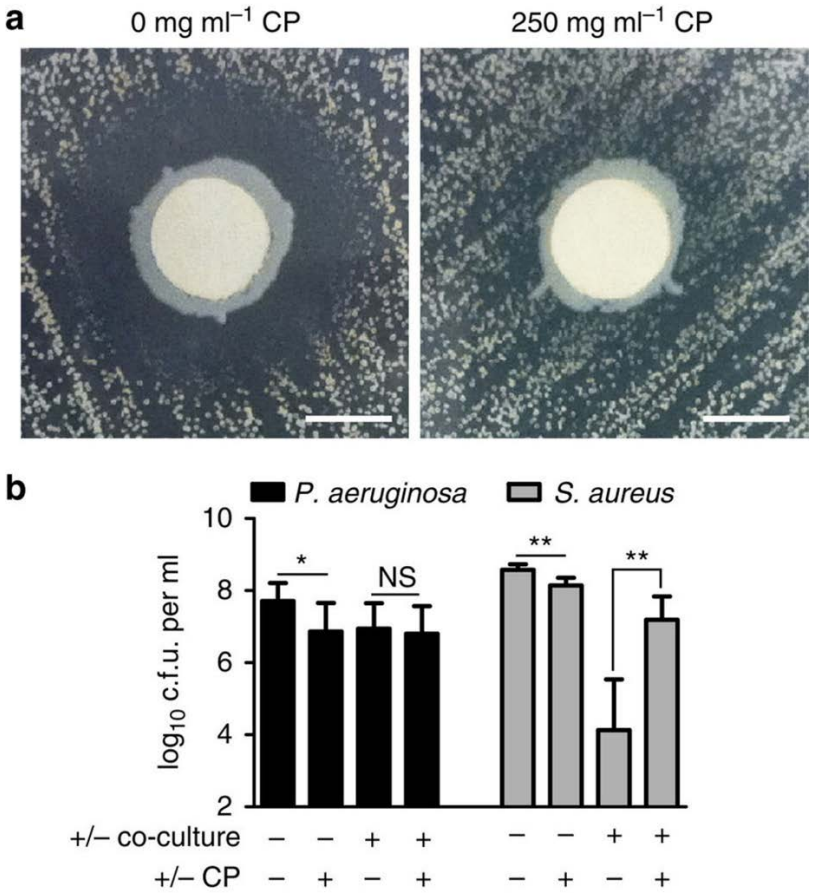

Figure 5.12: Calprotectin (CP) exposure promotes microbial interaction between *P. aeruginosa* and *S. aureus*

(a) Staphylococcal zones of inhibition on LB agar plates with or without the addition of CP. Lawns of *S. aureus* were spread onto plates and *P. aeruginosa* cultures were spotted onto paper disks. Zones of inhibition were visualized after 24 hours of incubation. Scale bars = 5 mm. (b) Colony forming units (cfus) obtained after liquid growth with or without 0.25 mg/mL CP. Error bars represent s.d. of replicate experiments from nine separate days. Experiments were performed in biological triplicate on each day. * designates $p<0.02$, ** designates $p<0.0002$ as determined by a Student's *t*-test. Reprinted from Nature Communications, vol 7, Wakeman and Moore et al, from "The innate immune protein calprotectin promotes Pseudomonas aeruginosa and Staphylococcus aureus interaction" 2016 with permission from Nature Publishing Group under a Creative Commons license.[29]

Co-Colonization is promoted in Diseases Hallmarked by Long-term Inflammation

Because calprotectin-treatment promoted microbial co-culture between *P. aeruginosa* and *S. aureus* under a variety of *in vitro* growth conditions, it seemed possible that this phenomenon might also occur upon calprotectin exposure experienced during infection. In order to test whether or not calprotectin production can promote the establishment of polymicrobial infections, calprotectin-deficient mice were obtained. Co-infections in these mice were compared to co-infections occurring in wildtype C57BL/6 mice, the parental background from which the calprotectin-deficient mouse strain was derived.[200] When calprotectin-deficient mice were intranasally inoculated with equal numbers of *P. aeruginosa* and *S. aureus*, *P. aeruginosa* outcompeted *S. aureus* by 38 hours post infection. However, when wildtype C57BL/6 mice were infected with the same inoculum, equivalent numbers of *P. aeruginosa* and *S. aureus* were present at 38 hours post infection (Figure 5.13). These data demonstrate that the presence of calprotectin can promote co-colonization of the murine lung.

While cystic fibrosis patients commonly become infected with both *P. aeruginosa* and *S. aureus*, it is unknown whether these organisms share common niches within the human lung or remain segregated from each other within specific pulmonary compartments. Optical images were obtained from a human cystic fibrosis lung explant known to be chronically co-infected with *P. aeruginosa* and *S. aureus*. The images revealed that bacteria with morphological and Gram-staining features consistent with *P. aeruginosa* and *S. aureus* occupied the same airspace within the diseased lung (Figure 5.14A). The portion of the lung that housed the polymicrobial infection exhibited a high degree of inflammation as determined by H&E staining as well as an associated accumulation of calprotectin as visualized by MALDI IMS (Figure 5.14B and C). Calprotectin accumulation was monitored by following the signal at *m/z* 10,836 indicative of the

S100A8 subunit of calprotectin.[201] These results strongly indicate that *P. aeruginosa* and *S. aureus* interactions can occur within a diseased lung and confirm that calprotectin is abundantly present at sites of inflammation and polymicrobial infection within the lungs of patients with cystic fibrosis.

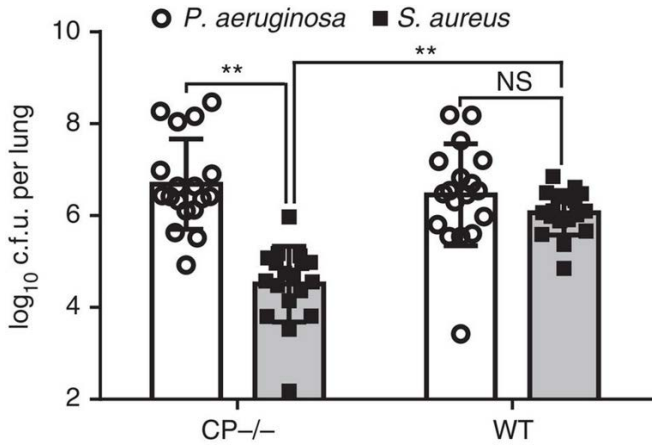

Figure 5.13: Calprotectin Production During Infection of the Murine Lung Promotes S. aureus and P. aeruginosa Co-colonization.

Wild-type (WT) or calprotectin-deficient (CP−/−) C57BL/6 mice were intranasally infected with equivalent amounts of *P. aeruginosa* and *S. aureus*. Bacterial burdens were enumerated 38 h post infection. Equivalent burdens of *P. aeruginosa* were obtained from both mouse strains. In WT mice, *S. aureus* levels were equivalent to the *P. aeruginosa* burden. However, in mice lacking calprotectin production, *P. aeruginosa* significantly outcompeted *S. aureus* during the course of infection. '**' designates P<0.0000001 as determined by a Student's t-test. Error bars represent s.d. of data that was replicated in two independent experiments performed on separate days. n=18 mice (shown as individual dots or squares) for both WT and CP−/− groups. NS, not significant. . Reprinted from Nature Communications, vol 7, Wakeman and Moore et al, from "The innate immune protein calprotectin promotes Pseudomonas aeruginosa and Staphylococcus aureus interaction" 2016 with permission from Nature Publishing Group under a Creative Commons license.[29]

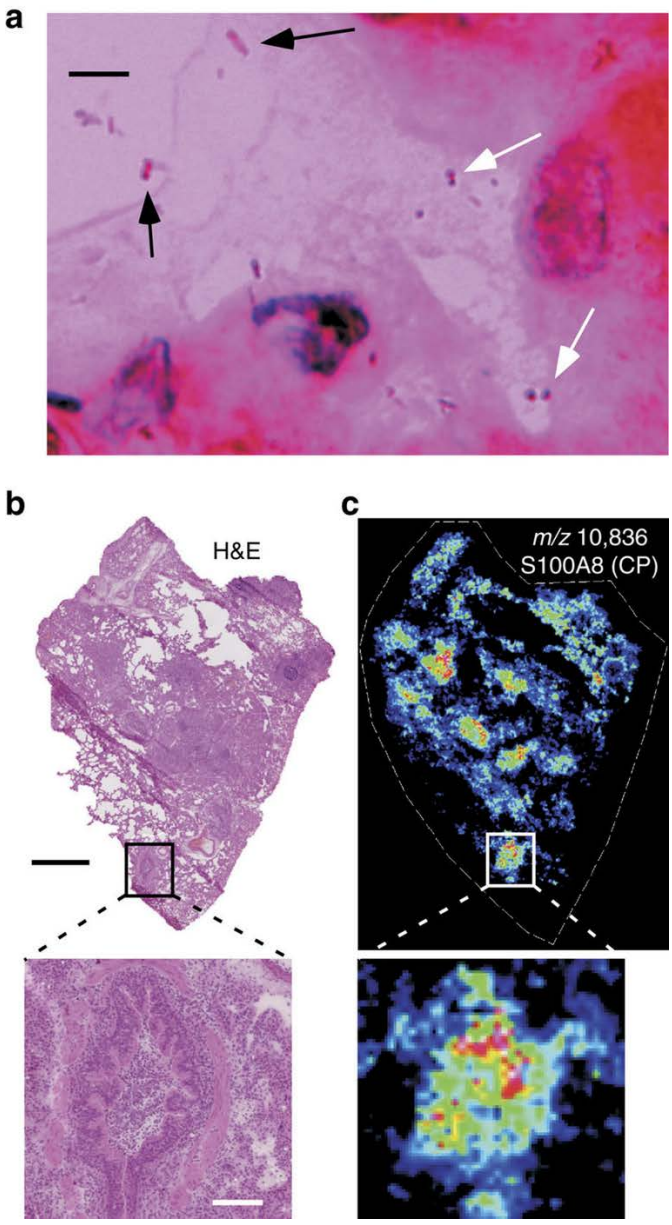

Figure 5.14: Polymicrobial Communities Exist within Calprotectin-replete Airways of a Cystic Fibrosis Lung Explant

(a) Gram-stain of an inflamed airspace of a cystic fibrosis lung explant containing bacterial morphologies consistent with both *S. aureus* (white arrows) and *P. aeruginosa* (black arrows). Scale bar, 5 μm. (b) H&E histology of the cystic fibrosis lung explant with the inflamed airspace that was visualized by Gram-stain enlarged (inset). Black scale bar, 2 mm; inset white scale bar, 200 μm. (c) MALDI IMS analysis of the lung explant reveals calprotectin-enrichment at inflammatory foci (inset). Reprinted from Nature Communications, vol 7, Wakeman and Moore et al, from "The innate immune protein calprotectin promotes Pseudomonas aeruginosa and Staphylococcus aureus interaction" 2016 with permission from Nature Publishing Group under a Creative Commons license.[29]

Cystic Fibrosis Lung Biopsies are Highly Heterogeneous

High-speed MALDI-TOF IMS protein data collected from human lung tissue from a cystic fibrosis patient is shown in Figure 5.15. Data were collected with the same experimental parameters as the previously described rat brain tissue imaging experiment. Figure 5.15A shows overlaid IMS data from the individual ions highlighted in Figure 5.15B-F. High spatial resolution (10 μm) MALD-TOF IMS data (Figure 5.15G) highlight the extreme spatial heterogeneity of the sample. Protein identifications were made based on mass accuracy from secondary MALDI FTICR IMS experiments (Data not shown). Hemoglobin subunit alpha (residues 2-142), is depicted in orange at *m/z* 15,145 and, aside from the airways, is observed throughout the lung. Hemoglobin is involved in oxygen transport from the lung to other cells in the body. Therefore, it is reasonable that this ion marks the majority of the lung cells. The observed ion at *m/z* 11,339 (dark blue) was determined to be Histone H4. Histones are abundant proteins involved in gene regulation. In addition, they protect DNA from damage by keeping non-transcriptionally active DNA tightly bound. Histone H4 was observed at higher abundance surrounding infected airways. This is likely to be associated with a change in cell density, as the areas around these airways show an increase in immune cell recruitment. S100A6 (calcyclin) was detected at *m/z* 10,095 (yellow), representing residues 2-90 with an acetylation. It is known to be found in higher concentrations when cells are under mechanical strain.[190] Here the protein is localized to large airways within the lung parenchyma, which supports previous work that such cells are sensitive to changes in mechanical force.[202] This could be a factor in breathing difficulties when airways are infiltrated with immune cells in cystic fibrosis patients. S100A8 was found to be spatially localized primarily within infected airways. S100A8, depicted in teal at *m/z* 10,846, is a subunit of the neutrophil-associated protein calprotectin. Neutrophilic recruitment to airways is a characteristic of cystic fibrosis.

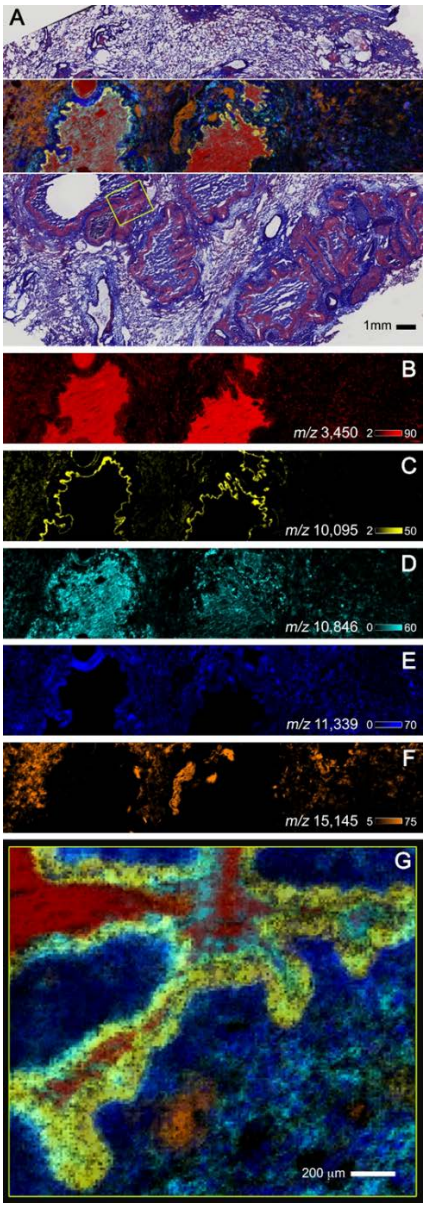

Figure 5.15: Cystic Fibrosis Lung Tissue is Heterogeneous

Selected ion images of human lung tissue from a cystic fibrosis patient collected using ultra-high speed MALDI-TOF IMS. Observed substructures in the overlaid 30 µm ion image of m/z 3,450 (neutrophil defensin 1, red), m/z 10,095 (S100A6, yellow), m/z 10,846 (S100A8, teal), m/z 11,339 (histone H4, blue) and m/z 15,145 (hemoglobin subunit alpha, orange) were consistent with the trichrome staining following IMS acquisition (A). To highlight the spatial diversity of the selected proteins, individual images of each ion are shown in (B-F). High spatial resolution (10 µm) MALD-TOF IMS data were collected from the area outlined in yellow (G). Reprinted with permission from Spraggins, Rizzo, Moore *et al.* "Next-Generation Technologies for Spatial proteomics: Integrating Ultra-High Speed MALDI-TOF and High Mass Resolution MALDI FTICR Imaging Mass Spectrometry for Protein Analysis." *Proteomics*, 2016, Reprinted with Permission from John Wiley and Sons.[2]

Calprotectin was originally isolated from cystic fibrosis patients and was later found to have extensive antimicrobial properties through the chelation of nutrient metals. Neutrophil defensin 1 (*m/z* 3,450, red) is an abundant antibacterial peptide involved in host innate immune defense. This protein is rich in lysine and arginine residues whose cationic properties contribute to the disruption of microbial membranes, aiding in the killing of pathogens. This analysis revealed how heterogeneous this tissue is, especially with the marked additional pathology of late-stage lung disease. Taken into consideration, this heterogeneity strengthens the idea that there are many niches for bacteria to occupy within host tissues.

Polymicrobial Infections and Cystic Fibrosis

The finding that *P. aeruginosa* can repress its anti-staphylococcal capacity in the presence of an abundant innate immune protein adds to the growing body of literature describing the role of the host environment in shaping the physiology of polymicrobial communities. Previous studies have described host and microbial factors that contribute to the switch from *S. aureus*- to *P. aeruginosa*-dominated infections that occur during the lifetime of many cystic fibrosis patients.[184, 203] The current manuscript provides insight into the impact of the host environment on the physiology of the stable *P. aeruginosa* and *S. aureus* co-infections that develop in a large population of cystic fibrosis patients. In total, these data provide an additional facet to the complex interactions occurring at the host-pathogen interface during chronic infection.

P. aeruginosa and *S. aureus* co-infections are associated with diseases characterized by high levels of inflammation and subsequent calprotectin accumulation such as chronic wound infection and the highly diverse morphology of pulmonary infection in cystic fibrosis patients.[204-206] Therefore, the finding that *P. aeruginosa* can dampen its anti-staphylococcal activity in

response to calprotectin-induced Zn starvation may have clinical implications regarding the common occurrence of *P. aeruginosa* and *S. aureus* co-infections. This response is surprising given that, under conditions of starvation, it would be advantageous to inhibit the growth of competing organisms. Therefore, an alternative evolutionary explanation for the development of this behavior must exist. One theory originates from the fact that *S. aureus* has acquired numerous mechanisms to counteract endogenous host defenses.[207] The infection course of cystic fibrosis patients typically begins with *S. aureus* colonization of the lung prior to infection with *P. aeruginosa*, hinting that *P. aeruginosa* might benefit from initial seeding of the lung environment with *S. aureus.* [208] Therefore, it is possible that over the course of chronic infection, *P. aeruginosa* might find it evolutionarily advantageous to maintain a population of *S. aureus* to combat the host immune response. These findings could have clinical ramifications owing to the unique physiology, antibiotic resistance, and disease severity associated with polymicrobial communities. [209, 210]

Imaging Mass Spectrometry Defines Microbial Subpopulations

Through the application of MALDI IMS, we were able to identify many different subpopulations within the microbial structure. Because the host environment at infectious foci is known to contain low levels of bioavailable Zn and Mn, the study of the populations arising within the Zn and Mn-deplete regions of the biomass may provide insight into the physiology of *P. aeruginosa* at the host-pathogen interface.[211, 212] Additionally, MALDI IMS enabled the identification of subpopulations within the nutrient-replete portions of the biomass as well as populations with no apparent correlation with nutrient gradients. Further study of each of these populations will expand our knowledge of biofilm architecture and provide insight into the

functionality of subpopulations in response to various environmental pressures. These studies complement previous research that has utilized MALDI IMS to explore molecular interactions occurring at the interface of competing microbial communities.[213, 214]

In total, these data demonstrate that the application of MALDI IMS and LA-ICP-IMS to the study of microbial community structure will further our understanding of the process of differentiation within a clonal population as well as enable studies into the role of nutritional gradients in the development of polymicrobial communities. The identification of multiple subpopulations and numerous differentially expressed proteins and small molecules in bacterial biofilms using MALDI IMS is a testament to the power of this technology for the study of microbial community structure as well as the analysis of sample heterogeneity in general. Future applications of MALDI IMS towards the study of biofilm architecture may uncover additional bacterial subpopulations, provide insight into the functionality of these populations, and reveal novel factors driving biofilm differentiation.

Methods

Bacterial Strains, Infections, and Clinical Samples

The *Pseudomonas aeruginosa* strain used in this study was the highly virulent human wound isolate PA14.[215] The transposon insertion mutants targeting *phzM* and *pqsC* were part of a transposon mutant library derived from this parental background.[216] The *Staphylococcus aureus* strain used was USA300 JE2 [217], a laboratory adapted strain derived from the parental USA300 strain isolated from a skin and soft tissue infection. [218]

All animal experiments were approved by the Vanderbilt Institutional Animal Care and Use Committee. The co-infection of mice was performed similarly to previously published procedures for acute polymicrobial pneumonia.[219] C57BL/6 mice were obtained from Jackson Laboratories. Calprotectin-deficient ($S100A9^{-/-}$) mice derived from a C57/BL6 background were a gift from Wolfgang Nacken (Institute of Experimental Dermatology, University of Münster, 48149 Münster, Germany). Nine-week-old male mice were intranasally infected as previously described [220] using 30 µL of a PBS suspension containing $1x10^6$ CFU of both *P. aeruginosa* and *S. aureus*. Infections were allowed to progress for 38 hours prior to organ harvest. Bacterial colonies were enumerated following organ homogenization and plating on both TSA and MSA agar.

Human lungs were obtained for research purposes from a patient with cystic fibrosis and end-stage lung disease at the time of lung transplantation. Informed consent was obtained and the protocol was approved by the Vanderbilt University Institutional Review Board.

Wild type and mutant calprotectin was expressed and purified as described previously. [65, 221]

Growth and Processing of Biofilms for IMS

Biofilms were grown in a Drip Flow Biofilm Reactor (DFR) (BioSurface Technologies, Bozeman, MT) similarly to previously described methods [193] using glass microscope slides as the growth surface. Glass microscope slides (VWR #48300-025) were treated overnight with filtered adult bovine plasma containing Na-EDTA (Lampire Biological Laboratories, Pipersville, PA) diluted to 20% concentration in carbonate-bicarbonate buffer and placed into the Drip Flow Reactor (DFR) chambers. Individual chambers were inoculated with 10 mL of a 1:10 dilution of

an overnight bacterial culture grown in YESCA medium (10 g/L casamino acids; 1 g/L yeast extract). Cultures were incubated statically for 18 hours at 37 °C before waste lines were opened and the chamber was tilted at a 10° angle to promote drainage of waste medium. Fresh YESCA medium was continuously supplied over the course of 6 days through the action of a peristaltic pump at a flow rate of ~0.3 mL/minute/chamber while incubation continued at 37 °C. At the end of the 6-day incubation, biofilms adhered to slides were removed from the DFR chambers and washed twice in 20 mL of Milli-Q water prior to subsequent processing. For calprotectin treatment of DFR biofilms, nutrient lines were detached after 5.5 days of incubation and replaced with lines containing calprotectin-treatment media (60% YESCA, 40 mM NaCl, 1.2 mM $CaCl_2$, 0.5 mM β-mercaptoethanol, 8 mM Tris, pH 7.5, and 0.25 mg/mL calprotectin). The calprotectin-treatment media was supplied to the biofilms over the course of 12 hours at a flow rate of ~0.3 mL/minute/chamber.

Biofilms to be cryosectioned were frozen in 25% Optimal Cutting Temperature Polymer (Tissue-Tek, SakuraFinetek, Torrance, CA). Biofilms analyzed by bottom-up proteomics and ICP-MS were frozen in Milli-Q water. Biofilms were sectioned at -20°C using a Leica CM 3050 S Cryostat (Leica Microsystems, Bannockburn, IL) or a Thermo Scientific Cryostar NX70 (Thermo Fisher Scientific, Waltham, MA). Sections for MALDI IMS were cut at a thickness of 12 µm and mounted onto chilled indium-tin oxide coated glass slides (Delta Technologies, Loveland, CO.) Sections prepared for LA-ICP IMS were cut at a thickness of 35 µm and mounted onto nitric-acid washed poly(L)lysine-coated vinyl slides (Electron Microscopy Sciences, PA).

MALDI IMS of Biofilm Sections

Biofilm sections analyzed by MALDI IMS were washed using sequential 30 second washes of 70, 90, and 95% ethanol. Matrix was applied as previously described for the agar colonies using only 8 total passes of the robotic sprayer. IMS of biofilms was performed at 50 µm step size using a rapifleX™ MALDI Tissuetyper™ operated in linear positive ion mode with 50 by 50 µm pixels with the laser in single beam mode. A total of 500 laser shots were collected per pixel in 50 shot increments. IMS of biofilms collected at greater than 50 µm step size was performed using an AutofleX Speed tandem time-of-flight (TOF/TOF) mass spectrometer (Bruker Daltonics, Billerica, MA) outfitted with a Gaussian beam profile Nd:YAG laser (355 nm) and operated in linear positive ion mode. A total of 50 laser shots were collected in random-walk mode at each pixel. Data were processed using fleXimaging version 4.1.

Protein Identification from MALDI IMS Data

Proteins of interest, selected based on unique *m/z* distributions in MALDI IMS experiments, were further purified by reversed-phase HPLC for identification. Protein extracts from the center and edge regions of the biofilm (Figure 5.8) were selected for protein fractionation. These samples were fractionated using a Waters 2690 Separations Module equipped with an offline fraction collector. Proteins were fractionated using a Vydak 208TP 150 mm 5 µm C8 column (Vydac Grace, Columbia, Maryland) and an aqueous to organic gradient over 120 minutes. Fractions were collected every minute. The separation was performed twice and fractions were combined. Fractions were dried using a Speedvac Concentrator and reconstituted in 30 µL of 40% acetonitrile. One µL of each well was spotted onto a MALDI anchor chip for analysis by MALDI MS. Wells containing proteins of interest were isolated and further fractionated onto Novex 16%

Tricine gels (Invitrogen, Carlsbad, CA) and stained using SimplyBlue SafeStain. Gel bands corresponding to the mass range of interest were extracted and subjected to in-gel reduction, alkylation, and tryptic digestion. The resulting peptides were sequenced as described below.

Peptide Sequencing for Protein Identification from MALDI IMS data

Peptides were sequenced using an Orbitrap Fusion Tribrid Mass Spectrometer (Thermo Scientific) coupled to an Easy-nLC 1000 (Thermo Fisher Scientific) ultrahigh pressure liquid chromatography (UHPLC) system. Peptides were separated on a 75 µm inner diameter, 25 cm long PepMap RSLC C18 column (2 µm, 100 Å, Acclaim) at a flow rate of 300 nL/min using mobile phases of 0.1% formic acid, 99.9% water (solvent A) and 0.1% formic acid, 99.9% acetonitrile (solvent B). The gradient consisted of 2-20%B in 100 min, 20-32%B in 20 min, 32-95%B in 1 min, 95%B for 4 min, 95-2%B for 2 min, and the column equilibrated at 2%B for 3 min. Upon gradient-elution, peptides were ionized via nanoelectrospray ionization using a Nanospray Flex ion source (Thermo Fisher Scientific). The instrument was operated in a 3 second top speed data-dependent acquisition mode, where precursor ions were selected for a maximum 3 second cycle. Fourier transform Mass Spectra (FTMS) were collected at 120,000 resolution using an automated gain control (AGC) target of 200,000 and a maximum injection time of 50 ms. Precursor ions were filtered according to charge state (9> z >1 required) and monoisotopic precursor assignment. Previously interrogated precursor ions were excluded using a dynamic window (30 s ± 10 ppm). Precursor ions for MS/MS analysis were isolated with a 1.5 *m/z* quadrupole mass filter isolation window. Precursor ions were fragmented with higher energy dissociation (HCD) using a normalized collision energy of 35%. Ion trap MS/MS spectra were acquired using an AGC target of 1,000 and maximum injection time of 40 ms. Data analyses were

performed using Protalizer software (Vulcan Analytical, Birmingham, AL). Spectra were searched against the *Pseudomonas aeruginosa* strain UCBPP-PA14 UniProt database using a target FDR of 1%. Searches were performed using a 20 ppm MS1 tolerance and a ±0.6 Da MS2 tolerance while allowing for up to 2 missed cleavages as well as carbamidomethyation, phosphorylation, and oxidation modifications.

Processing and Analysis of DFR Biofilms by Proteomics

Biofilms selected for bottom-up proteomics experiments were dissected into central channel and nutrient-deplete edge regions (Figure 5.6) and further dissected into four replicates prior to processing. Each region of biofilm was moved to a 15 mL conical tube for lysis and protein extraction. Cells were lysed using 1 mL of 80% Acetonitrile 5% Formic acid and 400 µL of Bacterial Protein Extraction Reagent (BPER) (Thermo Scientific, Rockford, IL). Biofilms were homogenized using an ultrasonicator dismembrator Model 150E (Fisher Scientific). Protein was quantified using a Bradford Assay (Thermo Scientific, Rockford, IL). Twenty-five µg of protein was removed from each sample, dried using a speedvac concentrator (Thermo Scientific), reconstituted in sample buffer, and loaded onto a 10% Novex Bis-Tris Gel (Invitrogen, Carlsbad, CA) with MES Running Buffer. Samples were run into the gel at 200 V for 5 minutes and stained using SimplyBlue^{TM} SafeStain (Invitrogen, Carlsbad, CA). Stained gel bands were removed and subjected to in-gel reduction, alkylation, and tryptic digestion. The resulting peptides were analyzed by data-dependent LC-MS/MS analysis as described below.

LC-MS/MS Analysis for Bottom-up Proteomics of PA14 Biofilms

Peptides were autosampled onto a 200 mm by 0.1 mm self-packed analytical column (Jupiter 3 µm, 300A) coupled directly to an LTQ (Thermo Scientific, Waltham, MA) using a nanoelectrospray source**.** Peptides were eluted over a 70 minute aqueous to organic gradient. A full scan mass spectrum followed by 5 data-dependent tandem mass spectra (MS/MS) was collected with enabled dynamic exclusion to minimize the acquisition of redundant spectra. Tandem mass spectra were searched using SEQUEST against the PA14 database containing both forward and reversed versions for each entry (UniProt *Pseudomonas aeruginosa* strain UCBPP-PA14, taxon 208963 reference proteome set). Identifications were filtered and compiled at the protein level using Scaffold 4 (Proteome Software) with a 5% FDR and 2 minimum peptide threshold. Differences in peptide enrichment in the biofilm center versus the biofilm edge were assessed using a three step process. First, peptides of interest were identified by assessing the peptide counts obtained from center-derived samples versus edge-derived samples and determining a statistically-significant enrichment in a biofilm compartment using a Student's *t*-test comparing the four technical replicates of a single run. Secondly, this statistically-significant peptide enrichment needed to be maintained in replicate biofilms in order for the protein of interest to make the final cut-off. Finally, the averaged peptide counts of all replicate biofilm edge and center samples needed to be significantly enriched in one of these compartments in order to be included in data, which is available at http://www.ebi.ac.uk/pride/archive/projects/PXD004081.

Processing and Analysis of Trace Metal in Biofilms by ICP-MS

Trace metals were quantified from homogenates extracted for bottom-up proteomic analysis. Samples were diluted to 10 µg of protein in 100 µL protein extraction buffer and moved

into 15 mL metal-free conical tubes (VWR, USA). Samples were digested with nitric acid by adding one milliliter of 50% HNO_3 (Optima grade; Fisher) to the 100 µL sample and incubating at 50°C for 18 hours with caps loosened. After digestion, samples were diluted to a 10-mL final volume in Milli-Q water. Five parts per billion Ga was included in each sample as an internal standard. Elemental quantification of these samples was performed on the ELEMENT 2™ inductively coupled plasma mass spectrometer (Thermo Fisher Scientific, Bremen, Germany) coupled with an ESI autosampler (Elemental Scientific, Omaha, NE). The ICP-MS was equipped with a PFA microflow nebulizer (Elemental Scientific, Omaha, NE), a double channel spray chamber (at room temperature), a magnetic sector followed by an electric sector, and a second electron multiplier. The sample uptake was achieved through self-aspiration via 0.50 mm ID sample probe and sample capillary which then introduced samples to the ICP-MS for the detection of isotopes of $^{25}Mg^+$, $^{44}Ca^+$, $^{55}Mn^+$, $^{56}Fe^+$, $^{66}Zn^+$, and $^{69}Ga^+$.

Processing and Analysis of Trace Metal in Biofilms by LA-ICP-IMS

Trace element imaging was performed using an LSX-213 laser ablation system (LA, CETAC, Omaha, USA) coupled with ELEMENT 2™ inductively coupled plasma mass spectrometer (Thermo Fisher Scientific, Bremen, Germany). Slide-mounted slices of biofilm were placed in a sealed ablation cell and ablated in multi-line mode (line-by-line) with a focused Nd:YAG laser beam with a spot size of 100 µm. The ablated sample particles were then online introduced to ICP-MS for the detection of isotopes of $^{44}Ca^+$, $^{55}Mn^+$, $^{56}Fe^+$, and $^{66}Zn^+$.

Analysis of Biofilms by Microscopy

Bacterial biofilms were grown as described above and analyzed by either scanning electron microscopy or confocal laser scanning microscopy as previously described.[222] Briefly, for electron microscopy, samples were fixed with 2.0% paraformaldehyde (Electron Microscopy Sciences, Hatfield, PA), 2.5% gluteraldehyde (Electron Microscopy Sciences) in 0.05 M sodium cacodylate (Electron Microscopy Sciences) buffer for 24 hours. After primary fixation, samples were washed three times with 0.05 M sodium cacodylate buffer before sequential dehydration with increasing concentrations of ethanol. After dehydration, samples were dried at the critical point using a Tousimis Critical Point Dryer machine, mounted onto aluminum SEM sample stubs (Electron Microscopy Sciences), and sputter-coated with 5 nm of gold-palladium. Afterward, samples were painted with a thin strip of colloidal silver (Electron Microscopy Sciences) at the edge to facilitate charge dissipation. Biofilms were imaged with an FEI Quanta 250 field-emission gun scanning electron microscope (Hillsboro, OR). For confocal microscopy, samples were stained with LIVE/DEAD® *Bac*Light™ bacterial viability kit which includes both Syto 9 (green) and propidium iodide (red) (Life Technologies, Carlsbad, CA) to visualize bacterial cells and calcofluor white (blue) (Sigma-Aldrich) to visualize carbohydrate capsule/matrix within the biofilm. Biofilms were mounted with ProLong Antifade (Life Technologies) and visualized with a Zeiss LSM 710 (Oberkochen, Germany). Images were analyzed and both ortho and 2D renderings were generated with Zen 2010 software. Micrographs shown are representative of three biological replicates.

Growth and Processing of Agar Colonies for IMS

Prior to addition of calprotectin to agar-based growth medium, the medium was cooled to 50°C. Agar-based co-culture assays were performed on LB agar embedded with appropriate calprotectin concentrations as mentioned in the text or the equivalent volume of calprotectin buffer (100 mM NaCl, 3 mM $CaCl_2$ 10 mM β-mercaptoethanol, 20 mM Tris, pH 7.5). A lawn of *S. aureus* was established on the media surface by spreading a 1:1000 dilution of an overnight culture onto solidified media using sterile cotton swabs. Sterile discs were placed on the agar surface and inoculated with 5 µL of a 1:1000 dilution of an overnight *P. aeruginosa* culture. Plates were incubated at 37 °C for 24 hours.

Agar colonies for MALDI IMS were grown on modified ISP2 agar medium (5 g/L proteose peptone #2; 3 g/L yeast extract; 3 g/L casamino acids; 10 g/L glucose; 20 g/L agar) similarly to previously described methods.[223] The medium was supplemented with appropriate calprotectin concentrations as mentioned in the text or an equivalent volume of calprotectin buffer. Ten-milliliters of medium were used per 100 mm by 15 mm petri dish to create a thin layer of growth medium that is more optimal for subsequent MALDI IMS. Two microliters of a 1:1000 dilution of an overnight *P. aeruginosa* culture were spotted onto solidified medium and plates were incubated at 37 °C for 24 hours prior to MALDI IMS.

Bacterial colonies were excised from the petri dish as previously described [223] and methanol soft-landed onto a Bruker 384-well stainless steel target. A mixture of 15 mg/mL 2,5-dihydroxybenzoic acid (*DHB*) and 5 mg/mL α-cyano-4-hydroxycinnamic acid (CHCA) was prepared in 90% acetonitrile with 0.2% trifluoroacetic acid and sonicated until crystals were fully dissolved. Matrix was applied to sample sections using a TM-Sprayer (HTX Imaging, Carrboro, NC). The matrix was sprayed onto the sections at a flow rate of 0.2 ml/min using a pushing solvent

of 90% acetonitrile. The TM-Sprayer was operated at a speed of 1200 mm/min and at a nozzle temperature of 80°C. The spray pattern was set to 2 mm spacing and 12 passes were applied. IMS of metabolites was collected in reflector positive ion mode on an AutofleX Speed mass spectrometer (Bruker Daltonics, Billerica, MA) at 400-micron spatial resolution. Fifty laser shots were acquired per pixel in random walk mode in 10 shot steps. Data were processed using flexImaging version 4.1.

Processing of Cystic Fibrosis Patient Lung Explants

Human lungs were obtained for research purposes from a patient with cystic fibrosis and end-stage lung disease at the time of lung transplantation. Informed consent was obtained and the protocol was approved by the Vanderbilt University Institutional Review Board. The right upper lobe was sectioned and frozen in 50% Optimal Cutting Temperature Polymer (Tissue-Tek, SakuraFinetek, Torrance, CA). The lung was sectioned at 10 μm thickness using a Leica CM 3050 S Cryostat (Leica Microsystems, Bannockburn, IL) and serial sections were prepared as follows: (i) stained with hematoxylin and eosin (H&E), (ii) Gram stained, and (iii) sectioned for MALDI IMS. Optical images of H&E stained lungs were obtained at 20x magnification using a Leica SCN400 Brightfield Slide Scanner. For MALDI IMS analysis, biopsies from explanted cystic fibrosis lung tissues were mounted onto chilled indium-tin oxide coated glass. Tissue was sequentially washed as follows: 70% ethanol for 30 seconds, 100% ethanol for 30 seconds, 6:2:1 ethanol:chloroform:acetic acid for 2 minutes, 100% ethanol for 30 seconds, water for 30 seconds, and 100% ethanol for 30 seconds.[224]

MALDI Imaging Mass Spectrometry of cystic fibrosis lungs

A solution of 15 mg/mL 2,5-dihydroxyacetphenone (*DHA*) was prepared in 90% acetonitrile with 0.2% trifluoroacetic acid and sonicated until crystals were fully dissolved. Matrix was applied to washed sample sections using a TM-Sprayer (HTX Imaging, Carrboro, NC). The matrix was sprayed onto the sections at a flow rate of 0.2 ml/min using a pushing solvent of 90% acetonitrile. The TM-Sprayer was operated at a speed of 1200 mm/min and at a nozzle temperature of 80°C. The spray pattern was set to 2 mm spacing and 6 passes were applied. The matrix coating was rehydrated using 1 mL of 50 mM acetic acid in a sealed petri dish at 85°C for 3 minutes. IMS was performed using a rapifleX™ MALDI Tissuetyper™ (Bruker Daltonics, Billerica, MA). The instrument was operated in linear positive ion mode with 50 by 50 µm pixels with the laser in single beam mode. A total of 500 laser shots were collected per pixel in 50 shot increments.

High-throughput and spatial resolution imaging experiments were performed using a rapifleX MALDI Tissuetyper (Bruker Daltonics, Billerica, MA, USA). The instrument is equipped with a Smartbeam 3D 10kHz Nd:YAG (355nm) laser. The instrument is capable of rapidly generating IMS data from discrete square pixels by moving the laser and the stage independently. This enables the stage to be moved continuously while the laser scans the full area of each pixel. All images were collected using the single spot laser setting (~5 µm) with a pixel scan size of 30 µm or 10 µm in both x and y dimensions. For protein analysis data were collected in positive ion mode from *m/z* 2,000 – 20,000 and each pixel consisted of an average of 300 laser shots. 30 µm ion images of rat brain and human lung tissue sections consisted of 144,682 and 140,772 pixels respectively. 10 µm ion images of rat brain and human lung tissue sections consisted of 24,218 and 29,236 pixels respectively. Lipid imaging data was collected in negative

ion mode from *m/z* 600 – 1,000 with 200 laser shots averaged per pixel. 10 μm lipid images of human lung tissue sections consisted of 1,015,083 pixels.

High-mass resolution imaging experiments were performed using a 15T Bruker SolariX MALDI FTICR mass spectrometer (Bruker Daltonics, Billerica, MA, USA). The instrument is equipped with an Apollo II dual MALDI/ESI ion source and a Smartbeam II 2kHz Nd:YAG (355nm) laser. All images were collected using the small laser setting (~50 μm) with a pixel spacing of 100 μm in both x and y dimensions. Data were collected from *m/z* 1,100 – 25,000 with a data size of 1MB per spectrum. Special tuning of the Funnel RF amplitude (250 Vpp), accumulation hexapole (1.4 MHz, 1950 Vpp), transfer optics (1 MHz, 380 Vpp), time-of-flight delay (2.8 ms), and ICR cell (Sweep excitation power: 48%) were required for high *m/z* analysis. External calibration was performed prior to analysis using CsI clusters. Ion images consisted of 13,596 pixels and 14,632 pixels for rat brain and ccRCC samples respectively. FlexImaging 4.1 (Bruker Daltonics, Billerica, MA, USA) was used to visualize ion images.

In vitro co-culture

P. aeruginosa and *S. aureus* mono-cultures were grown overnight in glucose-supplemented low nutrient broth (GLNB) (2 g/L tryptic soy broth; 2 g/L glucose) at 37 °C with shaking at 180 rpm. The next morning, cultures were metal-restricted by pelleting and suspending samples in Chelex 100-treated GLNB supplemented with 100 μM $CaCl_2$ and 1 mM $MgCl_2$. These cultures were grown at 37 °C with shaking at 180 rpm for 2 hours. Cultures were then pelleted, suspended in fresh metal-restricted GLNB, and grown for an additional 2 hours to produce metal-limited samples. Co-culture assays were performed in 96-well plates containing 150 μL of co-culture media (60% TSB; 40% calprotectin buffer [100 mM NaCl, 3 mM $CaCl_2$, 10 mM β-

mercaptoethanol, 20 mM Tris, pH 7.5]). When noted, co-culture media was supplemented with WT or ΔS1ΔS2 (transition metal-binding deficient) calprotectin at specified concentrations in the presence or absence of specified metal concentrations. The 96-well plate co-cultures were seeded with 1:100 dilutions of the metal-limited *P. aeruginosa* and *S. aureus* mono-cultures and grown for 44 hours statically at 37 °C. At the completion of co-culture growth assays, samples were mixed by repeated pipetting, serially diluted in PBS, and plated onto cetrimide agar and mannitol salt agar for the enumeration of *P. aeruginosa* and *S. aureus*, respectively.

Agar-based co-culture assays were performed on LB agar embedded with appropriate calprotectin concentrations as mentioned in the text or the equivalent volume of calprotectin buffer (100 mM NaCl, 3 mM $CaCl_2$ 10 mM β-mercaptoethanol, 20 mM Tris, pH 7.5). A lawn of *S. aureus* was established on the media surface by spreading a 1:1000 dilution of an overnight culture onto solidified media using sterile cotton swabs. Sterile discs were placed on the agar surface and inoculated with 5 µL of a 1:1000 dilution of an overnight *P. aeruginosa* culture. Plates were incubated at 37 °C for 24 hours.

qRT-PCR and RNA-seq

Samples for metabolite analysis or RNA extraction were grown in calprotectin-treatment media (60% TSB, 40 mM NaCl, 1.2 mM $CaCl_2$, 0.5 mM β-mercaptoethanol, 8 mM Tris, pH 7.5) in the presence or absence of 0.25 mg/mL calprotectin and/or 10 µM $ZnCl_2$. Five milliliter cultures were grown shaking at 180 rpm for 18 hours at 37 °C. Cells were pelleted and retained for RNA extraction. Supernatants were retained for metabolite measurement. Colony forming units were plated to determine culture density.

Total RNA was harvested using a combination of LETS buffer (0.1 M LiCl; 10 mM EDTA; 10 mM Tris-HCl pH 7.4; 1% SDS) and TRI Reagent as previously described [225]. qRT-PCR was performed using SYBR green supermix (Bio-Rad) following manufacturer's instructions using the primers listed in Supplementary Table 1. RNA samples for RNA-seq were submitted to HudsonAlpha (Huntsville, AL) for ribosomal reduction, 50 bp paired-end sequencing with 12.5 million reads per sample, and subsequent data analysis. The statistical test used for this data set was a moderated *t*-test with a corrected *p* value cutoff of 0.05, asymptotic *p* value computation, and Benjamini-Hochberg multiple testing correction.

Pyocyanin measurement

Pyocyanin measurements were performed similarly to previously described methods [226]. Briefly, the pyocyanin from 1 mL of supernatant obtained from samples of equivalent cell density was extracted with 0.5 mL chloroform after vigorous mixing. The chloroform layer was subsequently acidified with the addition of 0.5 mL 0.2N HCl upon vigorous mixing and the pyocyanin was eluted to the aqueous phase. Pyocyanin concentration was calculated by measuring absorbance at 520 nm.

CHAPTER VI

CONSPECTUS

A version of the following chapter was previously published and has been adapted from Moore et al., *Current Opinion in Microbiology,* Copyright 2014 by Elsevier[1] and from Moore et al., *Proceedings of the NATO Advanced Study Institute in Rapid Threat Detection,* Copyright 2017 by Springer.[3]

Overview

This work presented many examples in which Imaging Mass Spectrometry has been used to greatly enhance our knowledge of the intricate relationship between pathogen and host. As technologies continue to advance, the application of such work flows stands to only increase our understanding of microbial pathogenesis. In this conspectus, the current state of the field and the future directions of this project are discussed.

MALDI MS and the Clinical Laboratory

MALDI MS is a maturing technology; each technological advancement yields potential to enhance the capabilities of the diagnostic laboratory. As the clinical microbial laboratory embraces more advanced analytical technologies, the potential for rapid and accurate diagnostics becomes more realistic. Rapid diagnostics are currently attainable for cultured microorganisms, but signals from pathogens directly from the host specimens are more difficult to determine. The challenges arise from both the relative low abundance of microbial proteins and the small size of most

microorganisms. The substantial technological progress in MALDI MS solidifies its future in both research and clinical settings. Rapid diagnostic capabilities could make this technology a future point-of-care testing method, guiding the approaches of physicians for antibiotic administration and treatment regimens in an era of increased antibiotic resistance. MALDI MS remains a robust and high throughput discovery tool for novel biomarkers from complex mixtures.

MALDI MS and Infectious Diseases

MALDI mass spectrometry has had broad positive impacts on the field of infectious diseases. Through microbial biotyping by matching an intact bacterial colony's spectral fingerprint to known databases, the ability to rapidly identify pathogens from culture has enabled many clinicians to rapidly provide appropriate antimicrobial intervention for patients. Appropriate antimicrobial intervention in a timely manner saves lives, particularly in cases of sepsis. In one study of Gram-negative bacteremia, MALDI TOF identification altered the course of treatment in 35% of patients in a 202 patient cohort.[227] Through the integration of this technology into the clinical workflow, a rapid and cost-effective analytical approach has had dramatic impact on human health.

This can be further extrapolated to histology-directed MALDI mass spectrometry, where histological features within tissue sections can be targeted for interrogation with a mass spectrometer. Though still in elementary stages and without FDA approval, the application of similar technologies to tissue biopsies could aid the field of histopathology as MALDI MS profiling has aided diagnostic microbiology. Future work in this field could involve targeting areas within biopsies that were suspect for microbial infection and obtaining a spectral fingerprint to identify the pathogen causing disease from directly within host tissues. Additional studies could

attempt similar analyses from body fluids, including sputum, blood samples, and other wound exudates. Though this approach would inherently have sensitivity difficulties in attempting to detect pathogenic markers from within host fluids.

Imaging Mass Spectrometry takes these experiments one step further by systematically interrogating a tissue surface to reconstruct the molecular pathology of a biopsy. This allows researchers to target not only the pathogen signals but also the changing host environment surrounding the threat, allowing for unprecedented molecular study of the pathogen-host interface. The same sensitivity issues surrounding the detection of bacterial markers in host fluids is applicable here, though this approach remains more useful for primary scientific research and not clinical applications as microbial infections rarely require tissue resection. The future benchmark for clinical microbial identification remains pathogen identification without additional culture, directly from would fluids, sputum, and blood.

Next Generation IMS

MALDI IMS instrumentation has also experienced great advancements in the last five years, further enabling such analyses. For example, laser optics can be refined to decrease the footprint of the beam, allowing high spatial resolution experiments to be possible. [228] This has even included MALDI imaging of single cells.[229-231] Next generation instrumentation is being designed to rapidly and accurately interrogate tissue at higher spatial resolution, ideal for 3D data sets.[2, 17] In these examples, throughput is maximized using continuous laser raster sampling where the laser is continuously fired while the sample stage is moved laterally to the area of interest. Although this approach can achieve high data acquisition rates (>30 pixels/s for small molecules) this sampling approach introduces complications in defining the true pixel size. More recently, a unique

approach for performing continuous sampling in a way that still maintains discrete pixels was reported. Here the sample and laser are moved simultaneously so that discrete square pixels can be scanned as the sample target moves continuously. This platform also incorporates a 10kHz laser allowing for data acquisition rates of ~50 pixels/s to be achieved.

New detector systems allow for higher molecular weight proteins to be efficiently detected directly from complex environments, including tissue.[232] Improvement in sample preparation has focused on the enhanced sensitivity and ionization of selected analytes. For example, ionic matrices have detected signals from mouse blood and urine correlating to masses of cultured bacteria in an *in vivo* model of systemic bacteremia.[233] Such ionic matrices improve the ionization of proteins and reduce spot-to-spot variation, characteristics critical for clinical diagnostics.[234] MALDI-compatible surfaces have been designed to capture bacteria from biological solutions. Bacterial signatures from 10^4 colony forming units (CFU)/mL have been detected from titanium-based chips [235]; graphene magnetic nanosheets decorated with chitosan allow detection of bacterial signatures from 10^2 CFU/mL [236]; and zirconium hydroxide immobilization followed by direct cultivation enable detection of 32 CFU/mL of *Enterococcus faecalis* spiked into milk.[237] These technological advancements have allowed tissues to be studied at extremely high spatial resolution and are important innovations to support the continued study of the pathogen-host interface. [228, 231]

In situ Analyte Identification

Both MALDI profiling and MALDI imaging approaches yield a wealth of data from tissue. A number of analyses have been able to successfully perform diagnostic assays simply by fingerprint matching. For example, it is hypothesized that most of the signatures in microbial fingerprinting from agar are actually small ribosomal proteins.[238-241] These analytical strategies

have made a large impact on clinical microbiology and the time to diagnosis and antibiotic intervention even without knowing the identities of the peaks in the classifier. Recently, the field has begun the arduous task of identifying the proteins yielding the fingerprint patterns used in classification.[238, 240] Identification of analytes that denote antibiotic resistance or increased pathogenicity has utility not only in clinical settings but also in the primary research laboratory. MALDI profiling and imaging experiments performed in the research laboratory have the potential to reveal unprecedented information about microbial pathogenesis and the pathogen-host interaction by allowing for the study of bacteria within host tissues actively causing disease.

In addition to need for identification from intact cell MALDI MS for microbial identification, there is also a great need to identify analytes from both histology-directed MS and MALDI IMS experiments. Identification of analytes that are regiospecifically localized to areas of interest is paramount to enhance our knowledge of disease, making this area of research incredibly important to the field. Some researchers have worked to increase the charge state of MALDI ions, which are generally in a 1+ or 2+ charge state. Researchers have attempted to increase the charge state of ion generated directly from tissue or profiling experiments to assist in MALDI-based fragmentation. These studies utilize supercharging matrices- matrices that generate ions with higher charge states. Alternatively, others have attempted ESI surface analysis techniques, such as desorptive electrospray ionization and laser-ablation electrospray ionization.[242, 243] These technologies suffer from low spatial resolution due to solvent spread as it directly interacts with tissue, though they do provide an attractive alternative for on-tissue analyte identification.

Organ-Specific Variation in Pathogen-Host Interactions

Our laboratories have pioneered the use of IMS technology to study infection biology. [28, 124, 135, 244, 245] This work has focused extensively on characterizing staphylococcal lesions in kidney tissues. This is partially because the foci in this organ system are robust and ideal for method development. However, organ-specific colonization is still an area requiring extensive study. Chapter IV reveled that metal levels vary greatly among organs, providing individual microenvironments with individual proteomics niches that could affect pathogenesis. Additionally, the size of lesions in other organ systems is smaller, requiring high sensitivity high spatial resolution IMS analyses of both metals and proteins. These studies should be performed in depth at varying time points throughout the course of infection to fully characterize the biological nuances. Signals detected from the staphylococcal colonies in different tissue types should be compared along with proteomic data to determine factors affecting organ-specific colonization. Such data could help determine why bacteria prefer certain niches within the host.

Such organ-specific fluctuations in nutrients might also affect how bacteria form biofilms to colonize these niches. Continuation developing biofilm models that mimic environmental conditions experienced within the vertebrate host are important to continue to study how bacteria respond to host-imposed limitation of nutrients and nutritional immunity. Though research into these communities is hindered by challenges associated with studying intact biofilms, our laboratories use of a drip flow reactor has provided an unbiased view of the molecular heterogeneity within these microbial communities. [29, 246, 247]

Concluding Remarks

The application of advanced mass spectrometry technologies to study the pathogen-host interaction can provide novel information about the biological changes associated with microbial pathogenesis and therapeutic resistance. [1, 248, 249] Imaging mass spectrometry (IMS) is an ideal analytical technology to study the competition for metals at the host-pathogen interface because it allows for spatial visualization of metals, metalloproteins, and metal-associated small molecules. As this technology is further developed for imaging at higher spatial resolutions the ability to differentiate bacterial signals associated with microbial communities within the host becomes a possibility. Understanding how bacteria behave in a pathogenic environment allows us to develop ex *vivo* models that mimic infection. In this regard, the application of IMS to bacterial biofilm models has revealed the unique molecular diversity within microbial communities. [250] The unique opportunity to fuse different imaging modalities to visualize proteins and metals at high spatial resolution will provide the information necessary to redefine the study of nutritional immunity and uncover novel biological information about metal homeostasis during infection. IMS technologies enable the study of infectious diseases with unprecedented resolution and will generate opportunities to develop new antimicrobial strategies. In an era of antibiotic resistance, such studies are paramount for future successful treatment of bacterial infections.

REFERENCES

1. Moore, J. L., Caprioli, R. M., Skaar, E. P., Advanced mass spectrometry technologies for the study of microbial pathogenesis. *Current Opinion in Microbiology* **2014,** *19*, 45–51.
2. Spraggins, J. M.; Rizzo, D. G.; Moore, J. L.; Noto, M. J.; Skaar, E. P.; Caprioli, R. M., Next-generation technologies for spatial proteomics: Integrating ultra-high speed MALDI-TOF and high mass resolution MALDI FTICR imaging mass spectrometry for protein analysis. *PROTEOMICS* **2016,** *16* (11-12), 1678-1689.
3. Moore, J. L.; Skaar, E. P., *Imaging Infection*. Springer: 2017.
4. Norris, J. L.; Caprioli, R. M., Analysis of Tissue Specimens by Matrix-Assisted Laser Desorption/Ionization Imaging Mass Spectrometry in Biological and Clinical Research. *Chemical Reviews* **2013,** *113* (4), 2309-2342.
5. Angel, P. M.; Caprioli, R. M., Matrix-Assisted Laser Desorption Ionization Imaging Mass Spectrometry: In Situ Molecular Mapping. *Biochemistry* **2013,** *52* (22), 3818-3828.
6. Sud, M.; Fahy, E.; Cotter, D.; Dennis, E. A.; Subramaniam, S., LIPID MAPS-Nature Lipidomics Gateway: An Online Resource for Students and Educators Interested in Lipids. *Journal of Chemical Education* **2012,** *89* (2), 291-292.
7. Maier, S. K.; Hahne, H.; Gholami, A. M.; Balluff, B.; Meding, S.; Schoene, C.; Walch, A. K.; Kuster, B., Comprehensive identification of proteins from MALDI imaging. *Molecular & Cellular Proteomics* **2013,** *10*, 2901-2910.
8. Caprioli, R. M.; Farmer, T. B.; Gile, J., Molecular Imaging of Biological Samples: Localization of Peptides and Proteins Using MALDI-TOF MS. *Analytical Chemistry* **1997,** *69* (23), 4751-4760.
9. Kueger, S.; Steinhauser, D.; Willmitzer, L.; Giavalisco, P., High-resolution plant metabolomics: from mass spectral features to metabolites and from whole-cell analysis to subcellular metabolite distributions. *Plant Journal* **2012,** *70* (1), 39-50.
10. Schoenian, I.; Spiteller, M.; Ghaste, M.; Wirth, R.; Herz, H.; Spiteller, D., Chemical basis of the synergism and antagonism in microbial communities in the nests of leaf-cutting ants. *Proceedings of the National Academy of Sciences of the United States of America* **2011,** *108* (5), 1955-1960.
11. Rath, C. M.; Alexandrov, T.; Higginbottom, S. K.; Song, J.; Milla, M. E.; Fischbach, M. A.; Sonnenburg, J. L.; Dorrestein, P. C., Molecular Analysis of Model Gut Microbiotas by Imaging Mass Spectrometry and Nanodesorption Electrospray Ionization Reveals Dietary Metabolite Transformations. *Analytical Chemistry* **2012,** *84* (21), 9259-9267.
12. Kazuyuki Sogawa, M. W., Kenichi Sato, Syunsuke Segawa, Chisato Ishii, Akiko Miyabe, Syota Murata, Tomoko Saito, Fumio Nomura, Use of the MALDI BioTyper system with MALDI-TOF mass spectrometry for rapid identification of microorganisms. *Analytical and Bioanalytical Chemistry* **2011,** *400* (7), 1905-1911.
13. Chaurand, P.; Norris, J. L.; Cornett, D. S.; Mobley, J. A.; Caprioli, R. M., New developments in profiling and imaging of proteins from tissue sections by MALDI mass spectrometry. *Journal of Proteome Research* **2006,** *5* (11), 2889-900.
14. Taverna, D.; Pollins, A. C.; Nanney, L. B.; Caprioli, R. M., Histology-guided protein digestion/extraction from formalin-fixed and paraffin-embedded pressure ulcer biopsies. *Experimental Dermatology* **2016,** *25* (2), 143-146.

15. Chaurand, P.; Sanders, M. E.; Jensen, R. A.; Caprioli, R. M., Proteomics in Diagnostic Pathology : Profiling and Imaging Proteins Directly in Tissue Sections. *The American Journal of Pathology* **2004,** *165* (4), 1057–1068.
16. Norris, J. L.; Tsui, T.; Gutierrez, D. B.; Caprioli, R. M., Pathology interface for the molecular analysis of tissue by mass spectrometry. *J Pathol Inform* **2016,** *7* (13), PMC4837791.
17. Spraggins, J. M.; Caprioli, R. M., High-Speed MALDI-TOF Imaging Mass Spectrometry: Rapid Ion Image Acquisition and Considerations for Next Generation Instrumentation. *Journal of The American Society for Mass Spectrometry* **2011,** *22* (6), 1022-1031.
18. Marshall, A. G.; Hendrickson, C. L.; Jackson, G. S., Fourier transform ion cyclotron resonance mass spectrometry: A primer. *Mass Spectrometry Reviews* **1998,** *17* (1), 1-35.
19. Senko, M.; Hendrickson, C.; Emmett, M.; H Shi, S.; Marshall, A., External Accumulation of Ions for Enhanced Electrospray Ionization Fourier Transform Ion Cyclotron Resonance Mass Spectrometry. *Journal of the American Society of Mass Spectrometry* **1997,** *8* (9), 970–976.
20. Cornett, D. S.; Frappier, S. L.; Caprioli, R. M., MALDI-FTICR Imaging Mass Spectrometry of Drugs and Metabolites in Tissue. *Analytical Chemistry* **2008,** *80* (14), 5648-5653.
21. Wang, X.; Han, J.; Pan, J.; Borchers, C. H., Comprehensive Imaging of Porcine Adrenal Gland Lipids by MALDI-FTMS Using Quercetin as a Matrix. *Analytical Chemistry* **2014,** *86* (1), 638-646.
22. Becker, J. S.; Matusch, A.; Wu, B., Bioimaging mass spectrometry of trace elements - recent advance and applications of LA-ICP-MS: A review. *Analytica chimica acta* **2014,** *835*, 1-18.
23. Jurowski, K., Szewczyk, M., Piekoszewski, W., Herman, M., Szewczyk, B., Nowak, G., Walas, S., Miliszkiewicz, N., Tobiasz, A., Dobrowolska-Iwanek, J., A standard sample preparation and calibration procedure for imaging zinc and magnesium in rats' brain tissue by laser ablation-inductively coupled plasma-time of flight-mass spectrometry. *Journal of Analytical Atomic Spectrometry* **2014,** *29*, 1425-1431.
24. Zhang, Y.; Fonslow, B. R.; Shan, B.; Baek, M.-C.; John R. Yates, I., Protein Analysis by Shotgun/Bottom-up Proteomics. *Chemical Reviews* **2013,** *113* (4), 2343-2394.
25. Schwartz, S. A.; Weil, R. J.; Johnson, M. D.; Toms, S. A.; Caprioli, R. M., Protein Profiling in Brain Tumors Using Mass Spectrometry. *Clinical Cancer Research* **2004,** *10* (3), 981-987.
26. Kelleher, N. L., Peer Reviewed: Top-Down Proteomics. *Analytical Chemistry* **2004,** *76* (11), 196A-203A.
27. Schey, K. L.; Anderson, D. M.; Rose, K. L., Spatially-Directed Protein Identification from Tissue Sections by Top-Down LC-MS/MS with Electron Transfer Dissociation. *Analytical Chemistry* **2013,** *85* (14), 6767-6774.
28. Corbin, B. D.; Seeley, E. H.; Raab, A.; Feldmann, J.; Miller, M. R.; Torres, V. J.; Anderson, K. L.; Dattilo, B. M.; Dunman, P. M.; Gerads, R.; Caprioli, R. M.; Nacken, W.; Chazin, W. J.; Skaar, E. P., Metal Chelation and Inhibition of Bacterial Growth in Tissue Abscesses. *Science* **2008,** *319* (5865), 962-965.
29. Wakeman, C. A.; Moore, J. L.; Noto, M. J.; Zhang, Y.; Singleton, M. D.; Prentice, B. M.; Gilston, B. A.; Doster, R. S.; Gaddy, J. A.; Chazin, W. J.; Caprioli, R. M.; Skaar, E. P., The innate immune protein calprotectin promotes *Pseudomonas aeruginosa* and *Staphylococcus aureus* interaction. *Nature Communications* **2016,** *7*, 11951.

30. Spraggins, J. M.; Rizzo, D. G.; Moore, J. L.; Rose, K. L.; Hammer, N. D.; Skaar, E. P.; Caprioli, R. M., MALDI FTICR IMS of Intact Proteins: Using Mass Accuracy to Link Protein Images with Proteomics Data. *JASMS* **2015,** *26* (6), 974-985.
31. Lazova, R.; Seeley, E. H.; Keenan, M.; Gueorguieva, R.; Caprioli, R. M., Imaging Mass Spectrometry – a new and promising method to differentiate Spitz nevi from Spitzoid malignant melanomas. *Am J Dermatopathol* **2012,** *34* (1), 82-90.
32. Seeley, E. H.; Washington, M. K.; Caprioli, R. M., Proteomic patterns of colonic mucosal tissues delineate Crohn's colitis and ulcerative colitis. *PROTEOMICS - Clinical Applications* **2013,** *7* (7-8), 541-549.
33. Harris, G. A.; Nicklay, J. J.; Caprioli, R. M., A Localized In-Situ Hydrogel-Mediated Protein Digestion and Extraction Technique For On-Tissue Analysis. *Anal Chem* **2013,** *85* (5), 2717-23.
34. Taverna, D.; Norris, J. L.; Caprioli, R. M., Histology-Directed Microwave Assisted Enzymatic Protein Digestion for MALDI MS Analysis of Mammalian Tissue. *Analytical Chemistry* **2015,** *87* (1), 670-676.
35. (CDC), C. f. D. C. a. P. Threat Report 2013 | Antimicrobial Resistance | CDC. http://www.cdc.gov/drugresistance/threat-report-2013/ (accessed 05/12/2014).
36. Doron, S.; Davidson, L. E., Antimicrobial Stewardship. *Mayo Clin Proc* **2011,** *86* (11), 1113-23.
37. Clatworthy, A. E.; Pierson, E.; Hung, D. T., Targeting virulence: a new paradigm for antimicrobial therapy. *Nature Chemical Biology* **2007,** *3* (9), 541-548.
38. Boucher, H. W.; Talbot, G. H.; Bradley, J. S.; Edwards, J. E.; Gilbert, D.; Rice, L. B.; Scheld, M.; Spellberg, B.; Bartlett, J., Bad Bugs, No Drugs: No ESKAPE! An Update from the Infectious Diseases Society of America. *Clin. Infect Dis.* **2008,** *48* (1), 1-12.
39. Valentine, N.; Wunschel, S.; Wunschel, D.; Petersen, C.; Wahl, K., Effect of culture conditions on microorganism identification by matrix-assisted laser desorption ionization mass spectrometry. *Applied and Environmental Microbiology* **2005,** *71* (1), 58-64.
40. Coltella, L.; Mancinelli, L.; Onori, M.; Lucignano, B.; Menichella, D.; Sorge, R.; Raponi, M.; Mancini, R.; Russo, C., Advancement in the routine identification of anaerobic bacteria by MALDI-TOF mass spectrometry. *European Journal of Clinical Microbiology & Infectious Diseases* **2013,** *32* (9), 1183-1192.
41. Biswas, S.; Rolain, J.-M., Use of MALDI-TOF mass spectrometry for identification of bacteria that are difficult to culture. *Journal of Microbiological Methods* **2013,** *92* (1), 14-24.
42. Chalupova, J.; Martin Raus, M. S., Marek Sebela, Identification of fungal microorganisms by MALDI-TOF mass spectrometry. *Biotechnology Advances* **2014,** *32* (1), 230-241.
43. Drevinek, M.; Dresler, J.; Klimentova, J.; Pisa, L.; Hubalek, M., Evaluation of sample preparation methods for MALDI-TOF MS identification of highly dangerous bacteria. *Letters in Applied Microbiology* **2012,** *55* (1), 40-46.
44. Jackson, K. A.; Edwards-Jones, V.; Sutton, C. W.; Fox, A. J., Optimisation of intact cell MALDI method for fingerprinting of methicillin-resistant *Staphylococcus aureus*. *Journal of Microbiological Methods* **2005,** *62* (3), 273-284.
45. Toh-Boyo, G. M.; Wulff, S. S.; Basile, F., Comparison of Sample Preparation Methods and Evaluation of Intra- and Intersample Reproducibility in Bacteria MALDI-MS Profiling. *Analytical Chemistry* **2012,** *84* (22), 9971-9980.

46. Boehme, K.; Fernandez-No, I. C.; Barros-Velazquez, J.; Gallardo, J. M.; Calo-Mata, P.; Canas, B., Species Differentiation of Seafood Spoilage and Pathogenic Gram-Negative Bacteria by MALDI-TOF Mass Fingerprinting. *Journal of Proteome Research* **2010,** *9* (6), 3169-3183.
47. Marko, D. C.; Saffert, R. T.; Cunningham, S. A.; Hyman, J.; Walsh, J.; Arbefeville, S.; Howard, W.; Pruessner, J.; Safwat, N.; Cockerill, F. R.; Bossler, A. D.; Patel, R.; Richter, S. S., Evaluation of the Bruker Biotyper and Vitek MS matrix-assisted laser desorption ionization-time of flight mass spectrometry systems for identification of nonfermenting Gram-negative bacilli isolated from cultures from cystic fibrosis patients. *J Clin Microbiol* **2012,** *50* (6), 2034-9.
48. Mather, C. A.; Rivera, S. F.; Butler-Wu, S. M., Comparison of the Bruker Biotyper and Vitek MS Matrix-Assisted Laser Desorption Ionization–Time of Flight Mass Spectrometry Systems for Identification of Mycobacteria Using Simplified Protein Extraction Protocols. *Journal of Clinical Microbiology* **2014,** *52* (1), 130-138.
49. Rizzardi, K.; Wahab, T.; Jernberg, C., Rapid Subtyping of Yersinia enterocolitica by Matrix-Assisted Laser Desorption Ionization-Time of Flight Mass Spectrometry (MALDI-TOF MS) for Diagnostics and Surveillance. *Journal of Clinical Microbiology* **2013,** *51* (12), 4200-4203.
50. Boggs, S. R.; Cazares, L. H.; Drake, R., Characterization of a Staphylococcus aureus USA300 protein signature using matrix-assisted laser desorption/ionization time-of-flight mass spectrometry. *Journal of Medical Microbiology* **2012,** *61* (5), 640-644.
51. Wolters, M.; Rohde, H.; Maier, T.; Belmar-Campos, C.; Franke, G.; Scherpe, S.; Aepfelbacher, M.; Christner, M., MALDI-TOF MS fingerprinting allows for discrimination of major methicillin-resistant *Staphylococcus aureus* lineages. *International Journal of Medical Microbiology* **2011,** *301* (1), 64-68.
52. Vlek, A. L. M.; Bonten, M. J. M.; Boel, C. H. E., Direct Matrix-Assisted Laser Desorption Ionization Time-of-Flight Mass Spectrometry Improves Appropriateness of Antibiotic Treatment of Bacteremia. *Plos One* **2012,** *7* (3), e32589.
53. Miller, J. M., Cost-saving strategies for diagnostic microbiology laboratories. *Clinical Microbiology Newsletter* **2013,** *35* (24), 195–204.
54. Zilahi, G.; Artigas, A.; Martin-Loeches, I., What's new in multidrug-resistant pathogens in the ICU? *Annals of Intensive Care* **2016,** *6* (1), 96.
55. Ziegler, D.; Mariotti, A.; Pflueger, V.; Saad, M.; Vogel, G.; Tonolla, M.; Perret, X., *In Situ* Identification of Plant-Invasive Bacteria with MALDI-TOF Mass Spectrometry. *Plos One* **2012,** *7* (5), e37189.
56. Nicolaou, N.; Xu, Y.; Goodacre, R., Detection and Quantification of Bacterial Spoilage in Milk and Pork Meat Using MALDI-TOF-MS and Multivariate Analysis. *Analytical Chemistry* **2012,** *84* (14), 5951-5958.
57. Ng, P. C.; Ang, I. L.; Chiu, R. W. K.; Li, K.; Lam, H. S.; Wong, R. P. O.; Chui, K. M.; Cheung, H. M.; Ng, E. W. Y.; Fok, T. F.; Sung, J. J. Y.; Lo, Y. M. D.; Poon, T. C. W., Host-response biomarkers for diagnosis of late-onset septicemia and necrotizing enterocolitis in preterm infants. *Journal of Clinical Investigation* **2010,** *120* (8), 2989-3000.
58. Narayana, J. L.; Gopal, J.; Wu, H.-F., Wound infection kinetics probed by MALDI-MS: rapid profiling of *Staphylococcus aureus* in mice. *Analyst* **2012,** *137* (14), 3372-3380.
59. Norris, J. L.; Caprioli, R. M., Imaging mass spectrometry: A new tool for pathology in a molecular age. *Proteomics Clinical Applications* **2013,** *7* (11-12), 733-738.

60. Oswald-Richter, K. A.; Beachboard, D. C.; Seeley, E. H.; Abraham, S.; Shepherd, B. E.; Jenkins, C. A.; Culver, D. A.; Caprioli, R. M.; Drake, W. P., Dual Analysis for Mycobacteria and Propionibacteria in Sarcoidosis BAL. *Journal of Clinical Immunology* **2012,** *32* (5), 1129-1140.
61. Zipperer, A.; Konnerth, M. C.; Laux, C.; Berscheid, A.; Janek, D.; Weidenmaier, C.; Burian, M.; Schilling, N. A.; Slavetinsky, C.; Marschal, M.; Willmann, M.; Kalbacher, H.; Schittek, B.; Brötz-Oesterhelt, H.; Grond, S.; Peschel, A.; Krismer, B., Human commensals producing a novel antibiotic impair pathogen colonization. *Nature* **2016,** *535*, 511-516.
62. Cheng, A. G.; DeDent, A. C.; Schneewind, O.; Missiakas, D., A play in four acts: St*aphylococcus aureus a*bscess formationA play in four acts: Staphylococcus aureus abscess formation. *Trends in Microbiology* **2011,** *19* (5), 225-232.
63. Cheng, A. G.; DeDent, A. C.; Schneewind, O.; Missiakas, D., A play in four acts: Staphylococcus aureus abscess formation. *Trends in microbiology* **2011,** *19* (5), 225-32.
64. Cheng, A. G.; DeDent, A. C.; Schneewind, O.; Missiakas, D., A play in four acts: St*aphylococcus aureus* abscess formation. *Trends in Microbiology* **2011,** *19* (5), 225-232.
65. Damo, S. M.; Kehl-Fie, T. E.; Sugitani, N.; Holt, M. E.; Rathi, S.; Murphy, W. J.; Zhang, Y.; Betz, C.; Hench, L.; Fritz, G.; Skaar, E. P.; Chazin, W. J., Molecular basis for manganese sequestration by calprotectin and roles in the innate immune response to invading bacterial pathogens. *Proceedings of the National Academy of Sciences* **2013,** *110* (10), 3841-6.
66. Grass, G.; Rensing, L.; Rensing, C., Metal Toxicity. *Metallomics* **2011,** *3*, 1095-1097.
67. Waldron, K. J.; Rutherford, J. C.; Ford, D.; Robinson, N. J., Metalloproteins and metal sensing. *Nature* **2009,** *460* (7257), 823-830.
68. Skaar, E. P.; Raffatellu, M., Metals in infectious diseases and nutritional immunity. *Metallomics : integrated biometal science* **2015,** *7* (6), 926-8.
69. Hood, M. I.; Skaar, E. P., Nutritional immunity: transition metals at the pathogen-host interface. *Nature Reviews Microbiology* **2012,** *10* (8), 525-537.
70. Mazmanian, S. K.; Skaar, E. P.; Gaspar, A. H.; Humayun, M.; Gornicki, P.; Jelenska, J.; Joachmiak, A.; Missiakas, D. M.; Schneewind, O., Passage of Heme-Iron Across the Envelope of Staphylococcus aureus. *Science* **2003,** *299* (5608), 906-909.
71. Kehl-Fie, T. E.; Skaar, E. P., Nutritional immunity beyond iron: a role for manganese and zinc. *Current opinion in chemical biology* **2010,** *14* (2), 218-24.
72. Zackular, J. P.; Chazin, W. J.; Skaar, E. P., Nutritional Immunity: S100 Proteins at the Host-Pathogen Interface. *The Journal of Biological Chemistry* **2015,** *290*, 18991-18998.
73. Clohessy, P. A.; Golden, B. E., Calprotectin-mediated zinc chelation as a biostatic mechanism in host defence. *Scand J Immunol* **1995,** *42* (5), 551-6.
74. Steinbakk, M.; Naess-Andresen, C. F.; Lingaas, E.; Dale, I.; Brandtzaeg, P.; Fagerhol, M. K., Antimicrobial actions of calcium binding leucocyte L1 protein, calprotectin. *The Lancet* **1990,** *336* (8718), 763-5.
75. Sohnle, P. G.; Collins-Lech, C.; Wiessner, J. H., The zinc-reversible antimicrobial activity of neutrophil lysates and abscess fluid supernatants. *J Infect Dis* **1991,** *164* (1), 137-42.
76. Brodersen, D. E.; Nyborg, J.; Kjeldgaard, M., Zinc-binding site of an S100 protein revealed. Two crystal structures of Ca2+-bound human psoriasin (S100A7) in the Zn2+-loaded and Zn2+-free states. *Biochemistry* **1999,** *38* (6), 1695-704.
77. Damo, S. M.; Kehl-Fie, T. E.; Sugitani, N.; Holt, M. E.; Rathi, S.; Murphy, W. J.; Zhang, Y.; Betz, D.; Hench, L.; Fritz, G.; Skaar, E. P.; Chazin, W. J., Molecular basis for manganese

sequestration by calprotectin and roles in the innate immune response to invading bacterial pathogens. *Proc Natl Acad Sci U S A* **In Press**.
78. Moroz, O. V.; Blagova, E. V.; Wilkinson, A. J.; Wilson, K. S.; Bronstein, I. B., The crystal structures of human S100A12 in apo form and in complex with zinc: new insights into S100A12 oligomerisation. *Journal of molecular biology* **2009,** *391* (3), 536-51.
79. Ostendorp, T.; Diez, J.; Heizmann, C. W.; Fritz, G., The crystal structures of human S100B in the zinc- and calcium-loaded state at three pH values reveal zinc ligand swapping. *Biochimica et biophysica acta* **2011,** *1813* (5), 1083-91.
80. Damo, S.; Chazin, W. J.; Skaar, E. P.; Kehl-Fie, T. E., Inhibition of bacterial superoxide defense: A new front in the struggle between host and pathogen. *Virulence* **2012,** *3* (3), 325-328.
81. Hood, M. I.; Mortensen, B. L.; Moore, J. L.; Zhang, Y.; Kehl-fie, T. E.; Sugitani, N.; Chazin, W. J.; Caprioli, R. M.; Skaar, E. M., Identification of an Acinetobacter baumannii zinc acquisition system that facilitates resistance to calprotectin-mediated zinc sequestration. *PLOS Pathogens* **2012**.
82. Lusitani, D.; Malawista, S. E.; Montgomery, R. R., Calprotectin, an Abundant Cytosolic Protein from Human Polymorphonuclear Leukocytes, Inhibits the Growth of *Borrelia burgdorferi*. *Infection and Immunity* **2003,** *71* (8), 4711-4716.
83. Urban, C. F.; Ermert, D.; Schmid, M.; Abu-Abed, U.; Goosmann, C.; Nacken, W.; Brinkmann, V.; Jungblut, P. R.; Zychlinsky, A., Neutrophil extracellular traps contain calprotectin, a cytosolic protein complex involved in host defense against Candida albicans. *PLoS Pathog* **2009,** *5* (10), e1000639.
84. Gaddy, J. A.; Radin, J. N.; Cullen, T. W.; Chazin, W. J.; Skaar, E. P.; Trent, M. S.; Algood, H. M. S., *Helicobacter pylori* Resists the Antimicrobial Activity of Calprotectin via Lipid A Modification and Associated Biofilm Formation. *mBio* **2015,** *6* (6), e01349-15.
85. Zackular, J. P.; Moore, J. L.; Jordan, A. T.; Juttukonda, L. J.; Noto, M. J.; Nicholson, M. R.; Crews, J. D.; Semler, M. W.; Zhang, Y.; Ware, L. B.; Washington, M. K.; Chazin, W. J.; Caprioli, R. M.; Skaar, E. P., Dietary zinc alters the microbiota and decreases resistance to *Clostridium difficile* infection. *Nature Medicine* **2016,** *22*, 1330-1334.
86. Sohnle, P. G.; Hunter, M. J.; Hahn, B.; Chazin, W. J., Zinc-Reversible Antimicrobial Activity of Recombinant Calprotectin (Migration Inhibitory Factor—Related Proteins 8 and 14). *Journal of Infectious Diseases* **2000,** *182* (4), 1272-1275.
87. Kehl-Fie, T. E.; Chitayat, S.; Hood, M. I.; Damo, S.; Restrepo, N.; Garcia, C.; Munro, K. A.; Chazin, W. J.; Skaar, E. P., Nutrient Metal Sequestration by Calprotectin Inhibits Bacterial Superoxide Defense, Enhancing Neutrophil Killing of Staphylococcus aureus. *Cell Host & Microbe* **2011,** *10* (2), 158-164.
88. Charles A. Janeway, J. a.; Medzhitov, R., INNATE IMMUNE RECOGNITION. *Annual Review of Immunology* **2003,** *20*, 197-216.
89. Russell, D. G., Staphylococcus and the Healing Power of Pus. *Cell Host & Microbe* **2008,** *3* (3), 115-116.
90. Buckley, C. D.; Gilroy, D. W.; Serhan, C. N.; Stockinger, B.; Tak, P. P., The resolution of inflammation. *Nature Reviews Immunology* **2013,** *13* (1), 59-66.
91. Farrera, C.; Fadeel, B., Macrophage Clearance of Neutrophil Extracellular Traps Is a Silent Process. *The Journal of Immunology* **2013,** *191* (5), 2647-2656.
92. Friguet, B., Oxidized protein degradation and repair in ageing and oxidative stress. *FEBS Letters* **2006,** *580*, 2910-2916.

93. Baraibar, M. A.; Friguet, B., Oxidative proteome modifications target specific cellular pathways during oxidative stress, cellular senescence and aging. *Exp Gerontol* **2013,** *48* (7), 620-5.
94. Lowther, W. T.; Haynes, A. C., Reduction of Cysteine Sulfinic Acid in Eukaryotic, Typical 2-Cys Peroxiredoxins by Sulfiredoxin. *Antioxidants & Redox Signaling* **2011,** *15* (1), 99-109.
95. Gennaris, A.; Collet, J. F., The 'captain of the men of death', Streptococcus pneumoniae, fights oxidative stress outside the 'city wall'. *EMBO Molecular Medicine* **2013,** *2013* (5), 1798-1800.
96. Brinkmann, V.; Reichard, U.; Goosmann, C.; Fauler, B.; Uhlemann, Y.; Weiss, D. S.; Weinrauch, Y.; Zychlinsky, A., Neutrophil Extracellular Traps Kill Bacteria. *Science* **2004,** *303*, 1532-1535.
97. Hakkim, A.; Furnrohr, B. G.; Amann, K.; Laube, B.; Abed, U. A.; Brinkmann, V.; Herrmann, M.; Voll, R. E.; Zychlinsky, A., Impairment of neutrophil extracellular trap degradation is associated with lupus nephritis. *Proc Natl Acad Sci U S A* **2010,** *107* (21), 9813-8.
98. Clark, S. R.; Ma, A. C.; Tavener, S. A.; McDonald, B.; Goodarzi, Z.; Kelly, M. M.; Patel, K. D.; Chakrabarti, S.; McAvoy, E.; Sinclair, G. D.; Keys, E. M.; Allen-Vercoe, E.; Devinney, R.; Doig, C. J.; Green, F. H.; Kubes, P., Platelet TLR4 activates neutrophil extracellular traps to ensnare bacteria in septic blood. *Nat Med* **2007,** *13* (4), 463-9.
99. Dellinger, R. P.; Levy, M. M.; Rhodes, A.; Annane, D.; Gerlach, H.; Opal, S. M.; Sevransky, J. E.; Sprung, C. L.; Douglas, I. S.; Jaeschke, R.; Osborn, T. M.; Nunnally, M. E.; Townsend, S. R.; Reinhart, K.; Kleinpell, R. M.; Angus, D. K.; Deutschman, C. S.; Machado, F. R.; Rubenfeld, G. D.; Webb, S.; Beale, R. J.; Vincent, J.-L.; Moreno, R., Surviving Sepsis Campaign: International Guidelines for Management of Severe Sepsis and Septic Shock, 2012 | SpringerLink. *Intensive Care Medicine* **2012,** *39* (2), 165-228.
100. Moore, J. L.; Becker, K. W.; Nicklay, J. J.; Boyd, K. L.; Skaar, E. P.; Caprioli, R. M., Imaging mass spectrometry for assessing temporal proteomics: Analysis of calprotectin in *Acinetobacter baumannii* pulmonary infection. *Proteomics* **2013,** *14* (7-8), 820-828.
101. Bastiaens, P. L. H.; Pepperkok, R., Observing proteins in their natural habitat: the living cell. *Trends in Biochemical Sciences* **2000,** *25* (12), 631-637.
102. McDonnell, L. A.; Heeren, R. M. A., Imaging mass spectrometry. *Mass Spectrometry Reviews* **2007,** *26* (4), 606-643.
103. Phizicky, E.; Bastiaens, P. I.; Zhu, H.; Snyder, M.; Fields, S., Protein analysis on a proteomic scale. *Nature* **2003,** *422* (6928), 208-15.
104. Ciaccio, M. F.; Wagner, J. P.; Chuu, C.-P.; Lauffenburger, D. A.; Jones, R. B., Systems analysis of EGF receptor signaling dynamics with microwestern arrays. *Nature Methods* **2010,** *7* (2), 148-155.
105. Crompton, P. D.; Kayala, M. A.; Traore, B.; Kayentao, K.; Ongoiba, A.; Weiss, G. E.; Molina, D. M.; Burk, C. R.; Waisberg, M.; Jasinskas, A.; Tan, X.; Doumbo, S.; Doumtabe, D.; Kone, Y.; Narum, D. L.; Liang, X.; Doumbo, O. K.; Miller, L. H.; Doolan, D. L.; Baldi, P.; Felgner, P. L.; Pierce, S. K., A prospective analysis of the Ab response to Plasmodium falciparum before and after a malaria season by protein microarray. **2010,** *107* (15), 6958-6963.
106. Lee, M. V.; Topper, S. E.; Hubler, S. L.; Hose, J.; Wenger, C. D.; Coon, J. J.; Gasch, A. P., A dynamic model of proteome changes reveals new roles for transcript alteration in yeast. *Molecular Systems Biology* **2011,** *7* (1).

107. Attia, Ahmed S.; Schroeder, Kaitlin A.; Seeley, Erin H.; Wilson, Kevin J.; Hammer, Neal D.; Colvin, Daniel C.; Manier, M. L.; Nicklay, Joshua J.; Rose, Kristie L.; Gore, John C.; Caprioli, Richard M.; Skaar, Eric P., Monitoring the Inflammatory Response to Infection through the Integration of MALDI IMS and MRI. *Host & Microbe* **2012,** *11* (6), 664- 673.
108. Giamarellou, H.; Antoniadou, A.; Kanellakopoulou, K., Acinetobacter baumannii: a universal threat to public health? *International Journal of Antimicrobial Agents* **2008,** *32* (2), 106-119.
109. Müller-Redetzky, H.; Suttorp, N.; Witzenrath, M., Experimental models of pneumonia-induced sepsis. *Drug Discovery Today: Disease Models* **2012,** *9* (1), e23–e32.
110. Peleg, A. Y.; Seifert, H.; Paterson, D. L., Acinetobacter baumannii: Emergence of a Successful Pathogen. *Clinical Microbiology Reviews* **2008,** *21* (3), 538-582.
111. Vincent, J. L.; Rello, J.; Marshall, J.; Silva, E.; Anzueto, A.; Martin, C. D.; Moreno, R.; Lipman, J.; Gomersall, C.; Sakr, Y.; Reinhart, K., International study of the prevalence and outcomes of infection in intensive care. *Journal of the American Medical Association* **2009,** *302* (21), 2323-9.
112. Rice, L. B., Challenges in identifying new antimicrobial agents effective for treating. *Clinical Infectious Disease* **2006,** *43 Suppl 2*, S100-5.
113. Jean, S. S.; Hsueh, P. R.; Lee, W. S.; Chang, H. T.; Chou, M. Y.; Chen, I. S.; Wang, J. H.; Lin, C. F.; Shyr, J. M.; Ko, W. C.; Wu, J. J.; Liu, Y. C.; Huang, W. K.; Teng, L. J.; Liu, C. Y., Nationwide surveillance of antimicrobial resistance among non-fermentative. *International Journal of Antimicrobial Agents* **2009,** *33* (3), 266-71.
114. Werarak, P.; Waiwarawut, J.; Tharavichitkul, P.; Pothirat, C.; Rungruanghiranya, S.; Geater, S. L.; Chongthaleong, A.; Sittipunt, C.; Horsin, P.; Chalermskulrat, W.; Wiwatworapan, T.; Thummakul, T.; Mootsikapun, P.; Rungsrithong, N.; Supawita, S.; Chuchotthavorn, C.; Tongsai, S.; Thamlikitkul, V., Acinetobacter baumannii nosocomial pneumonia in tertiary care hospitals in. *Journal of the Medical Association of Thailand* **2012,** *95 Suppl 2*, S23-33.
115. Lee, Y. T.; Kuo, S. C.; Yang, S. P., Ling, Y. T.; Chiang, D. H., Tseng, F. C.; Chen, T. L.; Fung, C. P., Bacteremic nosocomial pneumonia caused by Acinetobacter baumannii and Acinetobacter nosocomialis: a single or two distinct clinical entities? *Clinical Microbiology and Infection* **2012**, in press.
116. Ketai, L.; Busby, H., - Pulmonary Infections in the Normal Host. In *Clinically Oriented Pulmonary Imaging*, Kanne, J. P., Ed. Humana Press: 2012; pp 41-60.
117. Faassen, H. v.; KuoLee, R.; Harris, G.; Zhao, X.; Conlan, J. W.; Chen, W., Neutrophils Play an Important Role in Host Resistance to Respiratory Infection with Acinetobacter baumannii in Mice. *Infectious Immunology* **2007,** *75* (12), 5597-5608.
118. Jacobs, A. C.; Hood, M. I.; Boyd, K. L.; Olsen, P. D.; Morrison, J. M.; Carson, S.; Sayood, K.; Iwen, P. C.; Skkar, E. P.; Dunman1, P. M., Inactivation of Phospholipase D Diminishes Acinetobacter baumannii Pathogenesis. *Infectious Immunology* **2010,** *78* (5), 1952-1962.
119. Duthie, E. S.; Lorenz, L. L., Staphylococcal Coagulase: Mode of Action and Antigenicity. *Microbiology* **1952,** *6*, 95-107.
120. Yang, J.; Caprioli, R. M., Matrix Sublimation/Recrystallization for Imaging Proteins by Mass Spectrometry at High Spatial Resolution. *Analytical Chemistry* **2011,** *83* (14), 5728-5734.
121. Cheng, A. G.; Kim, H. K.; Burts, M. L.; Krausz, T.; Schneewind, O.; Missiakas, D. M., Genetic requirements for Staphylococcus aureus abscess formation and persistence in host

tissues. *FASEB journal : official publication of the Federation of American Societies for Experimental Biology* **2009,** *23* (10), 3393-404.
122. Thammavongsa, V.; Missiakas, D. M.; Schneewind, O., *Staphylococcus aureus* Degrades Neutrophil Extracellular Traps to Promote Immune Cell Death. *Science* **2013,** *342* (6160), 863-866.
123. Steinbakk, M.; Naess-Andresen, C.-F.; Fagerhol, M. K.; Lingaas, E.; Dale, I.; Brandtzaeg, P., Antimicrobial actions of calcium binding leucocyte L1 protein, calprotectin. *The Lancet* **1990,** *336* (8718), 763-765.
124. Attia, A. S.; Schroeder, K. A.; Seeley, E. H.; Wilson, K. J.; Hammer, N. D.; Colvin, D. C.; Manier, M. L.; Nicklay, J. J.; Rose, K. L.; Gore, J. C.; Caprioli, R. M.; Skaar, E. P., Monitoring the Inflammatory Response to Infection through the Integration of MALDI IMS and MRI. *Cell Host & Microbe* **2012,** *11* (6), 664-673.
125. Lim, S. Y.; Raftery, M. J.; Geczy, C. L., Oxidative modifications of DAMPs suppress inflammation: the case for S100A8 and S100A9. *Antioxid Redox Signal* **2011,** *15* (8), 2235-48.
126. Gomes, L. H.; Raftery, M. J.; Yan, W. X.; Goyette, J. D.; Thomas, P. S.; Geczy, C. L., S100A8 and S100A9-oxidant scavengers in inflammation. *Free Radic Biol Med* **2013,** *58*, 170-86.
127. Schöneich, C.; Sharov, V. S., Mass spectrometry of protein modifications by reactive oxygen and nitrogen species. *Free Radical Biology & Medicine* **2006,** *41* (10), 1507–1520.
128. Lim, S. Y.; Raftery, M.; Cai, H.; Hsu, K.; Yan, W. X.; Hseih, H. L.; Watts, R. N.; Richardson, D.; Thomas, S.; Perry, M.; Geczy, C. L., S-nitrosylated S100A8: novel anti-inflammatory properties. *J Immunol* **2008,** *181* (8), 5627-36.
129. Sroussi, H. Y.; Kohler, G. A.; Agabian, N.; Villines, D.; Palefsky, J. M., Substitution of methionine 63 or 83 in S100A9 and cysteine 42 in S100A8 abrogate the antifungal activities of S100A8/A9: potential role for oxidative regulation. *FEMS Immunol Med Microbiol* **2009,** *55* (1), 55-61.
130. Fuchs, T. A.; Abed, U.; Goosmann, C.; Hurwitz, R.; Schulze, I.; Wahn, V.; Weinrauch, Y.; Brinkmann, V.; Zychlinsky, A., Novel cell death program leads to neutrophil extracellular traps. *J Cell Biol* **2007,** *176* (2), 231-41.
131. Buchanan, J. T.; Simpson, A. J. A., Ramy K.; Liu, G. Y.; Kristian, S. A.; Kotb, M.; Nizet, V., DNase Expression Allows the Pathogen Group A Streptococcus to Escape Killing in Neutrophil Extracellular Traps. *Current Biology* **2006,** *16* (4), 396-400.
132. Ryan, B. J.; Nissim, A.; Winyard, P. G., Oxidative post-translational modifications and their involvement in the pathogenesis of autoimmune diseases. *Redox Biology* **2014,** *in press*.
133. Ehrchen, J. M.; Sunderkötter, C.; Foell, D.; Vogl, T.; Roth, J., The endogenous Toll-like receptor 4 agonist S100A8/S100A9 (calprotectin) as innate amplifier of infection, autoimmunity, and cancer. *Journal of Leukocyte Biology* **2009,** *86* (3), 557-566.
134. Lim, S. Y.; Raftery, M. J.; Goyette, J.; Hsu, K.; Geczy, C. L., Oxidative modifications of S100 proteins: functional regulation by redox. *J Leukoc Biol* **2009,** *86* (3), 577-87.
135. Kehl-Fie, T. E.; Zhang, Y.; Moore, J. L.; Farrand, A. J.; Hood, M. I.; Rathis, S.; Chazin, W. J.; Caprioli, R. M.; Skaar, E. P., *MntABC* and *MntH* Contribute to Systemic *Staphylococcus aureus* Infection by Competing with Calprotectin for Nutrient Manganese. *Infection and Immunity* **2013,** *81* (9), 3395-3405.
136. Andreini, C.; Bertini, I.; Cavallaro, G.; Holliday, G. L.; Thornton, J. M., Metal ions in biological catalysis: from enzyme databases to general principles. *J Biol Inorg Chem* **2008,** *13* (8), 1205-18.

137. Waldron, K. J.; Robinson, N. J., How do bacterial cells ensure that metalloproteins get the correct metal? *Nat Rev Microbiol* **2009,** *7* (1), 25-35.
138. Waldron, K. J.; Rutherford, J. C.; Ford, D.; Robinson, N. J., Metalloproteins and metal sensing. *Nature* **2009,** *460* (7257), 823-30.
139. Hood, M. I.; Skaar, E. P., Nutritional immunity: transition metals at the pathogen-host interface. *Nature reviews. Microbiology* **2012,** *10* (8), 525-37.
140. Corbin, B. D.; Seeley, E. H.; Raab, A.; Feldmann, J.; Miller, M. R.; Torres, V. J.; Anderson, K. L.; Dattilo, B. M.; Dunman, P. M.; Gerads, R.; Caprioli, R. M.; Nacken, W.; Chazin, W. J.; Skaar, E. P., Metal chelation and inhibition of bacterial growth in tissue abscesses. *Science* **2008,** *319* (5865), 962-5.
141. Ammendola, S.; Pasquali, P.; Pistoia, C.; Petrucci, P.; Petrarca, P.; Rotilio, G.; Battistoni, A., High-affinity Zn2+ uptake system ZnuABC is required for bacterial zinc homeostasis in intracellular environments and contributes to the virulence of *Salmonella enterica*. *Infect Immun* **2007,** *75* (12), 5867-76.
142. Campoy, S.; Jara, M.; Busquets, N.; Perez De Rozas, A. M.; Badiola, I.; Barbe, J., Role of the high-affinity zinc uptake *znuABC* system in *Salmonella enterica* serovar typhimurium virulence. *Infect Immun* **2002,** *70* (8), 4721-5.
143. Davis, L. M.; Kakuda, T.; DiRita, V. J., A *Campylobacter jejuni znuA* Orthologue Is Essential for Growth in Low-Zinc Environments and Chick Colonization. *Journal of Bacteriology* **2008,** *191* (5), 1631-1640.
144. Kim, S.; Watanabe, K.; Shirahata, T.; Watarai, M., Zinc uptake system (*znuA* locus) of *Brucella abortus* is essential for intracellular survival and virulence in mice. *J Vet Med Sci* **2004,** *66* (9), 1059-63.
145. Lewis, D. A.; Klesney-Tait, J.; Lumbley, S. R.; Ward, C. K.; Latimer, J. L.; Ison, C. A.; Hansen, E. J., Identification of the *znuA*-encoded periplasmic zinc transport protein of *Haemophilus ducreyi*. *Infect Immun* **1999,** *67* (10), 5060-8.
146. Sabri, M.; Houle, S.; Dozois, C. M., Roles of the Extraintestinal Pathogenic *Escherichia coli* ZnuACB and ZupT Zinc Transporters during Urinary Tract Infection. *Infection and Immunity* **2008,** *77* (3), 1155-1164.
147. Weston, B. F.; Brenot, A.; Caparon, M. G., The metal homeostasis protein, Lsp, of *Streptococcus pyogenes* is necessary for acquisition of zinc and virulence. *Infect Immun* **2009,** *77* (7), 2840-8.
148. Anderson, E. S.; Paulley, J. T.; Gaines, J. M.; Valderas, M. W.; Martin, D. W.; Menscher, E.; Brown, T. D.; Burns, C. S.; Roop, R. M., 2nd, The manganese transporter MntH is a critical virulence determinant for *Brucella abortus* 2308 in experimentally infected mice. *Infect Immun* **2009,** *77* (8), 3466-74.
149. Bearden, S. W.; Perry, R. D., The Yfe system of *Yersinia pestis* transports iron and manganese and is required for full virulence of plague. *Mol Microbiol* **1999,** *32* (2), 403-14.
150. Berry, A. M.; Paton, J. C., Sequence heterogeneity of PsaA, a 37-kilodalton putative adhesin essential for virulence of *Streptococcus pneumoniae*. *Infect Immun* **1996,** *64* (12), 5255-62.
151. Dintilhac, A.; Alloing, G.; Granadel, C.; Claverys, J. P., Competence and virulence of *Streptococcus pneumoniae*: Adc and PsaA mutants exhibit a requirement for Zn and Mn resulting from inactivation of putative ABC metal permeases. *Mol Microbiol* **1997,** *25* (4), 727-39.

152. Horsburgh, M. J.; Wharton, S. J.; Cox, A. G.; Ingham, E.; Peacock, S.; Foster, S. J., MntR modulates expression of the PerR regulon and superoxide resistance in *Staphylococcus aureus* through control of manganese uptake. *Mol Microbiol* **2002,** *44* (5), 1269-86.
153. Janulczyk, R.; Ricci, S.; Bjorck, L., MtsABC is important for manganese and iron transport, oxidative stress resistance, and virulence of *Streptococcus pyogenes*. *Infect Immun* **2003,** *71* (5), 2656-64.
154. Sun, X.; Baker, H. M.; Ge, R.; Sun, H.; He, Q.-Y.; Baker, E. N., Crystal Structure and Metal Binding Properties of the Lipoprotein MtsA, Responsible for Iron Transport in *Streptococcus pyogenes*. *Biochemistry* **2009,** *48* (26), 6184-6190.
155. Papp-Wallace, K. M.; Maguire, M. E., Manganese transport and the role of manganese in virulence. *Annu Rev Microbiol* **2006,** *60*, 187-209.
156. Perry, R. D.; Mier, I., Jr.; Fetherston, J. D., Roles of the Yfe and Feo transporters of *Yersinia pestis* in iron uptake and intracellular growth. *Biometals* **2007,** *20* (3-4), 699-703.
157. Cassat, J. E.; Skaar, E. P., Iron in infection and immunity. *Cell host & microbe* **2013,** *13* (5), 509-19.
158. Reniere, M. L.; Skaar, E. P., Staphylococcus aureus haem oxygenases are differentially regulated by iron and haem. *Molecular microbiology* **2008,** *69* (5), 1304-15.
159. Wells, W. M., 3rd; Viola, P.; Atsumi, H.; Nakajima, S.; Kikinis, R., Multi-modal volume registration by maximization of mutual information. *Medical image analysis* **1996,** *1* (1), 35-51.
160. Akbar, S.; Lee, S. Y.; Boylan, S. A.; Price, C. W., Two genes from Bacillus subtilis under the sole control of the general stress transcription factor sigmaB. *Microbiology* **1999,** *145* (Pt 5), 1069-78.
161. Pragai, Z.; Harwood, C. R., Regulatory interactions between the Pho and sigma(B)-dependent general stress regulons of Bacillus subtilis. *Microbiology* **2002,** *148* (Pt 5), 1593-602.
162. Peschel, A.; Otto, M., Phenol-soluble modulins and staphylococcal infection (vol 11, pg 667, 2013). *Nat Rev Microbiol* **2013,** *11* (11).
163. Wang, R.; Braughton, K. R.; Kretschmer, D.; Bach, T. H. L.; Queck, S. Y.; Li, M.; Kennedy, A. D.; Dorward, D. W.; Klebanoff, S. J.; Peschel, A.; Deleo, F. R.; Otto, M., Identification of novel cytolytic peptides as key virulence determinants for community-associated MRSA. *Nature medicine* **2007,** *13* (12), 1510-1514.
164. Cheung, G. Y. C.; Yeh, A. J.; Kretschmer, D.; Duong, A. C.; Tuffuor, K.; Fu, C. L.; Joo, H. S.; Diep, B. A.; Li, M.; Nakamura, Y.; Nunez, G.; Peschel, A.; Otto, M., Functional characteristics of the Staphylococcus aureus delta-toxin allelic variant G10S. *Sci Rep-Uk* **2015,** *5*.
165. Yang, J. H.; Caprioli, R. M., Matrix Sublimation/Recrystallization for Imaging Proteins by Mass Spectrometry at High Spatial Resolution. *Analytical chemistry* **2011,** *83* (14), 5728-5734.
166. Prentice, B. M.; Chumbley, C. W.; Caprioli, R. M., High-speed MALDI MS/MS imaging mass spectrometry using continuous raster sampling. *Journal of Mass Spectrometry* **2016,** *50* (4), 703-710.
167. Morris, J. S.; Coombes, K. R.; Koomen, J.; Baggerly, K. A.; Kobayashi, R., Feature extraction and quantification for mass spectrometry in biomedical applications using the mean spectrum. *Bioinformatics* **2005,** *21* (9), 1764-75.
168. MacAleese, L.; Stauber, J.; Heeren, R. M. A., Perspectives for imaging mass spectrometry in the proteomics landscape. *Proteomics* **2009,** *9* (4), 819-834.

169. Attia, A. S.; Schroeder, K. A.; Seeley, E. H.; Wilson, K. J.; Hammer, N. D.; Colvin, D. C.; Manier, M. L.; Nicklay, J. J.; Rose, K. L.; Gore, J. C.; Caprioli, R. M.; Skaar, E. P., Monitoring the inflammatory response to infection through the integration of MALDI IMS and MRI. *Cell host & microbe* **2012,** *11* (6), 664-73.
170. Peters, B. M.; Jabra-Rizk, M. A.; O'May, G. A.; Costerton, J. W.; Shirtliff, M. E., Polymicrobial interactions: impact on pathogenesis and human disease. *Clinical microbiology reviews* **2012,** *25* (1), 193-213.
171. Davey, M. E.; O'Toole, G. A., Microbial biofilms: from ecology to molecular genetics. *Microbiology and Molecular Biology Reviews* **2000,** *64* (4), 847-67.
172. Kostakioti, M.; Hadjifrangiskou, M.; Hultgren, S. J., Bacterial biofilms: development, dispersal, and therapeutic strategies in the dawn of the postantibiotic era. *Cold Spring Harbor perspectives in medicine* **2013,** *3* (4), a010306.
173. Irie, Y.; Parsek, M. R., Quorum sensing and microbial biofilms. *Current topics in microbiology and immunology* **2008,** *322*, 67-84.
174. Floyd, K. A.; Moore, J. L.; Eberly, A. R.; Good, J. A.; Shaffer, C. L.; Zaver, H.; Almqvist, F.; Skaar, E. P.; Caprioli, R. M.; Hadjifrangiskou, M., Adhesive fiber stratification in uropathogenic *Escherichia coli* biofilms unveils oxygen-mediated control of type 1 pili. *PLoS pathogens* **2015,** *11* (3), e1004697.
175. Vlamakis, H.; Aguilar, C.; Losick, R.; Kolter, R., Control of cell fate by the formation of an architecturally complex bacterial community. *Genes & development* **2008,** *22* (7), 945-53.
176. Boles, B. R.; Thoendel, M.; Singh, P. K., Self-generated diversity produces "insurance effects" in biofilm communities. *Proceedings of the National Academy of Sciences* **2004,** *101* (47), 16630-5.
177. Brockhurst, M. A.; Hochberg, M. E.; Bell, T.; Buckling, A., Character displacement promotes cooperation in bacterial biofilms. *Current Biology* **2006,** *16* (20), 2030-4.
178. Kolter, R.; Greenberg, E. P., Microbial sciences: the superficial life of microbes. *Nature* **2006,** *441* (7091), 300-2.
179. Hood, M. I.; Skaar, E. P., Nutritional immunity: transition metals at the pathogen-host interface. *Nature Reviews Microbiology* **2012,** *10* (8), 525-37.
180. Banin, E.; Vasil, M. L.; Greenberg, E. P., Iron and *Pseudomonas aeruginosa* biofilm formation. *Proceedings of the National Academy of Sciences* **2005,** *102* (31), 11076-81.
181. DePas, W. H.; Hufnagel, D. A.; Lee, J. S.; Blanco, L. P.; Bernstein, H. C.; Fisher, S. T.; James, G. A.; Stewart, P. S.; Chapman, M. R., Iron induces bimodal population development by *Escherichia coli*. *Proceedings of the National Academy of Sciences* **2013,** *110* (7), 2629-34.
182. Nguyen, A. T.; Jones, J. W.; Ruge, M. A.; Kane, M. A.; Oglesby-Sherrouse, A. G., Iron Depletion Enhances Production of Antimicrobials by *Pseudomonas aeruginosa*. *Journal of bacteriology* **2015,** *197* (14), 2265-75.
183. Nguyen, A. T.; O'Neill, M. J.; Watts, A. M.; Robson, C. L.; Lamont, I. L.; Wilks, A.; Oglesby-Sherrouse, A. G., Adaptation of iron homeostasis pathways by a *Pseudomonas aeruginosa* pyoverdine mutant in the cystic fibrosis lung. *Journal of bacteriology* **2014,** *196* (12), 2265-76.
184. Filkins, L. M.; Graber, J. A.; Olson, D. G.; Dolben, E. L.; Lynd, L. R.; Bhuju, S.; O'Toole, G. A., Coculture of *Staphylococcus aureus* with *Pseudomonas aeruginosa* Drives *S. aureus* towards Fermentative Metabolism and Reduced Viability in a Cystic Fibrosis Model. *Journal of bacteriology* **2015,** *197* (14), 2252-64.

185. Mashburn, L. M.; Jett, A. M.; Akins, D. R.; Whiteley, M., *Staphylococcus aureus* serves as an iron source for *Pseudomonas aeruginosa* during in vivo coculture. *Journal of bacteriology* **2005,** *187* (2), 554-66.
186. Kofoed, M. V.; Nielsen, D. A.; Revsbech, N. P.; Schramm, A., Fluorescence *in situ* hybridization (FISH) detection of nitrite reductase transcripts (nirS mRNA) in *Pseudomonas stutzeri* biofilms relative to a microscale oxygen gradient. *Systematic and applied microbiology* **2012,** *35* (8), 513-7.
187. Caprioli, R. M.; Farmer, T. B.; Gile, J., Molecular imaging of biological samples: localization of peptides and proteins using MALDI-TOF MS. *Analytical chemistry* **1997,** *69* (23), 4751-60.
188. Stover, C. K.; Pham, X. Q.; Erwin, A. L.; Mizoguchi, S. D.; Warrener, P.; Hickey, M. J.; Brinkman, F. S. L.; Hufnagle, W. O.; Kowalik, D. J.; Lagrou, M.; Garber, R. L.; Goltry, L.; Tolentino, E.; Westbrock-Wadman, S.; Yuan, Y.; Brody, L. L.; Coulter, S. N.; Folger, K. R.; Kas, A.; Larbig, K.; Lim, R.; Smith, K.; Spencer, D.; Wong, G. K.-S.; Wu, Z.; Paulsen, I. T.; Reizer, J.; Saier, M. H.; Hancock, R. E. W.; Lory, S.; Olson, M. V., Complete genome sequence of Pseudomonas aeruginosa PAO1, an opportunisticpathogen. *Nature* **2000,** *406* (6799), 959-964.
189. Mesaros, N.; Nordmann, P.; Plesiat, P.; Roussel-Delvallez, M.; Van Eldere, J.; Glupczynski, Y.; Van Laethen, Y.; Jacobs, F.; Lebecque, P.; Malfroot, A.; Tulkens, P. M.; Van Bambeke, F., Pseudomonas aeruginosa: resistance and therapeutic options at the turn of the new millennium. *Clinical Microbiology and Infection* **2007,** *13* (6), 560-578.
190. Breen, E. C.; Fu, Z.; Normand, H., Calcyclin Gene Expression Is Increased by Mechanical Strain in Fibroblasts and Lung. *American Journal of Respiratory Cell and Molecular Biology* **1999,** *21* (6), 746-752.
191. Rowe, S. M.; Miller, S.; Sorscher, E. J., Cystic Fibrosis. *New England Journal of Medicine* **2005,** *352*, 1992-2001.
192. Smith, E. E.; Buckley, D. G.; Wu, Z.; Saenphimmachak, C.; Hoffman, L. R.; D'Argenio, D. A.; Miller, S. I.; Ramsey, B. W.; Speert, D. P.; Moskowitz, S. M.; Burns, J. L.; Kaul, R.; Olson, M. V., Genetic adaptation by *Pseudomonas aeruginosa* to the airways of cystic fibrosis patients. *Proceedings of the National Academy of Sciences* **2006,** *103* (22), 8487-92.
193. Schwartz, K.; Stephenson, R.; Hernandez, M.; Jambang, N.; Boles, B. R., The use of drip flow and rotating disk reactors for *Staphylococcus aureus* biofilm analysis. *Journal of Visualized Experiments* **2010,** (46).
194. Moormeier, D. E.; Endres, J. L.; Mann, E. E.; Sadykov, M. R.; Horswill, A. R.; Rice, K. C.; Fey, P. D.; Bayles, K. W., Use of microfluidic technology to analyze gene expression during *Staphylococcus aureus* biofilm formation reveals distinct physiological niches. *Applied and environmental microbiology* **2013,** *79* (11), 3413-24.
195. Panina, E. M.; Mironov, A. A.; Gelfand, M. S., Comparative genomics of bacterial zinc regulons: enhanced ion transport, pathogenesis, and rearrangement of ribosomal proteins. *Proceedings of the National Academy of Sciences* **2003,** *100* (17), 9912-7.
196. Fugere, A.; Lalonde Seguin, D.; Mitchell, G.; Deziel, E.; Dekimpe, V.; Cantin, A. M.; Frost, E.; Malouin, F., Interspecific small molecule interactions between clinical isolates of *Pseudomonas aeruginosa* and *Staphylococcus aureus* from adult cystic fibrosis patients. *PloS one* **2014,** *9* (1), e86705.

197. Williams, P.; Camara, M., Quorum sensing and environmental adaptation in *Pseudomonas aeruginosa*: a tale of regulatory networks and multifunctional signal molecules. *Current opinion in microbiology* **2009,** *12* (2), 182-91.
198. Redly, G. A.; Poole, K., Pyoverdine-mediated regulation of FpvA synthesis in *Pseudomonas aeruginosa*: involvement of a probable extracytoplasmic-function sigma factor, FpvI. *Journal of bacteriology* **2003,** *185* (4), 1261-5.
199. Wilderman, P. J.; Sowa, N. A.; FitzGerald, D. J.; FitzGerald, P. C.; Gottesman, S.; Ochsner, U. A.; Vasil, M. L., Identification of tandem duplicate regulatory small RNAs in *Pseudomonas aeruginosa* involved in iron homeostasis. *Proceedings of the National Academy of Sciences* **2004,** *101* (26), 9792-7.
200. Manitz, M. P.; Horst, B.; Seeliger, S.; Strey, A.; Skryabin, B. V.; Gunzer, M.; Frings, W.; Schonlau, F.; Roth, J.; Sorg, C.; Nacken, W., Loss of S100A9 (MRP14) results in reduced interleukin-8-induced CD11b surface expression, a polarized microfilament system, and diminished responsiveness to chemoattractants in vitro. *Molecular and cellular biology* **2003,** *23* (3), 1034-43.
201. Caldwell, R. L.; Caprioli, R. M., Tissue profiling by mass spectrometry: a review of methodology and applications. *Molecular & Cellular Proteomics* **2005,** *4* (4), 394-401.
202. Breen, E. C.; Tang, K., Calcyclin (S100A6) regulates pulmonary fibroblast proliferation, morphology, and cytoskeletal organization in vitro. *Journal of Cellular Biochemistry* **2003,** *88* (4), 848-854.
203. Pernet, E.; Guillemot, L.; Burgel, P. R.; Martin, C.; Lambeau, G.; Sermet-Gaudelus, I.; Sands, D.; Leduc, D.; Morand, P. C.; Jeammet, L.; Chignard, M.; Wu, Y.; Touqui, L., *Pseudomonas aeruginosa* eradicates *Staphylococcus aureus* by manipulating the host immunity. *Nature communications* **2014,** *5*, 5105.
204. Golden, B. E.; Clohessy, P. A.; Russell, G.; Fagerhol, M. K., Calprotectin as a marker of inflammation in cystic fibrosis. *Archives of disease in childhood* **1996,** *74* (2), 136-9.
205. Pastar, I.; Nusbaum, A. G.; Gil, J.; Patel, S. B.; Chen, J.; Valdes, J.; Stojadinovic, O.; Plano, L. R.; Tomic-Canic, M.; Davis, S. C., Interactions of methicillin resistant *Staphylococcus aureus* USA300 and *Pseudomonas aeruginosa* in polymicrobial wound infection. *PloS one* **2013,** *8* (2), e56846.
206. Sagel, S. D.; Gibson, R. L.; Emerson, J.; McNamara, S.; Burns, J. L.; Wagener, J. S.; Ramsey, B. W., Impact of *Pseudomonas* and *Staphylococcus* infection on inflammation and clinical status in young children with cystic fibrosis. *Journal of Pediatrics* **2009,** *154* (2), 183-8.
207. Spaan, A. N.; Surewaard, B. G.; Nijland, R.; van Strijp, J. A., Neutrophils versus *Staphylococcus aureus*: a biological tug of war. *Annual review of microbiology* **2013,** *67*, 629-50.
208. Hauser, A. R.; Jain, M.; Bar-Meir, M.; McColley, S. A., Clinical significance of microbial infection and adaptation in cystic fibrosis. *Clinical microbiology reviews* **2011,** *24* (1), 29-70.
209. Hoffman, L. R.; Deziel, E.; D'Argenio, D. A.; Lepine, F.; Emerson, J.; McNamara, S.; Gibson, R. L.; Ramsey, B. W.; Miller, S. I., Selection for *Staphylococcus aureus* small-colony variants due to growth in the presence of *Pseudomonas aeruginosa*. *Proceedings of the National Academy of Sciences of the United States of America* **2006,** *103* (52), 19890-5.
210. Short, F. L.; Murdoch, S. L.; Ryan, R. P., Polybacterial human disease: the ills of social networking. *Trends in microbiology* **2014,** *22* (9), 508-16.
211. Kehl-Fie, T. E.; Zhang, Y.; Moore, J. L.; Farrand, A. J.; Hood, M. I.; Rathi, S.; Chazin, W. J.; Caprioli, R. M.; Skaar, E. P., MntABC and MntH contribute to systemic *Staphylococcus aureus*

infection by competing with calprotectin for nutrient manganese. *Infection and immunity* **2013,** *81* (9), 3395-405.
212. Hood, M. I.; Mortensen, B. L.; Moore, J. L.; Zhang, Y.; Kehl-Fie, T. E.; Sugitani, N.; Chazin, W. J.; Caprioli, R. M.; Skaar, E. P., Identification of an *Acinetobacter baumannii* zinc acquisition system that facilitates resistance to calprotectin-mediated zinc sequestration. *PLoS pathogens* **2012,** *8* (12), e1003068.
213. Moree, W. J.; Phelan, V. V.; Wu, C. H.; Bandeira, N.; Cornett, D. S.; Duggan, B. M.; Dorrestein, P. C., Interkingdom metabolic transformations captured by microbial imaging mass spectrometry. *Proceedings of the National Academy of Sciences* **2012,** *109* (34), 13811-6.
214. Traxler, M. F.; Watrous, J. D.; Alexandrov, T.; Dorrestein, P. C.; Kolter, R., Interspecies interactions stimulate diversification of the *Streptomyces coelicolor* secreted metabolome. *mBio* **2013,** *4* (4).
215. Rahme, L. G.; Stevens, E. J.; Wolfort, S. F.; Shao, J.; Tompkins, R. G.; Ausubel, F. M., Common virulence factors for bacterial pathogenicity in plants and animals. *Science* **1995,** *268* (5219), 1899-902.
216. Liberati, N. T.; Urbach, J. M.; Miyata, S.; Lee, D. G.; Drenkard, E.; Wu, G.; Villanueva, J.; Wei, T.; Ausubel, F. M., An ordered, nonredundant library of *Pseudomonas aeruginosa* strain PA14 transposon insertion mutants. *Proceedings of the National Academy of Sciences* **2006,** *103* (8), 2833-8.
217. Fey, P. D.; Endres, J. L.; Yajjala, V. K.; Widhelm, T. J.; Boissy, R. J.; Bose, J. L.; Bayles, K. W., A genetic resource for rapid and comprehensive phenotype screening of nonessential *Staphylococcus aureus* genes. *mBio* **2013,** *4* (1), e00537-12.
218. Voyich, J. M.; Braughton, K. R.; Sturdevant, D. E.; Whitney, A. R.; Said-Salim, B.; Porcella, S. F.; Long, R. D.; Dorward, D. W.; Gardner, D. J.; Kreiswirth, B. N.; Musser, J. M.; DeLeo, F. R., Insights into mechanisms used by Staphylococcus aureus to avoid destruction by human neutrophils. *J Immunol* **2005,** *175* (6), 3907-19.
219. Baldan, R.; Cigana, C.; Testa, F.; Bianconi, I.; De Simone, M.; Pellin, D.; Di Serio, C.; Bragonzi, A.; Cirillo, D. M., Adaptation of *Pseudomonas aeruginosa* in Cystic Fibrosis airways influences virulence of *Staphylococcus aureus* in vitro and murine models of co-infection. *PloS one* **2014,** *9* (3), e89614.
220. Jacobs, A. C.; Hood, I.; Boyd, K. L.; Olson, P. D.; Morrison, J. M.; Carson, S.; Sayood, K.; Iwen, P. C.; Skaar, E. P.; Dunman, P. M., Inactivation of phospholipase D diminishes *Acinetobacter baumannii* pathogenesis. *Infection and immunity* **2010,** *78* (5), 1952-62.
221. Kehl-Fie, T. E.; Chitayat, S.; Hood, M. I.; Damo, S.; Restrepo, N.; Garcia, C.; Munro, K. A.; Chazin, W. J.; Skaar, E. P., Nutrient metal sequestration by calprotectin inhibits bacterial superoxide defense, enhancing neutrophil killing of *Staphylococcus aureus*. *Cell host & microbe* **2011,** *10* (2), 158-64.
222. Gaddy, J. A.; Tomaras, A. P.; Actis, L. A., The *Acinetobacter baumannii* 19606 OmpA protein plays a role in biofilm formation on abiotic surfaces and in the interaction of this pathogen with eukaryotic cells. *Infect. Immun* **2009,** *77* (8), 3150-60.
223. Phelan, V. V.; Fang, J.; Dorrestein, P. C., Mass Spectrometry Analysis of *Pseudomonas aeruginosa* Treated with Azithromycin. *Journal of the American Society for Mass Spectrometry* **2015,** *26* (6), 873-7.
224. Yang, J.; Caprioli, R. M., Matrix sublimation/recrystallization for imaging proteins by mass spectrometry at high spatial resolution. *Anal. Chem* **2011,** *83* (14), 5728-34.

225. Wakeman, C. A.; Stauff, D. L.; Zhang, Y.; Skaar, E. P., Differential activation of *Staphylococcus aureus* heme detoxification machinery by heme analogues. *Journal of bacteriology* **2014**.
226. Vinckx, T.; Wei, Q.; Matthijs, S.; Cornelis, P., The *Pseudomonas aeruginosa* oxidative stress regulator OxyR influences production of pyocyanin and rhamnolipids: protective role of pyocyanin. *Microbiology* **2010,** *156* (Pt 3), 678-86.
227. Clerc, O.; Prod'hom, G.; Vogne, C.; Bizzini, A.; Calandra, T.; Greub, G., Impact of Matrix-Assisted Laser Desorption Ionization Time-of-Flight Mass Spectrometry on the Clinical Management of Patients With Gram-negative Bacteremia: A Prospective Observational Study. *Clinical Infectious Diseases* **2013,** *56* (8), 1101-1107.
228. Zavalin, A.; Yang, J.; Caprioli, R., Laser Beam Filtration for High Spatial Resolution MALDI Imaging Mass Spectrometry. *Journal of the American Society for Mass Spectrometry* **2013,** *24* (7), 1153-1156.
229. Passarelli, M. K.; Ewing, A. G., Single-cell imaging mass spectrometry. *Current Opinion in Chemical Biology* **2013,** *17* (5), 854-859.
230. Thiery-Lavenant, G.; Zavalin, A. I.; Caprioli, R. M., Targeted Multiplex Imaging Mass Spectrometry in Transmission Geometry for Subcellular Spatial Resolution. *Journal of the American Society for Mass Spectrometry* **2013,** *24* (4), 609-614.
231. Zavalin, A.; Todd, E. M.; Rawhouser, P. D.; Yang, J.; Norris, J. L.; Caprioli, R. M., Direct imaging of single cells and tissue at sub-cellular spatial resolution using transmission geometry MALDI MS. *Journal of Mass Spectrometry* **2012,** *47* (11), 1473-1481.
232. van Remoortere, A.; van Zeijl, R. J. M.; van den Oever, N.; Franck, J.; Longuespee, R.; Wisztorski, M.; Salzet, M.; Deelder, A. M.; Fournier, I.; McDonnell, L. A., MALDI Imaging and Profiling MS of Higher Mass Proteins from Tissue. *Journal of the American Society for Mass Spectrometry* **2010,** *21* (11), 1922-1929.
233. Gopal, J.; Lee, C.-H.; Wu, H.-F., Rapid and direct detection of Invivo kinetics of pathogenic bacterial infection from mouse blood and urine. *Journal of Proteomics* **2012,** *75* (10), 2972-2982.
234. Abdelhamid, H. N.; Gopal, J.; Wu, H.-F., Synthesis and application of ionic liquid matrices (ILMs) for effective pathogenic bacteria analysis in matrix assisted laser desorption/ionization (MALDI-MS). *Analytica Chimica Acta* **2013,** *767*, 104-111.
235. Gopal, J.; Hasan, N.; Wu, H. F., Fabrication of titanium based MALDI bacterial chips for rapid, sensitive and direct analysis of pathogenic bacteria. *Biosensors & Bioelectronics* **2013,** *39* (1), 57-63.
236. Abdelhamid, H. N.; Wu, H.-F., Multifunctional graphene magnetic nanosheet decorated with chitosan for highly sensitive detection of pathogenic bacteria. *Journal of Materials Chemistry B* **2013,** *1* (32), 3950-3961.
237. Chen, C.-T.; Reddy, P. M.; Ma, Y.-R.; Ho, Y.-P., Mass spectrometric identification of pathogens in foods using a zirconium hydroxide immobilization approach. *International Journal of Mass Spectrometry* **2012,** *312*, 45-52.
238. Lasch, P.; Jacob, D.; Grunow, R.; Schwecke, T.; Doellinger, J., Matrix-assisted laser desorption/ionization time-of-flight (MALDI-TOF) mass spectrometry (MS) for the identification of highly pathogenic bacteria. *Trends in Analytical Chemistry* **2016,** *in press*.
239. Debois, D.; Hamze, K.; Guerineau, V.; Le Caer, J.-P.; Holland, B.; Lopez, P.; Ouazzani, J.; Seror, S. J.; Brunelle, A.; Laprevote, O., In situ localisation and quantification of surfactins in a

Bacillus subtilis swarming community by imaging mass spectrometry. *PROTEOMICS* **2008,** *8* (18), 3682-3691.
240. Holland, R. D.; Duffy, C. R.; Rafii, F.; Sutherland, J. B.; Heinze, T. M.; Holder, C. L.; Voorhees, K. J.; Lay Jr., J. O., Identification of Bacterial Proteins Observed in MALDI TOF Mass Spectra from Whole Cells. *Analytical Chemistry* **1999,** *71* (15), 3226-3230.
241. Fenselau, C.; Demirev, P., Characterization of intact microorganisms by MALDI mass spectrometry. *Mass Spectrometry Reviews* **2001,** *20* (4), 157-171.
242. Trimpin, S.; Inutan, E. D.; Herath, T. N.; McEwen, C. N., Laserspray Ionization, a New Atmospheric Pressure MALDI Method for Producing Highly Charged Gas-phase Ions of Peptides and Proteins Directly from Solid Solutions*. *Mol Cell Proteomics* **2010,** *9* (2), 362-7.
243. Trimpin, S., "Magic" Ionization Mass Spectrometry | SpringerLink. *Jounral of the american Society for Mass Spectrometry* **2016,** *27* (1), 4-21.
244. Hood, M. I.; Mortensen, B. L.; Moore, J. L.; Zhang, Y.; Kehl-Fie, T. E.; Sugitani, N.; Chazin, W. J.; Caprioli, R. M.; Skaar, E. P., Identification of an *Acinetobacter baumannii* Zinc Acquisition System that Facilitates Resistance to Calprotectin-mediated Zinc Sequestration. *PLoS Pathogens* **2012,** *8* (12), e1003068.
245. Moore, J. L.; Becker, K. W.; Nicklay, J. J.; Boyd, K. L.; Skaar, E. P.; Caprioli, R. M., Imaging mass spectrometry for assessing temporal proteomics: Analysis of calprotectin in *Acinetobacter baumannii* pulmonary infection. *Proteomics* **2013**, in press.
246. Stewart, P.; Franklin, M., Physiological heterogeneity in biofilms. *Nature Reviews Microbiology* **2008,** *6*, 199-210.
247. Phillips, N. J.; Steichen, C. T.; Schilling, B.; Post, D. M. B.; Niles, R. K.; Bair, T. B.; Falsetta, M. L.; Apicella, M. A.; Gibson, B. W., Proteomic Analysis of *Neisseria gonorrhoeae* Biofilms Shows Shift to Anaerobic Respiration and Changes in Nutrient Transport and Outermembrane Proteins. *PLoS ONE* **2012,** *7* (6), e38303.
248. Lima, T. B.; Pinto, M. F.; Ribeiro, S. M.; de Lima, L. A.; Viana, J. C.; Gomes Junior, N.; Candido Ede, S.; Dias, S. C.; Franco, O. L., Bacterial resistance mechanism: what proteomics can elucidate. *Faseb j* **2013,** *27* (4), 1291-303.
249. Sogawa, K.; Watanabe, M.; Sato, K.; Segawa, S.; Ishii, C.; Miyabe, A.; Murata, S.; Saito, T.; Nomura, F., Use of the MALDI BioTyper system with MALDI-TOF mass spectrometry for rapid identification of microorganisms. *Analytical and Bioanalytical Chemistry* **2011,** *400* (7), 1905-1911.
250. Floyd, K. A.; Moore, J. L.; Good, J. A. D.; Eberly, A. R.; Shaffer, C. L.; Zaver, H.; Almqvist, F.; Skaar, E. P.; Caprioli, R. M.; Hadjifrangiskou, M., Adhesive fiber stratification in uropathogenic *Escherichia coli* biofilms unveils oxygen-mediated control of type 1 pili. *PLoS Pathogens* **2015,** (In Review).

CURRICULUM VITAE

Jessica L. Moore

1021 Mitchell Road • Nashville, TN 37206
Jessica.Lindsey.Moore@Gmail.com • 573.820.2470

Education

- Doctor of Philosophy in Chemistry – in progress. Vanderbilt University, Nashville, TN
  Expected Graduation May 2017 CGPA: 3.84/4.00
- Master of Science in Chemistry – Murray State University, Murray, KY
  December 2011 CGPA: 3.85/4.00
- Bachelor of Science in Chemistry and Music Performance – Murray State University, Murray, KY
  May 2009, Honors Diploma, Magna Cum Laude CGPA: 3.79/4.00

Dissertation Abstract

Disease is characterized by signature molecular changes in affected tissues and organs. Diseases cause disruption and dysregulation of a number of biological molecules, including proteins, lipids, metal, and small molecules. Understanding the spatial distribution of biomolecules as it relates to human disease is incredibly important; it represents a way to study disease-associated changes in tissues. This work utilizes Imaging Mass Spectrometry (IMS), a discovery-based analytical approach that enables the detection of biological molecules spatially within diseased tissues, to study infectious diseases. IMS discovered molecular changes specific to areas in the tissue where pathogens interact with their vertebrate hosts. This region, deemed the pathogen-host interface, presents a wealth of information about how vertebrate hosts defend themselves from invading pathogens, including the accumulation and oxidative damage of the metal-chelating host protein calprotectin. In response to metal-starvation, bacteria also exhibit characteristic changes that are observable by mass spectrometry. Further study of these interactions is paramount to the understanding of microbial pathogenesis and to the continued treatment of infectious diseases.

Publications

- James E. Cassat, **Jessica L. Moore,** Kevin J Wilson, Zach Stark, Boone M. Prentice, Raf Van de Plas, Yaofang Zhang, Jack M. Virostko, Daniel C. Colvin, Kristie L. Rose, Audra M. Judd, Michelle L. Reyzer, Jeffrey M. Spraggins, John C. Gore, Richard Caprioli, and Eric Skaar. A Multi-Modality Imaging Platform for Identifying Molecular Alterations at the Host-Pathogen Interface. In progress
- Lillian J. Juttukiond, Matthew T. Stier, **Jessica L. Moore,** Yaofang Zhang, Jonathan E. Schmitz, William N. Beavers, Christiaan D. Wijers, Thomas Kehl-Fie, James Atkinson, R. Stokes Peebles, Richard M. Caprioli, Eric P. Skaar. Dietary Manganese Promotes Staphylococcal infection of the heart. Submitted
- **Jessica L. Moore**, Audra M. Judd, Emily Pennick, Thomas P. Conrads, Richard M. Caprioli, Jeremy L. Norris. Spatial Analysis of Ovarian Cancer Biopsies by Imaging Mass Spectrometry and

Hydrogel-Assisted Proteomics. Methods in Molecular Biology, Endometrial Cancer: Methods and Protocols. Submitted.

- **Jessica L. Moore,** Eric P. Skaar. MALDI Mass Spectrometry and Infectious Diseases. Proceedings of the NATO Advanced Study Institute for Threat Detection. Accepted.
- David G. Rizzo, Boone M. Prentice, **Jessica L. Moore,** Jeremy L. Norris, Richard M. Caprioli. Enhanced Spatially Resolved Proteomics Using On-Tissue Hydrogel-Mediated Protein Digestion. Analytical Chemistry, Accepted.
- Joseph P. Zackular, **Jessica L. Moore,** Ashley T. Jordan, Lillian J. Juttukonda, Michael J. Noto, Maribeth R. Nicholson, Jonathan D. Crews, Matthew W. Semler, Yaofang Zhang, Lorraine B. Ware, M. Kay Washington, Walter J. Chazin, Richard M. Caprioli, Eric P. Skaar. Dietary Zinc Alters the Microbiota and Decreases Resistance to *Clostridium difficile* Infection, 2016, 22, 1330-1334
- Catherine A. Wakeman[*], **Jessica L. Moore[*],** Michael J. Noto, Yaofang Zhang, Marc D. Singleton, Boone M. Prentice, Benjamin A. Gilston, Ryan S. Doster, Jennifer A. Gaddy, Walter J. Chazin, Richard M. Caprioli[*], Eric P. Skaar[*]. The Innate Immune Protein Calprotectin Promotes *Pseudomonas aeruginosa* and *Staphylococcus aureus* Interaction. *Nature Communications*, 2016, 7, 11951
- Jeffrey M. Spraggins, David G. Rizzo, **Jessica L. Moore**, Michael J. Noto, Eric P. Skaar, Richard M. Caprioli, Next-generation Technologies for Spatial Proteomics: Integrating Ultra-high Speed MALDI TOF and High Mass Resolution MALDI FTICR Imaging Mass Spectrometry for Protein Analysis. *Proteomics*, 2016, 16, 11-12, 1678-1689
- Jeffrey M. Spraggins, David G. Rizzo, **Jessica L. Moore**, Kristie L. Rose, Neal D. Hammer, Eric P. Skaar, Richard M. Caprioli, MALDI FTICR IMS of Intact Proteins: Using Mass Accuracy to Link Protein Images with Proteomics Data. *Journal of the American Society for Mass Spectrometry*, 2015, 26, 6, 974-985
- Kyle A. Floyd, **Jessica L. Moore,** Allison R. Eberly, James A. D. Good, Carrie L. Shaffer, Himesh Zaver, Fredrik Almqvist, Eric P. Skaar, Richard M. Caprioli, Maria. Hadjifrangiskou, Adhesive Fiber Stratification in Uropathogenic Escherichia coli Biofilms Unveils Oxygen-Mediated Control of Tyle 1 Pili. *PLoS Pathogens*, 2015, 11(3), e1004697
- **Jessica L. Moore,** Richard M. Caprioli*, Eric P. Skaar*, Advanced Mass Spectrometry Technologies for the Study of Microbial Pathogenesis. *Current Opinion in Microbiology*, 2014, 19, 45-51
- **Jessica L. Moore***, Kyle W. Becker*, Joshua J. Nicklay, Kelli L. Boyd, Eric P. Skaar*, Richard M. Caprioli*. Imaging mass spectrometry for assessing temporal proteomics: Analysis of calprotectin in Acinetobacter baumannii pulmonary infection. *Proteomics*, 2014, 14(7-8,) 820-828
- Thomas E. Kehl-Fie, Yaofang Zhang, **Jessica L. Moore**, Allison J. Farrand, M. Indriati Hood, Subodh Rathi, Walter J. Chazin, Richard M. Caprioli, and Eric P. Skaar. MntABC and MntH contribute to systemic Staphylococcus aureus infection by competing with calprotectin for nutrient manganese. *Infection and Immunity*. 2013 81(9), 3395-3405
- Laura A. Mike, Brendan F. Dutter, Devin L. Stauff, **Jessica L. Moore**, Nicholas P. Vitko, Olusegun Aranmolate, Thomas E. Kehl-Fie, Sarah Sullivan, Paul R. Reid, Jennifer L. DuBois, Anthony R. Richardson, Richard M. Caprioli, Gary A. Sulikowski, and Eric P. Skaar. Activation of heme biosynthesis by a small molecule that is toxic to fermenting Staphylococcus aureus. *Proceedings of the National Academy of Sciences of the United States of America*. 110(20), 8206-8211
- M. Indriati Hood, Brittany L. Mortensen, **Jessica L. Moore**, Yaofang Zhang, Thomas E. Kehl-Fie, Norie Sugitani, Walter J. Chazin, Richard M. Caprioli, Eric P. Skaar. Identification of an Acinetobacter baumannii Zinc Acquisition System that Facilitates Resistance to Calprotectin-mediated Zinc Sequestration. *PLoS Pathogens* 8(12): e1003068. doi:10.1371/journal.ppat.1003068
- Masters Thesis: "Construction, Standardization, and Implementation of a Centrifugally-Driven

Microfluidic Device." December 2012

- **Jessica L. Moore,** Austin McCuiston, Isaac Mittendorf, Rudy Ottway, R. Daniel Johnson. Behavior of Capillary Valves in Centrifugal Microfluidic Devices Prepared by Three-Dimensional Printing. *Microfluidics and Nanofluidics.* 2011, 10(4), 877-888
- Undergraduate Senior Honors Thesis: " The Age of the Castrati: A Lasting Legacy" May 2009. Murray State University Honors Program
- Senior Chemistry Research: "Construction of a Centrifugal Microfluidic Platform." May 2009. Murray State University Department of Chemistry

Presentations

- **Jessica L. Moore,** Neal D. Hammer, Kristie L. Rose, Jeffrey M. Spraggins, James Cassat, Eric P. Skaar, Richard M. Caprioli. "Redefining the Pathogen-Host Interaction: Imaging Mass Spectrometry Reveals *Staphylococcus aureus* Proteins with Host Tissues." Oral Presentation, 64th Conference on Mass Spectrometry and Allied Topics, June 5-9, 2016, San Antonio, TX
- **Jessica L. Moore**, Catherine A. Wakeman, Michael J. Noto, Boone M. Prentice, Jeffrey M. Spraggins, Michael Becker, Jeremy L. Norris, Eric P. Skaar, Richard M. Caprioli "Nutrient Sequestration at the Pathogen-Human Host Interface: Imaging Mass Spectrometry reveals subpopulations in Bacterial Biofilms." Poster, 63rd Conference on Mass Spectrometry and Allied Topics, May 31-June 4, 2015, St. Louis, MO
- **Jessica L. Moore**, "MALDI Imaging Mass Spectrometry: Providing Molecular Insight at the Host-Pathogen Interface." Oral Presentation, Mass Spectrometry: Applications to the Clinical Laboratory 2015 Annual Conference, San Diego, CA, March 30th, 2015
- **Jessica L. Moore**, "What Does the phox Say?" Oral Presentation, Vanderbilt University 3 Minutes Thesis Competition, Nashville, TN, March 27th, 2015
- **Jessica L. Moore**, "MALDI Imaging Mass Spectrometry: Providing Molecular Insight at the Host-Pathogen Interface." Oral Presentation, Chemical Biology Association of Students Seminar Series, Vanderbilt University, Nashville, TN March 2nd, 2015
- **Jessica L. Moore,** Jeffrey M. Spraggins, Neal D. Hammer, Kristie L. Rose, Eric P. Skaar, Richard M. Caprioli,"Oxidative Damage During *Staphylococcus aureus* Infection Revealed by High Mass Resolution MALDI Protein Imaging." Poster, 62nd Conference on Mass Spectrometry and Allied Topics, June 15-19, 2014, Baltimore MD
- **Jessica L. Moore,** Yaofang Zhang, Thomas E. Kehl-fie, Joshua J. Nicklay, Eric P. Skaar, Richard M. Caprioli, "Multimodality Imaging Mass Spectrometry for Co-localization of Trace Metals and Proteins in Murine Tissue Abscesses Elicited from *Staphylococcus aureus* Infection.: Poster, Vanderbilt Institute for Chemical Biology [VICB] Student Research Symposium Poster Session, August 8, 2013
- **Jessica L. Moore,** Yaofang Zhang, Thomas E. Kehl-fie, Joshua J. Nicklay, Eric P. Skaar, Richard M. Caprioli, "Multimodality Imaging Mass Spectrometry for Co-localization of Trace Metals and Proteins in Murine Tissue Abscesses Elicited from *Staphylococcus aureus* Infection." Poster, Chemistry-Biology Interface (CBI) Career Development Conference at the University of Illinois Urbana-Champaign, June 5-7, 2013
- **Jessica L. Moore,** Yaofang Zhang, Thomas E. Kehl-fie, Joshua J. Nicklay, Eric P. Skaar, Richard M. Caprioli, "Multimodality Imaging Mass Spectrometry for Co-localization of Trace Metals and Proteins in Murine Tissue Abscesses Elicited from *Staphylococcus aureus* Infection." Poster, 61st Conference on Mass Spectrometry and Allied Topics, June 9-13, 2013, Minneapolis, Mn
- **Jessica L. Moore,** Kyle W. Becker, Joshua J. Nicklay, Kelli Boyd, Eric P. Skaar, Richard M. Caprioli. "Assessing Temporal Proteomics using Imaging Mass Spectrometry in an *Acinetobacter baumannii* Pulmonary Infection" Vanderbilt Institute for Chemical Biology [VICB] 10th Anniversary Research Symposium Poster Session, March 12, 2013

- **Jessica L. Moore,** M. Indriati Hood, Erin H. Seeley, Eric P. Skaar, Richard M. Caprioli. "Imaging Mass Spectrometry as an Analytical Tool to Study Immune Response to Bacterial Challenge." Vanderbilt Institute for Chemical Biology [VICB] Student Research Symposium Poster Session, August 9, 2012
- **Jessica L. Moore**, Elizabeth Ellison, R. Daniel Johnson. "Rotating Disk Microfluidic Platforms prepared by Three-Dimensional Printing." The Pittsburg Conference for Analytical Chemistry, Atlanta, GA. March 13-18, 2011
- **Jessica L. Moore**, Elizabeth Ellison, R. Daniel Johnson. "Rotating Disk Microfluidic Platforms prepared by Three-Dimensional Printing." Kentucky EPSCOR Conference Poster Session, Lexington, KY. May 2010
- **Jessica L. Moore,** "Construction of a Three Dimensional Microfluidic Platform." Oral Presentation at the University of Tennessee at Martin. American Chemical Society Regional Meeting. April 10, 2010
- **Jessica L. Moore,** "The Castrati in Opera" Murray State University Scholars Week Presentation, May 2009
- **Jessica L. Moore,** "Samuel Barber's 'Hermit Songs'" Kentucky Honors Roundtable, Murray, KY. Lecture Recital, Spring 2009
- Senior Vocal Recital, March 2009
- **Jessica L. Moore,** "Voicing Gender in Baroque Opera." Kentucky Honors Round Table. University of Louisville, Fall 2008
- **Jessica L. Moore,** "Health Care in Mexico," Murray State University International Education Week Speaker, Spring 2007
- International Education Week Panelist. Spring 2007. "Study Abroad Program at Murray State University"
- **Jessica L. Moore,** "The Castrati in Opera," Southern Regional Honors Round table, Baton Rouge, Louisiana. Fall 2006
- **Jessica L. Moore,** "The Castrati in Opera," Kentucky Honors Round Table. University of Kentucky. Fall 2006
- **Jessica L. Moore, Charlie A. Adams,** "Alcoholism on Murray State's Campus," Kentucky Honors Round Table, University of Kentucky, Spring 2005

Research Experience

Vanderbilt University National Institute for Imaging Mass Spectrometry: Research Assistant
January 2012-Present
My current dissertation work focuses on integrating Imaging Mass Spectrometry technologies into the study of infectious diseases and the pathogen-host interaction. This work is performed under the direction of Dr. Richard Caprioli and Dr. Eric Skaar.

Murray State University Department of Chemistry Teaching Assistant
Fall 2010-Spring 2011
I taught laboratory sections of Chemistry 201 and 202, Basic College Chemistry; I also taught study and review sessions for Basic College Chemistry and Introduction to Chemistry, Chemistry 101 and 105.

Murray State University Department of Chemistry Research Assistant
Summer 2009-Spring 2011
I studied fluid dynamics of centrifugal microfluidics devices for point of care diagnostics under the direction of Dr. Daniel Johnson.

Graduate Awards

- Fall 2015 Vanderbilt Prize Scholar Student Award Recipient
- 2015 Vanderbilt Institute for Chemical Biology Prize finalist, Awarded Oral Presentation Award
- Fall 2014 Vanderbilt University Department of Chemistry Warren Graduate Research Fellow
- 2012 Vanderbilt University Chemical Biology Interface Training Grant Recipient (T32GM 065086)
- 2011-2012 Vanderbilt Institute for Chemical Biology Research Fellowship Recipient
- 2011-2012 Vanderbilt University David Hercules Fellowship Recipient
- 2010-2011 Murray State University Innovation Research Fellowship Recipient, August 2010-May 2011
- 2010-2011 Murray State University Hattie Mayme Ross Graduate Fellowship Recipient, August 2010-May 2011
- 2009-2010 Omicron Delta Kappa Leader of the Year Award Murray State University
- 2009-2010 Omicron Delta Kappa Leader of the Year Award (Regional)
- 2009-2010 Carl Fisher Book Award Recipient (Omicron Delta Kappa Outstanding Leader Award)

Teaching Experience

- Stratford High School Science Program Guest Lecturer, Fall 2016
- Advanced Imaging Mass Spectrometry Short Course Instructor
    - Microtome and Cryostat
    - Protein Identification
    - Histology-Directed Mass Spectrometry: Labcyte Acoustic Spotter
    - Time-of-Flight Mass Spectrometry
- National Institute for Imaging Mass Spectrometry Lecture Series Leader
    - ICP-MS, LA-ICP-MS, Magnetic Sector Mass Analyzers
    - Electron Transfer Dissociation
- CPBP 320, Foundations of Chemical Biology teaching assistant, Vanderbilt University, Spring 2013
- Vanderbilt Program for Talented Youth, The Chemistry of Everyday Things, Summer 2013
- Chemistry 201 and 202, General College Chemistry, Murray State University, Fall 2010-Spring 2011
- Vanderbilt University Aspirnaut Program, Summer 2014
    - Served as a mentor to an undergraduate researcher
- Undergraduate Research Mentor
    - Vanderbilt University, 2014-2016. I managed one undergraduate researcher in the field of Chemistry
    - Vanderbilt Aspirnaut Program, Summer 2015. I designed research strategies for a high school student summer researcher
    - Murray State University, 2009-2011. I managed two undergraduate researchers in the field of Chemistry